Advances in Materials Science and Engineering

The Influence of Bio, Physical, and Mechanical Attrition in Tribology

Lead Guest Editor: Adam Khan M
Guest Editors: JT Winowlin Jappes, Waleed Fekry Faris, and Temel Varol

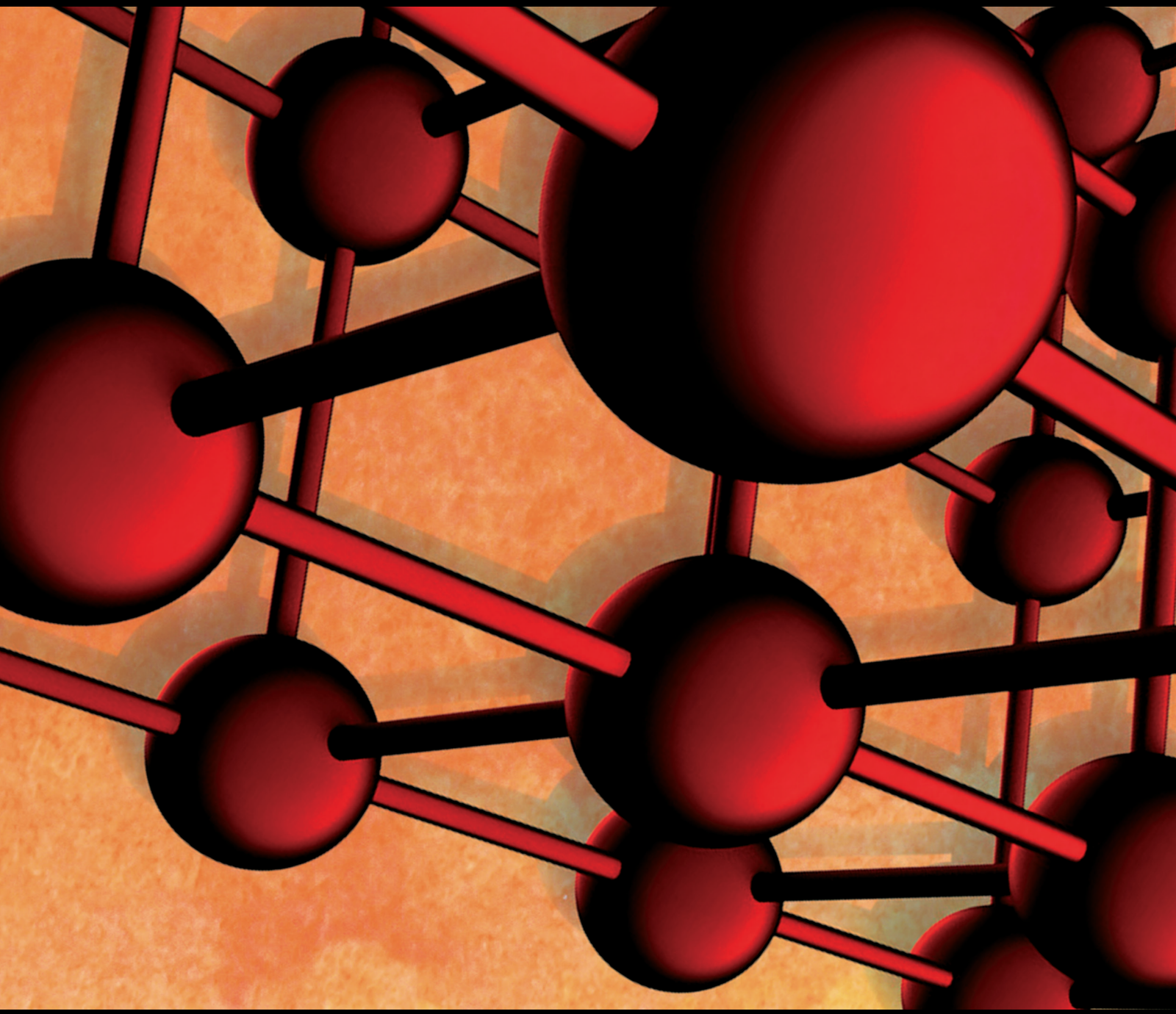

The Influence of Bio, Physical, and Mechanical Attrition in Tribology

Advances in Materials Science and Engineering

The Influence of Bio, Physical, and Mechanical Attrition in Tribology

Lead Guest Editor: Adam Khan M
Guest Editors: JT Winowlin Jappes, Waleed Fekry Faris, and Temel Varol

Copyright © 2022 Hindawi Limited. All rights reserved.

This is a special issue published in “Advances in Materials Science and Engineering.” All articles are open access articles distributed under the Creative Commons Attribution License, which permits unrestricted use, distribution, and reproduction in any medium, provided the original work is properly cited.

Chief Editor

Amit Bandyopadhyay, USA

Associate Editors

Vamsi Balla, India
Mitun Das, USA
Sandip Harimkar, USA
Ravi Kumar, India
Peter Majewski, Australia
Enzo Martinelli, Italy
Luigi Nicolais, Italy
Carlos R. Rambo, Brazil
Michael J. Schütze, Germany
Kohji Tashiro, Japan
Zhonghua Yao, China
Dongdong Yuan, China
Wei Zhou, China

Academic Editors

Antonio Abate, Germany
Hany Abdo, Saudi Arabia
H.P.S. Abdul Khalil, Malaysia
Ismael alejandro Aguayo villarreal, Mexico
Sheraz Ahmad, Pakistan
Michael Aizenshtein, Israel
Jarir Aktaa, Germany
Bandar AlMangour, Saudi Arabia
Huaming An, China
Alicia Esther Ares, Argentina
Siva Avudaiappan, Chile
Habib Awais, Pakistan
NEERAJ KUMAR BHOI, India
Enrico Babilio, Italy
Renal Backov, France
M Bahubalendruni, India
Sudharsan Balasubramanian, India
Markus Bambach, Germany
Irene Bavasso, Italy
Stefano Bellucci, Italy
Brahim Benmokrane, Canada
Jean-Michel Bergheau, France
Guillaume Bernard-Granger, France
Giovanni Berselli, Italy
Patrice Berthod, France
Michele Bianchi, Italy
Hugo C. Biscaia, Portugal
Antonio Boccaccio, Italy
Mohamed Bououdina, Saudi Arabia
Gianlorenzo Bussetti, Italy
Antonio Caggiano, Germany
Marco Cannas, Italy
Qi Cao, China
Gianfranco Carotenuto, Italy
Paolo Andrea Carraro, Italy
Jose Cesar de Sa, Portugal
Wen-Shao Chang, United Kingdom
Qian Chen, China
Francisco Chinesta, France
Er-Yuan Chuang, Taiwan
Francesco Colangelo, Italy
María Criado, Spain
Enrique Cuan-Urquizo, Mexico
Lucas Da Silva, Portugal
Angela De Bonis, Italy
Abílio De Jesus, Portugal
José António Fonseca De Oliveira Correia, Portugal
Ismail Demir, Turkey
Luigi Di Benedetto, Italy
Maria Laura Di Lorenzo, Italy
Marisa Di Sabatino, Norway
Luigi Di Sarno, Italy
Ana María Díez-Pascual, Spain
Guru P. Dinda, USA
Hongbiao Dong, China
Mingdong Dong, Denmark
Frederic Dumur, France
Stanislaw Dymek, Poland
Kaveh Edalati, Japan
Philip Eisenlohr, USA
Luís Evangelista, Norway
Michele Fedel, Italy
Francisco Javier Fernández Fernández, Spain
Isabel J. Ferrer, Spain
Massimo Fresta, Italy
Samia Gad, Egypt
Pasquale Gallo, Finland
Sharanabasava Ganachari, India
Santiago Garcia-Granda, Spain
Carlos Garcia-Mateo, Spain

Achraf Ghorbal, Tunisia
Georgios I. Giannopoulos, Greece
Ivan Giorgio, Italy
Andrea Grilli, Italy
Vincenzo Guarino, Italy
Daniel Guay, Canada
Jenö Gubicza, Hungary
Xuchun Gui, China
Benoit Guiffard, France
Zhixing Guo, China
Ivan Gutierrez-Urrutia, Japan
Weiwei Han, Republic of Korea
Simo-Pekka Hannula, Finland
A. M. Hassan, Egypt
Akbar Heidarzadeh, Iran
Yi Huang, United Kingdom
Joshua Ighalo, Nigeria
Saliha Ilican, Turkey
Md Mainul Islam, Australia
Ilia Ivanov, USA
Jijo James, India
Hafsa Jamshaid, Pakistan
Hom Kandel, USA
Kenji Kaneko, Japan
Rajesh Kannan A, Democratic People's Republic of Korea
Mehran Khan, Hong Kong
Akihiko Kimura, Japan
Ling B. Kong, Singapore
Pramod Koshy, Australia
Hongchao Kou, China
Alexander Kromka, Czech Republic
Abhinay Kumar, India
Avvaru Praveen Kumar, Ethiopia
Sachin Kumar, India
Paweł Kłosowski, Poland
Wing-Fu Lai, Hong Kong
Luciano Lamberti, Italy
Fulvio Lavecchia, Italy
Laurent Lebrun, France
Joon-Hyung Lee, Republic of Korea
Cristina Leonelli, Italy
Chenggao Li, China
Rongrong Li, China
Yuanshi Li, Canada
Guang-xing Liang, China
Barbara Liguori, Italy
Jun Liu, China
Yunqi Liu, China
Rong Lu, China
Zhiping Luo, USA
Fernando Lusquiños, Spain
Himadri Majumder, India
Dimitrios E. Manolakos, Greece
Necmettin Maraşlı, Turkey
Alessandro Martucci, Italy
Roshan Mayadunne, Australia
Mamoun Medraj, Canada
Shazim A. Memon, Kazakhstan
Pratima Meshram, India
Mohsen Mhadhbi, Tunisia
Philippe Miele, France
Andrey E. Miroshnichenko, Australia
Ajay Kumar Mishra, South Africa
Hossein Moayedi, Vietnam
Dhanesh G. Mohan, United Kingdom
Sakar Mohan, India
Namdev More, USA
Tahir Muhmood, China
Faisal Mukhtar, Pakistan
Dr. Tauseef Munawar, Pakistan
Roger Narayan, USA
Saleem Nasir, Pakistan
Elango Natarajan, Malaysia
Rufino M. Navarro, Spain
Miguel Navarro-Cia, United Kingdom
Behzad Nematollahi, Australia
Peter Niemz, Switzerland
Hiroshi Noguchi, Japan
Dariusz Oleszak, Poland
Laurent Orgéas, France
Togay Ozbakkaloglu, United Kingdom
Marián Palcut, Slovakia
Davide Palumbo, Italy
Gianfranco Palumbo, Italy
Murlidhar Patel, India
Zbyšek Pavlík, Czech Republic
Alessandro Pegoretti, Italy
Gianluca Percoco, Italy
Andrea Petrella, Italy

Claudio Pettinari, Italy
Giorgio Pia, Italy
Candido Fabrizio Pirri, Italy
Marinos Pitsikalis, Greece
Alain Portavoce, France
Simon C. Potter, Canada
Ulrich Prahl, Germany
Veena Ragupathi, India
Kawaljit singh Randhawa, India
Baskaran Rangasamy, Zambia
Paulo Reis, Portugal
Hilda E. Reynel-Avila, Mexico
Yuri Ribakov, Israel
Aniello Riccio, Italy
Anna Richelli, Italy
Antonio Riveiro, Spain
Marco Rossi, Italy
Fernando Rubio-Marcos, Spain
Francesco Ruffino, Italy
Giuseppe Ruta, Italy
Sachin Salunkhe, India
P Sangeetha, India
Carlo Santulli, Italy
Fabrizio Sarasini, Italy
Senthil Kumaran Selvaraj, India
Raffaele Sepe, Italy
Aabid H Shalla, India
Poorva Sharma, China
Mercedes Solla, Spain
Tushar Sonar, Russia
Donato Sorgente, Italy
Charles C. Sorrell, Australia
Damien Soulat, France
Adolfo Speghini, Italy
Antonino Squillace, Italy
Koichi Sugimoto, Japan
Jirapornchai Suksaeree, Thailand
Baozhong Sun, China
Sam-Shajing Sun, USA
Xiaolong Sun, China
Yongding Tian, China
Hao Tong, China
Achim Trampert, Germany
Tomasz Trzepieciński, Poland
Kavimani V, India
Matjaz Valant, Slovenia
Mostafa Vamegh, Iran
Lijing Wang, Australia
Jörg M. K. Wiezorek, USA
Guosong Wu, China
Junhui Xiao, China
Guoqiang Xie, China
YASHPAL YASHPAL, India
Anil Singh Yadav, India
Yee-wen Yen, Taiwan
Hao Yi, China
Wenbin Yi, China
Tetsu Yonezawa, Japan
Hiroshi Yoshihara, Japan
Bin Yu, China
Rahadian Zainul, Indonesia
Lenka Zaji#c#kova#, Czech Republic
Zhigang Zang, China
Michele Zappalorto, Italy
Gang Zhang, Singapore
Jinghuai Zhang, China
Zengping Zhang, China
You Zhou, Japan
Robert Černý, Czech Republic

Contents

Hindawi
Advances in Materials Science and Engineering
Volume 2022, Article ID 2165855, 16 pages
https://doi.org/10.1155/2022/2165855

Review Article

Effect of Nanomaterials on Tribological and Mechanical Properties of Polymer Nanocomposite Materials

M. S. Senthil Kumar,[1] Chithirai Pon Selvan,[2] K. Santhanam,[3] A. Kadirvel,[4] V. Chandraprabu ,[5] and L. SampathKumar[6]

[1]*Department of Mechanical Engineering, Builders Engineering College, Nathakadaiyur,Tirupur District, Kangeyam 638108, India*
[2]*Science and Engineering, Curtin University, Dubai International Academic City, Block 11,Fourth Floor,P. O. Box 345031, Dubai, UAE*
[3]*Department of Mechanical Engineering, K. S. Rangasamy College of Technology, Thokkavadi,Namakkal District, Tiruchengode 637215, India*
[4]*Department of Mechanical Engineering, R.M.K. Engineering College, Kavaraipettai, Gummidipoondi Taluk, Tiruvallur District 601 206, India*
[5]*School of Mechanical, Chemical & Materials Engineering, Adama Science & Technology University, Adama, Ethiopia*
[6]*Department of Physics, Builders Engineering College, Nathakadaiyur,Tirupur District, Kangeyam 638108, India*

Correspondence should be addressed to V. Chandraprabu; v.chandraprabu@astu.edu.et

Received 26 January 2022; Revised 3 April 2022; Accepted 4 April 2022; Published 31 May 2022

Academic Editor: Adam Khan M

Copyright © 2022 M. S. Senthil Kumar et al. This is an open access article distributed under the Creative Commons Attribution License, which permits unrestricted use, distribution, and reproduction in any medium, provided the original work is properly cited.

The good adhesion and interfacial interaction between the nanomaterial and the matrix show that the low content polymer nanocomposite has better tribological and mechanical properties such as strength, modulus, fracture toughness, and fatigue properties. This phenomenon has attracted the attention of many researchers in this field for the past two decades. Nanomaterials are available in many forms, such as nanotubes, nanoclays, nanofibers, nanoparticles, and graphene depending on the shape. This article summarizes the mechanical test results of different nanocomposite materials under various operating conditions. In addition, the current research clearly describes various decisive factors that affect material properties, such as the dispersion of nanoparticles, clay tactoids, processing conditions, agglomeration, and distribution status. The tribological properties and fatigue resistance of nanocomposites are also discussed in this study. In addition, the article also discusses the related issues of incorporating nanomaterials into the matrix.

1. Introduction

Composite materials are used in various fields such as aerospace, automobiles, structural elements, construction, and sporting goods due to its high strength-to-weight ratio [1]. The rapid development of nanoscience makes it possible to clearly identify potential applications in many fields through continuous research. The main research on nanocomposites is obviously limited to two-phase nanocomposites (contains polymers modified by nanofillers), such as nanoclay/epoxy resin nanocomposites, but in some cases, researchers are studying three-phase composites (fiber reinforced with the nanofillers-modified polymers), such as nanoclay/epoxy/glass fiber nanocomposites to improve mechanical properties, as shown in Figure 1 [2].

Nowadays, some researchers have widely used various nanofillers in their research to improve the performance of composite materials as the performance of composite materials will increase significantly under low load on the matrix. The nanofiller contains at least one of the three external dimensions in the nanometer range of 1 nm or 10^{-3} μm or 10^{-9} m [3, 4]. Different types of thermoplastic

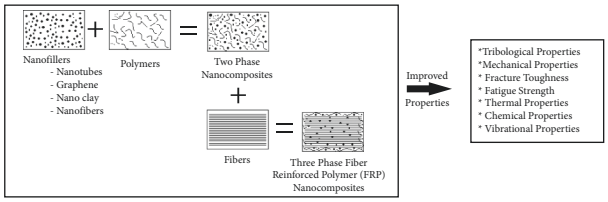

Figure 1: Scenario of property improvement by adding nanofillers with polymer and fiber.

and thermosetting polymer matrix like polyetherimide, polystyrene, polyester, epoxy, etc., are used to manufacture polymer matrix nanocomposite (PMNC) materials [5–8]. However, epoxy resin is a polymer matrix that is often used to make PMNC [9].

In general, depending upon the dimensions the nanofillers are classified as 1D (nanowires, nanorods, nanotubes, nanofibers), 2D (nanofilms, nanoplates, nanocoatings), and 3D (nanoparticles) [10, 11]. It is understood that carbon nanotubes (CNTs), halloysite nanotubes (HNTs), carbon nanofibers (CNFs) are the examples of 1D fibrous materials [8, 12–14]. Further, the 2D nanoclay contains a plate-like structure that has four groups such as smectite, illite, vermiculite, and kaolin-serpentine, and contains a high aspect ratio (30–1000) [6, 15]. Likewise, carbon black (CB), silica particles, fullerene, silica oxide, and titanium oxide are examples of 3D nanoparticles [12, 16].

Generally, the polymer matrix and the nanofiller are appropriately mixed through various methods, such as in-situ embedding polymerization, melt intercalation, polymer-particle direct mixing, in-situ polymerization, and sol-gel process [7, 17, 18]. However, among these various methods, the common methods for preparing polymer/nanomaterial mixtures are solution intercalation method, in-situ intercalation polymerization method, melt intercalation method, and direct in-situ synthesis method [19–23].

Based on the type and size of nanofiller, surface, aspect ratio, volume fraction, mixing method of polymer and nanofillers, operating parameters of mixing method, and the degree of mixing, researchers categorized four types of dispersions, namely, (1) phase separated or tactoid, (2) intercalated, (3) intercalated disordered, and (4) exfoliated [7, 8, 18, 24, 25]. In fact, the functioning of nanocomposites depends on the dispersion speed.

X-ray diffraction (XRD) and electron microscopy data confirmed the structure of the dispersed nano-filled polymer [8, 26]. Various researchers have shown that poor dispersion of the nanofiller/polymer mixture can cause agglomeration or factors in the matrix during their morphological studies. Using the method of nanocomposite materials, researchers found that the performance of nanocomposite materials will be reduced due to agglomeration. They also found that the lump formed led to a low degree of cross-linking of the filler matrix; however, with all the higher loads on the nanomaterials, agglomeration was inevitable [27–30].

The different varieties of agglomeration models were suggested by many researchers. The initial micromechanics model was developed by Shi et al. to study the waviness or curviness effect of carbon nanotubes [31]. Similarly, a lot of models were suggested by various researchers, for instance, the two-scale composite model and effective-medium theory used to predict the impact of graphene on the percolation threshold and overall conductivity [32, 33], micromechanics model to ascertain the coefficients of nonlinear thermal expansion of FRP laminates [34], a two-scale micromechanical model used to know the impact of nanotube collection and interface condition [35], Mori–Tanaka micromechanics method used to find the effect of elastic moduli [36], and Halpin–Tsai analytical models to find the effect of nanofiller loading on the thermal conductivity [37, 38].

In fact, the greater mechanical and thermal properties [25, 28–30], enhanced tribological properties [16, 39], superior morphological properties [7, 30], better dielectric properties [8, 32], increased vibration properties [26, 40], revised fatigue properties [41, 42], and commanding fracture toughness [43, 44] were attained for nanocomposites at low nanofiller loadings due to adhesion at the interface. Moreover, the interlaminar shear strength (ILSS) also increased greatly for the nanocomposites.

Mazumdar identified different manufacturing methods of the composite laminates like wet lay-up technique, pultrusion technique, resin transfer molding (RTM) process, vacuum-assisted resin transfer molding (VARTM) process, autoclave method, resin film infusion (RFI) process, prepreg technique, filament winding method, and fiber placement technique. Further, the researcher addressed that the degree of interaction between matrix and fiber is based upon the manufacturing methods. However, each method has certain disadvantages besides its advantages, for instance, void presence in wet lay-up technique, material accumulation at die in pultrusion technique, resin flow issue in RTM process, presence of dry spots in VARTM process, and higher fabrication in autoclave technique [45].

The current review provides detailed information about the effect of nanofiller reinforcements in nanocomposites on processing techniques of nanofiller/polymer blends, structure formation, manufacturing technique, characterization of nanocomposites, comparison of material properties with neat composites, and processability issues of nanocomposites. Moreover, this attempt would certainly attract both academic and industrial researchers in the field of nanocomposites.

2. Tribological Properties

Zhang et al. synthesized a nanocomposite with a Nomex fabric mixture filled with Polyfluo 150 wax (PFW) and nano-SiO_2. Nomex fibers were initially coated with phenolic resin. Tribological effects indicate that the inclusion of Polyfluo 150 wax and nanoparticles preferentially causes wear and reduced coefficient of friction (COF) for laminates. This development improved the tribological properties such as anti-wear and friction-reducing capabilities of nanocomposites. Furthermore, the optimum content of nano-SiO_2 in Nomex fabric composites revised the tribology property considerably [46]. With the assist of the Hysitron

Tribo Indenter system, Gu et al. performed the micro/nanoscale indentation and scratch tests on epoxy/silica nanocomposites coatings. The test results revealed that the silica particles decreased the friction coefficient and scratch depth [47]. In an another friction and wear research, the tribological properties of the nanocoatings were examined. The coatings were constructed from the blend of hydrophilic nano-silica particles and epoxy resin. From the test results, it is clear that the nano-silica particle interestingly altered the tribological properties. Additionally, the filler-loaded coatings significantly improved the surface roughness and water contact angle characteristics than the base epoxy coating [48].

The study by Thakur and Chauhan [49] portrayed the tribological properties of vinyl ester nanocomposites loaded with three different equally sized micron and submicron cenosphere particles with a diameter 400 nm, 900 nm, and 2 μm. The research was carried out using the Taguchi design technique as the design of experiments (DOE). The Taguchi design was created with an L_{27} (36) orthogonal array which includes six factors and three different levels as shown below. Finally, analysis of variance (ANOVA) was used in order to evaluate the impact of parameters on the COF and sliding wear resistance at the dry sliding conditions.

Factors and levels of variables in the DOE:

(A) Load (N) (level 1:10, level 2:40, level 3:70)

(B) Filler size (mm) (level 1:2, level 2:0.9, level 3:0.4)

(C) Filler content (%) (level 1:2, level 2:6, level 3:10)

(D) Roughness (mm) (level 1:0.02, level 2:0.2, level 3:0.7)

(E) Sliding speed (m/s) (level 1:1.3, level 2:3.2, level 3: 5.7)

(F) Sliding distance (m) (level 1:2000, level 2:4000, level 3:6000)

The tribological test found out that the wear properties of the submicron size filler particles contribute notably by 21.18% and 11.58% better than that of the micro-sized particles. The DOE corroborates the load, and particle content had been the essential constraints among the other factors which influenced the COF by 68.33% and 9.81% and wear resistance by 63.89% and 13.39%. In general, the wear properties of laminates had elevated with increasing content of the cenosphere. Microscopic observations of the worn surfaces demonstrated that the superior properties are achieved to 400 nm cenosphere particles-filled vinyl ester composite due to the uniform and robust adhesion to the counterface. Further, the result portrayed that the significant wear resistance occurred to the 6 wt.% nanoparticles-filled composites. The major wear in the mechanism of panels is exchanged from the hard abrasive wear to moderate abrasive wear.

The research of Akil et al. targeted on finding the impact of two different filler reinforcements: one is particulate (talc particles of an average particle size less than 45 μm), and another one is fiber (chopped strands E-glass fiber) composites on the wear and friction properties. The panels contain GUR 4120 grade ultra-high molecular weight polyethylene (UHMWPE) modified with 100 nm size zinc oxide (ZnO) nanofillers with 10 wt.%. The nanocomposite was fabricated in the hot compression molding machine. The entire tribological study was tested in a pin-on-disk testing machine based on the response of the surface Box–Behnken design (BBD) which is shown in Figure 2. The different input variables were applied load, sliding speed, and sliding distance. Basically, BBD is an experimental design for response surface methodology which does not include embedded factorial or fractional factorial design. It requires three levels of each factor. The design uses 12 middle edge positions and three center positions [50].

The input variables were placed as shown below at one of three equally spaced values, usually as −1, 0, and +1(minimum, center, and maximum), statistically generated by the MINITAB 16 software. The impact of input variables on the wear loss and the average COF of hybrid composites were analyzed by the response surface methodology method. The ANOVA was conducted with a confidence level of 95% on each model. The mathematical models showcased that the input variables significantly affect the tribological properties of composites under the given range of variables. The compounded effects of load and sliding distance greatly influenced on the wear loss and COF for both hybrid composites. The glass fiber-reinforced laminates have shown superior wear properties and less severity of worn-out surfaces than the talc-reinforced laminates.

Independent variables and variation levels of the BBD:

(X1) Applied load (N) (variation level −1: 9.81, variation level 0: 19.62, variation level 1: 29.43)

(X2) Sliding speed (m/s) (variation level −1: 0.2094, variation level 0: 0.4188, variation level 1: 0.6282)

(X3) Sliding distance (m) (variation level −1: 125.64, variation level 0: 251.28, variation level 1: 376.92)

In another study, Akil et al. investigated the tribological performances of ZnO nanoparticles-reinforced UHMWPE composite and demonstrated the response of filler loadings from 5 to 20 wt.%. The wear test was carried out in dry sliding situations with load varying between 5 and 35 N, and sliding speed varying between 0.209 m/s to 0.419 m/s in opposition to the silicon carbide abrasive paper. Wear resistance significantly stepped forward at 10 wt.% ZnO/UHMWPE nanocomposite. The average coefficient of friction of the UHMWPE composite showed a downward fashion while reinforcing with ZnO nanoparticles. Further, the severity of wear of the worn surface was found to be decreased due to the ZnO nanoparticle reinforcement [51].

Louis Winnubst et al. inspected the friction and wear properties of nanocomposites, made up through the compression molding consisting of silica (SiO_2) particles of nanometer-sized blended in the nylon-6 polymer. During the test, in the pin-on-disk test, the flat pin made up of steel was running toward a composite disk. Compared with pure nylon 6, adding 2% by weight of SiO_2 particles can reduce friction by 0.5–0.18. As a result, the low silica content reduced the wear rate by 140 times. The adhesion and interlocking of material into metal asperities have developed

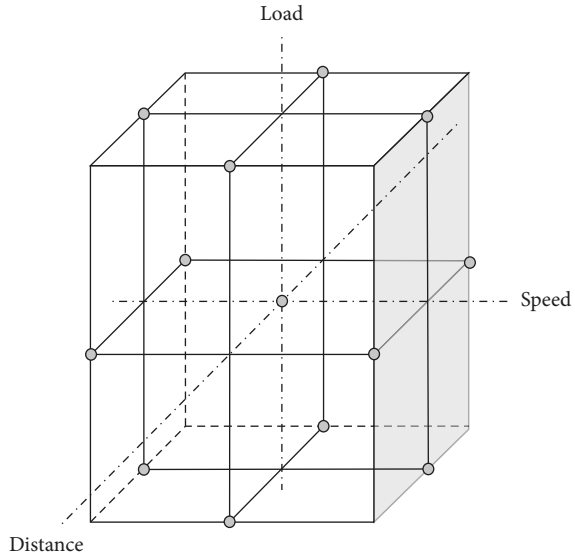

Figure 2: Box–Behnken design.

a transfer film over the steel pin. In addition, the test revealed two phenomena. First, the wear is based on the adhesion between the transfer film and the contact surface. The second is to use a transfer film to protect the polymer surface from metal roughness [52]. Similarly, a wear resistance study on the effect of SiC particles in laminated polyimide/SiC laminates obtained by hot dynamic compaction method confirmed that the abrasive and delamination were the dominant factors in wear mechanisms. In addition, the wear resistance of the samples filled with SiC nanoparticles decreases significantly with the increase in the number of SiC particles [16].

3. Tensile Strength

Qi et al. evaluated the material changes of nanocomposites that were prepared with the help of in-situ polymerization technique by including four types of montmorillonite (MMT) nanoclays, such as pristine (Na^+), Cloisite 30B (C30B), cetylpyridinium chloride (CPC), and Nanomer I.30E (NI.30E) in the base epoxy resin. The modulus of elasticity and fracture toughness are significantly improved [53]. In addition, as the load on the nanoclay increases, the tensile strength and deformation decrease significantly, as shown in Table 1. The declined trend could occur because of the improper dispersion rate of nanofillers in the matrix, which led to a high-stress concentration.

The researchers have dispersed different nanoclays in both thermoset and thermoplastic resins, for instance, Cloisite 15A, Cloisite 93A, and Cloisite Na dispersed with vinyl ester matrix by using ultrasonicator and twin-screw extruder [58], and Cloisite 30B and Cloisite 25A clays mixed with three resins diglycidyl ether of bisphenol A (DGEBA), hexanediol diglycidyl ether (HDE), and diglycidyl ether of bisphenol F (DGEBF) with the help of ultrasonicator [59]. Similarly, Cloisite Na+ and Cloisite 30B nanoclay content in epoxy [27] and Cloisite 25A nanoclay were dispersed with the aid of mechanical stirrer in epoxy resin [60]. Murthy et al. had obtained the tensile properties in the order of Cloisite 15A > Cloisite Na > Cloisite 93A [58]. Interestingly, Dorigatoa and Pegorettia detected the amplified tensile properties for smaller clay content [59]. Similarly, Basara et al. got better tensile properties for Cloisite 30B nanoclay at lower clay content than the Cloisite Na+ [27]. Contrarily, the authors notified the improved tensile modulus for both the nanoclays in increasing nanoclay content.

In another case, due to the presence of nanoclay, the analyst realized a reduction in the thermomechanical value [60]. The investigations of Panneerselvam and Daniel on polypropylene/Cloisite 15A nanocomposites and polymer matrix/spherical glass particle composites noticed a significant improvement in tensile strength for both materials [61]. However, when compared with nanocomposite materials, composite laminates have a commanding improvement in tensile strength.

Generally, carbon nanotubes (CNTs) are available in various forms like cup-stacked carbon nanotubes (CSCNTs), single-wall carbon nanotubes (SWCNTs), double-walled carbon nanotubes (DWCNTs), and multi-walled carbon nanotubes (MWCNTs). When CSCNT and MWCNT are dispersed together with the matrix, the tensile strength performance of the nanocomposite laminate has shown significant development as in Table 1. The tensile properties were enhanced commandingly when carbon fibers, basalt fibers, and polyacrylonitrile-based T650 and IM-7 carbon fibers were reinforced with the CNTs-functionalized matrix [54, 55, 62]. Besides that, some researchers had used different nanoreinforcements to functionalize the epoxy resins like Somasif ME-100 layered silicate [57] and nanocalcium carbonate (nano-$CaCO_3$) [63]. Table 1 expresses the experimental results of Kornmann et al. that the 10 wt.% nanocomposites were superior to the neat laminates. In a similar way, carbon fibers and carbon nanofibers are used to improve tensile properties by directly embedding them in a pure matrix or a matrix loaded with nanofillers [63–65].

Interestingly, Baur et al. directly grew multi-walled carbon nanotubes (MWCNTs) on two different polyacrylonitrile-based carbon fibers during the thermal chemical vapor deposition process [62]. As shown in Figure 3, the mixture of ferrocene/xylene vapor, argon, and hydrogen is heated from 700°C to 800°C in a quartz glass tube. Finally, CNTs were grown on the carbon fiber substrate inside the tube. The author studied in detail the chemical vapor deposition (CVD) growth conditions of individual fibers and the influence of MWCNT morphology. The tensile strength of the hybrid fiber depends on the type, size, or coating of the carbon fiber, temperature and growth time, and atmospheric conditions in the tube. In addition, the tensile strength of the sized carbon fiber decreases, in the initial stage of the carbon nanotube growth process. This phenomenon is due to the lack of organic materials at the growth temperature, leading to mechanical defects.

4. Flexural Strength

Manfredi et al. produced three E-type glass fiber-reinforced nanocomposites by adding 3 wt.% and 5 wt.% of Cloisite 30B, and 3 wt.% of Cloisite 10A nanoclays to the base matrix

Table 1: Tensile testing results of different nanocomposites.

Nanocomposites	Young's modulus (GPa)	Tensile strength (MPa)	Ref.
Neat DGEBA epoxy	2.71 ± 0.11	72.06 ± 1.37	[53]
2 wt.% Na+/DGEBA epoxy	2.79 ± 0.07	68.04 ± 4	[53]
5 wt.% Na+/DGEBA epoxy	2.92 ± 0.17	57.2 ± 2.22	[53]
10 wt.% Na+/DGEBA epoxy	3.44 ± 0.29	57.68 ± 3.69	[53]
2 wt.% C30B/DGEBA epoxy	3.11 ± 0.09	62.19 ± 2.56	[53]
5 wt.% C30B/DGEBA epoxy	3.10 ± 0.08	58.35 ± 5.87	[53]
10 wt.% C30B/DGEBA epoxy	3.12 ± 0.23	57.31 ± 6.97	[53]
2 wt.% NI.30E/DGEBA epoxy	2.68 ± 0.26	64.58 ± 6.56	[53]
5 wt.% NI.30E/DGEBA epoxy	2.82 ± 0.12	59.94 ± 9.01	[53]
10 wt.% NI.30E/DGEBA epoxy	3.04 ± 0.11	58.23 ± 4.39	[53]
2 wt.% CPC/DGEBA epoxy	2.57 ± 0.15	49.03 ± 2.72	[53]
5 wt.% CPC/DGEBA epoxy	2.79 ± 0.08	50.14 ± 2.80	[53]
Neat DGEBA epoxy/carbon fiber	46.5 ± 0.6	848 ± 18.2	[54]
5 wt.% CSCNT/DGEBA epoxy/carbon fiber	47.9 ± 0.7	844 ± 5.3	[54]
10 wt.% CSCNT/DGEBA epoxy/carbon fiber	48.3 ± 1.7	850 ± 40.0	[54]
Neat DGEBA epoxy/basalt fiber	27.65 ± 0.41	584.7 ± 10.3	[55]
0.5 wt.% raw MWCNT/DGEBA epoxy/basalt fiber	27.44 ± 0.76	564.0 ± 31.0	[55]
0.5 wt.% o-MWCNT(acid treated)/DGEBA epoxy/basalt fiber	30.41 ± 1.31	635.7 ± 33.8	[55]
0.5 wt.% PGE-MWCNT(phenyl glycidyl ether added)/DGEBA epoxy/basalt fiber	29.92 ± 0.83	608.8 ± 20.0	[55]
1.5 wt.% raw MWCNT/DGEBA epoxy/basalt fiber	28.53 ± 1.18	504.0 ± 42.0	[55]
1.5 wt.% o-MWCNT/DGEBA epoxy/basalt fiber	36.4 ± 0.97	627.7 ± 25.5	[55]
1.5 wt.% PGE-MWCNT/DGEBA epoxy/basalt fiber	34.90 ± 0.77	615.1 ± 19.7	[55]
1.25 wt.% attapulgite clay(ATT)/DGEBA epoxy/basalt fiber	29.85 ± 1.03	530.9 ± 43.4	[55]
2.5 wt.% ATT/DGEBA epoxy/basalt fiber	28.06 ± 2.62	465.4 ± 94.5	[55]
Neat poly(ethylene terephthalate) (PET) polyclear-machine direction (MD)	2.0 ± 0.1	62.6 ± 0.7	[56]
1 wt.% MWCNT/PET-MD	2.25 ± 0.07	66.9 ± 0.8	[56]
2 wt.% MWCNT/PET- MD	2.57 ± 0.08	72.5 ± 0.2	[56]
4 wt.% MWCNT/PET- MD	2.80 ± 0.32	89.1 ± 4.2	[56]
Neat PET-transverse direction (TD)	1.93 ± 0.01	59.0 ± 1.2	[56]
1 wt.% MWCNT/PET- TD	2.13 ± 0.08	65.4 ± 0.7	[56]
2 wt.% MWCNT/PET- TD	2.34 ± 0.20	68.2 ± 1.0	[56]
4 wt.% MWCNT/PET- TD	2.75 ± 0.08	76.5 ± 0.8	[56]
Neat DGEBA epoxy	3062 ± 47	80.3 ± 0.8	[57]
10 wt.% Somasif M-100/DGEBA epoxy	4719 ± 130	51.5 ± 1.4	[57]

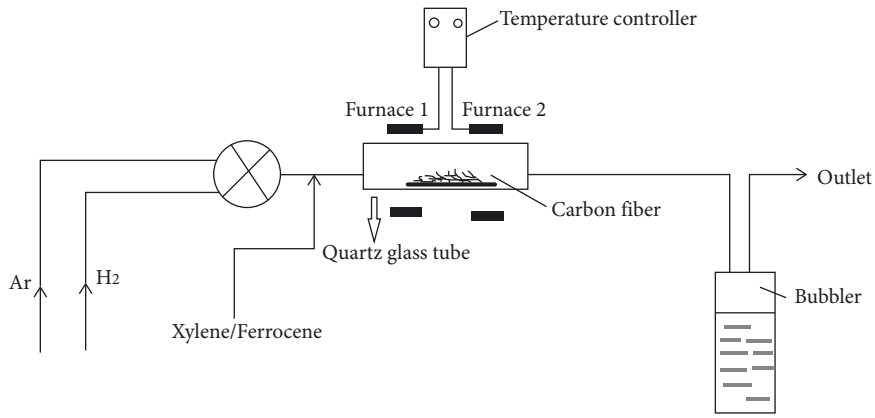

Figure 3: Schematic illustration for the development of CNT on the CF.

(epoxy resin) [66]. The mechanical properties, ILSS, and glass transition temperature were evaluated before and after immersing the sample in water. The study exposed that the higher flexural modulus and flexural strength have attained at 3 wt.% Cloisite 10A and 5 wt.% Cloisite 10A loaded glass fiber-reinforced polymer (GFRP) laminates, respectively. Through the water absorption test, the authors identified that the Cloisite 10A nanocomposites hold the less hydrophilic modifier, due to its superior flexural properties than the others. Furthermore, it was found that the reduced cross-linking density of the nanoclay results in absorbing more water than neat epoxy.

Hossain et al. had prepared the E-glass fiber-reinforced nanocomposites by VARTM machine by modifying the polyester resin with carbon nanofibers [67]. The flexural test on laminates revealed that commanding improvement on flexural strength and modulus was attained in nanocomposites than glass fiber-reinforced conventional composites. Karippal et al. had used Nanomer 1.30E nanoclay in the range of 0–6 wt.% to prepare epoxy/glass/nanoclay hybrid nanocomposite laminates through the use of the hand lay-up technique [25]. Based on the experimental results, the researchers concluded that the higher flexural properties were attained because of the best dispersion of 5 wt.% nanoclay in the base matrix. In the same manner, Sharma et al. synthesized Cloisite 30B (1, 3, and 5 wt.%)/epoxy resin/E-glass unidirectional fiber-reinforced nanocomposite laminates with the aid of using the usage of the hand lay-up method. Authors attained the commanding flexural strength for 5 wt.% clay loading GFRP laminates [68]. Again, the same trend was attained using 5 wt.% CNF-loaded carbon fiber/CNF/matrix nanocomposites. This trend took place because of the lesser open and closed porosity on the interface [69].

Alireza Ashori et al. analyzed the characteristics of wood-plastic composite (WPC) panels made of medium-density fiberboard and Cloisite 15A nanoclay residue sanding dust (SD). The polypropylene pellets, maleate-grafted polypropylene, SD, and nanoclay blends are first added in different proportions, and then the blends are directly fed into the counter-rotating twin-screw extruder. All the extruded filaments were pelletized by passing through a water bath, and finally, the pellets are placed in a hot press and made into a laminate. The flexural test shows that SD and nanoclay have achieved exceptional results in the flexural properties of the WPCs. By adding 2 wt.% of Cloisite 15A nanoclay to the matrix, the flexural strength is significantly improved, but the flexural properties are significantly reduced at 4% and 6% by weight. In contrast, due to the reduced adhesion in the fiber-matrix interface, the flexural properties of the laminate after the addition of SD are significantly reduced [70]. The flexural strength of polyamide 66/polypropylene (PA66/PP) mixture, graphite (Gr)-introduced PA66/PP, nanoclay-introduced PA66/PP, and short carbon fiber (SCF)-reinforced nanoclay-introduced PA66/PP laminates were studied. All composite panels use twin-screw extruder and injection molding. Experimental analysis shows that the presence of 2 wt.% nanoclay and 10% SCF increases the flexural strength and flexural modulus of the PA66/PP blend to 52 MPa and 1010 MPa, respectively [71].

In addition, electrospun polyether ketone nanofibers are applied to carbon fabrics to improve the flexural property of nanocomposites. In the course of their work, the researchers found that thinner nanofibers have higher bending properties, but as the thickness of the interlayer of nanofibers increases, these properties deteriorate [72]. Researchers added a small amount (0.25 wt.%) of electrospun glass nanofibers (EGNFs) to the epoxy resin/glass microfiber-reinforced hybrid nanocomposite made by the VARTM process, as shown in Figure 4, and achieved significant improvement in flexural properties. Xu and Hoa used hot melt lay-up and autoclave techniques to study the flexural properties of carbon fiber/epoxy/clay nanocomposite laminates [73]. The composite material made of carbon fiber-reinforced polymer (CFRP) has achieved a significant increase in flexural strength with 2 phr nanoclay loaded.

5. Compression Strength

Carbon nanofiber-reinforced hierarchical nanocomposites with multi-scale reinforcement fabrics have been synthesized in two stages by Minai et al. First, a multi-scale reinforced fabric (MRF) is synthesized by electrophoretic deposition of carboxylic acid or amine-functionalized CNF on the surface of a sized or unsized carbon fiber layer in an aqueous medium. In the next step, the MRF is placed first, and then the epoxy-amine resin mixture is poured into the resulting preform using a vacuum-assisted resin transfer molding machine. The superior compressive strength is attained to the resulting hierarchical nanocomposites with the amine-functionalized CNFs [74].

Uddin and Sun used nano-silica particles to modify DGEBA epoxy resin and developed a nano-silica/unidirectional glass fiber/epoxy laminate [75]. The uniform distribution of nano-silica particles in the epoxy resin significantly improves the longitudinal compressive strength. In addition, by incorporating nano-silica particles into epoxy resin, Manjunatha et al. [76] have achieved an equivalent increase in compressive strength. In their research, the authors used GFR nanocomposite laminates made by resin infusion under flexible tooling. Further, the compression test was carried out by Yokozeki et al. and proved evidence that there are no global buckling and no visible damage. As seen, Table 2 highlights the trend of increasing compressive strength of the CSCNT/epoxy/carbon fiber nanocomposites with respect to growing CNT content material due to commanding stiffness [51].

Arun and Sun used TEM instruments to observe the introduction of resin between the gallery spaces of Nanomer clay with a few exfoliated regions. In addition, the SEM image shows the presence of double platelets in better clay inclusion. This phenomenon will affect the longitudinal compression strength (off-axis) of the higher clay-loaded samples produced by the vacuum-assisted wet lay-up process. The self-adjusting mechanism is used for off-axis compression testing. During the test, the bending moment was eliminated by the complete contact between the load surface and the cemented carbide block. In the case of fiber composites modified with nanoclay, the compressive strength is increased by about 22%. The elastoplastic model created by the researchers confirmed the same trend [77]. In another study, Yutaka et al. performed static compression tests on two-phase nanocomposites and three-phase nanocomposites [78]. Cup-stack carbon nanofiber (CSNF) and CSNT/carbon nanofibers/resin are added to the resin to make two-phase and three-phase nanocomposites. The two-phase specimens are compressed in between the two hydraulic grips of the testing machine as shown in Figure 5(a) and the three-phase specimens were compressed by hydraulic grips as shown in Figure 5(b).

The authors found that the compressive properties of two-phase and three-phase laminates have improved.

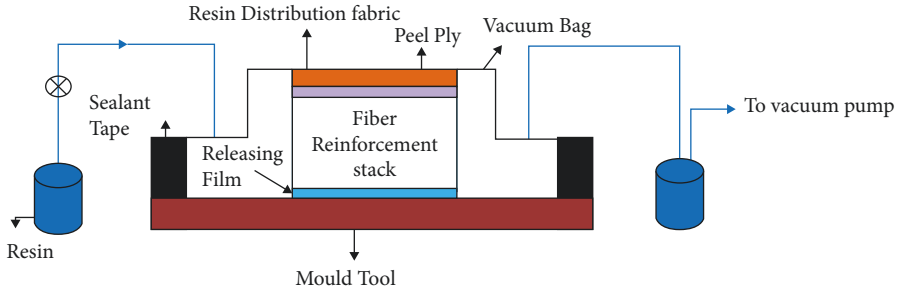

Figure 4: The schematic diagram of VARTM.

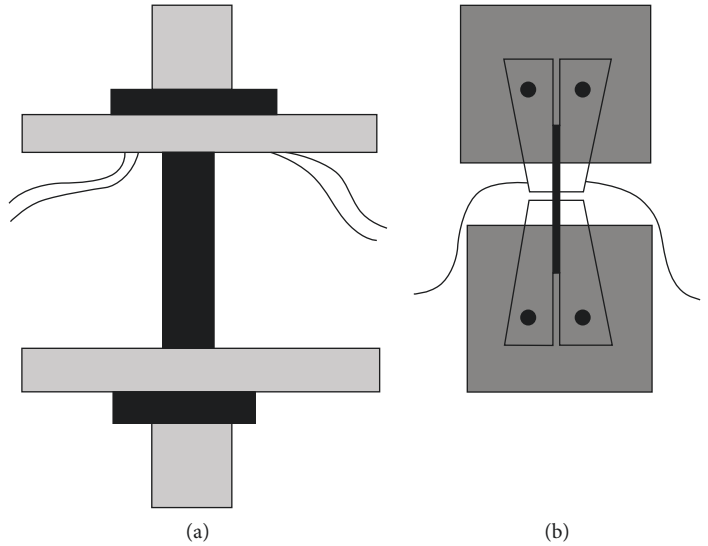

Figure 5: The schematic diagram of compressive modulus test: (a) two-phase composite and (b) three-phase composite.

Table 2: Summary of compression experimental results.

	0 wt.%	5 wt.%	10 wt.%
Compressive modulus (GPa)	42.9 (1.6)	43.2 (1.5)	45.1 (1.5)
Compressive strength (MPa)	488 (16.6)	501 (25.8)	539 (26.8)

However, they did not observe a monotonous relationship between the CSNF filler content and the compression properties of the three-phase composites. Surprisingly, better nanofillers provide excellent two-phase bond strength by weight. MWCNT/epoxy nanocomposite also has the same trend. Regardless of the technical strategy used to manufacture nanocomposites, higher concentrations of reinforcing fillers can provide superior compressive strength [79]. In contrast, the higher Nanomer I.28 nanoclay content in the matrix leads to a decrease in compressive strength due to the subtle interfacial adhesion between the clay and the base resin and the existence of nanovoids [80].

6. Fatigue Strength

Sumfleth et al. carried out each static and dynamic fatigue test to discover the fatigue property of glass fiber-reinforced (GFR) epoxy resin composites changed with a low quantity of fumed silica particles and MWCNT [81]. The dynamic fatigue test results confirmed that the inclusion of nanoparticles enhanced the inter-fiber fracture strength and leads to improved fatigue properties in high cycle fatigue. Similarly, Zhou et al. studied the fatigue performances of carbon nanofiber/epoxy/carbon fiber laminates [82]. During the investigation, the uniform mixture between the epoxy resin and CNF was acquired with the aid of a high-intensity ultrasonic liquid processor and an excessive pace mechanical agitator. The experimental results revealed that the 2 wt.% CNF-filled matrix possessed the highest fatigue strength. The researchers further fabricated the 2 wt.% CNF-modified epoxy/satin carbon fabric-reinforced nanocomposite panels in a VARTM machine. The fatigue test results of nanofiller-filled CFRP laminates revealed a commanding development than neat CFRP laminates.

Manjunatha et al. produced two kinds of GFRP composites neat epoxy (GFRP-neat) and hybrid particle-modified epoxy (GFRP-hybrid) using resin infusion method under flexible tooling setup. The hybrid particles which were used to modify the resin contain 9 wt.% of carboxyl-terminated butadiene-acrylonitrile (CTBN) rubber microparticles and 10 wt.% of silica nanoparticles [41, 42, 68, 83, 84]. The fatigue test was carried out according to the WISPERX load sequence for both GFRP-neat and GFRP-hybrid laminates. The test results seem to reflect the fatigue life of the

nanocomposite. Due to the suppression of matrix cracks and the reduction in the growth rate of delamination, the fatigue performance of the GFRP-hybrid laminate is 4 to 5 times higher than that of the GFRP-neat laminate. For all stress ratios of tension-tension, tension-compression, and compression-compression sections, both the laminates achieve constant amplitude fatigue life. In addition, it was found that the fatigue life calculated from the WISPERX load spectrum was significantly correlated with the experimental observations of both GRP laminates [41]. The author studied the similar fatigue behavior of GFRP-neat and the GFRP-hybrid epoxy laminates with a stress coefficient of $R = 0.1$. As in the previous case, researchers attained 6 to 10 times longer fatigue life for GFRP-hybrid epoxy composite laminates. This is achieved by suppressed matrix cracking and reduced cracking propagation in the particles-filled epoxy. This phenomenon is caused by the mechanism of cavitation, plastic deformation of rubber particles, and the growth of plastic cavities due to the fragmentation of silica particles [83]. The researchers studied the fatigue life of GFRP-neat and the GFRP-hybrid epoxy laminates under three different amplitude loading sequences, namely, three-step increasing block, three-step decreasing block, and random block load sequence. Due to the fracture of the matrix and the decrease in stiffness, the fatigue life of the GFRP-hybrid laminate is achieved in all load sequences with variable amplitudes [84].

7. Fracture Toughness

Nowadays, in industries, the thermoset polymer is widely used to create engineering components than the thermoplastic polymer on account of its appreciable mechanical properties. For the most part, the thermoset polymers are brittle in nature and exposed to crack. But, this property can be modified by including appropriate micro-sized or nano-sized particles in the base matrix. The current review by Lee et al. attempts to improve the fracture toughness of thermoset polymers by adding nano-sized conductive carbon black particles and Cloisite 93A nanoclay in the epoxy resin [85]. The procedure for mixing nanoparticles in the matrix contains three steps. First, mix the nanofiller with the epoxy resin by hand, and then mix it with a magnetic stirrer at 60°C for 60 minutes. Second, the mixture is added to the three rolls through the hopper for high shear mixing. Finally, use a magnetic stirrer to thoroughly mix the slurry and hardener under vacuum.

The fracture toughness test was performed at room temperature and cryogenic temperature. The test revealed that in room temperature the nanofillers notably improved the toughness than in the cryogenic temperature. Phonthammachai et al. stepped forward the overall performance of multilayer CFRP laminates with the aid of using unmodified nanoclay in epoxy [54]. The addition of 0.6 vol.% clay significantly improved the viscosity of the resin. The improved properties of resin brought improved toughness of cured nanocomposites. Martín-Martínez et al. [86] fabricated the laminates by adding high-performance clay in unsaturated polyester resin (UPR) coating on brown emperor natural stone and studied the fracture toughness properties. At the end of the study, it had been ascertained that the nanocomposites with a low clay content of 0.5 and 1 wt.% clay improved the fracture toughness significantly due to decreased gel time and decreased shrinkage degree of the UPR base matrix during curing. Kim et al. examined the mode I interlaminar fracture behavior of carbon fiber/nanoclay/epoxy matrix with the assist of a double cantilever beam (DCB) test setup [87]. The dimensions and preliminary crack size with Teflon film of DCB specimen are depicted in Figure 6. A good bonding was formed between the toughness of the clay-filled matrix and carbon fiber. Therefore, the fracture toughness property of laminates improved with increasing clay content during initiation and propagation stages. Especially, the propagation of crack was almost doubled for 7 wt.% nanofiller loadings. Likewise, the same trend was continued to nanocomposites which are manufactured by the vacuum infusion method with woven glass fabrics and clay-filled matrix [88].

The mode I (G_{Ic}) and mode II (G_{IIc}) fracture toughness of carbon fiber-reinforced laminates made of epoxy-filled nano-silica particles was studied. The epoxy resin contains 10% and 20% by weight of nanoparticles. The G_{Ic} improved when nano-silica loadings in resins were increased. On the contrary, G_{IIc} decreased with increasing nano-silica content. Similar research was carried out in CNT/epoxy/carbon fiber laminates. The G_{IIc} and G_{Ic} decreased considerably to silica nanoparticles-filled laminates than CNT-filled laminates. Further, from the fractographic study, it was evident that more interfacial failure happened between epoxy and CF particularly at higher loading for nano-silica particles-loaded laminates [89]. Davis and Whelan had conducted an experimental study on fracture toughness to CFRP laminates made by using fluorine-functionalized carbon nanotubes (f-CNTs)-modified epoxy. First, the f-CNT is applied to the center plane of the carbon fiber fabric of the laminate, thereby achieving a very good interlayer thickness enhancement. Davis and Whelan used four-point end notch flexure (4ENF) test setup to examine the critical strain energy release rate of nanocomposites. Figure 7 shows the 4ENF sample loaded in the four-point bend loading mode. Due to the strong covalent bond between carbon fiber and polymer resin, the use of 0.5 wt.% f-CNTs-loaded fabric resulted in an unexpectedly significant improvement in toughness. The covalent bond leads to an increase in the interface resistance between the fiber and the matrix [90]. In addition, Chan et al. studied the fracture toughness properties of nanocomposites made of carbon fiber reinforced by halloysite nanotubes in a hardened epoxy resin matrix. The toughness properties of the panel were calculated by using a double cantilever beam (DCB) test setup to conduct mode I and mode II fracture toughness tests. The test results show that due to the uniform distribution of HNT in the matrix, the participation of HNT in the panels significantly increases the fracture strength [91].

Kostopoulos et al. improved the toughness of CFRP by modifying CNF resin with piezoelectric particles (PZT). The experimental results show that when 1% by weight of CNF is introduced together with the matrix, the effect of CNF and resin leads to the bridging properties of the fiber, and a huge

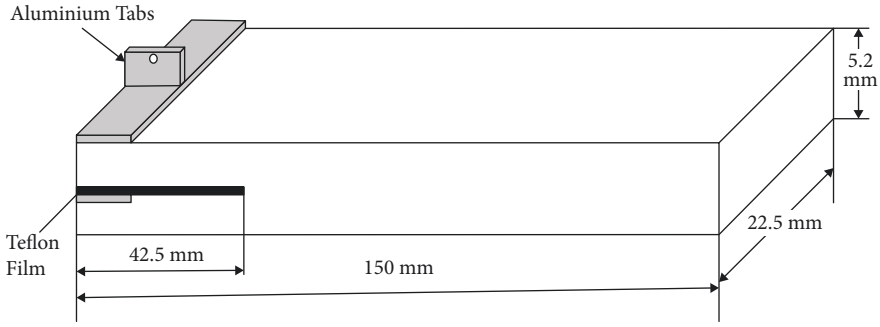

Figure 6: Geometry of DCB specimens.

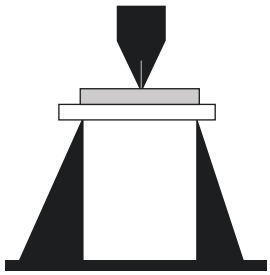

Figure 7: The schematic diagram of 4ENF specimen in a four-point bend mode.

Table 3: Effect of clay content on impact strength for nanocomposites.

Nanocomposites	Impact strength (J/m)
Neat TPO resin	80.00
5%Na-MMT/TPO resin	96.00
5%C20A/TPO resin	127.86
5%C30B/TPO resin	121.2
5%C20A5%COM/TPO resin	328.3
5%C30B5%COM/TPO resin	241.4

increase in the destruction energy of 100% is achieved. In contrast, due to the brittleness of particle inclusions, the addition of PZT particles results in lower fracture toughness [92]. Yao et al. synthesized the SiO_2 matrix nanocomposite using the sol-gel technique by magnetic force and ultrasonicator. The matrix contains a combination of three parts, namely, diglycidyl ether of bisphenol F (DGEBF), poly(-propylene glycol) diglycidyl ether (PPGDE), and diethyltoluene diamine (DETD). The mixture ratio of A and B parts is 1 : 1. The digital speckle correlation technique addressed that the distribution of displacement field in nanocomposites was happening at the initial edge crack tip. The three-point bending test results depicted that at low particle loading, the higher fracture toughness and larger deformation opposing capability were attained [93]. Ye et al. used 35 nm carbon black superconducting nanoparticles and a small amount of copper chloride (CC) as nanofillers and glass fibers for the manufacture of nanocomposites using vacuum resin infusion (VARI) technology. The electrical resistance tomography method was used to evaluate the transverse impact damage of laminates. This method is used to evaluate both damages such as in-plane and through-thickness directions of conductive points of GFRP laminates. This study investigated the improvement of G_{Ic} and G_{IIc} in laminates due to the presence of CB and CC nanoparticles. At the end of the test, delamination growth is characterized by changes in in-situ electrical resistance [94].

8. Impact Strength

The reason for this research was to ascertain the improvement of impact strength of laminates which are fabricated by polylactic acid filled with cellulose nanofiber and compatibilized with maleated PLA. The composite laminate was originally made by melt blending 5 wt.% maleated PLA and then using a twin-screw extruder to blend with two different nanofiber fillers, viz. 3 and 5 wt.%. The impact test shows that, compared with pure PLA, the addition of nanocellulose without maleated PLA will not significantly increase the impact strength of the laminate. Surprisingly, the results show that the 5 wt.% cellulose nanofiber-added nanocomposites have a significant increase in impact strength of 131% compared to pure PLA. This improvement is due to the uniform dispersion of CNF with the PLA matrix in the presence of maleated PLA [14]. In addition, compared with Cloisite Na + nanoclay, Basara et al. determined that Cloisite 30B nanoclay has higher impact strength because of the greater d-spacing at low clay content [27]. Similarly, due to the improved resin viscosity and lower resin shrinkage at curing, the commanding impact strength was achieved by adding 0.5 and 1% by weight of unmodified nanoclay in base matrix UPR [86].

Melt-extrusion nanocomposites contain three different montmorillonite nanoclays as reinforcing elements, namely, Cloisite Na-MMT, Cloisite 20A (C20A), and Cloisite 30B (C30B). The matrix contains thermoplastic polyolefin (TPO) resin and polypropylene grafted maleic anhydride (PP-g-MA) compatibilizer. Nanoclay is added in an amount of three percent, such as 3, 5, and 7 wt.% with the matrix. As shown in Table 3, the 5 wt.% C20A composites with 5 wt.% compatibilizer show better mechanical properties than other nanocomposites. The table clearly portrayed the improvement in impact strength of 5 wt.% C20A nanocomposites when compared to Na-MMT nanocomposites as 33% for C20A and 26% for C30B without compatibilizer due to the insertion of polymeric chain inside the clay platelet. But surprisingly, when adding 5% compatibilizer with the

composite, the IS increased to 242% for C20A and 151% for C30B due to the appreciable reinforcing effect made between clay and polymer.

Lou et al. conducted a detailed study to determine the impact strength (IS) of pure polyamide 6 (PA6) matrix and melt-blended nanocomposites [95]. Researchers melt-blended PA6 with Cloisite Na+, Cloisite 20A, and Cloisite 30B MMT nanoclays in a 30 mm twin-screw extruder and injection molding machine. Initially, PA6/Cloisite 20A MMT nanocomposites were manufactured at screw speeds of 100, 140, and 180 rpm. Here, the laminates were called as 20A100, 20A140, and 20A180. At the same speed, the neat PA6 matrices were melt-blended and the specimens were referred to as PA6100, PA6140, and PA6180. Second, the PA6/MMT nanocomposite was melt-blended with Cloisite Na+, Cloisite 20A, and Cloisite 30B at a screw speed of 140 rpm. The nanocomposites were named as Na + 140, 20A140, and 30B140, respectively. Surprisingly, the impact strength of the PA6/Cloisite 20A nanocomposite is lower than that of the pure matrix. This is because when fillers are added to the polymer matrix, microvoids are formed between the interfaces. The first three cycles have no effect on the impact strength of laminate 30B140. Similarly, the number of melt cycles has almost no effect on impact strength of Na + 140.

9. Interlaminar Shear Strength

Lu et al. tested the impact of 20 nm nano-SiO_2 by including in epoxy emulsifiers at the interfacial adhesion of carbon fiber-reinforced composites. The size of the carbon fibers used on this observation was approximately 7 μm and polyacrylonitrile (PAN) based. The various tests confirmed the interfacial interaction between carbon fiber and the modified epoxy. This phenomenon brought about the revised hydroxyl groups on the surface of carbon fibers after treating with nano-SiO_2 changed sizing. Consequently, the interlaminar shear strength of both unmodified and nano-SiO_2-modified sizing composite panels was superior to the unsized panels. The morphology test was carried out at the fractured surface of the ILSS specimen, and the outcomes affirmed that the nano-SiO_2-modified sizing shows excellent compact than the unmodified sizing [96]. With the assist of compression shear test, Santare et al. mentioned that 0.5 wt.% MWCNTs-loaded laminates yielded superior ILSS than unfilled laminates. The ILSS results lead to an increase in the shear strength of the matrix in a few instances or increased the strength of the fiber-matrix interface. Both shear punch and microdroplet tests absolutely concluded that the ILSS in particular trusted the fiber-matrix interface and did not rely on the shear strength of the matrix [97]. Likewise, the improved ILSS was detected for the CFRP nanocomposites with HNTs and CNFs toughened epoxy matrix by using a short-beam shear test [57, 92].

Kamae and Drzal advised a brand new approach for the motive of uniformly coating the CNTs to carbon fibers that permit the scalable fabrication of CNT-stuffed carbon fiber/epoxy nanocomposites [98]. The uniform coating between CNTs and carbon fibers is attained by dipping CFs into CNT/water suspension. Due to the repulsive force and attractive forces between CNTs and carbon fibers, an amazing dispersion rate was achieved. With the assist of single fiber fragmentation tests under shear loading, the shear strength was calculated. The test results show that the noticed improvement in interfacial shear strength was attained due to CNT-coated CFs. As shown in Table 4, the similar trend is portrayed in Table 4 showing the ILSS property for various nanofillers.

10. X-Ray Diffraction

Fuet al. synthesized the aircraft-grade epoxy-clay nanocomposite laminates and further examined the dispersion rate by using XRD. The nanofiller/polymer mixture was made with the aid of using a high-pressure mixing technique. Authors initially dispersed the nanoclay thoroughly in the acetone and later in the acetone epoxy solution. After that, the basal spacing between each nanoclay plate was tested by using the diffraction test. The test results revealed that the basal spacing of the nanoclay has increased from 2.37 nm to 3.22 nm due to the application of high shear and collision forces generated by mixing under high pressure. This large space between the individual platelet allows easy intercalation of acetone. As a result, the attractive force between the nanoclay layers is reduced. Therefore, the epoxy resins and curing agents easily entered into the nanoclay [100]. Dean et al. studied the dispersion rate of nanocomposite laminates made of organo-clay. The test results showed that with the increase of curing temperature and the increase of interlayer spacing, intercalated morphology with different interlayer gains was obtained. In addition, the rheological test showed that intergallery diffusion before curing has a decisive effect on the formation of exfoliation [101].

Initially, Singh et al., 2006, used the high shear mixing to obtain the uniform dispersion pattern between epoxy-nanoclay mixtures. The XRD results of fabricated epoxy/nanoclay laminates revealed that the complete exfoliation was occurring even to higher nanoclay loadings. Further, no outstanding peak appeared within the diffractograms for any samples produced by high shear mixer, and hence, complete exfoliation dispersion was ensured to all samples. But, a noticeable peak was obtained for 4 wt.% nanoclay loading samples dispersed by ultrasonication process [102].

Tolle and Anderson analyzed the role of preconditioning of organically modified clay in thermoset polymer during the fabrication process of laminates by using XRD and identified the sensitivity of exfoliation based on material conditions. The test results indicate the occurrence and extent of exfoliation morphology with various silicate preconditioning processes. In addition, due to the aging of the epoxy resin/nanoclay mixture and pretreatment, the delamination was obtained earlier and showed intercalation dispersion [103]. Krikorian and Pochan used polylactic acid resin (PLLA) and three organically modified MMTs, Cloisite 30B, Cloisite 25A, and Cloisite 15A, to synthesize nanocomposite laminates using an ultrasonicator, and then used a dryer to evaporate the solvent. Studies have shown that the

Table 4: ILSS property for various nanofillers.

Nanofiller	Dispersion status	ILSS property comments	Ref.
Cloisite 30B RXG 7000	1 wt.%, 3 wt.% 3 wt.%	Greater enhancement attained for 3 wt.% Cloisite 30B	[99]
Nano-silica	10 wt.%, 20 wt.%	12% greater reduction for 20 wt.% nano-silica-modified epoxy laminate	[89]
Nano-SiO_2	Unsized composites Unmodified sizing composites Nano-SiO_2-modified sizing composites	9% enhancement for unmodified sizing composites; 14% enhancement for nano-SiO_2-modified sizing composites	[96]
MWNT	0.5 wt.% unfunctionalized MWNT-modified epoxy 0.5 wt.% amino-functionalized MWNT-modified epoxy	41% increase than neat epoxy/glass fiber composites 61% increase than neat epoxy/glass fiber composites	[97]
Na + MMT clay	1, 3, 6, and 10% wt. of unmodified montmorillonite 1, 3, 6, and 10% wt. of organo-modified montmorillonite	ILSS reduced slightly and greater reduction for OMMT clay particles	[88]

scattering pattern depends upon basal spacing. In addition, due to the layered structure, the addition of nanoclay limits the PLLA. They also pointed out that adding more clay to the exposed matrix causes the material to become tougher [104]. However, Akbari and Bagheri achieved a combination of intercalated and exfoliated dispersions in polymer-layered silicate nanocomposites. Perform XRD testing to understand the dispersion pattern of epoxy-clay. From the XRD pattern, it was found that the significant improvement on $d_{(001)}$ spacing was attained to 5 wt.% MMT clay-epoxy matrix. The study further concluded that the interaction of clay-epoxy matrix decreases with the increasing clay content due to the presence of microvoids created by the rapid increase in viscosity. Therefore, the lower interaction of the mixture leads to a decrease in tensile strength [105]. Alamri and Low also based on the TEM test results of epoxy hybrid nanocomposites filled with cellulose fiber-reinforced clay platelets confirmed the same tendency of intercalation dispersion structure and exfoliation combination [106].

11. Chemical Analysis

Mansuri et al. made nanocomposites by grafting polystyrene on to Cloisite 20A. Infrared spectroscopy, thermogravimetric analysis (TGA), and dynamic thermal analysis are used to examine nanocomposite materials. Free radical polymerization is carried out during the synthesis process to form the homo-polymer into styrene, which results in the chemical grafting of polystyrene to the surface of the MMT clay and finally extraction from the grafted clay. The FTIR spectrum confirms the chemical grafting of polystyrene to the nanoclay surface. The test results show that polystyrene is chemically grafted to clay with a lower clay content [107].

Muhammad Sarfraz produced nanocomposites based on electroconductive structural polymers by adding carbon nanotubes (CNTs) to a Polybond matrix using a melt compounding method. In this research, Fourier transform infrared (FTIR) spectroscopy was used to examine the chemical structure of the nanocomposite. The results confirm the successful combination of CNT functional groups and multiple linking chains. Compared with pure laminates, nanocomposites have higher chemical resistance [108]. Similarly, You et al. used FTIR spectroscopy to chemically analyze nanoclay and carbon microfiber-loaded composites and to measure the chemical bonding of binders. During the manufacturing process, four different nanoclays and micromodifiers are added to the asphalt binder, namely, Nanomer I.44P, carbon micro-fiber, unmodified nanoclay, and polymer-modified nanoclay. The test results show that the addition of modifiers further improves the chemical stability and further delays the effects of aging and oxidation [109].

Ghorbel et al. used attenuated total reflectance/Fourier transform infrared (ATR/FTIR) spectroscopy to do interesting work on the chemical characterization of nanocomposite films. Nanocomposite films were produced using nano-whiskers made of cellulose (CNW) and nano-fibrillated cellulose (NFC) as the reinforcing phase and natural rubber latex as the matrix. In this research work, the ATR/FTIR method was used to examine the chemical bonds of natural rubber and the chemical bonds of nano-whiskers in the spectral range of 4000–600 cm^{-1}. The infrared spectroscopy test results witnessed that many vibrational modes were identified while adding cellulose nanoparticles (CNW/NFC) into the natural rubber matrix. Research also shows that the interface adhesion of NFC/natural rubber nanocomposite film is higher than that of CNW/natural rubber, due to the presence of residual lignin in NFC. It has also been observed that when the filler content is increased from 1% to 10%, with a significant effect on the vibration behavior [110].

12. Thermal Analysis

Altan et al. produced three sets of laminates, such as pure epoxy laminates, unfilled GFRP laminates, and Cloisite 25A-filled GFRP laminates. Dynamic mechanical analysis showed that the glass transition temperature of the nanoclay-filled GRP nanocomposite laminate was significantly higher than that of the other two laminates, due to the exfoliation properties of the nanoclay-loaded matrix [111]. Philippe et al. used a melting process to synthesize nanocomposite laminates from plasticized PLA and four different nanoclays (i.e., Cloisite Na +, Cloisite 25A, Cloisite 20A, and Cloisite

Table 5: Thermal properties of PI hybrid films (adapted from reference [113]).

FGS in PI (wt.%)	HDA-GS				AHB-GS			
	T_g (°C)	T_D^{ia} (°C)	wt_R^{600b} (%)	CTE^c (ppm/°C)	T_g (°C)	T_D^{ia} (°C)	wt_R^{600b} (%)	CTE^c(ppm/°C)
0 (pure PI)	260	539	85	61	260	539	85	61
3	242	499	88	58	251	530	86	53
5	236	468	87	55	239	471	85	51
10	210	439	85	46	221	443	85	41

30B). Thermal analysis of laminates was performed using differential scanning calorimetry and thermogravimetric analysis in an air stream heated at 20 K/min from 25 to 600°C. The test results show that the clay modified with bis(2-hydroxyethyl) methyl (hydrogenated tallow alkyl) ammonium cation has higher thermal stability [112]. In addition, it is also confirmed that as the clay content increases, the thermal decomposition of the resin is found to be delayed.

Tanoglu et al. described that the clay loading altered the thermal behavior of GFR clay/epoxy laminates. In addition, the study concluded that the addition of MMT clay significantly improved the fire resistance of the composite material [88]. Jin-Hae Chang's research focuses on combining polyimide with two different new functionalized graphene sheets (FGSs), namely, hexadecylamine-graphene sheets (HDA-GSs) and 4-amino-N-hexadecylbenzamide-graphene sheets (AHB-GSs) to synthesize mixed films by the solution intercalation method. The content of FGS filler in the hybrid film solution varies from 0 to 10% by weight. He then analyzed the effect of filler content material fabric on the nanocomposite to determine thermal performance. Extensive thermal studies have shown that adding a small amount of filler can significantly increase the coefficient of thermal expansion. Furthermore, as the filler content increases, the glass transition temperature and initial decomposition temperature of the hybrid film tend to decrease as shown in Table 5. The AHB-GS hybrids had predominant thermal properties than the HDA-GS nanocomposite films [113]. Krishnaswami et al. discussed the thermal insulation properties of aerogel/PA6 composites manufactured using a twin-screw extruder at two different speeds (65 rpm and 5 rpm) and a compression molding machine. Thermal analysis shows that low-speed laminates have the main thermal conductivity compared to high-speed laminates; however, the thermal conductivity of both nanocomposites is inferior to the virgin polymer. Furthermore, the thermal stability was improved for the polyamide 6/polypropylene blend with the inclusion of both Na-MMT and OMMT [114].

13. Conclusion

In recent years, nanocomposites have attracted many researchers based on the reports from Toyota and Giannelis research groups on improved performance. Nowadays, nanocomposites are popular in many industries in the manufacture of computer chips, food packaging, batteries, engine components, fuel tanks, impellers, and oxygen gas barriers. This overview outlines the impact of nanoparticles in the basic matrix on the production of nanocomposites and the factors that affect their performance.

Depending upon the diverse shapes, the nano-sized substances are used as particles (e.g., nanoparticles), sheets (e.g., nanoclay), fibers (e.g., carbon nanofibers), and tubes (e.g., carbon nanotubes). The addition of small nanofiller content material improved mechanical properties (like strength, modulus), thermal stability, interlaminar properties (like ILSS, fracture toughness), tribology properties (like the coefficient of friction), dielectric properties, and chemical resistance. Generally, the nanofillers contain a high aspect ratio and high surface-to-volume ratio. From the various researches carried out on different nanocomposites, it is determined that the nanofillers are included in the range of 0.5 to 10% by weight with the matrix. However, the superior properties can be acquired at a low filler content material of 0.5 wt.% to 5 wt.% dispersion with the base matrix.

The review showed that the mixture is dispersed at a high speed, and when using high-frequency dispersion equipment such as ultrasonicator, the nanofillers are agglomerated in high content loading due to the high aspect ratio and high surface-to-volume ratio. This leads to the formation of pores and weaker areas, and results in the formation and propagation of cracks. It was also found in this review that the viscosity of the clay matrix achieves the best improvement at low content due to good interfacial adhesion. In addition, improved viscosity leads to improved mechanical properties and thermal stability.

The review work elucidated that the dispersion rate of the clay matrix mixture can be divided into intercalation or exfoliation according to the d-spacing between each clay platelet. Generally, the d-spacing of nanoclay was increased appreciably at low clay content due to easy dispersion with matrix, so that enhanced surface binding was exhibited. Additionally, this work further investigated the dispersion of the curing agent into the nanoclay-epoxy blend and its effects. The study corroborates that the dispersion promotes the reaction with the matrix. Further, in some cases, the treatment of MMT nanoclay with the coupling agent brought a hydrophilic nature, which altered all properties considerably. The interlayer spacing varies according to the use of the swelling agent, whether it is a monomer or a polymer. This change finally ends in the attainment of intercalating or exfoliating smectite clay which inherently altered the properties. In most of the cases, the review work has analyzed the effect of nanofillers with the preparation techniques of composite laminates. The overall review

reveals that the inclusion of a less amount of nanofillers in polymers will be becoming more perfect in the property enhancement of composite materials.

Conflicts of Interest

The authors declare that there are no conflicts of interest or personal relationships that could have appeared to influence the work reported in this paper.

References

[1] R. L. Carlson, G. A. Kardomateas, and J. I. Craig, *Mechanics of Failure Mechanisms in Structures*, Springer, Berlin, Germany, 1st edition, 2012.

[2] T. Yokozeki, Y. Iwahori, and S. Ishiwata, "Matrix cracking behaviors in carbon fiber/epoxy laminates filled with cup-stacked carbon nanotubes (CSCNTs)," *Composites Part A: Applied Science and Manufacturing*, vol. 38, no. 3, pp. 917–924, 2007.

[3] S. Komarneni, "Feature article. Nanocomposites," *Journal of Materials Chemistry*, vol. 2, no. 12, pp. 1219–1930, 1992.

[4] E. P. Giannelis, "Polymer layered silicate nanocomposites," *Advanced Materials*, vol. 8, no. 1, pp. 29–35, 1996.

[5] M. S. Senthil Kumar, N. MohanaSundara Raju, P. S. Sampath, and L. S. JayaKumari, "Effects of nano-materials on polymer composites - an expatiate view," *Reviews on Advanced Materials Science*, vol. 38, pp. 40–54, 2014.

[6] R. Boujmal, C. A. Kakou, S. Nekhlaoui et al., "Alfa fibers/clay hybrid composites based on polypropylene: mechanical, thermal, and structural properties," *Journal of Thermoplastic Composite Materials*, vol. 31, no. 7, pp. 974–991, 2018.

[7] Y. Zhu, J. O. Iroh, R. Rajagopolan, A. Aydin, and V. Richard, "Optimizing the synthesis and thermal properties of conducting polymer–montmorillonite clay nanocomposites," *Energies*, vol. 15, pp. 1–18, 2022.

[8] K. P. Rajan, A. Al. Ghamdi, S. P. Thomas, A. Gopanna, and M. Chavali, "Dielectric analysis of polypropylene (PP) and polylactic acid (PLA) blends reinforced with halloysite nanotubes," *Journal of Thermoplastic Composite Materials*, vol. 31, no. 8, pp. 1042–1053, 2018.

[9] D. B. Miracle and S. L. Donaldson, *ASM Handbook Volume 21: Composites*, D. B. Miracle and S. L. Donaldson, Eds., ASM International, Materials Park, OH, USA, 2001.

[10] International Organization for Standardization, *Nanotechnologies - Vocabulary - Part 2:Nano-Objects (ISO/TS 80004-2: 2015)*, International Organization for Standardization, Switzerland, Geneva, 1st edition, 2015.

[11] M. Hosokawa, K. Nogi, M. Naito, and T. Yokoyama, *Nanoparticle Technology Handbook*, Elsevier Science, Oxford, UK, 2007.

[12] D. Schmidt, D. Shah, and E. P. Giannelis, "New advances in polymer/layered silicate nanocomposites," *Current Opinion in Solid State & Materials Science*, vol. 6, no. 3, pp. 205–212, 2002.

[13] D. Yang, H. Xu, and W. Yu, "Comparative study on the dielectric properties of three polyvinylidene fluoride nanocomposites incorporated with carbon filler," *Journal of Thermoplastic Composite Materials*, vol. 31, no. 8, pp. 1102–1111, 2018.

[14] S. Ghasemi, R. Behrooz, I. Ghasemi, R. S. Yassar, and F. Long, "Development of nanocellulose-reinforced PLA nanocomposite by using maleated PLA (PLA-g-MA)," *Journal of Thermoplastic Composite Materials*, vol. 31, no. 8, pp. 1090–1101, 2018.

[15] M. Alexandre and P. Dubois, "Polymer-layered Silicate Nanocomposites: preparation, properties and uses of a new class of materials," *Materials Science and Engineering: R: Reports*, vol. 28, no. 1–2, pp. 1–63, 2000.

[16] R. He, F. Niu F, and Q. Chang, "Tribological properties of PI-SiC nanocomposite prepared by hot dynamic compaction," *Journal of Thermoplastic Composite Materials*, vol. 31, no. 8, pp. 1066–1077, 2018.

[17] K. Müller, E. Bugnicourt, M. Latorre et al., "Review on the Processing and properties of polymer nanocomposites and nanocoatings and their applications in the packaging, automotive and solar energy fields," *Nanomaterials*, vol. 7, no. 74, pp. 1–47, 2017.

[18] J. Zhou, Z. Lin, H. Ren et al., "Layered intercalation materials," *Advanced Materials*, vol. 33, no. 25, pp. 1–23, 2021.

[19] J. Costa de Macedo Neto, N. Reis do Nascimento, R. Hoel Bello, L. Antonio de Verçosa, J. Evangelista Neto, and J. Carlos Martins da Costa and Francisco Rolando Valenzuela Diaz, "Kaolinite review: intercalation and production of polymer nanocomposites," *Engineered Science*, vol. 17, pp. 28–44, 2022.

[20] S. Kenig, *Processing of Polymer Nanocomposites*, pp. 1–497, Hanser Publications, Munich, Germany, 2019.

[21] S. Pavlidou and C. D. Papaspyrides, "A review on polymer– layered silicate nanocomposites," *Progress in Polymer Science*, vol. 33, no. 12, pp. 1119–1198, 2008.

[22] D. R. Paul and L. M. Robeson, "Polymer nanotechnology: nanocomposites," *Polymer*, vol. 49, no. 15, pp. 3187–3204, 2008.

[23] L. Mrah and R. Meghabar, "In situ polymerization of styrene–clay nanocomposites and their properties," *Polymer Bulletin*, vol. 78, pp. 3509–3526, 2021.

[24] C. IlPark, O. OkPark, J. GonLim, and H. Joon Kim, "The fabrication of syndiotactic polystyrene/organophilic clay nanocomposites and their properties," *Polymer*, vol. 42, no. 17, pp. 7465–7475, 2001.

[25] S. K. Zhade, S. K. Chokka, V. S. Babu, and K. V. Sai Srinadh, "A review on mechanical properties of epoxy-glass composites reinforced with nanoclay," in *Epoxy-Based Composites*, S. Chelladurai, Ed., Intech Open, London, UK, 2022.

[26] S. S. Chee, M. Jawaid, O. Y. Alothman, and H. Fouad, "Effects of nanoclay on mechanical and dynamic mechanical properties of bamboo/kenaf reinforced epoxy hybrid composites," *Polymers*, vol. 13, no. 3, pp. 1–17, 2021.

[27] H. Wang, A. Sun, X. Qi, Y. Dong, and B. Fan, "Experimental and analytical investigations on tribological properties of PTFE/AP composites," *Polymers*, vol. 13, no. 24, pp. 1–14, 2021.

[28] B. Anitha, B. V. Vibitha, P. S. P. Jyothi, and J. N. Tharayi, "Structural and morphological studies of conducting polymer nanocomposites," *AIP Conference Proceedings*, vol. 2287, no. 1, pp. 1–4, 2020.

[29] A. Dorigato and A. Pegorettia, "Nanocomposite and its morphological characterization -review," *IOP Conference Series: Materials Science and Engineering*, vol. 640, pp. 1–9, 2019.

[30] K. Mohan Babu and M. Mettilda, "Morphological studies on renewable castor oil-based nanocomposites with modified clay and MWCNTs as fillers," *Polymers and Polymer Composites*, vol. 29, no. 1 – 8, 2020.

[31] D. L. Shi, X. Q. Feng, Y. Y. Huang, K.-C. Hwang, and H. Gao, "The effect of nanotube waviness and agglomeration on the

elastic property of carbon nanotube-reinforced composites," *Journal of Engineering Materials and Technology*, vol. 126, no. 3, pp. 250–257, 2004.

[32] Y. Wang, J. W. Shan, and G. J. Weng, "Percolation threshold and electrical conductivity of graphene-based nanocomposites with filler agglomeration and interfacial tunneling," *Journal of Applied Physics*, vol. 118, pp. 1–10, Article ID 065101, 2015.

[33] S. Gong, Z. H. Zhu, and S. A. Meguid, "Carbon nanotube agglomeration effect on piezoresistivity of polymer nanocomposites," *Polymer*, vol. 55, no. 21, pp. 5488–5499, 2014.

[34] J. Pan and L. Bian, "Coefficients of nonlinear thermal expansion for fiber-reinforced composites," *Acta Mechanica*, vol. 228, no. 12, pp. 4341–4351, 2017.

[35] P. Barai and G. J. Weng, "A theory of plasticity for carbon nanotube reinforced composites," *International Journal of Plasticity*, vol. 27, no. 4, pp. 539–559, 2011.

[36] X.-Y. Ji, Y. Cao, and X.-Q. Feng, "Micromechanics prediction of the effective elastic moduli of graphene sheet-reinforced polymer nanocomposites," *Modelling and Simulation in Materials Science and Engineering*, vol. 18, no. 4, pp. 1–16, Article ID 045005, 2010.

[37] E. W. Tiedje and P. Guo, "Modeling the influence of particulate geometry on the thermal conductivity of composites," *Journal of Materials Science*, vol. 49, no. 16, pp. 5586–5597, 2014.

[38] A. Tessema, D. Zhao, J. Moll et al., "Effect of filler loading, geometry, dispersion and temperature on thermal conductivity of polymer nanocomposites," *Polymer Testing*, vol. 57, pp. 101–106, 2017.

[39] M. S. Senthil Kumar, N. Mohana Sundara Raju, P. S. Sampath, and U. Vivek, "Tribological analysis of nano clay/epoxy/glass fiber by using Taguchi's technique," *Materials & Design*, vol. 70, pp. 1–9, 2015.

[40] M. S. Senthil Kumar, A. Adugna, K. Balasundaram, and A. Ashok Kumar, "Vibration analysis of nanoclay reinforced glass fiber/epoxy nanocomposite," *Journal of Recent Research in Engineering and Technology*, vol. 4, no. 5, pp. 1–6, 2017.

[41] C. M. Manjunatha, R. Bojja, N. Jagannathan, A. J. Kinloch, and A. C. Taylor, "Enhanced fatigue behavior of a glass fiber reinforced hybrid particles modified epoxy nanocomposite under WISPERX spectrum load sequence," *International Journal of Fatigue*, vol. 54, pp. 25–31, 2013.

[42] C. M. Manjunatha, N. Jagannathan, K. Padmalatha, A. C. Taylor, and A. J. Kinloch, "The effect of micron-rubber and nano-silica particles on the fatigue crack growth behavior of an epoxy polymer," *International Journal of Nanoscience*, vol. 10, no. 4, pp. 1095–1099, 2011.

[43] G. Hug, P. Thévenet, J. Fitoussi, and D. Baptiste, "Effect of the loading rate on mode I interlaminar fracture toughness of laminated composites," *Engineering Fracture Mechanics*, vol. 73, pp. 2456–2462, 2006.

[44] M. H. Woldemariam, G. Belingardi, E. G. Koricho, and D. T. Reda, "Effects of nanomaterials and particles on mechanical properties and fracture toughness of composite materials: a short review," *AIMS Materials Science*, vol. 6, no. 5, pp. 1191–1212, 2019.

[45] S. Mazumdar, *Composites Manufacturing, Materials, Product and Process Engineering*, CRC Press, Boca Raton, FL, USA, 1st edition, 2001.

[46] F. H. Su, Z. Z. Zhang, and W. M. Liu, "Tribological and mechanical properties of Nomex fabric composites filled with polyfluo 150 wax and nano-SiO_2," *Composites Science and Technology*, vol. 67, pp. 102–110, 2007.

[47] Z. Z. Wang, P. Gu, Z. Zhang, L. Gu, and Y. Z. Xu, "Mechanical and tribological behavior of epoxy/silica nanocomposites at the micro/nanoscale," *Tribology Letters*, vol. 42, pp. 185–191, 2011.

[48] Y. Kang, X. Chen, S. Song, L. Yu, and P. Zhang, "Friction and wear behavior of nanosilica-filled epoxy resin composite coatings," *Applied Surface Science*, vol. 258, pp. 6384–6390, 2012.

[49] S. Thakur and S. R. Chauhan, "Friction and sliding wear characteristics study of submicron size cenosphere particles filled vinylester composites using Taguchi design of experimental technique," *Journal of Composite Materials*, vol. 48, no. 23, pp. 1–12, 2013.

[50] B. P. Chang, H. M. Akil, M. G. Affendy, A. Khan, and R. Bt Md Nasir, "Comparative study of wear performance of particulate and fiber-reinforced nano-ZnO/ultra-high molecular weight polyethylene hybrid composites using response surface methodology," *Materials & Design*, vol. 63, pp. 805–819, 2014.

[51] B. P. Chang, H. M. Akil, R. B. M. Nasir, I. M. C. C. D. Bandara, and S. Rajapakse, "The effect of ZnO nanoparticles on the mechanical, tribological and antibacterial properties of ultra-high molecular weight polyethylene," *Journal of Reinforced Plastics and Composites*, vol. 33, no. 7, pp. 1–13, 2014.

[52] M. Garcia, M. D. Rooij, L. Winnubst, W. E. Van Zyl, and H. Verweij, "Friction and wear studies on nylon-6/SiO_2 nanocomposites," *Journal of Applied Polymer Science*, vol. 92, pp. 1855–1862, 2004.

[53] B. Qi, Q. X. Zhang, M. Bannister, and Y.-W. Mai, "Investigation of the mechanical properties of DGEBA-based epoxy resin with nanoclay additives," *Composite Structures*, vol. 75, pp. 514–519, 2006.

[54] T. Yokozeki, Y. Iwahori, S. Ishiwata, and K. Enomoto, "Mechanical properties of CFRP laminates manufactured from unidirectional prepregs using CSCNT-dispersed epoxy," *Composites Part A: Applied Science and Manufacturing*, vol. 38, no. 10, pp. 2121–2130, 2007.

[55] W. Chen, H. Shen, M. L. Auad, C. Huang, and S. Nutta, "Basalt fiber–epoxy laminates with functionalized multiwalled carbon nanotubes," *Composites Part A: Applied Science and Manufacturing*, vol. 40, no. 8, pp. 1082–1089, 2009.

[56] F. Nanni, B. L. Mayoral, F. Madau, G. Montesperelli, and T. Mc Nally, "Effect of MWCNT alignment on mechanical and selfmonitoring properties of extruded PET–MWCNT nanocomposites," *Composites Science and Technology*, vol. 72, no. 10, pp. 1140–1146, 2012.

[57] X. Kornmann, M. Rees, Y. Thomann, A. Necola, M. Barbezat, and R. Thomann, "Epoxy-layered silicate nanocomposites as matrix in glass fibre-reinforced composites," *Composites Science and Technology*, vol. 65, no. 14, pp. 2259–2268, 2005.

[58] R. Pal, H. N. H. Murthy, K. S. Rai, and M. Krishna, "Influence of organo modified nanoclay on the mechanical behaviour of vinylester/glass nanocomposites," *International Journal of ChemTech Research*, vol. 6, pp. 916–928, 2014.

[59] A. Dorigato and A. Pegorettia, "Development and thermomechanical behavior of nanocomposite epoxy adhesives," *Polymers for Advanced Technologies*, vol. 23, pp. 660–668, 2011.

[60] L. Aktas, Y. K. Hamidi, and M. C. Altan, "Dispersion characterization of nanoclay in molded epoxy disks by combined image analysis and wavelength dispersive spectrometry," *Journal of Engineering Materials and Technology*, vol. 130, pp. 1–9, 2005.

[61] K. Panneerselvam and J. Daniel, "An experimental investigation on polymeric nanocomposite material," in *Proceedings of the All India Manufacturing Technology, Design and Research Conference (AIMTDR 2014)*, p. 298, IIT Guwahati, Guwahati, India, December 2014.

[62] Q. Zhang, J. Liu, R. Sager, L. Dai, and J. Baur, "Hierarchical composites of carbon nanotubes on carbon fiber: influence of growth condition on fiber tensile properties," *Composites Science and Technology*, vol. 69, no. 5, pp. 594–601, 2009.

[63] H. He, K. Li, J. Wang, G. Sun, Y. Li, and J. Wan, "Study on thermal and mechanical properties of nano-calcium carbonate/epoxy Composites," *Materials & Design*, vol. 32, no. 8–9, pp. 4521–4527, 2011.

[64] D. R. Bortz, C. Merino, and I. Martin-Gullon, "Mechanical characterization of hierarchical carbon fiber/nanofiber composite laminates," *Composites Part A: Applied Science and Manufacturing*, vol. 42, no. 11, pp. 1584–1591, 2011.

[65] N. Phonthammachai, X. Li, S. Wong, H. Chia, W. Weei Tjiu, and C. He, "Fabrication of CFRP from high performance clay/epoxy nanocomposite: preparation conditions, thermal–mechanical properties and interlaminar fracture characteristics," *Composites Part A: Applied Science and Manufacturing*, vol. 42, no. 8, pp. 881–887, 2011.

[66] L. B. Manfredi, H. D. Santis, and A. Vázquez, "Influence of the addition of montmorillonite to the matrix of unidirectional glass fibre/epoxy composites on their mechanical and water absorption properties," *Composites Part A: Applied Science and Manufacturing*, vol. 39, no. 11, pp. 1726–1731, 2008.

[67] M. K. Hossain, M. E. Hossain, M. V. Hosur, and S. Jeelani, "Flexural and compression response of woven E-glass/polyester–CNF nanophased composites," *Composites Part A: Applied Science and Manufacturing*, vol. 42, no. 11, pp. 1774–1782, 2011.

[68] B. Sharma, S. Mahajan, R. Chhibber, and R. Mehta, "Glass fiber reinforced polymer-clay nanocomposites: processing, structure and hygrothermal effects on mechanical properties," *Procedia Chemistry*, vol. 4, pp. 39–46, 2012.

[69] J. Li and R. Luo, "Study of the mechanical properties of carbon nanofiber reinforced carbon/carbon composites," *Composites Part A: Applied Science and Manufacturing*, vol. 39, no. 11, pp. 1700–1704, 2008.

[70] M. Madhoushi, A. Chavooshi, A. Ashori, M. P. Ansell, and A. Shakeri, "Properties of wood plastic composite panels made from waste sanding dusts and nanoclay," *Journal of Composite Materials*, vol. 48, no. 14, pp. 1–9, 2014.

[71] B. Suresha, B. N. Ravi Kumar, M. Venkataramareddy, and T. Jayarajua, "Role of micro/nano fillers on mechanical and tribological properties of polyamide66/polypropylene composites," *Materials & Design*, vol. 31, no. 4, pp. 1993–2000, 2010.

[72] J. Zhang, T. Lin, and X. Wang, "Electrospun nanofibre toughened carbon/epoxy composites: effects of polyetherketone cardo (PEK-C) nanofibre diameter and interlayer thickness," *Composites Science and Technology*, vol. 70, no. 11, pp. 1660–1666, 2010.

[73] Y. Xu and S. V. Hoa, "Mechanical properties of carbon fiber reinforced epoxy/clay Nanocomposites," *Composites Science and Technology*, vol. 68, no. 3-4, pp. 854–861, 2008.

[74] A. J. Rodriguez, M. E. Guzman, C. S. Lim, and B. Minaie, "Mechanical properties of carbon nanofiber/fiber-reinforced hierarchical polymer composites manufactured with multiscale-reinforcement fabrics," *Carbon*, vol. 49, no. 3, pp. 937–948, 2011.

[75] M. F. Uddin and C. T. Sun, "Strength of unidirectional glass/epoxy composite with silica nanoparticle-enhanced matrix," *Composites Science and Technology*, vol. 68, no. 7–8, pp. 1637–1643, 2008.

[76] C. M. Manjunatha, A. C. Taylor, A. J. Kinloch, and S. Sprenger, "The tensile fatigue behavior of a silica nanoparticle modified glass fibre reinforced epoxy composite," *Composites Science and Technology*, vol. 70, no. 1, pp. 193–199, 2010.

[77] A. K. Subramaniyan and C. T. Sun, "Enhancing compressive strength of unidirectional polymeric composites using nanoclay," *Composites Part A: Applied Science and Manufacturing*, vol. 37, no. 12, pp. 2257–2268, 2006.

[78] Y. Iwahori, S. Ishiwata, T. Sumizawa, and T. Ishikawa, "Mechanical properties improvements in two-phase and three-phase composites using carbon nano-fiber dispersed resin," *Composites Part A: Applied Science and Manufacturing*, vol. 36, no. 10, pp. 1430–1439, 2005.

[79] S. Arun, M. Maharana, and S. Kanagaraj, "Optimizing the processing conditions for the reinforcement of epoxy resin by multiwalled carbon nanotubes," *Journal of Nanotechnology*, vol. 2013, Article ID 634726, 6 pages, 2013.

[80] A. Jumahat, C. Soutis, J. Mahmud, and N. Ahmad, "Compressive properties of nanoclay/epoxy nanocomposites. International symposium on robotics and intelligent sensors," *Procedia Engineering*, vol. 41, pp. 1607–1613, 2012.

[81] L. Böger, J. Sumfleth, H. Hedemann, and K. Schulte, "Improvement of fatigue life by incorporation of nanoparticles in glass fiber reinforced epoxy," *Composites Part A: Applied Science and Manufacturing*, vol. 41, no. 10, pp. 1419–1424, 2010.

[82] Y. Zhou, F. Pervin, S. Jeelani, and P. K. Mallick, "Improvement in mechanical properties of carbon fabric–epoxy composite using carbon nanofibers," *Journal of Materials Processing Technology*, vol. 198, no. 1–3, pp. 445–453, 2008.

[83] C. M. Manjunatha, S. Sprenger, A. C. Taylor, and A. J. Kinloch, "The tensile fatigue behavior of a glass-fiber reinforced plastic composite using a hybrid toughened epoxy matrix," *Journal of Composite Materials*, vol. 44, no. 17, pp. 2095–2109, 2010.

[84] C. M. Manjunatha, N. Jagannathan, K. Padmalatha, A. J. Kinloch, and A. C. Taylor, "Improved variable-amplitude fatigue behavior of a glass-fiber-reinforced hybrid-toughened epoxy composite," *Journal of Reinforced Plastics and Composites*, vol. 30, no. 21, pp. 1783–1793, 2011.

[85] B. C. Kim, S. W. Park, and D. G. Lee, "Fracture toughness of the nanoparticle reinforced epoxy composites," *Composite Structures*, vol. 86, no. 1–3, pp. 69–77, 2008.

[86] V. Morote-Martínez, R. Torregrosa-Coque, and J. M. Martín-Martínez, "Addition of unmodified nanoclay to improve the performance of unsaturated polyester resin coating on natural stone," *International Journal of Adhesion and Adhesives*, vol. 31, no. 3, pp. 154–163, 2011.

[87] N. A. Siddiqui, R. S. C. Woo, J. K. Kim, C. C. K. Leung, and A. Munir, "Mode I interlaminar fracture behavior and mechanical properties of CFRPs with nanoclay-filled epoxy matrix," *Composites Part A: Applied Science and Manufacturing*, vol. 38, no. 2, pp. 449–460, 2007.

[88] E. Bozkurt, E. Kaya, and M. Tanoglu, "Mechanical and thermal behavior of non-crimp glass fiber reinforced layered clay/epoxy nanocomposites," *Composites Science and Technology*, vol. 67, no. 15–16, pp. 3394–3403, 2007.

[89] Y. Tang, L. Ye, D. Zhang, and S. Deng, "Characterization of transverse tensile interlaminar shear and interlaminate

fracture in CF/EP laminates with 10 wt.% and 20 wt.% silica nanoparticles in matrix resins," *Composites Part A: Applied Science and Manufacturing*, vol. 42, no. 12, pp. 1943–1950, 2011.

[90] D. C. Davis and B. D. Whelan, "An experimental study of interlaminar shear fracture toughness of a nanotube reinforced composite," *Composites Part B: Engineering*, vol. 42, no. 1, pp. 105–116, 2011.

[91] Y. Ye, H. Chen, J. Wu, and C. M. Chan, "Interlaminar properties of carbon fiber composites with halloysite nanotube-toughened epoxy matrix," *Composites Science and Technology*, vol. 71, no. 5, pp. 717–723, 2011.

[92] V. Kostopoulos, P. Tsotra, P. Karapappas et al., "Mode I interlaminar fracture of CNF or/and PZT doped CFRPs via acoustic emission monitoring," *Composites Science and Technology*, vol. 67, no. 5, pp. 822–828, 2007.

[93] X. F. Yao, D. Zhou, and H. Y. Yeh, "Macro/microscopic fracture characterizations of SiO_2/epoxy nanocomposites," *Aerospace Science and Technology*, vol. 12, no. 3, pp. 223–230, 2008.

[94] D. Zhang, L. Ye, D. Wang, Y. Tang, S. Mustapha, and Y. Chen, "Assessment of transverse impact damage in GF/EP laminates of conductive nanoparicles using electrical resistivity tomography," *Composites Part A: Applied Science and Manufacturing*, vol. 43, no. 9, pp. 1587–1598, 2011.

[95] J. H. Lin, C. W. Lin, C. H. Huang, C.-L. Huang, and C.-W. Lou, "Manufacturing technique and mechanical properties of plastic nanocomposite," *Composites Part B: Engineering*, vol. 44, no. 1, pp. 34–39, 2013.

[96] Y. Yang, C. X. Lu, X. L. Su, and G. P. Wu, "Effect of nano SiO_2 modified emulsion sizing on the interfacies adhesion of carbon filers reinforced composites," *Materials Letters*, vol. 61, no. 17, pp. 3601–3604, 2007.

[97] V. C. S. Chandrasekaran, S. G. Advani, and M. H. Santare, "Influence of resin properties on interlaminar shear strength of glass/epoxy/MWNT hybrid composites," *Composites Part A: Applied Science and Manufacturing*, vol. 42, no. 8, pp. 1007–1016, 2011.

[98] T. Kamae and L. T. Drzal, "Carbon fiber/epoxy composite property enhancement through incorporation of carbon nanotubes at the fiber–matrix interphase – Part I: the development of carbon nanotube coated carbon fibers and the evaluation of their adhesion," *Composites Part A: Applied Science and Manufacturing*, vol. 43, no. 9, pp. 1569–1577, 2012.

[99] M. Quaresimin, M. Salviato, and M. Zappalorto, "Fracture and interlaminar properties of clay-modified epoxiesand their glass reinforced laminates," *Engineering Fracture Mechanics*, vol. 81, pp. 80–93, 2012.

[100] S. Fu, Z. Sun, P. Huang, Y. Li, and N. Hu, "Some basic aspects of polymer nanocomposites: a critical review," *Nano Materials Science*, vol. 1, no. 1, pp. 2–30, 2019.

[101] D. Dean, R. Walker, M. Theodore, E. Hampton, and E. Nyairo, "Chemorheology and properties of epoxy/layered silicate nanocomposites," *Polymer*, vol. 46, no. 9, pp. 3014–3021, 2005.

[102] S. C. Zunjarrao, R. Sriraman, and R. P. Singh, "Effect of processing parameters and clay volume fraction on the mechanical properties of epoxy-clay nanocomposites," *Journal of Materials Science*, vol. 41, no. 8, pp. 2219–2228, 2006.

[103] T. B. Tolle and D. P. Anderson, "The role of preconditioning on morphology development in layered silicate thermoset nanocomposites," *Journal of Applied Polymer Science*, vol. 91, no. 1, pp. 89–100, 2004.

[104] V. Krikorian and D. J. Pochan, "Poly (L-Lactic Acid)/layered silicate nanocomposite: fabrication, characterization and properties," *Chemistry of Materials*, vol. 15, no. 22, pp. 4317–4324, 2003.

[105] B. Akbari and R. Bagheri, "Deformation mechanism of epoxy/clay nanocomposite," *European Polymer Journal*, vol. 43, no. 3, pp. 782–788, 2007.

[106] H. Alamri and I. M. Low, "Effect of water absorption on the mechanical properties of nanoclay filled recycled cellulose fibre reinforced epoxy hybrid nanocomposites," *Composites Part A: Applied Science and Manufacturing*, vol. 44, pp. 23–31, 2013.

[107] Y. Mansoori, K. Roojaei, M. R. Zamanloo, and G. Imanzadeh, "Polymer-clay nanocomposites: chemical grafting of polystyrene onto Cloisite 20A," *Chinese Journal of Polymer Science*, vol. 30, pp. 815–823, 2012.

[108] M. Sarfraz, "Upgrading electrical, mechanical, and chemical properties of CNTs/polybond nanocomposites: pursuit of electroconductive structural polymer nanocomplexes," *International Journal of Polymer Science*, vol. 2016, Article ID 2396817, 8 pages, 2016.

[109] H. Yao, Z. You, Li L. Liang et al., "Rheological properties and chemical analysis of nanoclay and carbon microfiber modified asphalt with Fourier transform infrared spectroscopy," *Construction and Building Materials*, vol. 38, pp. 327–337, 2013.

[110] F. Agrebi, N. Ghorbel, S. Bresson, O. Abbas, and A. Kallel, "Study of nanocomposites based on cellulose nanoparticles and natural rubber latex by ATR/FTIR spectroscopy: the impact of reinforcement," *Polymer Composites*, vol. 40, no. 5, pp. 2076–2087, 2019.

[111] L. Aktas, Y. K. Hamidi, and M. C. Altan, "Characterisation of nanoclay dispersion in resin transfer moulded glass/nanoclay/epoxy composites," *Plastics, Rubber and Composites*, vol. 33, no. 6, pp. 267–272, 2004.

[112] M. A. Paul, M. Alexandre, P. Degée, C. Henrist, A. Rulmont, and P. Dubois, "New nanocomposite materials based on plasticized poly(L-lactide) and organo-modified montmorillonites: thermal and morphological study," *Polymer*, vol. 44, no. 2, pp. 443–450, 2003.

[113] J. H. Chang, "Polyimide nanocomposites with functionalized graphene sheets: thermal property, morphology, gas permeation, and electroconductivity," *Journal of Thermoplastic Composite Materials*, vol. 31, no. 6, pp. 837–861, 2018.

[114] S. Krishnaswamy, L. Tinsley, V. Marchante, S. Addepalli, Z. Huang, and H. Abhyankar, "Effect of extrusion and compression moulding on the thermal properties of nylon-6/silica aerogel composites," *Journal of Thermoplastic Composite Materials*, vol. 31, no. 7, pp. 992–1009, 2018.

Hindawi
Advances in Materials Science and Engineering
Volume 2022, Article ID 8196347, 12 pages
https://doi.org/10.1155/2022/8196347

Research Article

Analysis of Turning Performance on AISI O1 Steel Using VO+nMoS$_2$ as Coolant

V. Sivaraman,[1] S. J. Davis Hans,[2] Kumaran Palani,[3] Tsegaye Alemayehu Atiso,[4] Jafferson JM,[5] and Nimel Sworna Ross[6]

[1]*Department of Mechanical Engineering, Panimalar Polytechnic College, Chennai, India*
[2]*Department of Mechanical Engineering, Jansons Institute of Technology, Coimbatore, India*
[3]*Department of Mechanical Engineering, College of Engineering, Wolaita Sodo University, Wolaita Sodo, Ethiopia*
[4]*Dean for College of Engineering, Wolaita Sodo University, Wolaita Sodo, Ethiopia*
[5]*Director CoE for Additive Manufacturing, VIT University, Chennai Campus, Vellore, India*
[6]*Department of Mechanical Engineering, Saveetha School of Engineering, Saveetha Institute of Medical and Technical Sciences, Chennai 602105, Tamil Nadu, India*

Correspondence should be addressed to Kumaran Palani; pkumaran2003et@gmail.com and Nimel Sworna Ross; nimelross@gmail.com

Received 14 February 2022; Revised 15 March 2022; Accepted 28 March 2022; Published 23 April 2022

Academic Editor: Adam Khan M

Copyright © 2022 V. Sivaraman et al. This is an open access article distributed under the Creative Commons Attribution License, which permits unrestricted use, distribution, and reproduction in any medium, provided the original work is properly cited.

AISI O1 cold work steel is a hard-to-machine material as a reason of its good temperature resistance, superficial hardness, and lesser response to wear. Hence, material removal from such hard materials is both cost- and time-consuming. Conventional cutting fluids fail to lessen the hotness at the tool-work junction. This research work explores the effects of a uniquely prepared and eco-friendly cutting fluid on the cutting performance of AISI O1 steel using tool inserts of three different materials. The prepared cutting fluid, molybdenum disulfide nanoparticle (MoS2) blended in biodegradable vegetable oil (VO) was distributed into the cutting zone with the help of the minimum quantity lubricant (MQL) technique. The integrated approach of Taguchi's average normalized S/N ratio-based RSM method was employed to model the parameters for better responses. The optimal condition predicted by the approach (the type of insert – CBN, Vc – 110.12 m/min, f – 0.08 mm/rev, and DOC – 0.20076 mm) was observed to produce noteworthy improvements in tool wear and lessen the cutting force in addition to a good surface finish. The study will offer the required guidance for tool and die industries handling AISI O1 steel and help researchers work towards sustainable machining.

1. Introduction

AISI O1 is a cold worked, low alloy steel with high demand in industries manufacturing tools and dies [1]. It is an oil-hardening tool steel with higher chromium and tungsten content and hence an improved wear resistance. It has an elevated hardness of 56–62 HRC because of its high carbon content and high resistance to wear at moderate temperatures (Navas et al. 2008). The machining of quenched steels is accomplished by employing grinding wheels due to their increased hardness [2]. High temperatures produced during dry machining diminish the strength of cutting tools because of plastic deformation [3]. An investigational trial on dry machining of 17–4 PH stainless steel has detected more cutter wear due to its higher temperature at the cutting zone [4]. Heavy mechanical and thermal loading during dry cutting results shows severe imperfections on the machined surface, such as grooves creating microfracture and smearing [5]. Hence, the heat evolved in the machining region must be controlled effectively by an appropriate selection of correct machining parameters with effective cutting fluids (CFs) [6]. The CFs are not only used for the lubrication process but also to provide good cooling and clearing of chips from the machining zone. The tribological features of CFs create a thin protective film layer over the machining zone, reducing the friction and wear [7]. Conventional CFs make a stringent environmental impact, affecting employee health. The production cost is increased for

separating the chips from CFs [8]. In the MQL technique, also known as near-dry machining, a minor amount of vegetable-based oil or biodegradable synthetic esters were delivered along with compressed air to the site of machining in the range of 10–100 ml/hr [9]. It was found that the approach has provided significant improvements in machined surfaces and the life of cutting tools [10]. The MQL method minimized the cutter wear and promisingly augmented the material removal rate in the turning of nickel-chromium alloy [11]. MQL improves the cutting tool life and decreases the cutting forces [12]. Response surface methodology (RSM) was explored to investigate the parameter effects in machining titanium alloy under the MQL environment. The developed mathematical equations were observed to predict the performance of turning characteristics close to the investigational results [13]. Experimental investigations quantified that MQL can curtail together manufacturing costs and ecological hazards hence an effective alternative to conventional flood cooling [14]. Biodegradable vegetable oils are used in the MQL technique to induce sustainability during the machining process. Although biodegradable oils have good lubricant qualities, their low thermal properties limit their usage as CFs in the machining industry [15]. Modern-day studies have revealed that distinct nanoparticles are added to the CF to surge the efficacy of the MQL system in the machining method [16]. The polymer polyether ether ketone with varying size and concentration of solid lubricants (MoS2 and WS2) reduced the friction up to 30%. The nano-sized solid lubricant particles reduced the tool wear significantly by providing an effective low friction tribofilm [17]. Greater nanoparticle levels increase the thermal conductivity of nanofluids. MoS2 was found to be nonreactive [18]. The machining characteristics of nano MoS2 in the MQL technique with various base fluids such as palm oil, soyabean oil, rapeseed oil, and paraffin oil were studied. Palm oil effectively decreases the cutting forces and grinding energy, although soya bean oil with a 6% concentration of nMoS2 particles provides more cooling and lubrication than palm oil due to its higher viscosity [19]. The inclusion of nanoparticles in the base CF improves heat conductivity, lowering the cutting temperature [20]. Machining of AISI 1040 steel with nMoS2 with vegetable oil under the MQL technique reduced the coefficient of friction by 37% and cutting temperature by 21% compared to dry machining [21]. RSM is perceived as an interesting tool by many researchers for various applications. The prediction model for surface roughness was formed using RSM to determine the surface quality in the machining process [22]. RSM is a practical method for modelling any industrial process for sustainable manufacturing.

In this view, it was decided to realize the potential of molybdenum disulfide nanoparticles blended with biodegradable vegetable oil on turning. Nanofluid was prepared under laboratory conditions. Traditional dry turning, flood cooling, and nanofluid expelled using the MQL system were employed, and the results were compared. Machining parameters such as cutting speed (Vc), feed rate (f), and depth of cut (DOC) were considered independent variables, and the effect of these parameters on surface roughness, tool wear, and chip morphology has been investigated. In this study, an integrated approach of principal component-based RSM was used for designing, analyzing, and optimizing the hard turning of AISI O1 cold work tool steel.

2. Experimental Procedure

2.1. Material and Tool. CNC lathe, Super Jobber 500 has been used to carry out the turning operations on AISI O1 cold work tool steel. The 50 mm long workpiece is a round bar of 30 mm diameter. Three different types of ISO-designated cutting inserts (PVD-TiAlN, ceramic, and CBN) were used. The inserts were mechanically clamped on tool holders (Teknik PCLNR 2525M12). The experimental setup is shown in Figure 1. The chemical composition of the workpiece is as follows: Fe – 95.4%, Mn – 1.35%, C – 0.90%, Si – 0.37%, Cr – 0.56%, W – 0.47%, Ni – 0.29%, V – 0.30%, Cu – 0.22%, P – 0.03%, and S – 0.03%. Table 1 shows the process parameters of the experimental work.

2.2. Machining Environments. The nMQL was made by dissolving 0.2 %wt. of nMoS2 in 100 ml of castor oil with a mechanical stirrer. Castor oil has a viscosity of 0.535 Pa s. At an air pressure of 8 bar, the MQL system (KENCO brand) was programmed to produce 50 ml/h (flow rate). The distance between the nozzle and tool-work interface was 15 mm with the nozzle directed at a spray angle of 30°. Experiments were conducted for the fixed ranges under controllable process parameters.

2.3. Experimentation. The studies are created following Taguchi's design of experiments concept. Preliminary experimental trials are conducted to identify the most influencing parameters and the range of their levels. The f, depth of cut, and Vc are the most important turning factors, and they can be modified at three levels. The L27 orthogonal array (OA) was chosen to accommodate the turning parameters. The experiments were conducted according to the designed OA at random experimental to avoid the extraneous effects of uncontrollable parameters, and two replications were performed at each condition. Surface roughness (Ra), flank wear (Vb), temperature (T), and cutting force (Fc) are considered as the outcomes influencing the machining performance. The output responses are displayed in Table 2.

2.4. Measurement. A dynamometer was used to evaluate the cutting force. Taylor Hobson Surtronic 3+ was used to quantify the machined surface's roughness. A video measuring system was used to assess tool wear (VMS-1020F). An HTC-IR noncontact thermometer with an accuracy level of ±1 was utilized to quantify the temperature during turning. The surface topography, tool damage, and chip formation were examined using a Hitachi scanning electron microscope (SEM).

Figure 1: Experimental setup.

Table 1: Experimental parameters.

Workpiece	AISI O1 steel
Cutting insert	PVD – TiAlN, ceramic, CBN
Insert model – TiAlN, ceramic, CBN	TNMG 160408 TFTNGA160408T01020 TNMG 160408
Axial DOC (mm) conditions, Vc (m/min)	0.2, 0.45, 0.7 nMQL 110, 140, 170
f (mm/rev)	0.02, 0.05, 0.08
Hardness (HRC)	62
Nose radius (mm)	0.8

Table 2: Experimental condition and observed responses.

		Parameters			Responses							
Ex. No.	Type of insert	Vc	*f*	Depth of cut	Surface roughness, Ra (μm)		Flank wear, Vb (mm)		Temperature, *T* (°C)		Cutting force, Fc (*N*)	
1	TiAlN	110	0.02	0.2	0.602	0.602	0.021	0.021	84	85	345	345
2	TiAlN	110	0.05	0.45	0.934	0.918	0.023	0.023	88	88	332	335
3	TiAlN	110	0.08	0.7	1.334	1.346	0.028	0.028	104	103	358	359
4	TiAlN	140	0.02	0.45	0.664	0.693	0.027	0.026	102	102	321	321
5	TiAlN	140	0.05	0.7	0.764	0.784	0.030	0.029	105	105	349	352
6	TiAlN	140	0.08	0.2	0.590	0.602	0.030	0.029	112	111	359	360
7	TiAlN	170	0.02	0.7	0.570	0.579	0.027	0.027	115	115	285	284
8	TiAlN	170	0.05	0.2	0.544	0.544	0.030	0.031	121	122	337	338
9	TiAlN	170	0.08	0.45	0.824	0.804	0.034	0.034	125	125	378	378
10	Ceramic	110	0.02	0.2	0.620	0.649	0.022	0.022	88	88	315	317
11	Ceramic	110	0.05	0.45	0.790	0.794	0.025	0.025	100	100	326	326
12	Ceramic	110	0.08	0.7	0.970	0.954	0.032	0.033	109	109	348	346
13	Ceramic	140	0.02	0.45	0.770	0.790	0.024	0.023	95	94	325	327
14	Ceramic	140	0.05	0.7	0.870	0.874	0.028	0.028	107	107	392	390
15	Ceramic	140	0.08	0.2	0.740	0.764	0.022	0.021	98	97	253	255
16	Ceramic	170	0.02	0.7	0.480	0.484	0.025	0.025	103	103	276	277
17	Ceramic	170	0.05	0.2	0.450	0.434	0.029	0.028	105	104	321	322
18	Ceramic	170	0.08	0.45	0.670	0.650	0.032	0.032	108	108	342	341
19	CBN	110	0.02	0.2	0.495	0.491	0.022	0.022	83	82	355	354
20	CBN	110	0.05	0.45	0.565	0.549	0.023	0.022	74	74	277	276
21	CBN	110	0.08	0.7	0.635	0.635	0.026	0.025	92	91	354	354
22	CBN	140	0.02	0.45	0.425	0.405	0.023	0.023	96	96	273	274
23	CBN	140	0.05	0.7	0.605	0.625	0.025	0.025	85	85	296	296
24	CBN	140	0.08	0.2	0.535	0.543	0.023	0.022	90	91	268	271
25	CBN	170	0.02	0.7	0.410	0.439	0.024	0.024	103	103	246	247
26	CBN	170	0.05	0.2	0.320	0.349	0.021	0.022	98	98	263	263
27	CBN	170	0.08	0.45	0.425	0.441	0.025	0.025	100	101	289	287

3. Average Normalized S/N Ratio-Based RSM (ASN-RSM)

RSM is a statistical tool with a module on the modelling of variables and optimization of multiple outcomes using the desirability approach. RSM can illustrate the effect of turning parameters via the response surface graphs [22]. When multiples responses are involved in a problem, the RSM technique generates individual polynomial models for each response. For simultaneous optimization, the multiple responses are converted into a single quality index, which is incorporated into necessary algorithms for predicting the optimal condition. The single quality index is fed into the RSM technique to predict the optimal condition of turning parameters. The algorithm of an ASN-RSM is as follows:

Step 1: Estimate the value of the S/N ratio (η_{ij}) for each response using a suitable formula based on its quality characteristics. The S/N ratio condenses the observation with replications of a certain trial by considering the mean and standard deviation of its replications. The observed responses such as flank wear (Vb), temperature (T), and cutting force (Fc) are the "smaller-the-better" quality characteristics.

The goal point of smaller-the-better quality characteristics is the attainment of value 0 (zero). The S/N ratio (η_{ij}) for such a characteristic is evaluated by means of the following equation:

$$\frac{S}{N}\text{Ratio}\left(\eta_{ij}\right) = -10.\ \log_{10}\frac{1}{r}\sum_{i=1}^{r} y_{ij}^{2}, \tag{1}$$

where r is the quantity of repetitions; $i = 1, 2, 3, \ldots, n$; $j = 1, 2, 3, \ldots, m$; m is the number of responses, and n is the number of experimental trials.

Step 2: Compute the normalized S/N ratio (Z_{ij}) using equation (2) to minimize the influence of the variability of the S/N ratio among responses. The values of the normalized S/N ratio vary between 0 and 1.

$$Z_{ij} = \frac{\eta_{ij} - \min\left(\eta_{ij}, i = 1, 2, 3 \ldots, n\right)}{\max\left(\eta_{ij}, i = 1, 2, 3 \ldots, n\right) - \min\left(\eta_{ij}, i = 1, 2, 3 \ldots, n\right)}. \tag{2}$$

Step 3: Analyze the average normalized S/N ratio (ASN) value of each trial using the following equation:

$$ASN_i = \frac{\sum_{j=1}^{m}\left(Z_{ij}\right)}{m}. \tag{3}$$

Step 4: Develop a polynomial regression model that constructs a relationship between ASN and turning parameters to depict the behavior of parameters in the experimental domain.

Step 5: Perform the analysis of variance (ANOVA) with ASN values to find the contribution and statistical significance of different turning parameters on the responses.

Step 6: Make the 3D response surface plots to reveal the effects of parameter levels on the ASN and find out the near-optimal condition of turning parameters using the desirability approach.

Step 7: Conduct the confirmation experiments for authenticating the optimal parameter setting predicted using RSM.

4. Results and Discussion

4.1. Implementation of ASN-RSM. As an initial step of the proposed algorithm, the observed data is transformed as the S/N ratio where the quality characteristics of responses were converted into larger-the-better irrespective of the quality characteristics of responses. The responses are transformed as S/N ratio values of the smaller-the-better condition, and the variability among the S/N ratio of responses is reduced by the normalizing process. The calculated S/N ratio and normalized S/N ratio (NSNR) are shown in Table 3. An individual set of normalized S/N ratio values is obtained for each response procedure, and the normalized S/N ratio values are combined by calculating the average of them. For ensuring the equal importance of responses, the average normalized S/N ratio value is considered for further analysis [23]. The calculated single quality index "average normalized S/N ratio" (ASN) for each trial is presented in Table 3.

The ASN value of experiment number 26 appears high among the set of ASN values, which indicates that the corresponding turning condition is adjacent to the optimal turning condition. The dispersion of ASN values for various trials is plotted and shown in Figure 2. The variation of ASN to the adjacent trial shows that there is minimal effect of extraneous factors on the responses.

4.2. Development of Polynomial Model Using RSM. A second-order polynomial equation was generated using the software Design Expert V7.0 that constructs a relationship between the parameters of the turning process and ASN. The model was reduced by the backward elimination method in which the elimination of insignificant model terms originates from its highest order. The mathematical models to predict the ASN value using coded factors and models for each level of categorical factor "type of insert" are presented in equations (4)–(7), respectively. The pooled ANOVA was established with significant model terms, and the model coefficient is shown in Table 4. The model fitness and model terms are verified at the confident level of 99% and 95%, respectively. The calculated F-ratio of the developed model was 25.06, and p-value was less than 0.0001, displaying model fitness and adequacy of model terms. The model terms A, B, C, D, BC, BD, and CD were identified as significant model terms.

Table 3: Calculated S/N ratio, normalized S/N ratio, and ASN values.

Ex. No.	S/N ratio				Normalized S/N ratio (NSN)				ASN
	Ra	Vb	*T*	Fc	Ra	Vb	*T*	Fc	
1	4.408	33.432	−38.486	−50.756	0.557	1.000	0.758	0.274	0.647
2	0.593	32.956	−38.890	−50.423	0.250	0.884	0.669	0.357	0.540
3	−2.503	30.964	−40.341	−51.078	0.000	0.400	0.351	0.195	0.236
4	3.557	31.437	−40.172	−50.130	0.489	0.515	0.388	0.429	0.455
5	2.338	30.516	−40.424	−50.857	0.390	0.291	0.333	0.249	0.316
6	4.583	30.400	−40.984	−51.102	0.571	0.263	0.209	0.189	0.308
7	4.876	31.437	−41.214	−49.097	0.595	0.515	0.159	0.684	0.488
8	5.288	30.574	−41.656	−50.553	0.628	0.305	0.062	0.324	0.330
9	1.681	29.319	−41.938	−51.550	0.337	0.000	0.000	0.078	0.104
10	4.152	33.311	−38.890	−49.966	0.537	0.970	0.669	0.469	0.662
11	2.047	32.217	−40.000	−50.264	0.367	0.704	0.426	0.396	0.473
12	0.265	29.843	−40.749	−50.832	0.223	0.127	0.261	0.256	0.217
13	2.270	32.432	−39.554	−50.238	0.385	0.757	0.523	0.402	0.517
14	1.210	31.213	−40.588	−51.866	0.299	0.460	0.297	0.000	0.264
15	2.615	33.351	−39.825	−48.062	0.413	0.980	0.464	0.940	0.699
16	6.375	32.217	−40.257	−48.818	0.716	0.704	0.369	0.753	0.636
17	6.936	30.873	−40.424	−50.130	0.761	0.378	0.333	0.429	0.475
18	3.479	29.924	−40.668	−50.681	0.482	0.147	0.279	0.293	0.300
19	6.108	33.073	−38.382	−51.005	0.694	0.913	0.781	0.213	0.650
20	4.959	32.841	−37.385	−48.850	0.602	0.856	1.000	0.745	0.801
21	3.945	31.869	−39.276	−50.980	0.520	0.620	0.585	0.219	0.493
22	7.432	32.803	−39.645	−48.723	0.801	0.847	0.504	0.776	0.732
23	4.365	32.217	−38.588	−49.426	0.554	0.704	0.736	0.603	0.654
24	5.433	32.728	−39.085	−48.563	0.640	0.829	0.627	0.816	0.728
25	7.744	32.324	−40.257	−47.819	0.826	0.730	0.369	1.000	0.745
26	9.897	33.432	−39.825	−48.399	1.000	1.000	0.464	0.857	0.830
27	7.432	31.938	−40.000	−49.218	0.801	0.637	0.426	0.654	0.636

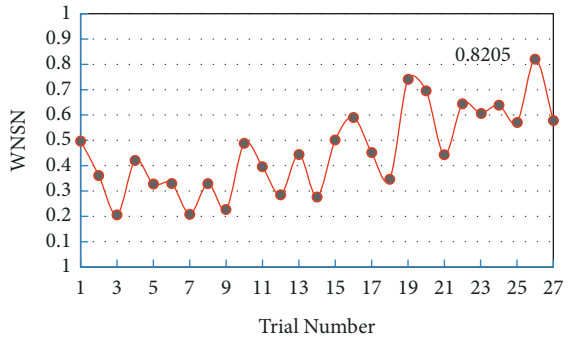

Figure 2: Variation of ASN for different trials.

Table 4: Results of ANOVA on ASN.

Source	Sum of squares	Degrees of freedom	Mean sum of square	*F*-value	*p*-value	Remarks
Model	0.92	10	0.092	13.2	<0.0001	Significant
A – type of coating	0.48	2	0.24	34.02	<0.0001	
B – Vc	0.043	1	0.043	6.21	0.024	
C – F	0.18	1	0.18	26.03	0.0001	
D – depth of cut	0.091	1	0.091	13.03	0.0024	
AB	0.053	2	0.026	3.76	0.0457	
AC	0.038	2	0.019	2.69	0.0985	
CD	0.082	1	0.082	11.78	0.0034	
Residual	0.11	16	7.00E-03			
Cor total	1.04	26				

4.2.1. Final Equation in terms of Coded Factors

$$\begin{aligned}\text{ASN} = {} & +0.52 - 0.14 * \text{A}[1] - 0.045 * \text{A}[2] - 0.062 * \text{B} - 0.10 * \text{C} - 0.071 * \text{D} - 0.074 * \text{A}[1]\text{B} \\ & + 0.020 * \text{A}[2]\text{B} - 0.056 * \text{A}[1]\text{C} + 9.844\text{E} - 004 * \text{A}[2]\text{C} - 0.10 * \text{CD}.\end{aligned} \tag{4}$$

4.2.2. Final Equation in terms of Actual Factors

Insert – TiAlN

$$\begin{aligned}\text{ASN} = {} & +1.09071 - 4.53446\text{E} - 003 * \text{B} + 1.05560 * \text{C} \\ & + 0.41437 * \text{D} - 13.98142 * \text{C} * \text{D}.\end{aligned} \tag{5}$$

Insert – Ceramic

$$\begin{aligned}\text{ASN} = {} & +0.64936 - 1.41701\text{E} - 003 * \text{B} + 2.97103 * \text{C} \\ & + 0.41437 * \text{D} - 13.98142 * \text{C} * \text{D}.\end{aligned} \tag{6}$$

Insert – CBN

$$\begin{aligned}\text{ASN} = {} & +0.62236 - 2.65526\text{E} - 004 * \text{B} + 4.78802 * \text{C} \\ & + 0.41437 * \text{D} - 13.98142 * \text{C} * \text{D}.\end{aligned} \tag{7}$$

The value of coefficient of determination (R^2) was computed as 0.8919, which is nearer to the value 1 and assures the ability of the model in predicting the ASN precisely. There was a closeness between the adjusted R-squared value (0.8244) and the predicted R-squared value (0.6712) that states that the contribution of insignificant terms in arriving at the model fitness is minimum (Table 5). The adequate precision is 13.858, which is greater than 4 that evidences the adequate model discrimination. Moreover, the values of predicted ASN values using the polynomial model and actual ASN values of corresponding machining condition were compared, and the predicted values of ASN fall very closer to the actual values (Figure 3(a)). Figure 3(b) displays the normal probability plot. It was found that the residuals are spread along the straight line closely indicating that normal distribution exists and no other pattern is followed.

4.3. Effect of Parameters on ASN. The ASN value is the single representative of all the responses (surface roughness (Ra), flank wear (Vb), temperature (T), and cutting force (Fc)) and is to be maximized in order to find the optimal cutting condition. The types of inserts contributed to the ASN values significantly. The variation of ASN with the levels of inserts is plotted by varying the Vc (Figure 4(a)). The ASN value was minimum while using the TiAlN insert (0.2445), whereas it appears maximum while using of the CBN insert (0.6884). From Figure 4(a), there is an interaction between ceramic and CBN while varying the Vc (B). The influence of different tool inserts on ASN was plotted for different f (C). It was found that there is no interaction among the levels of tool inserts and the performance of CBN insert (0.7416) was improved at minimum f (Figure 4(b)). Hence, the information from Figure 4 confirms that the insert – CBN produces better values of responses at different cutting conditions of the remaining parameters.

The predicted values of ASN at the Vc of 140 m/min with TiAlN insert were plotted as a 3D response surface graph (Figure 5(a)) by varying the f (C) and DOC (D). The ASN value (0.5718) was better at a lower level of f and higher DOC at a constant Vc. From Figure 5(a), it was found that there is a significant improvement in ASN, when the f is reduced from 0.08 mm/rev to 0.02 mm/rev at a higher depth of cut. There was no substantial improvement in ASN even when the f is reduced at a lower level of DOC (Figure 5(a)). The performance of the machining process was improved with the decrease of DOC (D) at a constant f. The ASN value is enhanced as 0.6047 at the lower level of f (C) and a higher level of DOC (D) with a ceramic insert (Figure 5(b)). A significant influence on ASN is identified with the variation of f (C) from a higher level to lower level at the maximum DOC as well as with the change of DOC (D) at higher f (C) while using ceramic insert (Figure 5(b)). The ASN value reached a higher value (nearer to 0.8271) for the DOC values from 0.7 mm to 0.2 mm, at a constant f of 0.08 mm/rev using CBN insert (Figure 5(c)). The growth rate of ASN was more extensive at a higher level than of lower-level f (C) when the DOC is reduced.

The value of ASN appeared high at the lower level of DOC and higher-level f, while the Vc is maintained at a constant level (Vc = 140 m/min). It was identified that there is a substantial change in ASN value while varying the DOC at a higher level of f (Figure 5(c)). The improvement of the ASN value describes the growth of all the responses, which was maximized at lower DOC (Figure 5(c)).

4.4. Influence of Machining Parameters on Responses. Improved response values are observed while using the CBN insert for turning using nano coolant (Figure 6(a)). A significant improvement was identified in surface roughness, and it is reduced to Ra = 0.48 μm from the value Ra = 0.76 μm obtained with TiAlN insert. The required cutting force is reduced due to the high hardened nature of the CBN insert, and heat generation is also minimal compared to other inserts. The influence of Vc on surface roughness, flank wear, temperature, and cutting force are illustrated in Figure 6(b). Even the higher Vc increases the rate of production, the generation of heat and cutting force is observed to be high due to high friction stress between tool and workpiece. The temperature of the insert varied from 91.3°C to 108.67°C when the Vc is increased from 110 m/min to 170 m/min. The

Table 5: *R*-squared and adequate precision value of the model.

Std. Dev.	0.0837	*R*-squared	0.8919
Mean	0.5161	Adj *R*-squared	0.8244
CV, %	16.2076	Pred *R*-squared	0.6712
PRESS	0.3406	Adeq precision	13.8582

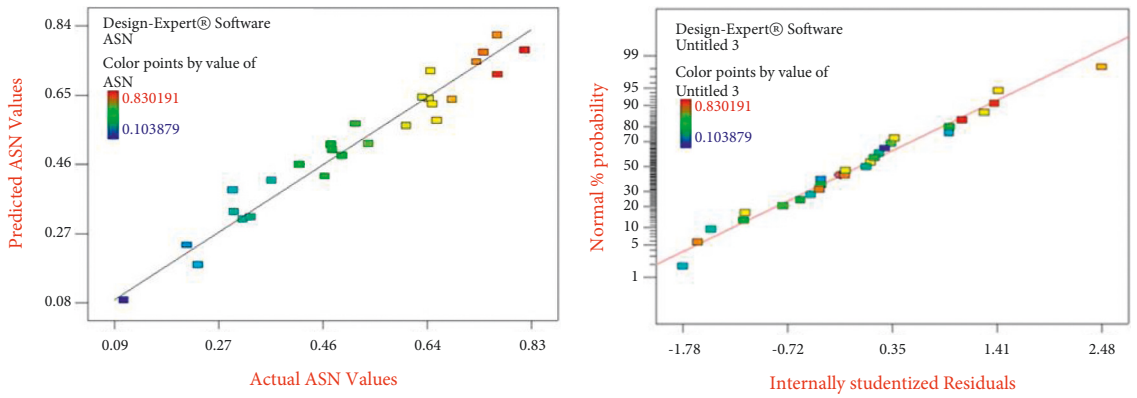

Figure 3: Plot of (a) predicted and actual ASN and (b) normal percentage probability to residuals.

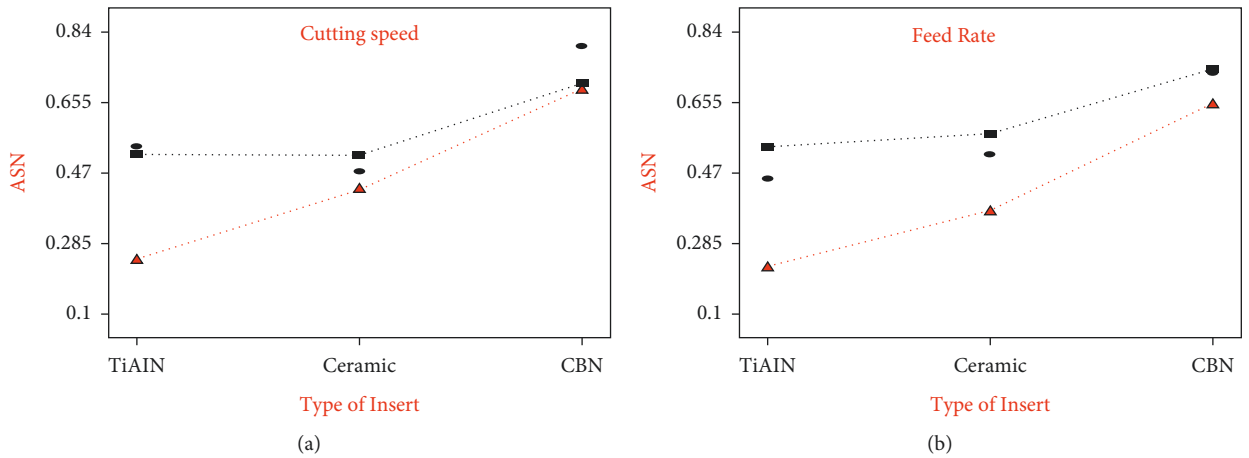

Figure 4: Effect of tool inserts on (a) ASN with cutting speed and (b) ASN with feed rate.

flank wear is enhanced by the thermal softening of the cutting tool due to the high temperature generated at the machining interface. The flank wear is increased at high Vc due to large size of built-up edge (BUE), and the unstable BUE protects the flank face from further wear. An increase in *f* increased the surface roughness (Figure 6(c)). At higher *f*, the gap between peel-off layers was maximum that left ploughing marks and uncut materials on the machined surfaces. Thereby, the surface roughness was measured high, and the required cutting force was also more due to the depth of penetration of the insert along the axis of rotation of the workpiece at a higher *f*. The effect of DOC is shown in Figure 6(d). The higher DOC produces the additional cutting force, which increases the heat generation. At higher temperatures, the responses include poor surface finish and flank wear. Hence, the higher DOC reduces the productivity of the cutting tool.

4.5. Desirability. The parameter setting possessing a higher desirability index is chosen as the optimal setting. The ramp functional graph of the optimal condition is shown in Figure 7. The red dot on each ramp indicates the optimal set of parameters at the most desirable condition. The prediction of ASN appears higher than that of experimental values. Table 6 shows the optimal condition and predicted value of ASN. The predicted optimal condition includes the following: type of insert – CBN, Vc – 110.12 m/min, *f* – 0.079 mm/rev, and DOC – 0.20076 mm. The predicted ASN value at the optimal condition was observed as 0.8328. The expected value falls in the range of 95% confidence interval.

4.6. Validation of Experiments. The confirmation trials were performed with the parameter setting obtained using the ASN-RSM algorithm to validate the efficiency of the

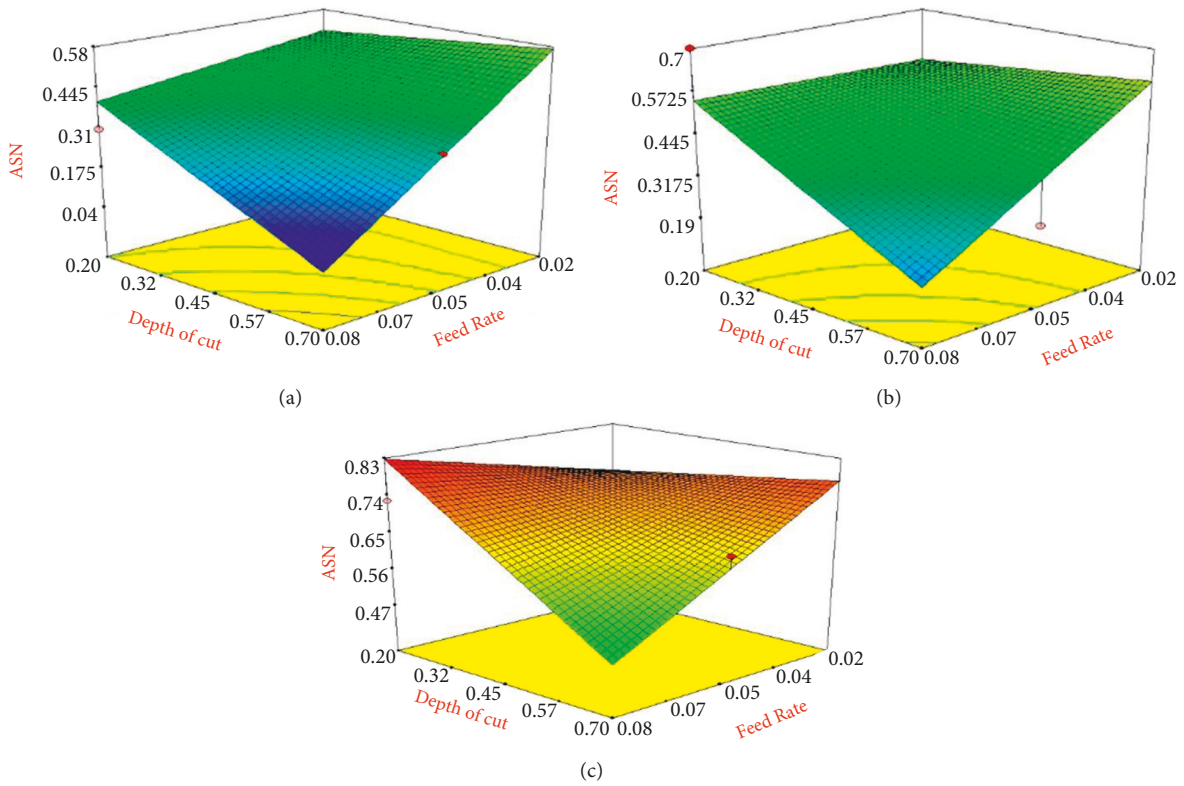

Figure 5: 3D response surface plots: (a) TiAlN, (b) ceramic, and (c) CBN.

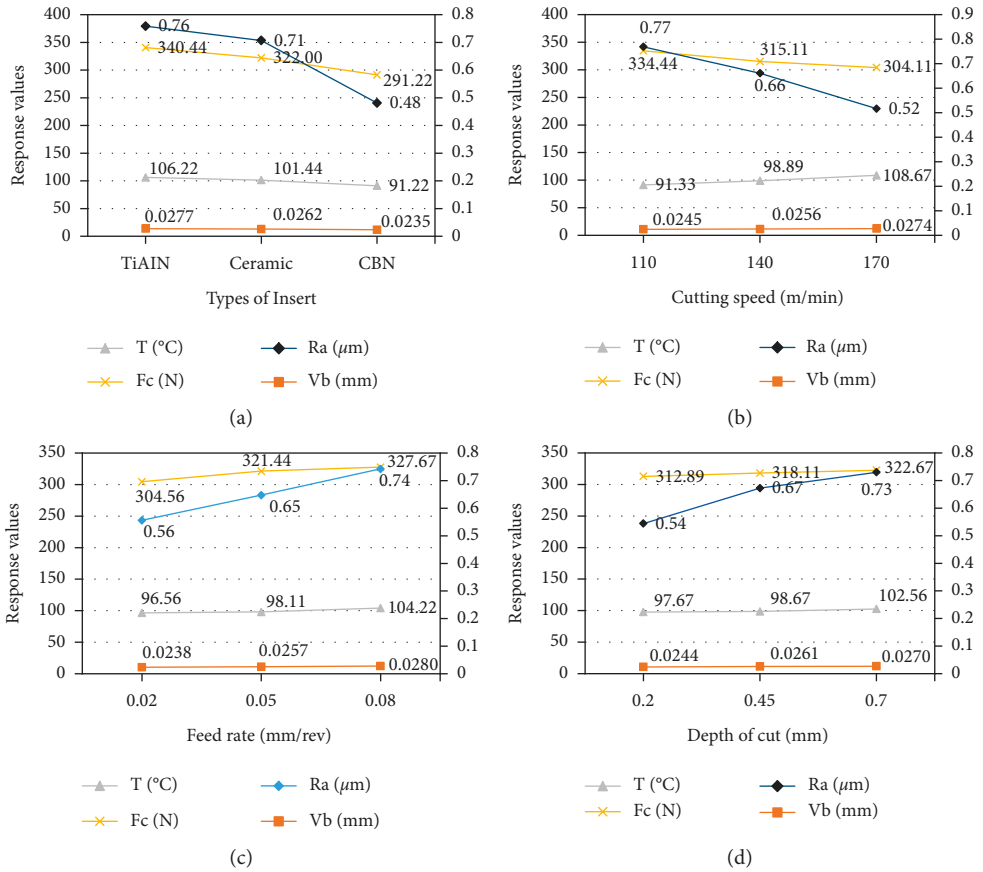

Figure 6: Effect of responses on (a) type of insert, (b) cutting speed, (c) feed rate, and (d) depth of cut.

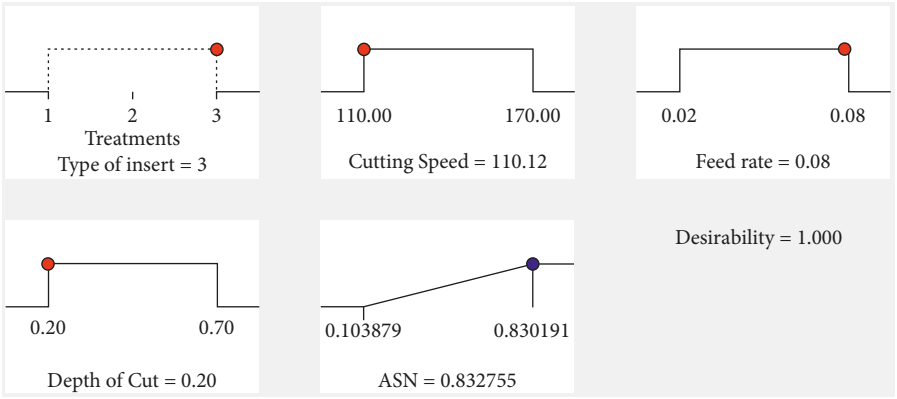

Figure 7: Ramp graph for desirability index.

Table 6: Optimal machining condition.

Factor	Name	Optimal level	Low level	High level
A	Type of insert	CBN	TiAlN	CBN
B	Vc	110.12	110	170
C	F	0.079	0.02	0.08
D	Depth of cut	0.20076	0.2	0.7
Response	Prediction	SE mean	95% CI low	95% CI high
ASN	0.8328	0.073	0.68	0.999

Table 7: Comparison of the response values of ASN setting and confirmation experiment.

Responses	ASN setting	Confirmation experiment	Improvement	Improvement in percentage
ASN	0.8301	0.8328	0.0027	0.3253
Surface roughness, SR (μm)	0.32	0.317	0.003	0.9375
Flank wear, FW (mm)	0.0213	0.0202	0.0011	5.1643
Temperature, T (°C)	98	76	22	22.4490
Cutting force, Fc (N)	289	259.2	29.8	10.3114

predicted optimal condition in improving the responses. The combo of turning variables with the highest ASN (0.8301) value, trial number 26 is used for comparison (Table 7). While turning with the ideal condition forecasted by the merged ASN-RSM method, there is a substantial improvement in the answers.

SEM images observed under the highest ASN setting (experiment no. 26) and confirmation experiment are displayed in Figure 8. The surface roughness profile, SEM images of machined surface, worn-out insert, and chips observed at experiment no. 26 (Figure 8(a)) were analyzed and compared with the confirmation experiment (Figure 8(b)). The machined profile reveals a better surface finish obtained during the confirmation experiment with the same setting used in trial 26. The surface waviness is restricted as well, and it is visualized in the P-profile graph. The SEM images of the machined surface show minimal and near-uniform machining marks in the surface obtained using the same setting. As explained in the previous sections, the cooling and lube nature of nMoS2 restrict the marks on the machined face. Reduced flank wear was seen in the confirmation experiment with the same setting and the improvement was around 0.0011. The received setting during the optimization has a positive effect on sustainable manufacturing. Similar to roughness and flank wear, the temperature and cutting force results are good with the same setting of experiment no. 26. Under the ASN setting and confirmation experiment, less jagged teeth were formed.

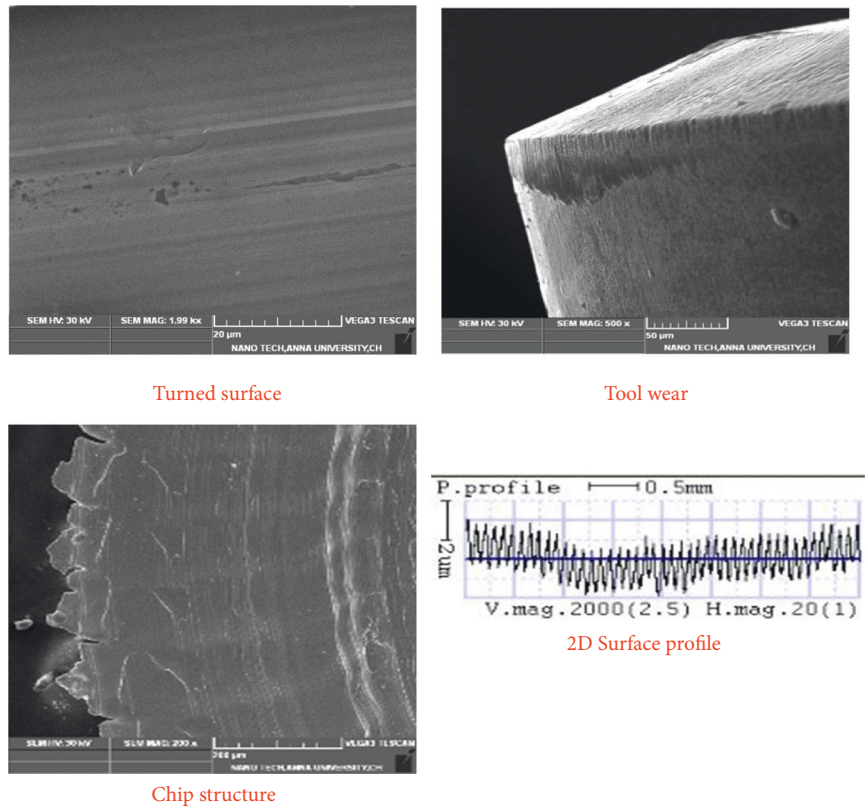

(a)

Figure 8: Continued.

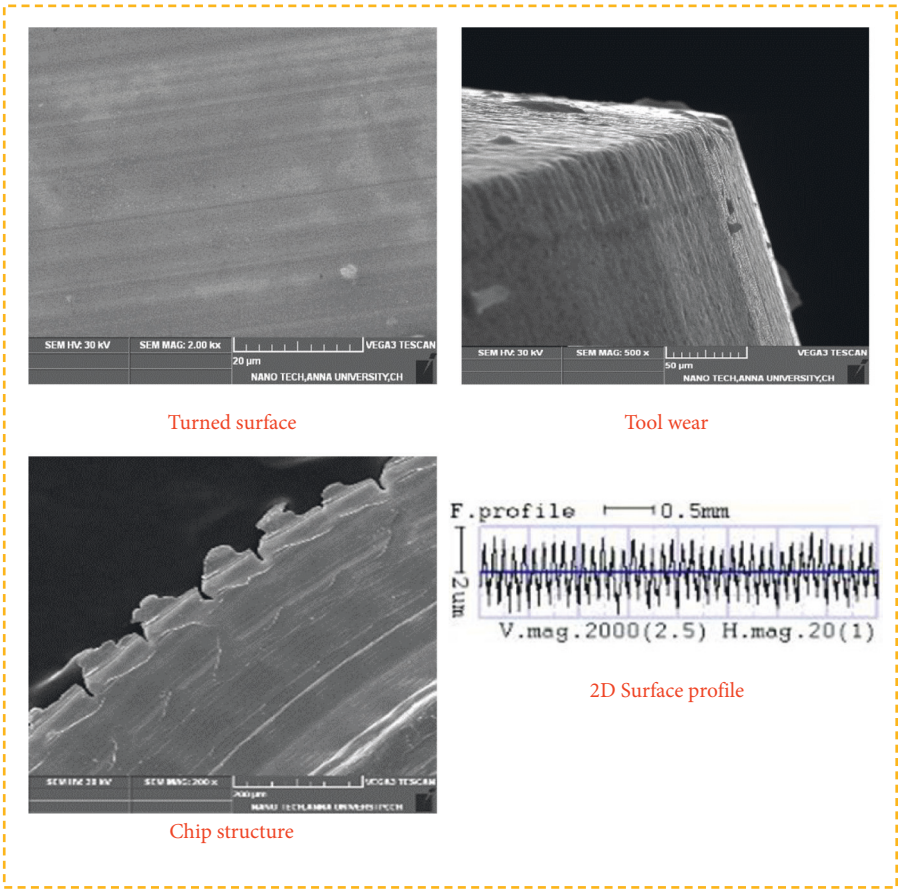

(b)

Figure 8: (a) Surface roughness profile and SEM images experiment no. 26 and (b) surface roughness profile and SEM images observed at the confirmation experiment.

5. Conclusions

The technique of MQL was observed to be effective in improving the machining characteristics of AISI O1 steel. An integrated approach of ASN-RSM was used to model the parameter for better responses and the desirability-based approach to arrive at the optimal parameter setting was validated through confirmation experiments. The following conclusions were drawn.

(i) The nMoS2 blended in biodegradable castor oil employed for lubrication had ensured a considerable reduction in temperature at the tool-work interface and hence could be a viable alternative to the traditional cutting fluids.

(ii) The optimal parameter setting under MQL environment is identified as follows: type of insert – CBN, Vc – 110.12 m/min, f – 0.079 mm/rev, and DOC – 0.20076 mm.

(iii) The statistical supremacy of both Taguchi's S/N ratio concept and RSM are combined to arrive at the optimal setting of parameters. The integration of the two techniques can be realized as the multiple variables are transformed into a single quality index (ASN), which acts as the representative of the various responses. The predicted polynomial model was also observed to be fit and precise.

(iv) The surface finish and tool wear observed at the optimal machining condition were significantly lower than that obtained using the initial setting of parameters. The work offers the necessary direction to handle AISI O1 steel in tool and dies industries under the MQL environment.

Data Availability

The data used to support the findings of this study are included in the article. Should further data or information be required, these are available from the corresponding author upon request.

Conflicts of Interest

The authors declare that they have no conflicts of interest.

References

[1] L. Bourithis, G. D. Papadimitriou, and J. Sideris, "Comparison of wear properties of tool steels AISI D2 and O1 with the same hardness," *Tribology International*, vol. 39, no. 6, pp. 479–489, 2006.

[2] V. García Navas, I. Ferreres, J. A. Marañón, C. Garcia-Rosales, and J. Gil Sevillano, "Electro-discharge machining (EDM) versus hard turning and grinding-Comparison of residual stresses and surface integrity generated in AISI O1 tool steel," *Journal of Materials Processing Technology*, vol. 195, pp. 186–194, 2008.

[3] C. Ezilarasan, V. S. Senthil kumar, and A. Velayudham, "An experimental analysis and measurement of process performances in machining of nimonic C-263 super alloy," *Measurement*, vol. 46, no. 1, pp. 185–199, 2013.

[4] S. Khani, M. Farahnakian, and M. R. Razfar, "Experimental study on hybrid cryogenic and plasma-enhanced turning of 17-4PH stainless steel," *Materials and Manufacturing Processes*, vol. 30, no. 7, pp. 868–874, 2015.

[5] A. Thakur and S. Gangopadhyay, "State-of-the-art in surface integrity in machining of nickel-based super alloys," *International Journal of Machine Tools and Manufacture*, vol. 100, pp. 25–54, 2016.

[6] S. Debnath, M. M. Reddy, and Q. S. Yi, "Environmental friendly cutting fluids and cooling techniques in machining: a review," *Journal of Cleaner Production*, vol. 83, pp. 33–47, 2014.

[7] Ç. Yildirim, T. Kivak, F. Erzincanli, İ. Uygur, and M. Sarikaya, "Optimization of MQL parameters using the Taguchi method in milling of nickel based waspaloy," *Gazi Univ. J. Sci.*vol. 30, pp. 173–186, 2017.

[8] E. Kuram, B. Ozcelik, and P. E. Demirbas, "Environmentally friendly machining: vegetable based cutting fluids," *Presented at the January*, vol. 1, 2013.

[9] M. H. S. Elmunafi, D. Kurniawan, and M. Y. Noordin, "Use of Castor oil as cutting fluid in machining of hardened stainless steel with minimum quantity of lubricant," *Procedia CIRP*, vol. 26, pp. 408–411, 2015.

[10] R. W. Maruda, G. M. Krolczyk, E. Feldshtein, P. Nieslony, B. Tyliszczak, and F. Pusavec, "Tool wear characterizations in finish turning of AISI 1045 carbon steel for MQCL conditions," *Wear*, vol. 372, pp. 54–67, 2017.

[11] D. A. Stephenson, S. J. Skerlos, A. S. King, and S. D. Supekar, "Rough turning Inconel 750 with supercritical CO2-based minimum quantity lubrication," *Journal of Materials Processing Technology*, vol. 214, no. 3, pp. 673–680, 2014.

[12] R. Heinemann, S. Hinduja, G. Barrow, and G. Petuelli, "Effect of MQL on the tool life of small twist drills in deep-hole drilling," *International Journal of Machine Tools and Manufacture*, vol. 46, no. 1, pp. 1–6, 2006.

[13] M. K. Gupta, P. K. Sood, and V. S. Sharma, "Machining parameters optimization of titanium alloy using response surface methodology and particle swarm optimization under minimum-quantity lubrication environment," *Materials and Manufacturing Processes*, vol. 31, no. 13, pp. 1671–1682, 2016.

[14] R. Saidur, K. Y. Leong, and H. A. Mohammed, "A review on applications and challenges of nanofluids," *Renewable and Sustainable Energy Reviews*, vol. 15, no. 3, pp. 1646–1668, 2011.

[15] C. Mao, Y. Huang, X. Zhou, H. Gan, J. Zhang, and Z. Zhou, "The tribological properties of nanofluid used in minimum quantity lubrication grinding," *International Journal of Advanced Manufacturing Technology*, vol. 71, no. 5-8, pp. 1221–1228, 2014.

[16] M. Zalaznik, M. Kalin, S. Novak, and G. Jakša, "Effect of the type, size and concentration of solid lubricants on the tribological properties of the polymer PEEK," *Wear*, vol. 364-365, pp. 31–39, 2016.

[17] A. K. Sharma, A. K. Tiwari, and A. R. Dixit, "Progress of nanofluid application in machining: a review," *Materials and Manufacturing Processes*, vol. 30, no. 7, pp. 813–828, 2015.

[18] Y. Zhang, C. Li, D. Jia, D. Zhang, and X. Zhang, "Experimental evaluation of MoS2 nanoparticles in jet MQL grinding with different types of vegetable oil as base oil," *Journal of Cleaner Production*, vol. 87, pp. 930–940, 2015.

[19] R. K. Singh, A. K. Sharma, A. R. Dixit, A. K. Tiwari, A. Pramanik, and A. Mandal, "Performance evaluation of alumina-graphene hybrid nano-cutting fluid in hard turning," *Journal of Cleaner Production*, vol. 162, pp. 830–845, 2017.

[20] R. Padmini, P. Vamsi Krishna, and G. Krishna Mohana Rao, "Effectiveness of vegetable oil based nanofluids as potential cutting fluids in turning AISI 1040 steel," *Tribology International*, vol. 94, pp. 490–501, 2016.

[21] P. Sivaiah, "Experimental investigation and modelling of MQL assisted turning process during machining of 15-5 PH stainless steel using response surface methodology," *SN Applied Sciences*, vol. 1, 2019.

[22] E. Bair, T. Hastie, D. Paul, and R. Tibshirani, "Prediction by supervised principal components," *Journal of the American Statistical Association*, vol. 101, no. 473, pp. 119–137, 2006.

[23] K. Ganesan, M. Naresh Babu, M. Santhanakumar, and N. Muthukrishnan, "Experimental investigation of copper nanofluid based minimum quantity lubrication in turning of H 11 steel," *Journal of the Brazilian Society of Mechanical Sciences and Engineering*, vol. 40, no. 3, p. 160, 2018.

[24] V. G. Navas, I. Ferreres, J. A. Maranon, C. G. Rosales, and J. G. Sevillano, "White layers generated in AISI O1 tool steel by hard turning or by EDM," *International Journal of Machining and Machinability of Materials*, vol. 4, no. 4, pp. 287–301, 2008.

[25] H. A. Kishawy, M. Dumitrescu, E.-G. Ng, and M. A. Elbestawi, "Effect of coolant strategy on tool performance, chip morphology and surface quality during high-speed machining of A356 aluminum alloy," *International Journal of Machine Tools and Manufacture*, vol. 45, no. 2, pp. 219–227, 2005.

Hindawi
Advances in Materials Science and Engineering
Volume 2022, Article ID 6804011, 13 pages
https://doi.org/10.1155/2022/6804011

Research Article

Effect of TaC/Ti/Si_3N_4 Hard Ceramics on Mechanical and Microstructural Behaviour of AA7075 Processed through Stir Casting Process

J. Pradeep Kumar [1], **D. S. Robinson Smart** [2], **Stephen Manova** [1] and **N. Ummal Salmaan** [3]

[1]*Department of Mechanical Engineering, Karunya Institute of Technology and Sciences, Coimbatore 641114, Tamilnadu, India*
[2]*Department of Aerospace Engineering, Karunya Institute of Technology and Sciences, Coimbatore 641114, Tamilnadu, India*
[3]*Department of Automotive Engineering, Aksum University, Axum, Ethiopia*

Correspondence should be addressed to N. Ummal Salmaan; ummalsalmaan90@gmail.com

Received 10 February 2022; Revised 5 March 2022; Accepted 4 April 2022; Published 21 April 2022

Academic Editor: Adam Khan M

Copyright © 2022 J. Pradeep Kumar et al. This is an open access article distributed under the Creative Commons Attribution License, which permits unrestricted use, distribution, and reproduction in any medium, provided the original work is properly cited.

A liquid metallurgical stir casting route was utilized for developing aluminium alloy (7075) matrix composites blended with fluctuating wt% of silicon nitride (Si_3N_4), tantalum carbide (TaC), and titanium (Ti) for sake of generating a profitable composite with enhanced properties. The physical, microstructural, and mechanical characteristics such as density, high temperature tensile, fatigue, and time-dependent creep experiments were conducted and evaluated. SEM microstructural examinations were performed on the composite samples and proved that there was a good interfacial bonding and uniform dissemination among the reinforcement particulates in the matrix. Physical characteristics were analysed and the outcomes showed that AA7075 blended with 1 wt% TaC, 8 wt% Si_3N_4, and 0.5 wt% Ti proved higher experimental and theoretical densities of 3.2464 g/cm^3 and 3.3038 g/cm^3, respectively, with maximum porosity of 1.7758%. At 30°C, the tensile properties of the developed MMCs showed improved ultimate tensile strength (UTS) of 137.64 N/mm^2. Beyond 100°C, AA7075 reinforced with 0.75 wt% TaC, 6 wt% Si_3N_4, and 1 wt% Ti proved to have a higher strength of 232.17 N/mm^2. Fatigue properties of the developed MMCs discovered were found to be reformed when proportionate to the base alloy by operating at 14×10^3 cycles at the stress of 42.72 MPa. Time-dependent creep analysis of the developed MMCs found to be advanced due to the addition of tough ceramic particulates.

1. Introduction

Human capabilities are the key to realizing the potential of materials. Progression of materials is only possible through the continuous improvement of human behaviour and science [1]. The betterment of novel lightweight structural composites with exceptional mechanical behaviour is a productive methodology to improve the energy effectiveness of components used in military, defence, aerospace, armor, and automotive applications for enhancing reducing CO_2 emissions and fuel efficiency through a reduction in weight of interior and exterior components. These hard ceramic materials gain importance in turbine and aircraft industries and their components such as turbine blades, rivets, and aircraft outer components that are exposed to elevated atmospheric conditions [2]. Lightweight aluminium metal matrix composites (MMCs) are of immense attention in the present situation as a consequence of their high-level electrical, thermal, and mechanical aspects [3]. Properties such as exceptional toughness, higher stiffness and strength, low specific gravity and coefficient of thermal expansion, good wear and corrosion inheritance, high thermal conductivity, and high dimensional accuracy shifted the research from monolithic material to the composites [4]. The MMCs are amalgamations of two or more distinct materials with one being metal and the other being hard ceramics. When not less than two or more than two reinforcements are assimilated, then it is designated as hybrid composites [5]. MMCs are extensively used in various product development such as camera domes, wheel covers, rivets, turbine blades,

and so on in critical applications such as automobile, turbine sectors, aerospace, defence, and military [6]. Recently, there has been a spreading curiosity about using MMCs for high-temperature applications, especially under creep conditions, in aircraft and automobile engines technologies [7]. Particulate blended MMCs have numerous benefits, and it was manufactured certainly with minimal cost in comparison with fibre-blended MMCs [8]. Aluminium-based MMCs can be produced by liquid metallurgical stir casting methodology. Thus, many researchers focus on the influence of nanoparticles on the structure evolution in matrix alloy [9]. The procedure for fabricating the MMCs had a strong dominance on the tribological and mechanical characteristics of any material [10]. The mechanism of conventional casting came into actuality in 1968 by Ray [11], when he stirred the molten alloy of aluminium by encompassing alumina ceramic particulates into the melt, and in this process, the discontinuous reinforcement phases are incorporated into a matrix formed by a mechanical stirrer. Jiang et al. [12] investigated the creep and morphological aspects of high-pressure die-cast Mg–9Al–1Zn–1Sr alloy at 130 to 170°C and stresses from 30 to 80 MPa. The rate of creep at 70 MPa enhanced, and thus, a tertiary stage was noticed. The majority of the intermetallic regions were proliferated on the eutectic zones so that they constituted a continuous reticular region. The origin of the threshold stress could be confederate with the Orowan strengthening of γ-$Mg_{17}Al_{12}$ platelets that dynamically precipitated in the magnesium. Dai et al. [13] synthesized in situ TiB_2/$Al_{12}Si_4Cu_2NiMg$ (mentioned as "Al-12Si") composite processed by salt metal reaction methodology. The influence of reinforcements in wt% and heat treatment on creep deformation was evaluated at 632 K under steady force in the air. It was also noticed that the steady-state rate of creep was minimal at 4 wt% TiB_2/Al-12Si composite. The creep dislocation of the 4 wt% TiB_2/Al-12Si composite material was influenced by the climb of dislocations in the matrix. Coyal et al. [14] investigated various mechanical wear aspects of AA6061 alloy blended with jute ash (50 μm) and SiC (10 μm) reinforcements using conventional casting techniques. The tensile behaviour of the developed hybrid MMCs drastically enhanced because of the strongly bonded ceramic material in the matrix. Enhancement in microhardness can be attributed to the dynamic process of recovery and recrystallization. Wear resistance was mainly dependent on the hardness of the material. Onoro et al. [15] estimated the high-temperature mechanical properties such as hardness and tensile of AA6061 and AA7075 reinforced with boron carbide particles. All the composites were prepared by hot extrusion. Microstructural analysis reveals that the chemical reactions that occur may alter the interfacial characteristics of AMCs. Diffusion mechanism was found to be influential betwixt reinforcements and matrix. At 200 to 300°C, the tensile performance reduces drastically due to the matrix that loses the aging heat treatment by growing coherent hardened precipitates with a subsequent softening. From 200 to 400°C, the mechanical aspects of the 7015 alloy diminish more drastically than those of the 6061 alloy. The interaction betwixt the particulates and dislocations leads to an increment in strength, which is consorted with the Orowan mechanism. Sethi et al. [16] synthesized and characterized AA7075 reinforced with TiB_2 formed through stir casting. It was noticed that TiB_2 particles were homogeneously disseminated in both intra- and intergranular regions and an insignificant quantity of agglomeration was seen at 9 and 12 wt%, respectively. Reduction in grain size results in an increase in microhardness with an increment in wt% of the reinforcements. Strength due to the tension was found to be enhanced due to the restriction of cracks by reinforcements due to its load bearing capacity.

The mechanical characteristics at ambient and elevated temperatures of AA7075-based multihybrid MMCs blended with hard ceramic particulates have been extensively examined. Therefore, in the present research paper, AA7075 matrix composites were fabricated through a low-cost conventional stir casting technique by adding Si_3N_4, TaC, and Ti particles as reinforcement particles. Eventually, there are several facts on the influence of wt%, shape, size, and orientation of the reinforcements on the failure modes and fracture approach. Moreover, literature represent minimal information on the effects of Si_3N_4, TaC, and Ti particulates as blended MMCs at escalated temperatures. In our present research work, tantalum carbide (TaC) is one of the primary and most expensive ceramic reinforcement materials that could serve the purpose of withstanding high temperatures. Therefore, for low economy applications, this particular reinforcement cannot be used. In order to enhance the hardness above a particular limit, the material becomes more brittle. Therefore, the material may not be suitable for applications such as heavy cutting tools due to its extreme hardness. AA7075 reinforced hybrid MMCs can be utilized for all other engineering applications related to high- and low-temperature environmental conditions. Therefore, this research article aims to attain the optimum combination of the reinforcements in the AA7075 matrix material and estimate the influence of temperature on the mechanical behaviour of AA7075 multihybrid MMCs blended with distinct wt% of Si_3N_4/TaC and Ti particulates. Furthermore, a detailed experimental study on microstructural, high temperature tensile, creep, and low-cycle fatigue characterization of fabricated MMCs (AA7075) was carried out for the proposed hybrid MMCs.

2. Materials and Its Processing Technology

2.1. Material Preference. Aluminium-zinc alloy is also called aluminium 7000 series alloy because of the utmost zinc quantity proportion betwixt 5.1 and 6.1 percentages. In 1943, these series were first confidentially evolved by the Japanese company, Sumitomo Metal, ultimately for the manufacturing of the airframe in the Imperial Japanese Navy [17]. In the present study, AA7075 grade has been utilized as a base alloy for setting up aluminium-based hybrid MMCs using the conventional stir casting technique. This material was chosen as a matrix because of its high weight to strength proportion, high strength, less density, minimal cost, and exceptional material quality, which are generally encountered by the scientists for defence, military, armor, marine,

and automobile applications [18]. Table 1 displays the description of the chemical configuration of the AA7075 matrix utilized in the fabrication of the hybrid MMCs. The density of MMCs plays a crucial role in selecting the material for functional and structural applications, particularly for marine and automobile sectors.

Table 2 shows the various physical, mechanical, and thermal properties of the selected matrix and reinforcement materials. Ceramic reinforcement materials such as Si_3N_4, TaC, and Ti were chosen to improve various desired mechanical, fatigue, and creep characteristics of the proposed MMCs. The selected reinforcement particles were acquired from Saveer Matrix Nano Private Limited, Greater Noida, Uttar Pradesh, India. Table 3 shows the various proportions of matrix and reinforcements used for this research. Hard ceramic particles such as Si_3N_4 act as solid lubricants that enhance the tribological behaviour of materials and are a good replacement for graphite. Si_3N_4 was selected as reinforcement that provides sustainability at high temperatures [19]. Si_3N_4 particulates of 99.9% fineness with 20 μm particulate size were chosen. TaC is an appealing material among the transition metal carbide. The interest in TaC has been growing in recent years due to its wide applications in industry as cutting tools and hard coatings owing to its chemical inertness, high hardness, and exceptional corrosion resistance and more essentially its ability to form solid solutions [20]. TaC of 99.9% purity with 200–250 nm was used for this research. Ti is very hard compared with aluminium, and more essentially, it does not have to fend for any chemical reaction with aluminium to form any reactive product. Due to the enhanced specific strength and corrosion resistance in aggressive media, certain aluminium alloys can operate in corrosive environments without any strong restrictions on their service life. This particular set of characteristics makes aluminium alloys the material of selection for the needs of the automobile industry in several applications. The titanium of 99.9% purity with 70 μm particulate size was utilized for this present study. The range of reinforcements as shown in Table 3 was finalized based on previous literature.

2.2. Preparation of Materials. In the present experimental investigation, liquid metallurgical stir casting methodology was utilized for fabricating MMCs. The uniform dissemination of added ceramic particles in the matrix was acquired by the pertinent mechanical stirring route. In the inducement, the predefined wt% of AA7075 was partitioned from bar stock and heated to a molten state in the electric muffle furnace. Table 4 shows the detailed and optimum process parameters utilized [21] for developing the multihybrid MMCs. Furthermore, Si_3N_4, TaC, and Ti particles were preheated to about 250 and 300°C accordingly before inclusion in the smelted metal. Once the metal reached the semiliquid state, the preheated ceramic particulates of Si_3N_4, TaC, and Ti with distinct wt% were added to the matrix to fabricate AA7075/Si_3N_4/TaC/Ti MMCs, respectively.

It is pivotal to observe that the mechanical mixing was executed at a pace of 200 rpm every 2 to 3 minutes to validate the homogeneous dispersion of Si_3N_4, TaC, and Ti particulates in the AA7075 matrix. Once the blending of alloy in the liquid form was completed, it was sluiced into the preheated casting mould through a preheated run-away channel and allowed it to solidify. A similar approach was repeated with distinct wt% of Si_3N_4, TaC, and Ti, and multihybrid aluminium MMCs were prepared accordingly. Once the composite mould was cooled at ambient temperature, various testing specimens were adapted in accordance with ASTM standards.

3. Experimentation

3.1. Density and Porosity Examination. Density is a significant parameter that reflects the quality and desired characteristics of the composite materials. Experimental and theoretical densities were obtained to estimate the percentage porosity of the developed multihybrid MMCs. Theoretical and experimental densities were evaluated using the rule of mixtures and Archimedes' principle. By computing the mass and volume of the composite samples, the densities can be quantified. With such a simple approach, even the closed porosity will be considered into account. Sample sizes of $20 \times 10 \times 10\ mm^3$ were utilized for examining both experimentally and theoretically densities according to the ASTM D792 standard.

3.2. Microstructural Analysis. The square samples with $10 \times 10 \times 10\ mm^3$ were processed to inspect the microstructural of the manufactured hybrid MMCs according to ASTM standards as shown in Figure 1. To polish the test samples, distinct grades (400, 600, 1,000, and 1,200) of emery papers were utilized. In continuation with that distinct grade of diamond, paste was applied on the samples and polished utilizing a twin-disc polisher machine to obtain a shiny surface. Keller's reagent was etched on the specimens to disclose the grain boundaries and eliminate impurities. An optical metallurgical microscope (Model: QS Metrology, XJL–17) was utilized for examination as displayed in Figure 2(a). As shown in Figure 2(b), scanning electron microscope (SEM), X-ray diffraction (XRD), and energy-dispersive X-ray spectroscopy (EDX) were performed to confirm the homogeneous dissemination of reinforcements and to observe the occurrence of morphology and structure of reinforcement particulates in the AA7075 alloy.

3.3. High-Temperature Tensile Analysis. Tensile experiments were conducted to evaluate the tensile nature (percentage elongation, yield point, ultimate point, and breakpoint) of the selected AA7075 and fabricated hybrid MMCs. High-temperature tensile experiments have been conducted at ambient conditions (30°C, 60°C, 90°C, and 120°C). For elevated-temperature tensile analysis, an induction coil sort of heating furnace with an attached temperature control arrangement was developed and utilized for heating the tensile specimens. The temperature was measured directly on samples that were heated until their temperature stabilized at the required level. The specimens were held at the set point temperature for half an

Table 1: Chemical arrangement of AA7075.

Particulars	Si	Fe	Cu	Mn	Mg	Cr	Zn	Ti	Ni	Zr	Al
Minimum (wt%)	0.4	0.5	1.2	0.3	2.1	0.18	5.1	0.10	0.01	0.02	Balance
Maximum (wt%)			2.0		2.9	0.28	6.1				

Table 2: Properties of matrix and reinforcing phase.

S. No.	Properties	Matrix	Reinforcement materials		
		AA7075	Si_3N_4	TaC	Ti
1	Density (g/cm^3)	2.81	3.17	14.3	4.506
2	Melting point (°C)	700	1900	3900	1668
3	Hardness	60–150 BHN	13.5–20 HV	830–2340 HV	2,200 BHN
4	Elastic modulus (GPa)	70–80	28–46	537	106 psi
5	Tensile strength (MPa)	280	490	—	345

Table 3: Control factors – stir casting process.

S. No.	Quantity of matrix (wt%)	Quantity of reinforcements (wt%)		
	AA7075	Si_3N_4	TaC	Ti
C1	100	0	0	0
C2	95.75	2	0.25	2
C3	94	4	0.5	1.5
C4	92.25	6	0.75	1
C5	90.5	8	1	0.5

Table 4: Control factors – stir casting process.

S. No.	Processing conditions	Values
1	Time for stirring	5 minutes
2	Stirring speed	200 rpm
3	Temperature of melt	650°C
4	Temperature during stirring	670 to 700°C
4	Preheating temperature	250 to 300°C
5	Crucible size/company	4/bell
6	Maximum temperature of the furnace	750°C
7	Type of furnace	Electric muffle furnace
8	Mould size	$100 \times 100 \times 10$ mm^3

hour for homogeneity before loading the actual experiments. The operating temperature of the test samples was perceived by thermocouples during experimentation. The UTS of the matrix and developed MMCs were premeditated using a digitalized universal testing machine (UTM) as displayed in Figure 3 with 50 kN of ultimate load. In accordance with the ASTM E8 standard, the specimens as shown in Figure 4 were shaped and clamped in the UTM machine and pulled until deformation. During the analysis, the load applied and the displacement together with the sample deformation was recorded using a high-temperature extensometer. Later, the load and displacement plots were brought about on a computer that was synchronized with the machine. Using load and area of the tensile test samples, UTS was obtained at a distinct temperature range. Experiments were performed five times to ensure repeatability and average was considered.

3.4. Low-Cycle Fatigue Strength Analysis. Fatigue is an important characteristic of the material put through cyclic loading failure used to achieve robust performance. Considerable plastic distortion and short lifetime corresponds to low-cycle fatigue. Primarily in the loading region, the materials suffer distortion in an undistinguishable manner. The fatigue test samples as shown in Figure 5 were developed as per ASTM E606 with a gauge length of 40 mm. The fatigue test was conducted on a computerized fatigue testing machine (AVG Engineering Pvt. Ltd., Coimbatore, Tamilnadu, India) as shown in Figure 6 with tension-compression cyclic loading of 30 to 40 cycles/min and an uttermost force of 1 ton. The prepared fatigue test samples were equipped axially and clamped rigidly to the fixtures. The load was applied to the specimens, and then the cycle to failure was established. The experiments were carried out at an ambient temperature and prolonged till the final fracture. Fatigue life (N_f) was considered as the number of cycles to cause complete failure. Based on the load applied and stress obtained, S-N curves were plotted for different weight fractions of hybrid MMCs. An average of five outcomes was examined as fatigue life (N_f) of each sample.

3.5. Elevated Temperature Creep Analysis. Creep is stated as the accelerating fracture of material under the action of a steady force. Creep occurs as the result of prolonged exposures to stresses that are below the yield strength of the material. Since the mechanisms implicated in creep are thermally stimulated, creep does not become considerable until temperatures of the order of 0.3 T_m for pure metals and 0.4 T_m for alloys. Creep test samples were shaped as per ASTM E139 as shown in Figure 7. Tensile creep analysis was executed at 423.15 K under constant applied stress in the limit of 40 to 60 MPa on the time-dependent creep testing equipment (AVG Engineering Pvt. Ltd., Coimbatore, Tamilnadu, India) as displayed in Figure 8. Before clamping the specimens into the creep test machine, all the specimens were precisely polished to diminish the influence of machining deficiency. The temperature of the specimens was quantified utilizing a separate thermocouple that was attached exactly at the middle of the gauge length inside the

Figure 1: Test specimens for microstructural analysis.

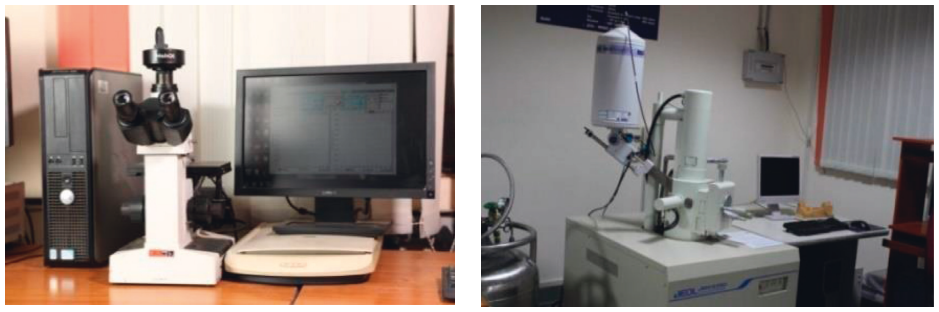

(a) (b)

Figure 2: Microstructural test setup: (a) optical microscope and (b) scanning electron microscope.

Figure 3: Universal tensile testing machine attached with heating chamber and temperature controller (Model: CUTM-50 kN).

heating furnace as shown in Figure 8. The strain was measured using an extensometer, and the data acquisition was formulated every 60 seconds during the entire experiment. All specimens were kept steady at the target temperature; the constant temperature was maintained for 10 minutes; and then the steady load was applied until failure. The rupture time was recorded, and the strain was calculated. Creep plots (strain vs. creep time) for the developed multihybrid MMCs at the different compositions of reinforcements was obtained experimentally.

4. Results and Discussion

4.1. Metallographic Aspects of AA7075/TaC/Ti/Si_3N_4 Hybrid Composites. The SEM analysis was done to obtain good-quality microstructural images on the surface of the base alloy and the fabricated MMC specimens. Figure 9 shows the SEM micrographs of various compositions of cast AA7075 reinforced with TaC/Ti/Si_3N_4 hybrid metal matrix composites. There is good dissemination of TaC, Ti, and Si_3N_4 ceramic particles over the AA7075 interface. This authenticates to the effectiveness of the liquid metallurgical stir casting route used in manufacturing the MMCs. Figure 9(a) displays the micrographs of the cast AA7075 matrix; it was evident that the entire grey region represents the matrix without reinforcement. As the particulate of TaC/Ti/Si_3N_4 is amalgamated into the melt pool of the molten metal (AA7075), a whitish region was noticed that depicts the occurrence of foreign ceramic particulates (TaC/Ti/Si_3N_4) embedded in the matrix alloy shown in Figures 9(b) to 9(e). It is justifiable to note that as the wt% of the particulate enhances, the whitish region becomes heavy and well disseminated homogeneously. From the SEM micrographs, it was observed that there were no voids, and cracks were identified on the matrix, which ensured the unblemished bonding betwixt reinforcement and matrix. The strong intermetallic bonding, exceptional wettability betwixt the discontinuous reinforcement phase and continuous metal phase, and the homogeneous dissemination [22, 23] can be endorsed as the optimum process parameters utilized through the liquid metallurgical route.

Figure 10 shows the EDAX pattern of the AA7075 alloy and the developed multihybrid composite material. The EDAX pattern clearly reveals various elements present in the composite material. Figure 10(a) clearly reveals the presence of Mg, Al, and

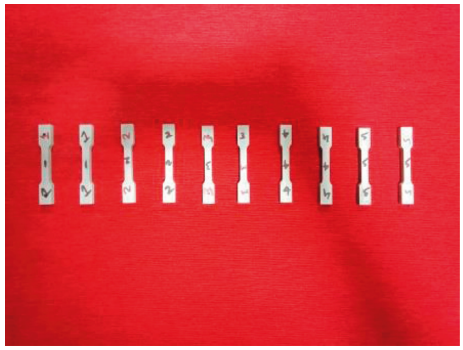

Figure 4: Test samples for tensile strength analysis.

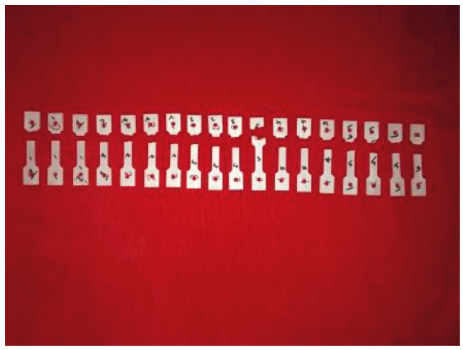

Figure 5: Fatigue test samples as per ASTM.

Figure 6: Hydraulic universal fatigue and creep testing machine (Model: AVJ-10T).

Zn as the primary alloying elements that provide additional strength and enhanced characteristics of the material. Additionally, EDAX pattern of the developed multihybrid MMCs is displayed in Figure 10(b), and various reinforcing elements such as Ta, C, Zn, C, and Cu can be clearly seen. This EDAX compositional analysis has been used to confirm the elemental presence. Since magnesium and silicon are major alloying elements, secondary precipitates such as Mg_2Si can be observed from the SEM analysis of the developed hybrid MMCs.

4.2. Density and Porosity Analysis of AA7075/TaC/Ti/Si_3N_4 Hybrid Composites. The density of MMCs primarily reckons on various attributes for instance nature, orientation, shape, and size of the reinforcement particulates. In the current exploration, the porosity of the manufactured MMCs has been inspected both theoretically and experimentally. Figure 11 shows the combined variation in theoretical, experimental densities, and percentage porosity of the developed AA7075/TaC/Ti/Si_3N_4 multihybrid composite materials. The obtained results reveal that the selected reinforcement materials such as TaC, Si_3N_4, and Ti have an infinitesimal influence on the overall density of the developed multihybrid composite materials. Due to the hard nature of the selected ceramic reinforcements, the overall density of the developed composite materials was found to be higher [24]. Since the density of the Si_3N_4 is comparatively higher with 3.44 g/cm^3 when compared to other reinforcements, it has a greater influence on the density of the hybrid composites. The AA7075 base alloy showed the experimental and theoretical density of 2.80 g/cm^3 and 2.81 g/cm^3, respectively, and porosity of 0.3559%. When ceramic reinforcement particulates were mixed with AA7075 base alloy (2.80 g/cm^3), the developed composite showed higher density with a reasonable amount of porosity. From the obtained experimental outcomes, it was observed that AA7075 reinforced with 8 wt% Si_3N_4, 1 wt% TaC, and 0.5 wt % Ti (sample C5) enhanced the experimental and theoretical densities up to 3.2464 g/cm^3 and 3.3038 g/cm^3 with maximum porosity of 1.7758%. This clearly shows that the increment in the density of the MMCs may be ascribed to the high density of Si_3N_4 than that of AA7075. This rise in porosity may be due to the existence of impurities in both the matrix material and reinforcement particulates. It can be inferred that because of the increment in wt% of distinct percentage compositions of hybrid MMCs, there has been an enhancement in cohesive bonding betwixt the matrix and the reinforcements. Also, because of the discrepancy in wt% of the hard particulates by performing steady stirring, the dispersoid concentration has been homogeneous with a minimal amount of porosity, and no enormous clustering has been noticed. It has been stated that [25] due to the increment in weight percentage of the reinforcements, the dissemination is more dependable with insignificant porosity.

4.3. High-Temperature Tensile Behaviour of AA7075/TaC/Ti/Si_3N_4 Hybrid Composites. Figure 12 displays the deviation of UTS of the developed composite materials concerning various operating temperatures (30, 60, 90, and 120°C). The outcomes are the average data depending on the indistinguishable tests. AA7075 matrix aluminium alloy is stronger, with and without TaC, Ti, and Si_3N_4 reinforced particles, at every temperature. It can be concluded that at higher temperatures, the UTS of the fabricated multihybrid MMCs was more than that of the base metal, which means that the ceramic reinforcements can withstand the temperature by developing a strong bond between the matrix and reinforcements. At ambient temperature (30°C), the MMCs

Figure 7: Creep test samples as per ASTM standard.

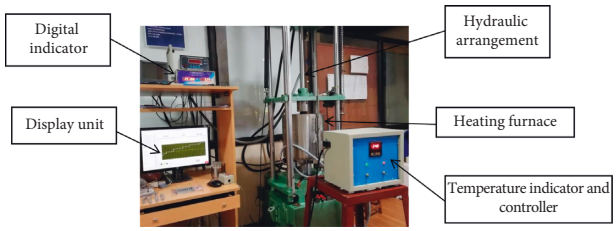

Figure 8: Time-dependent creep experimental test equipment.

showed an improved tensile strength of 137.64 N/mm^2. Later, when the temperature enhances from 30°C to 60°C, the composite material with 0.5 wt% TaC, 4 wt% Si_3N_4, and 1.5 wt% Ti showed a higher tensile strength of 230.07 N/mm^2. When the temperature reached beyond 100°C, the composite material with 0.75 wt% TaC, 6 wt% Si_3N_4, and 1 wt% Ti proved to have a higher strength of 232.17 N/mm^2. This shows that ceramic reinforcement has the capability of operating at higher temperatures. The tension properties enhance as anticipated, but the process is not homogeneous, owing to the fact that several metallurgical phenomena are embroiled synchronically [26]. At room temperature (30°C), it was noticed that the tensile strength of the fabricated MMCs enhanced; it implies that ductility has upgraded with the introduction of reinforcements. This revamp in ductility can be justified by proper dissemination and abutting packing of the reinforcement particulates in the AA7075 alloy. Also, improved tensile strength was observed at elevated temperatures. The selected ceramic reinforcement particulates increase the mechanical characteristics of matrix alloy over the consolidated temperature. The TaC, Ti, and Si_3N_4 particles improve the tensile properties at distinct temperatures primarily by stress transference from the aluminium ally to the reinforced ceramics [27]. The interactivity betwixt the dislocations and particulates culminates in enhancement in strength, which is syndicated with the Orowan strengthening procedure [28] by which a dislocation bypasses impervious obstacles, where a dislocation bows out tremendously to leave a dislocation loop around a particulate.

4.4. Morphology of the Fractured Tensile Samples. Figures 13(a) and 13(b) depict the SEM analysis of the fractured AA7075 tensile samples reinforced with 1wt%TaC/8wt%Si_3N_4/0.5wt%Ti at 30 and 120°C. Dispersed and pulled out TaC/Si_3N_4/Ti ceramic particulates was observed on the fracture sample of the developed composite material. At ambient conditions, the composites exhibit uniform or notched features, indicating the preferential ductile mechanism of MMCs. At escalated temperatures, bonding of ceramic particulates can be observed from the fractured tensile samples. As percentage elongation depicts the ductile nature of the material, the composite with 1wt%TaC/8wt%Si_3N_4/0.5wt%Ti reinforcement was more ductile in nature without the decline in tensile behaviour of the developed composite material.

4.5. Low-Cycle Fatigue Behaviour of AA7075/TaC/Ti/Si_3N_4 Hybrid Composites. Figure 14 displays the typical deviation of low cycle fatigue stress versus a number of cycles. From the obtained experimental outcomes, enhanced fatigue life was observed from the developed hybrid MMCs by operating at higher number of cycles. Especially, the addition of Si_3N_4 improved the fatigue life of the composites. This can be attributed to the occurrence of hard ceramic particulates with homogeneous distribution throughout the alloy material. The MMCs with AA7075 reinforced with 0.5 wt% TaC, 4 wt% Si_3N_4, and 1.5 wt% Ti proved to operate at a higher number of cycles of 14×10^3 cycles with maximum elongation of 0.180 mm. This inspection is in good agreement with the outcomes of Senthil Kumar et al. [29] who disclosed the low-cycle fatigue characteristics of AA2014-Al_2O_3 hybrid MMCs. The above manifestation can be validated to the dislocation slip-dominated distortions on account of tension-compression distortion due to the AA7075 matrix material whose structure is face-centred cubic. This is an outcome of cyclic hardening of successive cycle distortions. AA7075/TaC/Ti/Si_3N_4 MMCs display a balanced plastic strain for the cyclic contortion. Reduction in porosity and higher yield strength of the MMCs attributed to enhanced fatigue life. In addition to this, the excellent bonding betwixt matrix and reinforcement and finer grain size [30] is also a crucial parameter, which inveigled the improved resistance to fatigue of the manufactured MMCs.

4.6. Morphology of the Fractured Fatigue Samples. Figure 15 displays the fractured fatigue sample of AA7075 and the developed multihybrid MMCs. All the fracture

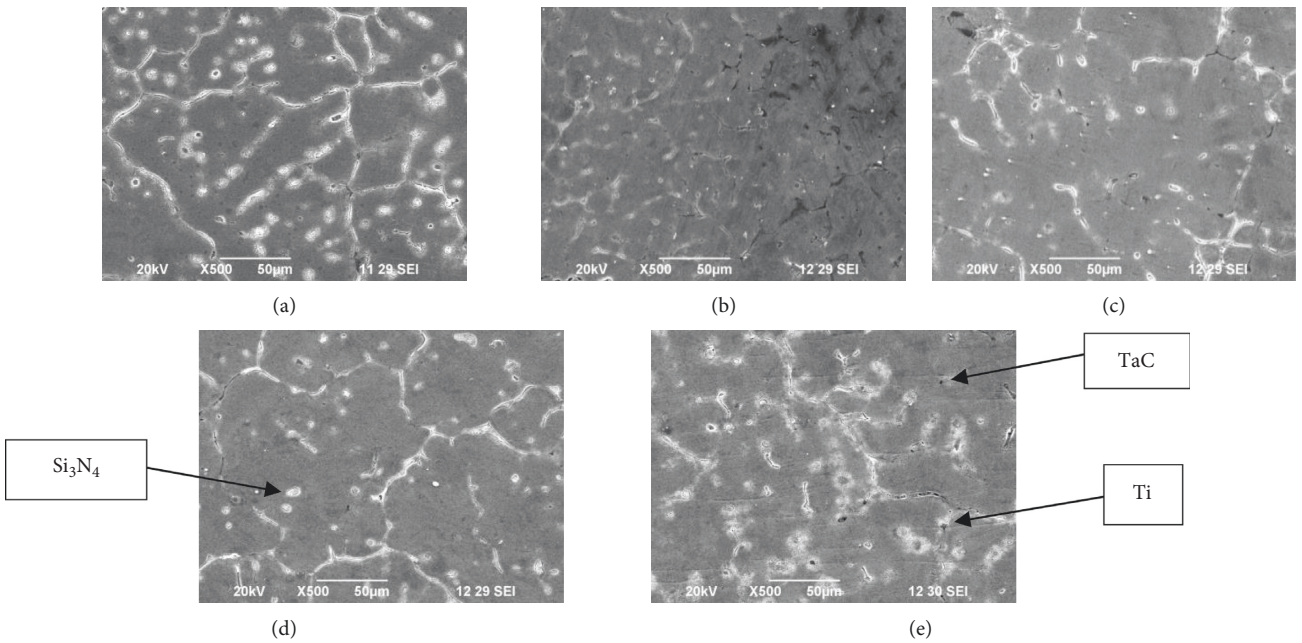

Figure 9: SEM morphology of the developed composites: (a) pure AA7075, (b) AA7075 + 0.25wt%TaC + 2wt%Si_3N_4 + 2wt%Ti, (c) AA7075 + 0.5wt%TaC + 4wt %Si3N4 + 1.5wt%Ti, (d) AA7075 + 0.75wt%TaC + 6wt% Si_3N_4 + 1wt%Ti, and (e) AA7075 + 1wt%TaC + 8wt% Si_3N_4 + 0.5wt%Ti.

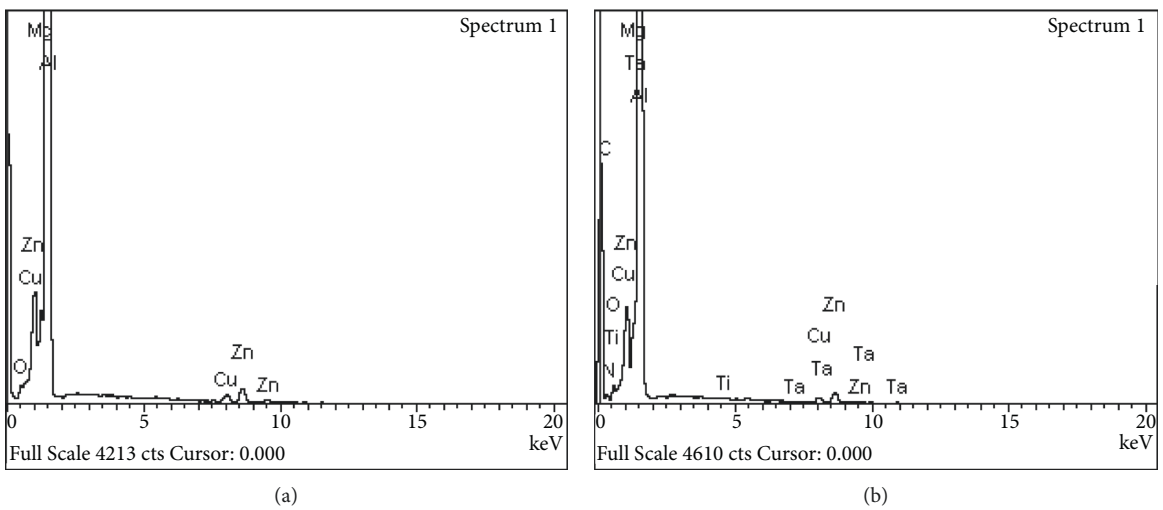

Figure 10: EDAX pattern of (a) AA7075 and (b) AA7075 + 1wt%TaC + 8wt%Si_3N_4 + 0.5wt%Ti.

composite samples are composed mostly of dimples with the TaC/Si_3N_4 and Ti particle clusters inside. At lower exacerbation, the fractured creep sample of AA7075 alloy was observed as displayed in Figure 15(a). Various morphological parameters such as crack instigation, near crack instigation site, and fast fracture surface were evidently noticed and evaluated. The occurrence of severe clusters has caused irregular dimples with distinct sizes, demonstrating the detrimental influence on the creep resilience. It is obvious that the larger size of such a brittle phase is detrimental to creep life. At last, the enhanced dislocation density at the edges and corners of reinforcements may quicken the breakdown of the brittle phase, which should reduce the creep resistance of the AA7075/Si_3N_4/TaC/Ti hybrid composite in this work. Also, it displays the occurrence of fracture surfaces with limited dimple structure and more reinforcement particles. It indicates the presence of a stronger reinforcement and matrix interface. Figure 15(b) shows the crack growth near the initiation site occurred primarily in the matrix phase material. There is an excellent particle and matrix interface cracking or reinforcements cracking, and a fast fracture site was also evidently noticed. It is also presumed that the dimple density of the MMCs was more than that of the AA7075 alloy.

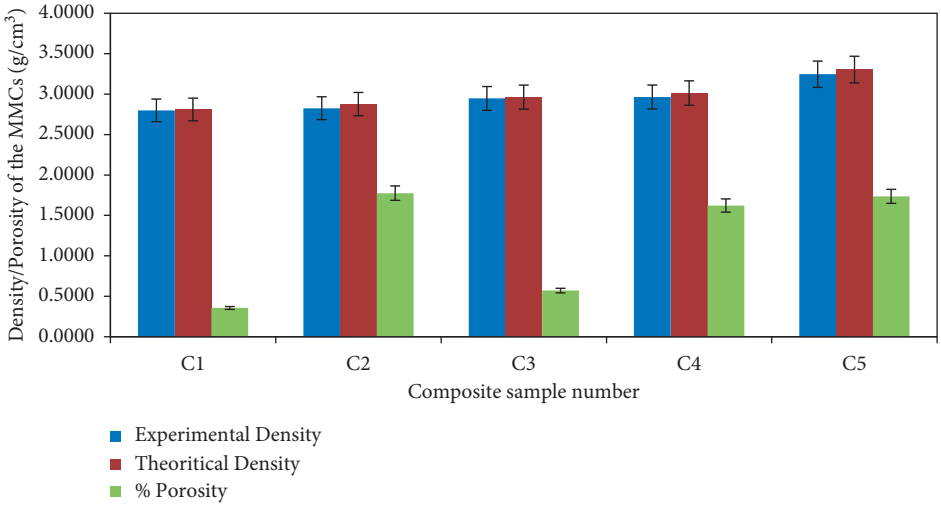

Figure 11: Deviation of density and percentage porosity of the developed hybrid MMCs.

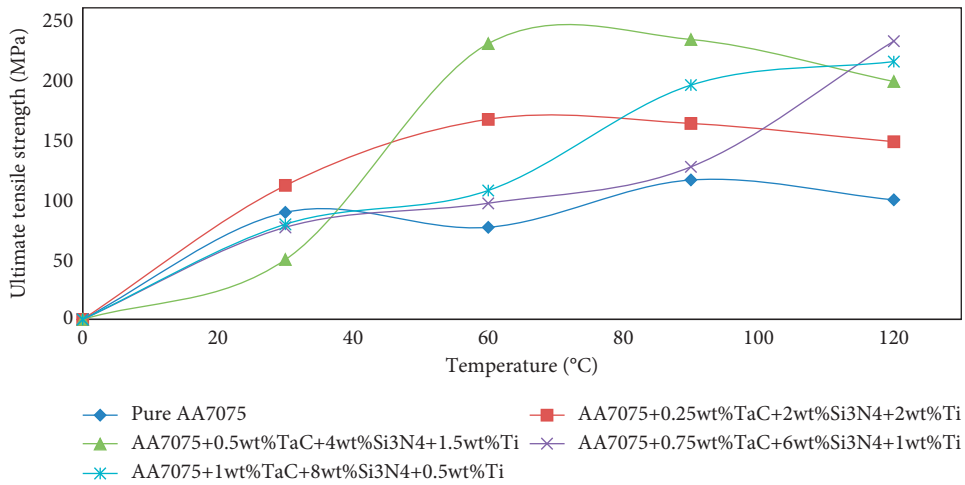

Figure 12: Deviation of UTS versus temperatures of the developed MMCs.

4.7. Creep Deformation of AA7075/TaC/Ti/Si_3N_4 Hybrid Composites. Figure 16 shows the change in displacement with respect to time of rupture for various compositions of aluminium-based MMCs. AA7075 alloy reinforced with 1 wt % TaC, 8 wt% Si_3N_4, and 0.5 wt% Ti operated at the higher period of time of 33,558 seconds with a maximum displacement of 2.61 mm. The higher weight fraction of Si_3N_4 and TaC showed higher creep strength with a minimum amount weight fraction of titanium. The creep strength of the developed MMCs enhanced due to the homogeneous dissemination of Si_3N_4/TaC/Ti particulates over the matrix alloy. This shows that the secondary creep stage is more lineated with the addition of Si_3N_4/TaC/Ti. Sample C3 with AA7075 reinforced with 0.5 wt% TaC, 4 wt% Si_3N_4, and 1.5 wt% Ti operated at a minimum time period but elongated up to 16.08 mm showed the ductile nature of the material. This can be attributed to the advent of damage mechanisms [31] within the matrix such as the prevalence of debonding at the interfaces between the reinforcement and matrix.

4.8. Morphology of the Fractured Creep Composite Samples. Figures 17(a) and 17(b) display the SEM microstructure of the deformed creep samples of AA7075 and the developed hybrid composites at constant stress and temperature. Exceptionally, for those on the prior austenite grain boundaries and on the lath boundaries, the morphology of the fractured samples discloses eminent coarsening of the precipitates. The fractured morphology reveals cup and cone fractures as shown in the microstructure. The justification for this catastrophe is that the creep deformation (or cracks) develops inwards after instigating the outer layer of the sample. The presence of many voids was noticed in the central equiaxed regions. Figures 17(a) and 17(b) show few areas of small pores filled with ceramic reinforcement particulates. The AA7075/TaC/Si_3N_4/Ti cyclic creep samples disclose regular transgranular fracture ensuing from microvoid coalescence. It was noticed that in the time-dependent creep analysis, all of the ruptured specimens exhibit similar transgranular fractures [32] regardless of the creep experimental

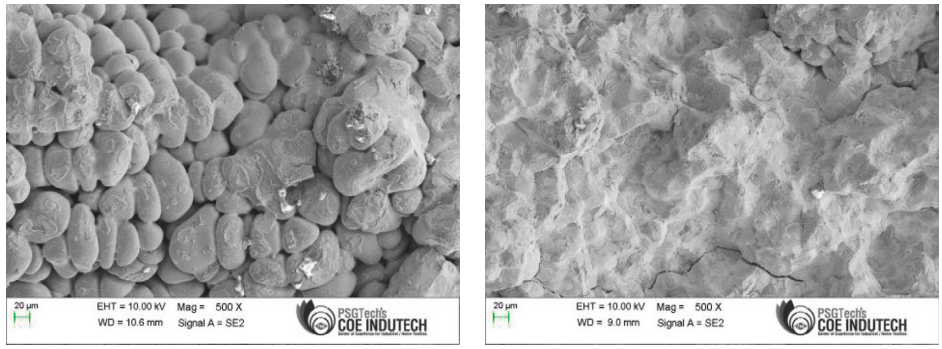

(a) (b)

Figure 13: SEM morphology of fractured AA7075/1wt%TaC/8wt%Si_3N_4/0.5wt%Ti tensile sample: (a) 30°C and (b) 120°C.

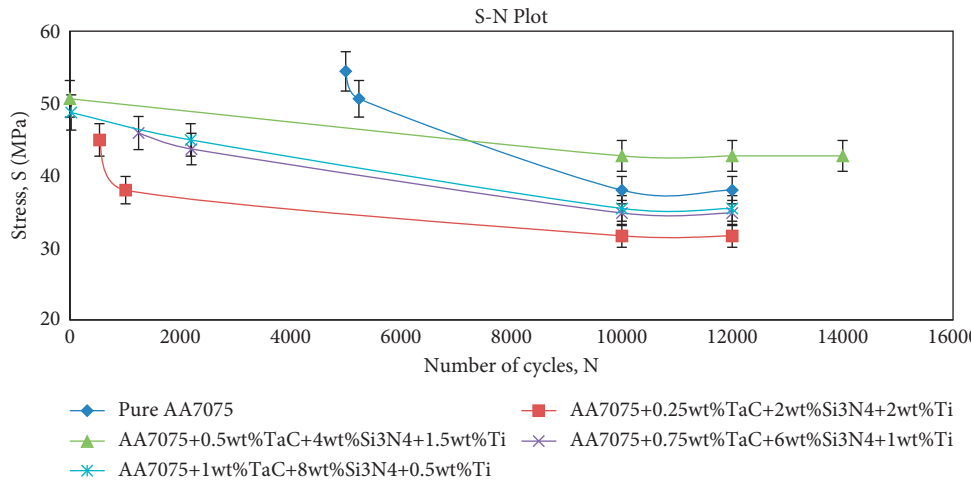

Figure 14: Deviation of cyclic stress with respect to the number of cycles.

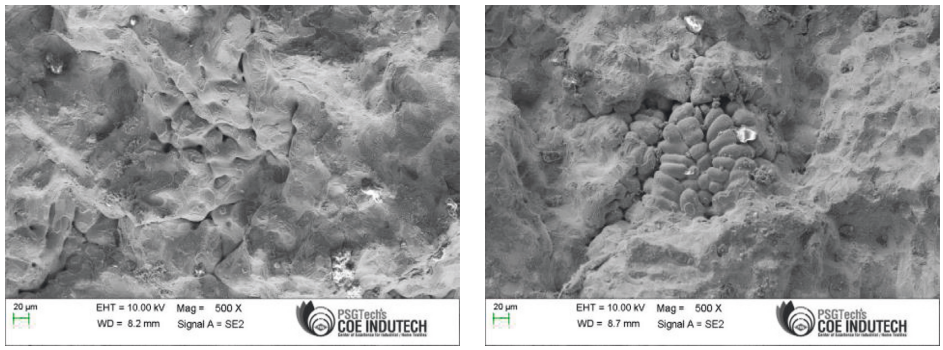

(a) (b)

Figure 15: SEM analysis of fractured fatigue samples: (a) AA7075 and (b) AA7075/0.5wt%TaC/4wt% Si_3N_4/1.5wt% Ti.

conditions. An increase in the coarsening kinetics was notable with an increment in temperature, for extended creep exposures. However, in the case of elevated temperature creep analysis with shorter rupture lives, the lath structure within the prior austenitic grain boundaries did not display much change on a macroscale.

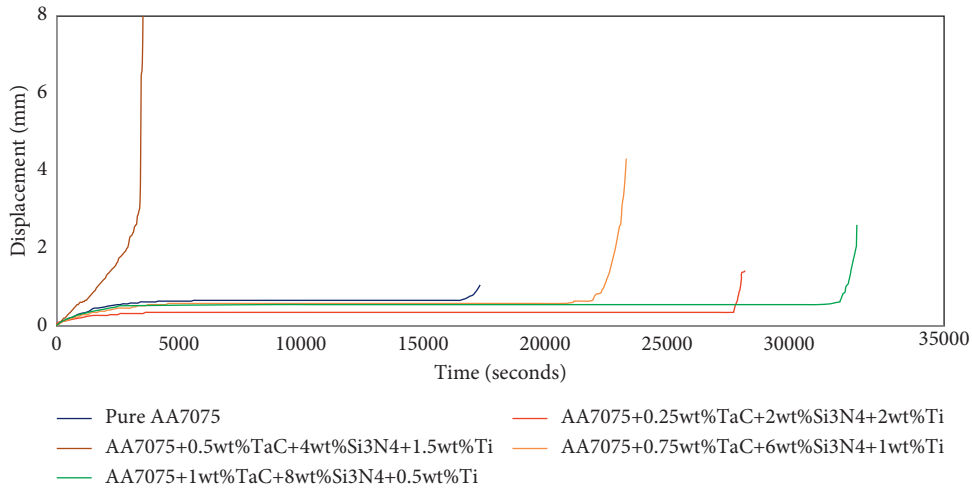

Figure 16: Variation of strain with respect to time of rupture of MMCs.

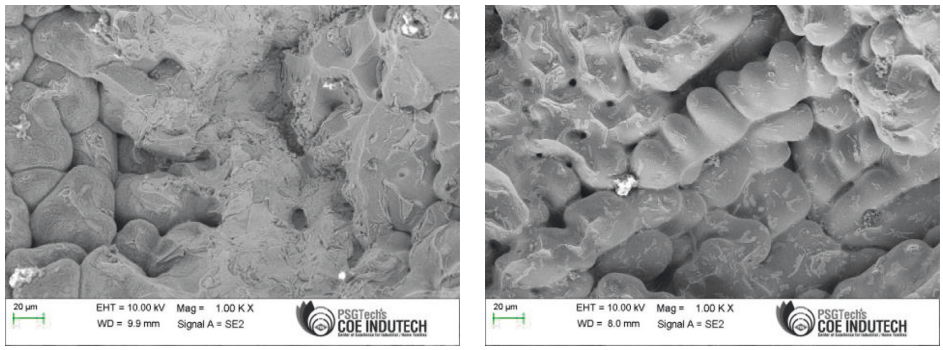

(a) (b)

Figure 17: SEM analysis of fractured creep samples: (a) AA7075 and (b) AA7075/1wt%TaC/8wt% Si_3N_4/0.5wt%Ti.

5. Conclusions

The traditional stir casting procedure was adopted in sprouting AA7075 reinforced with TaC/Ti/Si_3N_4 hard ceramic particulates. High-temperature tensile, fatigue, and creep deformation were inspected experimentally. The subsequent conclusions can be exploited.

(i) Microstructural study shows fairly homogeneous dissemination of TaC/Ti/Si_3N_4 in the AA7075 matrix material. The SEM interpretations also exhibited a ductile and brittle mode of terminations for pure AA7075 alloy and fabricated MMCs, correlatively.

(ii) SEM morphology also reveals good wettability and proper mixing. Strong interfacial bonding between the matrix and reinforcement material was observed, and this proves the optimum process parameters and the quality of the casting process.

(iii) Experimental and theoretical densities of the developed AA7075 reinforced with 8 wt% Si_3N_4, 1 wt% TaC, and 0.5 wt% Ti (sample C5) MMCs were found to be enhanced up to 3.2464 g/cm^3 and 3.3038 g/cm^3, respectively, with maximum porosity of 1.7758% because of the inclusion of hard particulates and excellent cohesive bonding among the reinforcement and matrix.

(iv) The tensile strength of the MMCs has been enhanced by the inclusion of hard ceramic particulates. Higher content of TaC/Si_3N_4/Ti improves the tensile nature of the MMCs at room temperature. Beyond 100°C, the MMCs with 0.75 wt% TaC, 6 wt% Si_3N_4, and 1 wt% Ti proved to have a higher strength of 232.17 N/mm^2. At elevated temperatures beyond 100°C, the material softening takes place beyond which the reinforcement enters the voids and pores thus restrict the crack propagation. At 30°C, uniform dimple features of

the composites indicates the preferentially ductile mechanism of the composite. At elevated temperatures, good bonding of ceramic particulates can be observed from the fractured tensile samples.

(v) Increased wt% of Si_3N_4/TaC/Ti improves the fatigue characteristics of the developed MMCs. AA7075 reinforced with 0.5 wt% TaC, 4 wt% Si_3N_4, and 1.5 wt% Ti proved to operate at a higher number of cycles of 14×10^3 cycles with maximum elongation of 0.180 mm. Due to the continuous cyclic deformation, cyclic hardening takes place. Reduction in porosity and higher yield strength of the MMCs attributed to improved fatigue life. The excellent bonding betwixt matrix and reinforcement and finer grain size is also a significant consideration, which influenced the improved fatigue resistance.

(vi) Creep analysis reveals that AA7075 blended with 1 wt% TaC, 8 wt% Si_3N_4, and 0.5 wt% Ti operated at the higher period of time of 33,558 seconds with a maximum displacement of 2.61 mm. This shows that the presence of reinforcement material proved sustainability at higher temperatures and at higher stress levels.

Data Availability

The data used to support the findings of this study are included within the article.

Conflicts of Interest

The authors declare that there are no conflicts of interest regarding the publication of this article.

Acknowledgments

This research work was not funded by any organization.

References

[1] M. Y. Zhou, L. B. Ren, L. L. Fan et al., "Progress in research on hybrid metal matrix composites," *Journal of Alloys and Compounds*, vol. 838, Article ID 155274, 2020.

[2] M. B. A. Shuvho, M. A. Chowdhury, M. Kchaou, B. K. Roy, A. Rahman, and M. A. Islam, "Surface characterization and mechanical behavior of aluminum based metal matrix composite reinforced with nano Al2O3, SiC, TiO2 particles," *Chemical Data Collections*, vol. 28, Article ID 100442, 2020.

[3] M. Gao, H. Kang, Z. Chen et al., "Enhanced strength-ductility synergy in a boron carbide reinforced aluminum matrix composite at 77 K," *Journal of Alloys and Compounds*, vol. 818, Article ID 153310, 2020.

[4] R. Manikandan, T. V. Arjunan, and O. P A. R. Nath, "Studies on micro structural characteristics, mechanical and tribological behaviours of boron carbide and cow dung ash reinforced aluminium (Al 7075) hybrid metal matrix composite," *Composites Part B: Engineering*, vol. 183, Article ID 107668, 2020.

[5] J. M. Mistry and P. P. Gohil, "Experimental investigations on wear and friction behaviour of Si3N4p reinforced heat-treated aluminium matrix composites produced using electromagnetic stir casting process," *Composites Part B: Engineering*, vol. 161, pp. 190–204, 2019.

[6] C. Kar and B. Surekha, "Characterisation of aluminium metal matrix composites reinforced with titanium carbide and red mud," *Materials Research Innovations*, vol. 25, no. 2, pp. 67–75, 2021.

[7] S. H. Park, D. H. Cho, K. M. Cho, and I. M. Park, "Creep properties of squeeze-infiltrated carbon nanotube and aluminum borate whisker reinforced AS52 Mg metal matrix composites," *Metals and Materials International*, vol. 24, no. 5, pp. 1162–1171, 2018.

[8] H. A. Al-Salihi, A. A. Mahmood, and H. J. Alalkawi, "Mechanical and wear behavior of AA7075 aluminum matrix composites reinforced by Al2O3nanoparticles," *Nanocomposites*, vol. 5, no. 3, pp. 67–73, 2019.

[9] S. Suresh, G. H. Gowd, and M. L. S. Deva Kumar, "Tribological behavior of Al 7075/SiC metal matrix nano-composite by stir casting method," *Journal - The Institution of Engineers: Series D*, vol. 100, no. 1, pp. 97–103, 2019.

[10] P. Loganathan, A. Gnanavelbabu, and K. Rajkumar, "Influence of ZrB2/hBN particles on the wear behaviour of AA7075 composites fabricated through stir followed by squeeze cast technique," *Proceedings of the Institution of Mechanical Engineers-Part J: Journal of Engineering Tribology*, vol. 235, no. 1, pp. 149–160, 2021.

[11] N. Panwar and A. Chauhan, "Fabrication methods of particulate reinforced Aluminium metal matrix composite-A review," *Materials Today Proceedings*, vol. 5, no. 2, pp. 5933–5939, 2018.

[12] B. Jiang, D. Zhang, C. Sun, N. Li, Y. Liu, and Z. Cao, "Microstructure evolution and creep behavior of high-pressure die-cast Mg-9Al-1Zn-1Sr alloy," *Materials Science and Engineering A*, vol. 766, Article ID 138388, 2019.

[13] S. Dai, Z. Bian, M. Wang et al., "The high-temperature creep behavior of in-situ TiB2 particulate reinforced Al12Si4Cu2-NiMg composite," *Metals*, vol. 8, no. 11, pp. 917–1016, 2018.

[14] A. Coyal, N. Yuvaraj, R. Butola, and L. Tyagi, "An experimental analysis of tensile, hardness and wear properties of aluminium metal matrix composite through stir casting process," *SN Applied Sciences*, vol. 2, no. 5, pp. 892–910, 2020.

[15] J. Oñoro, M. D. Salvador, and L. E. G. Cambronero, "High-temperature mechanical properties of aluminium alloys reinforced with boron carbide particles," *Materials Science and Engineering A*, vol. 499, no. 1-2, pp. 421–426, 2009.

[16] D. Sethi, S. Kumar, S. Choudhury, S. Shekhar, and B. Saha Roy, "Synthesis and characterization of AA7075/TiB2 aluminum matrix composite formed through stir casting method," *Materials Today Proceedings*, vol. 26, pp. 1908–1913, 2020.

[17] M. Imran and A. R. A. Khan, "Characterization of Al-7075 metal matrix composites: a review," *Journal of Materials Research and Technology*, vol. 8, no. 3, pp. 3347–3356, 2019.

[18] N. Ramadoss, K. Pazhanivel, and G. Anbuchezhiyan, "Synthesis of B4C and BN reinforced Al7075 hybrid composites using stir casting method," *Journal of Materials Research and Technology*, vol. 9, no. 3, pp. 6297–6304, 2020.

[19] J. Fayomi, A. P. I. Popoola, O. P. Oladijo, O. M. Popoola, and O. S. I. Fayomi, "Experimental study of ZrB2-Si3N4 on the microstructure, mechanical and electrical properties of high grade AA8011 metal matrix composites," *Journal of Alloys and Compounds*, vol. 790, pp. 610–615, 2019.

[20] C. Zhang, A. Loganathan, B. Boesl, and A. Agarwal, "Thermal analysis of tantalum carbide-hafnium carbide solid solutions from room temperature to 1400 °C," *Coatings*, vol. 7, 2017.

[21] B. Das, S. Roy, R. N. Rai, S. C. Saha, and P. Majumder, "Effect of in-situ processing parameters on microstructure and mechanical properties of TiC particulate reinforced Al-4.5Cu alloy MMC fabricated by stir-casting technique - optimization using grey based differential evolution algorithm," *Measurement*, vol. 93, pp. 397–408, 2016.

[22] P. S. Reddy, R. Kesavan, and B. Vijaya Ramnath, "Investigation of mechanical properties of aluminium 6061-silicon carbide, boron carbide metal matrix composite," *Silicon*, vol. 10, no. 2, pp. 495–502, 2018.

[23] C. Sivakandhan, G. Babu Loganathan, G. Murali et al., "Material characterization and unconventional machining on synthesized Niobium metal matrix," *Materials Research Express*, vol. 7, no. 1, Article ID 15018, 2020.

[24] T. Satish Kumar, G. Suganya Priyadharshini, S. Shalini, K. Krishna Kumar, and R. Subramanian, "Characterization of NbC-reinforced AA7075 alloy composites produced using friction stir processing," *Transactions of the Indian Institute of Metals*, vol. 72, no. 6, pp. 1593–1596, 2019.

[25] S. A. M. Krishna, T. N. Shridhar, and L. Krishnamurthy, "Computational investigation on thermal conductivity behavior of Al 6061-SiC-Gr hybrid metal matrix composites," *International Journal of Computational Materials Science and Engineering*, vol. 4, no. 4, Article ID 1550021, 2015.

[26] C. Zheng and W. Yu, "Effect of low-temperature on mechanical behavior for an AISI 304 austenitic stainless steel," *Materials Science and Engineering A*, vol. 710, pp. 359–365, 2018.

[27] F. Rezaei, M. G. Kakroudi, V. Shahedifar, N. P. Vafa, and M. Golrokhsari, "Densification, microstructure and mechanical properties of hot pressed tantalum carbide," *Ceramics International*, vol. 43, no. 4, pp. 3489–3494, 2017.

[28] K. Munir, C. Wen, and Y. Li, "Graphene nanoplatelets-reinforced magnesium metal matrix nanocomposites with superior mechanical and corrosion performance for biomedical applications," *Journal of Magnesium and Alloys*, vol. 8, no. 1, pp. 269–290, 2020.

[29] R. Senthilkumar, N. Arunkumar, and M. Manzoor Hussian, "A comparative study on low cycle fatigue behaviour of nano and micro Al 2 O 3 reinforced AA2014 particulate hybrid composites," *Results in Physics*, vol. 5, pp. 273–280, 2015.

[30] N. K. Bhoi, H. Singh, and S. Pratap, "Developments in the aluminum metal matrix composites reinforced by micro/nano particles - a review," *Journal of Composite Materials*, vol. 54, no. 6, pp. 813–833, 2020.

[31] Z. Wang and H. Xiao, "A simulation of low and high cycle fatigue failure effects for metal matrix composites based on innovative J2-flow elastoplasticity model," *Materials*, vol. 10, no. 10, p. 1126, 2017.

[32] V. Sklenicka, K. Kuchařová, M. Kvapilová, and M. Svoboda, "Factors influencing creep resistance in discontinuously reinforced magnesium metal matrix composites," *Metallic Materials*, vol. 53, no. 4, pp. 221–229, 2016.

Hindawi
Advances in Materials Science and Engineering
Volume 2022, Article ID 4029882, 8 pages
https://doi.org/10.1155/2022/4029882

Research Article

Mechanical Loading and Tribological Studies on Boron Carbide (B_4C) and Lead (Pb) Particles Dispersed Epoxy-Based Multilayered Composites

S. Vignesh[1], **J. T. Winowlin Jappes**[1], **Khan M. Adam**[1] and **Temal Varol**[2]

[1]*Department of Mechanical Engineering, Kalasalingam Academy of Research and Education, Krishnankoil, India*
[2]*Department of Metallurgical Engineering, Karadeniz Technical University, Trabzon, Turkey*

Correspondence should be addressed to J. T. Winowlin Jappes; winowlin@klu.ac.in

Received 10 February 2022; Revised 15 March 2022; Accepted 31 March 2022; Published 16 April 2022

Academic Editor: Michael Aizenshtein

Copyright © 2022 S. Vignesh et al. This is an open access article distributed under the Creative Commons Attribution License, which permits unrestricted use, distribution, and reproduction in any medium, provided the original work is properly cited.

The study aims in the development of functionally graded epoxy-based layered composites dispersed with B_4C and lead particles. The development route adopted for the composites is a novel route called layered molding and curing. Various compositions of single and trilayered composites were prepared through the abovementioned route. The samples prepared were subjected to mechanical and tribological studies, and the results were reported in this article. It is found that the mechanical properties of the single-layered composites consisting of 20% lead and 20% B4C show superior characteristics than those of the samples with increased addition of lead. However, the trilayered samples with lead core showcased excellent mechanical properties. On the other hand, the wear rate and mass loss of the trilayered samples with B_4C cladding show minimum wear rate than the samples with lead cladding. Furthermore, the coefficient of friction of the samples also showcases the better performance of single-layered samples with 20% lead. The worn surface analysis done through scanning electron microscopy and stereo zoom microscopy reveals the reason for the low specific wear rate of 20% lead sample as the self-hindrance of wear debris evolved during the wear study.

1. Introduction

There is an increasing need in material research to meet out the demand of high-performance materials in the global automotive, aerospace, structural, and other sophisticated sectors. This led to the development of mechanically strong and tribologically better composite materials. Composite materials are even preferred for its multifunctionality, for its life span, for its economical prices, or even its role in improving the material aesthetically. Composite materials, the product of mixing or stacking two or more materials, are a promising attraction to researchers in replacing conventional metallic materials. Although the problem of the product lies in its weak matrix constituting polymers that result in weak interlaminar shear strength, the best use of composite is because of its high specific strength, stiffness, fatigue behavior, and density [1–4]. There is a greater need for a better material in order to transport and store the spent nuclear fuel, since the conventional lead caskets are found to be heavy and not safe due to its chemical characteristics. Epoxy is proposed by several researchers for its greater performance in mechanical and structural applications. It possesses excellent hardness, fatigue resistance, and very small contraction during curing that makes it more suitable for mechanical applications. Similarly, the epoxy serves as an excellent matrix material owing to the adhesion behavior to varieties of reinforcements. Furthermore, it also possesses excellent stability and resilience behavior when exposed to neutrons which is also an obvious reason to use epoxy in many sophisticated applications [5]. However, it lags in antiwear and antiabrasive properties which are not up to the mark. Nowadays, boron carbide (B_4C), a ceramic material, has created attention among the research groups owing to its excellent mechanical, tribological, and structural properties.

Moreover, the properties such as hardness and density make it more suitable for some rugged applications like abrasives, products with good wear resistance, and even in ballistics. Similarly, B_4C has good neutron absorption cross section for catering the thermal neutrons and also possesses an atomic number density of 0.11 $Å^{-3}$, owing to which, it is nowadays used in nuclear industries for effective shielding of ionizing radiations [6]. Research studies support the development of B_4C reinforced epoxy composites for the improvement of mechanical and tribological properties. Furthermore, the reports suggest the improvement of wear resistance of the B_4C composites through increased particle addition by facilitating the anchoring mechanism. However, research suggests the effective addition in the epoxy environment as the increased addition of the same will detriment the mechanical properties [7]. Similarly, lead (Pb) is a widely used potential radiation shielding material which can also be used for packaging, storage, and transportation of radioactive fuels. Pb finds a wide variety of applications particularly in the field of radioactivity and shielding of radioactive environment. In nuclear power industries, the storage of cooled spent nuclear fuel plays an uncompromised role in terms of safety of both biotic and abiotic species [8, 9]. Presently, lead caskets serve the purpose of storing and transporting the cooled spent nuclear fuel. However, because of its high density leading to enormous weight and poor mechanical and tribological properties, there is a profound need of a suitable alternative material that can cater the above needs. Hence, in this work, an attempt is made to develop high mechanically and tribologically efficient B_4C particles along with lead (Pb) dispersed epoxy laminates. Furthermore, the need of irradiation shielding can be ensured by incorporating lead (Pb) particles. Moreover, a storage container is expected to have good mechanical and tribological properties, particularly wear resistance [10]. On the other hand, owing to safety issues, the research on pure lead-based epoxy laminates is almost a void. Hence, in this work, an attempt is made to produce epoxy-based single- and trilayered composites dispersed with varying composition of B_4C and Pb particles through layered molding and curing route for industrial packaging and transportation caskets.

2. Materials and Methods

2.1. Materials. The matrix epoxy LY566 and its corresponding hardener were procured from Vasavi Resins Pvt. Ltd., Chennai. The powdered boron carbide (B_4C) particles (99.9%) with particle size 10 μm were procured from Neena Metal Mart, New Delhi, and the powdered lead (Pb) particles (99.9%) of particle size 10 μm were procured from Alpha Chemika, Mumbai. The metallic particles were subjected to SEM to confirm the particle size.

2.2. Experimental Methods. The required composite material using lead, boron carbide, and epoxy is made using the layered molding and curing method as shown in Figure 1. For this, powdered lead and boron carbide were mixed and made into several composite samples in a mold with several

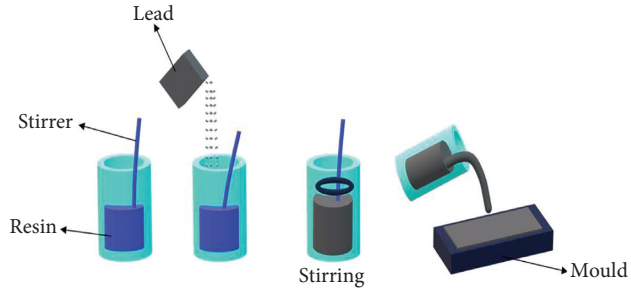

Figure 1: Schematic of layered molding and curing route.

Table 1: Composition of single-layered samples and the density of the samples.

Samples	Composition of single-layered composites		Density (g/cm^3)
	B_4C	Pb	
A	20	10	1.38
B	20	20	1.55
C	20	30	1.78
D	20	40	1.89

different propositions. Six samples were made of various propositions with different processes. Few glass molds were made for preparing the composites.

The dimension of the mold is 300 mm × 137 mm × 3 mm, and all the samples were made with a thickness of 3 mm. OHP sheets were placed over the molds for easy removal of the material. Wax is applied to the mold and over the OHP sheets before every sample is made, for easy removal of the composite material after curing. After getting the molds ready, 6 samples were made, each one had a different proposition of lead, boron carbide, and epoxy. The measurements of the powders and the development of the composites were done with proper care using masks and gloves and in an isolated chamber, respectively, to avoid the contact of any lead or boron carbide powder, which when contacted directly becomes hazardous. The details of the samples prepared and the density are tabulated in Tables 1 and 2.

Thorough mixing is done through mechanical mixing and ultrasonication process as well in order to avoid agglomeration of the particles. The whole mixing process is done at a slow pace to avoid any air bubble formation, which might affect the material quality. After mixing the liquid mixture for 45 mins, the mixture is poured in the glass mold and made to spread uniformly. Similarly, layered samples were made in a definite interval of 45 minutes after the pouring of first and the subsequent layers. The samples were allowed to cure for 24 hours before removing from the mold. The schematic of the layered samples is depicted in Figure 2.

2.3. Mechanical Studies. The samples prepared were tested for its tensile strength after carefully adhering to the ASTM standard ASTM D638 ($165 \times 13 \times 5$ mm^3). The flexural testing was carried out in accordance to the ASTM standard

Table 2: Composition of trilayered samples and the density of the samples.

Samples	Layer layout of the samples			Composition of the trilayered samples		Density (g/cm^3)
	Layer 1	Layer 2	Layer 3	B_4C	Pb	
E	B_4C	Pb	B_4C	20	20	1.58
F	Pb	B_4C	Pb	20	20	1.88

Figure 2: Schematic of the trilayered samples fabricated through layered molding and curing.

of dimensions $127 \times 13 \times 5\,\text{mm}^3$, and the impact test was done in accordance with ASTM D256 with specifications $60 \times 13 \times 5\,\text{mm}^3$ using an Izod impact tester with a v-notch cut in the samples. The fractography of the tested samples were done by using a JEOL-JSM-5600LV scanning electron microscope equipped with EDS.

2.4. Tribological Study. A pin-on-disc wear tester (Magnum Engineers, Bengaluru, as per ASTM G-99 standard) was used to carry out the friction and wear test for all the samples. Five sets of tests were conducted on each sample for a span of 30 min. The ambient temperature and the relative humidity during the run were 23°C and 50 ± 5%, respectively. The specimen used for the test was $10\,\text{mm} \times 10\,\text{mm} \times 3\,\text{mm}$ and was made in contact with a hardened alloy steel (62 HRC and surface roughness $R_a = 0.54\,\mu\text{m}$) disc. The samples were kept in such a way that the thickness of the sample was perpendicular to the counter body that rotates. The samples were initially recorded for its weight and also after the conduction of the test in order to calculate the specific wear rate of the samples. The test conditions of the wear studies are given in Table 3. The specific wear rate was then calculated using the following equation:

$$K_s = \frac{\Delta V}{L\,d}\,\frac{m^3}{Nm}, \tag{1}$$

where ΔV is the volume loss of the material during the wear test, L is the load, and d is the distance of sliding or abrading distance.

2.5. Scanning Electron Microscope and Stereo Zoom Microscope Images. The tensile and flexural fractured samples and the worn surface of the samples were scanned and analyzed using a JEOL-JSM-6390 scanning electron microscope with X250–X1000 magnification. Furthermore, the counterpart surface was inspected using a Motic SMZ-168 stereo zoom microscope in order to identify the residues and debris resulting from the wear studies.

Table 3: Wear test conditions.

Normal load (N)	Sliding velocity (m/s)	Sliding distance (m)
20	3.5	2000
20	4.5	2000
20	5.5	2000

3. Results and Discussion

3.1. Tensile, Flexural, and Impact Characteristics. The tensile strength of the samples is depicted in Figures 3(a) and 3(b). It is evident from the figures that the maximum tensile strength of 49.5 MPa is obtained for the sample with 20% Pb. It is further evident that the addition of Pb content beyond 20% reduces the tensile strength of the sample. It may be attributed to the increase in brittleness of the sample beyond the addition of 20%. Furthermore, it should be noted that some research studies revealed the similar scenario of embrittlement upon the addition of B_4C beyond 20%. Also, the trilayered samples exhibit different nature of tensile properties which is evident from the figure shown above. The sample E layered with 20% Pb as core and with B_4C cladding exhibited good tensile strength. On the other hand, the sample F with Pb cladding was found to have poor tensile strength.

Similarly, the elastic modulus of the samples decreased with an increase in the addition of the particles. The reduction in elastic modulus is as evident from the stress-strain diagram depicted in Figure 3(a) which further shows the similar trend for the trilayered samples. It is well obvious from the stress-strain curve that the embrittlement of the material took place and the same behaved more like a brittle material.

Figure 3(c) clearly depicts the trend of flexural strength of the various samples. It is obvious from the figure that the single-layered sample loaded with 20% of Pb and B_4C exhibited a good flexural strength of 50.4 MPa. Furthermore, it is evident that the increase in the composition of lead beyond 30% decreases the flexural strength. On the other hand, the triple-layered sample with B_4C core exhibits lower flexural strength. However, the sample with B_4C cladding has witnessed the increase in flexural strength which may be attributed to superior properties of B_4C. It is evident from Figure 3(d) that the impact performance of the samples yields more at 20% of lead. As the composition of lead increases, the energy absorbed by the specimen decreases, and it decreases steeply with 40% addition of lead.

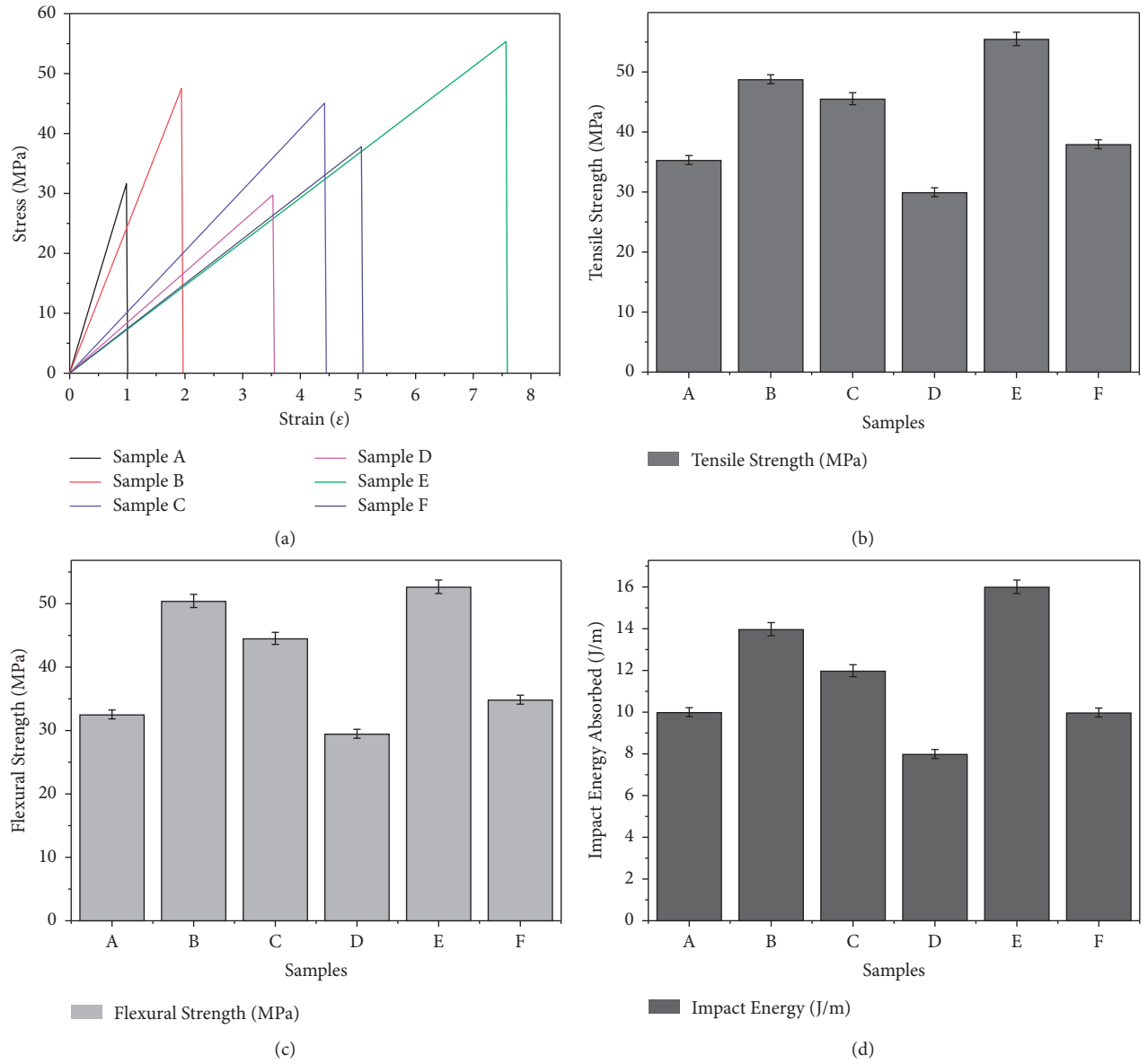

Figure 3: (a) Stress-strain curve. (b) Tensile strength of the samples. (c) Flexural strength of the samples. (d) Impact energy absorbed.

3.2. Fractography Studies. The tensile fractography in Figure 4(a) reveals the presence of agglomeration of the particles which may also be a reason for failure due to embrittlement. Furthermore, the chevron-like pattern in Figure 4(b) indicates the fracture of the sample due to brittleness [11–14]. On the other hand, the reason for the above failure can be evident from the fractograph shown in Figure 4(c). It shows the failure of the sample due to poor adhesion at higher loadings particularly in the sample with lead cladding. Figure 5 depicts the flexural fractograph, and it is evident from the figure that the added particles while loading tend to pullout from the epoxy matrix. This could be the obvious reason behind the failure of the specimen. On the other hand, the triple-layered sample with B_4C core exhibits lower flexural strength. However, the sample with B_4C cladding has witnessed the increase in flexural strength which may be attributed to superior properties of B_4C.

The impact energy absorbed by the specimen showcased superior results by the sample with 20% of lead, whereas the impact performance reduced significantly as the addition of lead is increased. This may be because of the poor particle distribution in the matrix and is evident from the SEM microscopy depicted in Figure 6. However, the trilayered samples witnessed similar trend as that of the tensile and flexural studies, that is, the sample with lead core absorbed energy to a greater extent while compared with the sample with B_4C core. This could be attributed because of the uniform dispersion of the lead particles and also because of softer nature of lead.

3.3. Tribological Studies. Figure 7(a) shows the specific wear rate of the samples and also the comparison with other composites. It is evident from the graph that the samples

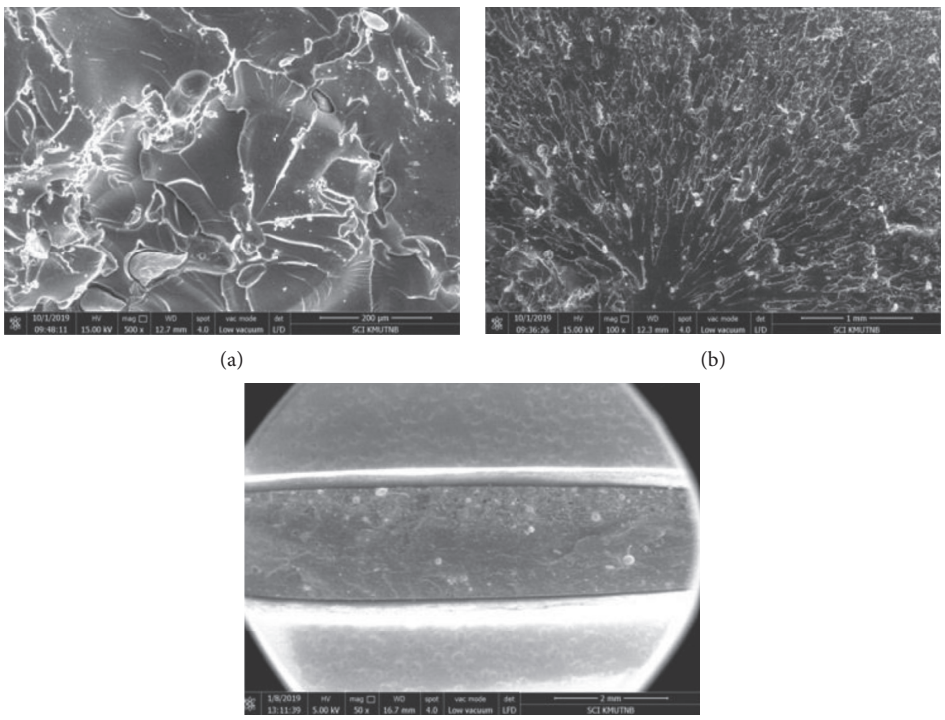

(a) (b)

(c)

Figure 4: (a) SEM image depicting the agglomeration of dispersed particles. (b) SEM image depicting chevron pattern. (c) Delamination of trilayered specimen.

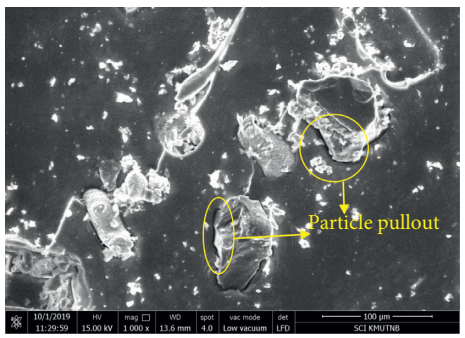

Figure 5: SEM image depicting the particle pullout from the matrix.

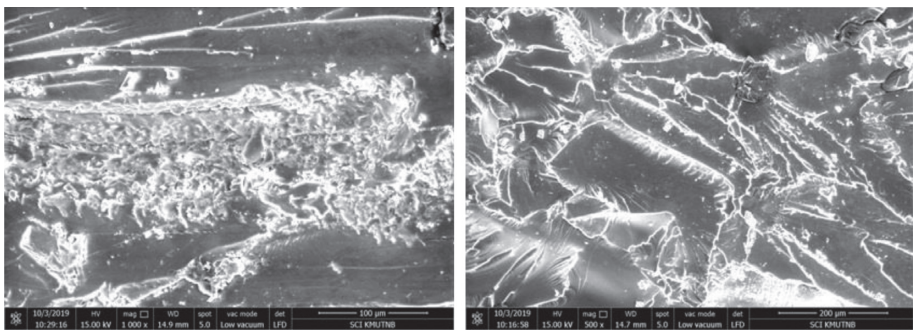

Figure 6: Impact fracture SEM image depicting agglomeration of the particles.

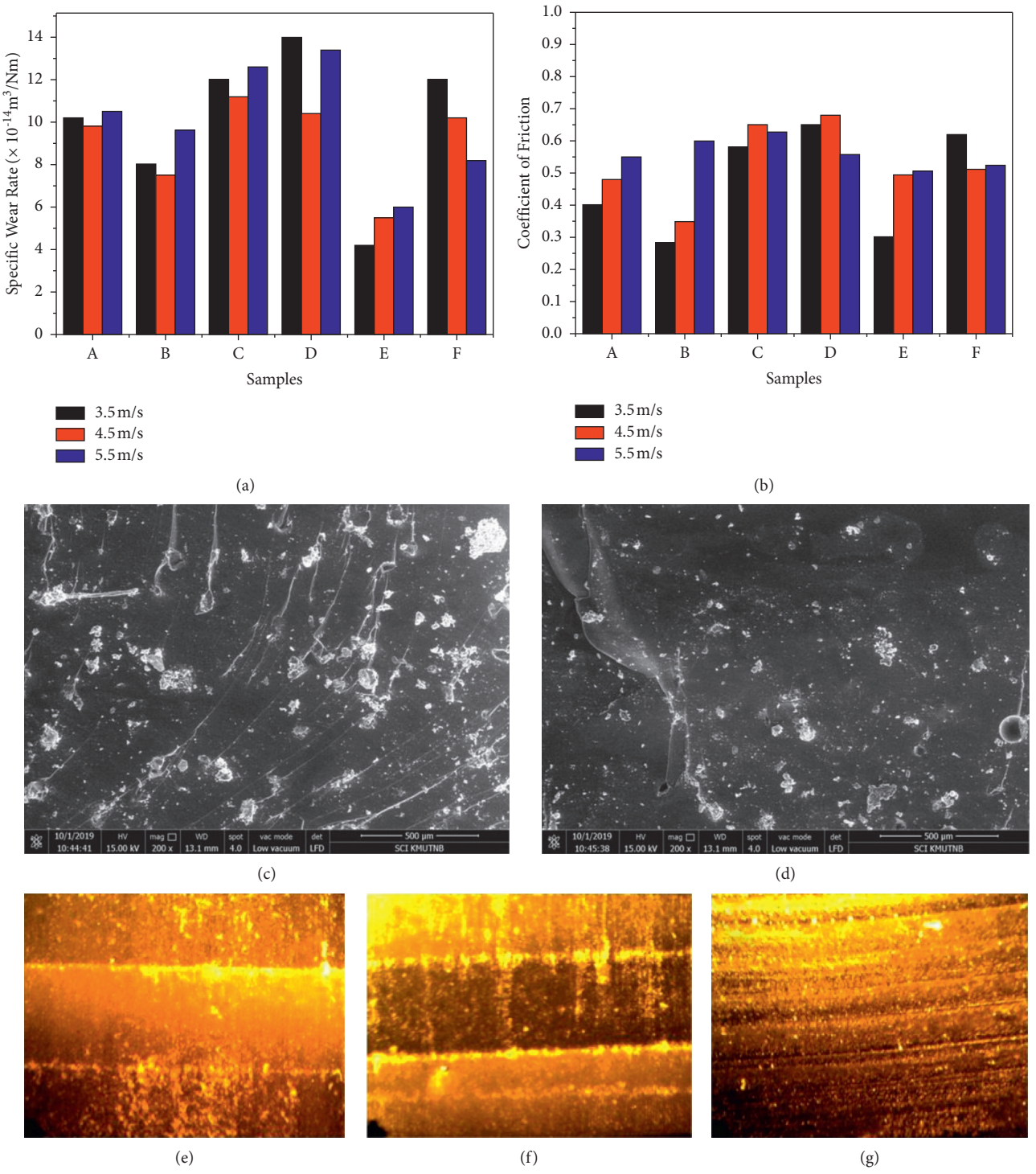

Figure 7: (a) Specific wear rate of the samples. (b) Coefficient of friction of the samples. (c, d) SEM image depicting the wear surfaces. (e–g) Stereo microscope images of the worn surface of the trilayered samples.

with increasing lead content reduce the wear performance of the composites. The specific wear rate of the sample with 20% lead content showcases excellent wear resistance. This may be owing to the strong bond existing between the epoxy matrix and the boron carbide particles. However, the scanning electron microscopic image depicted in Figures 7(c) and 7(d) clearly shows the length trace of wear path. This may be because of the inherent resistant behavior of the wear debris from forming further wear in the surface owing to its strong interfacial bonding with the matrix [15–17]. This could be the reason that the wear debris itself acts as an inhibitor to the wear. Furthermore, Figure 7(b) elucidates the coefficient of friction of the various samples under study. It clearly confirms that the sample with 20%

lead possesses excellent wear resistance. Furthermore, Figures 7(e)–7(g) clearly illustrate the worn surface of the trilayered samples. The trilayered sample with Pb core possesses excellent wear resistance which may be due to the fact that boron carbide, being a very hard material, possesses inherent wear resistance which acted as a protective layer. This avoided the wear track to reach the inner core of the sample and is clearly evident from Figure 7(e). At high speeds, the samples showcased lower wear resistance owing to the generation of frictional heat which makes the epoxy matrix weaker [18–22]. On the other hand, the sample with lead cladding had resulted poor wear resistance even at low speeds which may be attributed to the softer nature of the lead. Furthermore, it is evident from the SEM analysis that the formation of surface fatigue, grooving, and crazing could also be the reason for the poor wear resistance in the samples with increased lead content [6, 22–26].

4. Conclusion

In this work, different layered composite samples of epoxy matrix dispersed with boron carbide and lead were fabricated through the layered molding and curing technique. The samples were studied for the mechanical and tribological properties, and the conclusion is as follows:

(i) The tensile strength, flexural strength, and impact energy of the single-layered sample with 20% B_4C and 20% Pb exhibited good performance owing to the even particle distribution during the dispersion process.

(ii) However, the mechanical properties were found to decrease with an increase in addition of lead content. This could be because of the softer nature of lead and the agglomeration of the particle around the B_4C particles as well as around the matrix.

(iii) The mechanical properties of the trilayered sample exhibited different trend. The sample with B_4C cladding showcased better performance than the sample with Pb cladding. It was because of the softer core with a harder cladding. Furthermore, the major phenomenon of the failure of the specimen is brittle failure.

(iv) The trilayered sample with B_4C cladding showcased poor mechanical properties which may be because of the hard and brittle nature of B_4C.

(v) On the other hand, all the samples exhibited good specific wear properties. The single-layered composites with 20% Pb and 20% B_4C evidenced the better wear performance compared to all the other single-layered samples.

(vi) The reason for the wear performance could be the self-hindering property of the wear debris which was evident from the worn surface analysis. The wear debris had followed deep and long tracks which shows the strong interfacial bonding of the particles around the matrix.

(vii) Furthermore, the trilayered samples with B_4C cladding exhibited good wear resistance as the hard B_4C cladding hindered the propagation of wear tracks to the core.

(viii) On the other hand, the sample with Pb cladding showcased poor wear resistance due to the soft nature of the Pb cladding.

(ix) Moreover, from the wear surface analysis, it is evident that the surface fatigue, grooving, and crazing were the reasons of failure of the samples due to wear.

Data Availability

No data were used to support this study.

Conflicts of Interest

The authors declare that there are no conflicts of interest regarding the publication of this paper.

References

[1] X.-J. Shen, X.-Q. Pei, Y. Liu, and S.-Y. Fu, "Tribological performance of carbon nanotube-graphene oxide hybrid/epoxy composites," *Composites Part B: Engineering*, vol. 57, pp. 120–125, 2014.

[2] I. Neitzel, V. Mochalin, J. A. Bares, R. W. Carpick, A. Erdemir, and Y. Gogotsi, "Tribological properties of nanodiamond-epoxy composites," *Tribology Letters*, vol. 47, no. 2, pp. 195–202, 2012.

[3] W. Chonkaew, N. Sombatsompop, and W. Brostow, "High impact strength and low wear of epoxy modified by a combination of liquid carboxyl terminated poly(butadiene-co-acrylonitrile) rubber and organoclay," *European Polymer Journal*, vol. 49, no. 6, pp. 1461–1470, 2013.

[4] S. Bhatia, S. Angra, and S. Khan, "A review on mechanical and tribological characterization of boron carbide reinforced epoxy composite," *Advanced Composite Materials*, vol. 30, no. 4, pp. 307–337, 2021.

[5] S. A. Hallad, N. R. Banapurmath, A. S. Bhadrakali et al., "Nanoceramic composites for nuclear radiation attenuation," *Materials*, vol. 15, no. 1, p. 262, 2021.

[6] J. Abenojar, M. A. Martínez, F. Velasco, V. Pascual-Sánchez, and J. M. Martín-Martínez, "Effect of boron carbide filler on the curing and mechanical properties of an epoxy resin," *The Journal of Adhesion*, vol. 85, no. 4-5, pp. 216–238, 2009.

[7] J. Abenojar, J. C. Del Real, M. A. Martinez, and M. C. de Santayana, "Effect of silane treatment on SiC particles used as reinforcement in epoxy resins," *The Journal of Adhesion*, vol. 85, no. 6, pp. 287–301, 2009.

[8] L. B. T. La, C. Leatherday, Y.-K. Leong, H. P. Watts, and L.-C. Zhang, "Green lightweight lead-free Gd 2 O 3/epoxy nanocomposites with outstanding X-ray attenuation performance," *Composites Science and Technology*, vol. 163, pp. 89–95, 2018.

[9] S. Avcıoğlu, M. Buldu, F. Kaya et al., "Processing and properties of boron carbide (B4C) reinforced LDPE composites for radiation shielding," *Ceramics International*, vol. 46, no. 1, pp. 343–352, 2020.

[10] K. von der Ehe, M. Jaunich, D. Wolff, B. Martin, and H. Goering, "Radiation induced structural changes of (U) HMW polyethylene with regard to its application for radiation shielding," *PATRAM 2010-16th International symposium on the packaging and transport of radioactive materials (Proceedings)*, pp. 1–8, 2010.

[11] P. R. Pati and M. P. Satpathy, "Investigation on red brick dust filled epoxy composites using ant lion optimization approach," *Polymer Composites*, vol. 40, no. 10, pp. 3877–3885, 2019.

[12] P. Ranjan Pati, M. Prasad Satpathy, A. Satapathy, and A. Satapathy, "Experimental investigation on Linz-Donawitz slag filled polypropylene composites using teaching-learning based optimization approach," *Polymer Composites*, vol. 39, no. 11, pp. 3944–3951, 2018.

[13] P. R. Pati and A. Satapathy, "Processing, characterization and erosion wear response of Linz-Donawitz (LD) slag filled polypropylene composites," *Journal of Thermoplastic Composite Materials*, vol. 29, no. 9, pp. 1282–1296, 2016.

[14] P. R. Pati and A. Satapathy, "A study on processing, characterization and erosion wear response of Linz–Donawitz slag filled epoxy composites," *Advances in Polymer Technology*, vol. 34, no. 4, 2015.

[15] S. Vignesh, P. Jothiraj, J. T. W. Jappes et al., "Investigation on mechanical behavior of B4C dispersed advanced novel composites fabricated through molding and curing," *Materials Today Proceedings*, vol. 46, pp. 7639–7642, 2021.

[16] P. R. Pati, "Prediction and wear performance of red brick dust filled glass-epoxy composites using neural networks," *International Journal of Plastics Technology*, vol. 23, no. 2, pp. 253–260, 2019.

[17] P. Ranjan Pati, "Characterization of glass-epoxy composites using red brick dust particles," *Materials Today Proceedings*, vol. 18, pp. 3775–3779, 2019.

[18] P. R. Pati and A. Satapathy, "Prediction and simulation of wear response of Linz-Donawitz (LD) slag filled glass-epoxy composites using neural computation," *Polymers for Advanced Technologies*, vol. 26, no. 2, pp. 121–127, 2015.

[19] C. Kanchanomai, N. Noraphaiphipaksa, and Y. Mutoh, "Wear characteristic of epoxy resin filled with crushed-silica particles," *Composites Part B: Engineering*, vol. 42, no. 6, pp. 1446–1452, 2011.

[20] A. K. Kadiyala and J. Bijwe, "Surface lubrication of graphite fabric reinforced epoxy composites with nano-and micro-sized hexagonal boron nitride," *Wear*, vol. 301, pp. 802–809, 2013.

[21] G. Zhang, R. Sebastian, T. Burkhart, and K. Friedrich, "Role of monodispersed nanoparticles on the tribological behavior of conventional epoxy composites filled with carbon fibers and graphite lubricants," *Wear*, vol. 292-293, pp. 176–187, 2012.

[22] H. R. Le, A. Howson, M. Ramanauskas, and J. A. Williams, "Tribological characterisation of air-sprayed epoxy-CNT nanocomposite coatings," *Tribology Letters*, vol. 45, no. 2, pp. 301–308, 2012.

[23] M. R. Ayatollahi, E. Alishahi, S. Doagou-R, and S. Shadlou, "Tribological and mechanical properties of low content nanodiamond/epoxy nanocomposites," *Composites Part B: Engineering*, vol. 43, no. 8, pp. 3425–3430, 2012.

[24] J.-C. Lin, "Compression and wear behavior of composites filled with various nanoparticles," *Composites Part B: Engineering*, vol. 38, no. 1, pp. 79–85, 2007.

[25] P. R. Pati and M. Prasad Satpathy, "Effect of process parameters on sliding wear performance of red brick dust-filled glass–epoxy composites," *Proceedings of the Institution of Mechanical Engineers - Part J: Journal of Engineering Tribology*, p. 13506501211010553, 2021.

[26] Y. Gao, W. Zhang, P. Xu, X. Cai, and Z. Fan, "Influence of epoxy adhesive layer on impact performance of TiB2-B4C composites armor backed by aluminum plate," *International Journal of Impact Engineering*, vol. 122, pp. 60–72, 2018.

Hindawi
Advances in Materials Science and Engineering
Volume 2022, Article ID 4861346, 8 pages
https://doi.org/10.1155/2022/4861346

Research Article

Studies on Mechanical Attrition and Surface Analysis on Heat-Treated Nickel Alloy Developed through Additive Manufacturing

B. Anush Raj,[1] J. T. Winowlin Jappes,[1] M. Adam Khan,[1] V. Dillibabu,[2] and N. Rajesh Jesudoss Hynes[3]

[1]*Department of Mechanical Engineering & Centre for Surface Engineering, Kalasalingam Academy of Research & Education, Virudhunagar, Tamilnadu, India*
[2]*Small Turbo Fan Section, Gas Turbine Research Establishment (GTRE), DRDO, Bangalore, India*
[3]*Department of Mechanical Engineering, Mepco Schlenk Engineering College, Sivakasi-626005, India*

Correspondence should be addressed to M. Adam Khan; adamkhanm@gmail.com

Received 19 October 2021; Revised 9 March 2022; Accepted 18 March 2022; Published 9 April 2022

Academic Editor: Alicia E. Ares

Copyright © 2022 B. Anush Raj et al. This is an open access article distributed under the Creative Commons Attribution License, which permits unrestricted use, distribution, and reproduction in any medium, provided the original work is properly cited.

In this paper, the nickel-based superalloy SU718 is developed through the Direct Metal Laser Sintering (DMLS), an additive manufacturing process. Further, the material has been focused to study the effect of heat treatment and abrasive particle erosion. Two different heat treatment (HT) cycles are planed with ageing and annealing to enrich the metallurgical quality of the DMLS processed SU718 alloy. The heat treatment is performed with two different combinations of temperatures for annealing/solutionizing followed by ageing to improve the metallurgical properties. The influence of heat treatment on additively manufactured IN718 is imparting variations in the hardness, microstructure, and erosion resistance. Vickers hardness for as built, HT 1, and HT 2 of DMLS alloy is 264.15, 385.55, and 352.43 Hv; which has been increased for 45% for HT 1 and 33% for HT 2 from the as built DMLS alloy. After solutionizing, the grains are refined within the track boundary and the majority of the grains are homogenized. The air jet erosion test arrangement is used to conduct the study at a velocity of 250 m/s and impact angle of 90° at room temperature. The hardness of the treated samples has taken vital role to resist the erosion. The rate of erosion is higher for bare DMLS alloy whereas HT 1 has low erosion rate when compared with HT 2 and bare DMLS alloy. The erosion morphology of the samples was carried out by SEM images, and erosion mechanism is discussed. The ploughing and microcutting were found in all the impact angles, whereas erodent impingement is found in the bare DMLS alloy in additional. The good erosion resistance is observed for HT 1 DMLS alloy in all the impact angles.

1. Introduction

In the past decade, additive manufacturing is used to produce the prototype models, but nowadays researcher finds interest to manufacture components by additive manufacturing process due to its accuracy in dimension and can produce complex shape. The additive manufactured components are mainly used in the automobile, gas turbine, space, marine, and power generation application [1]. The additive manufacturing converts the three-dimensional virtual model of CAD data into two-dimensional layer and builds the object in the incremental form of layer by layer [2]. Mang et.al investigated on the additive manufactured IN718 and found that because of the highest cooling rate, the columnar grains are produced and built along the build direction. The samples fabricated by additive manufacturing process have anisotropic property [3]. The IN718 specimens fabricated by direct metal laser sintering (DMLS) were evaluated. IN718 alloy is the nickel-based super alloy which has good corrosion resistance and erosion resistance at high temperature; it is broadly used in aviation, aeronautical application, and marine and power generating application

[4]. The IN718 can be altered by proper heat treatment, and crystallographic changes can be made [5]. The alloy consists in major phases of gamma prime (γ'), gamma double prime (γ"), and delta (δ) phases and minor phases of laves and carbides. The chemical composition of Ni_3Nb is in the form of two structures, namely, tetragonal unit cell as γ" phase and orthorhombic unit cell as δ phase. Therefore, if the δ phase is increased, there is a decrease in the γ" phase which reduces the strength of the alloy [6].

Surface degradation is due to the wear and corrosion in gas turbine. The nickel-based super alloy used in the gas turbine provides good erosion resistance [7]. The degradation of the surface is caused due to the suspended particles in the liquid or gases. This suspended particles are rough irregular shapes and cause abrasion on the turbine blades. Due to the abrasion, the degradation of surface takes place and reduces the performance of the system. Also, it reduces the life of the system [8]. With the increase in hardness, the erosion resistance is increased [4]. Due to the solid particle erosion of the material, the surface damage and microstructure development also took place. The development of new microstructure on the eroded surface can change the erosion mechanism of the material [9].

The erosion mechanism of IN718 manufactured by DMLS process which is an additive manufacturing is not reported in any literature. The main objective of this paper is to understand the erosion mechanism of heat-treated IN718 manufactured by DMLS process with erodent velocity as constant and varying the impingement angle. The erosion scar is studied through macrograph of the sample.

2. Experimental Materials and Procedures

The IN718 powder of size of about 10–45 μm is used to fabricate, and the chemical composition of IN718 powder is shown in Table 1. The IN718 is fabricated with DMLS process (Model: EOS M280). The IN718 powders used of manufacturing are gas atomized with argon, and the grains are in spherical in size. The samples are manufactured in the horizontal orientation. The optimum parameter used for manufacturing is shown in Table 2. The average surface roughness of the fabricated samples is 2-3 μm.

The samples prepared by the DMLS process were subjected to different heat treatment. The heat treatment chart of the above heat treatment is shown in Figure 1, and corresponding details are furnished in Table 3. For HT 1, samples are solutionized at a temperature of 980°C for one hour followed by air cooling and double ageing at a temperature of 720°C for eight hours, furnace cooling to 620°C at the rate of 55°C/hr and maintained for eight hours, and cooled to room temperature by furnace cooling. For HT 2, the sample is homogenized at a temperature of 1100°C for two hours followed by air cooling and ageing at a temperature of 845°C for 24 hours and cooled to room temperature by furnace cooling. To reveal the microstructure, the samples are etched with solution composed of 16 ml H_2O + 4g $CuSO_4$ + 1 ml H_2SO_4 + 20 ml HCL.

In order to study the effect of heat treatment, the samples are metallurgically polished to measure the surface hardness. Based on the surface hardness, the metallurgical changes are predicted. To confirm the metallurgical changes, the samples are further subjected to X-ray diffraction analysis to read the changes in atomic level. The science of heat treatment with the peaks of X-ray diffraction and respective surface hardness is correlated. Subsequently, the air jet erosion testing machine (TR-470, Ducom, Bangalore, India) was used to investigate the erosion behavior of all test samples as per ASTM G76 standards. The erodent mix compressed air passes through the nozzle and strikes the sample which is placed on the angle sample holder at particular angle. The Alumina oxide particles size of 20–50 μm is widely used for the erosion testing. Table 4 shows the erosion test parameter used for evaluation. Therefore, the samples were cleaned with acetone and dried and weighted before erosion test and after erosion test in the electronic balance having an accuracy of ±0.01 mg. By using the change in mass, erodent flow rate (E_f), and discharge time (t), the erosion rate (E_r) of each sample is calculated using the equation as follows: erosion rate (E_r) = ($W_{initial}$−W_{final})/(E_f x t) where $W_{initial}$ is the weight of the sample before erosion test in g, Wfinal is the weight of the sample after erosion test in g, E_f is the erodent flow rate in g/sec, and t is the discharge time of erodent in sec.

The metallographic observation and crystallography of bare and heat treated DMLS samples are obtained by optical microscope and X-ray diffractometer (Bruker ECO D8 Advance), respectively. Scanning electron microscope (Make: Zeiss–FE SEM) attached with energy dispersive X-ray (EDAX) analysis is used to reveal the characterization of the eroded samples.

3. Results and Discussion

The microstructure of the bare DMLS sample observed on the building direction is shown in Figure 2(a). The laser beam scanning path is observed throughout the sample. The morphology of the metal pool appearance in the form of arc shape was found throughout the sample. In the overlap region, broad columnar grains are formed when it is seen in the building direction. The columnar grains represent hatch distance of the scanning path. This columnar region and dendrites are formed along the build direction. These dendrites in the DMLS samples make the sample anisotropy. To eliminate these nonequilibrium phases, the samples are repaired by suitable heat treatment process. After HT 1, the grains are refined within the columnar grain which is shown in Figure 2(b). Also, for HT 2, the grains are homogenized within the layer which is clearly shown in Figure 2(c). After heat treatment, the hardness is increased for 45% for HT 1 and 33% for HT 2 DMLS alloy. It is due to the repeated melting of metal powder and rapid solidification. While building a new layer, the reheating of existing layer may lead to produce metal carbide and it may invary at the end of DMLS process. It was observed that during solution treatment, γ'' and γ' phases are dissolved and the enrichment in δ phase was revealed. Figure 3 shows the XRD peak of the heat treated samples and the as built sample. After heat treating the HT1 DMLS alloy, the improvement of γ'' phase is due to

Table 1: The chemical composition of IN718 used for fabrication.

Element	C	Si	Co	Cu	W	Al	Ti	Mo	Nb	Cr	Fe	Ni
Wt. %	0.05	0.13	0.16	0.23	0.23	0.59	1.11	3.38	4.77	17.13	19.78	Bal

Table 2: Parameter for manufacturing IN718 samples in DMLS machine.

Parameter	Range
Power	285 W
Scan rate	970 mm/s
Hatching distance	0.15 mm
Layer thickness	40 μm
Beam diameter	80 μm

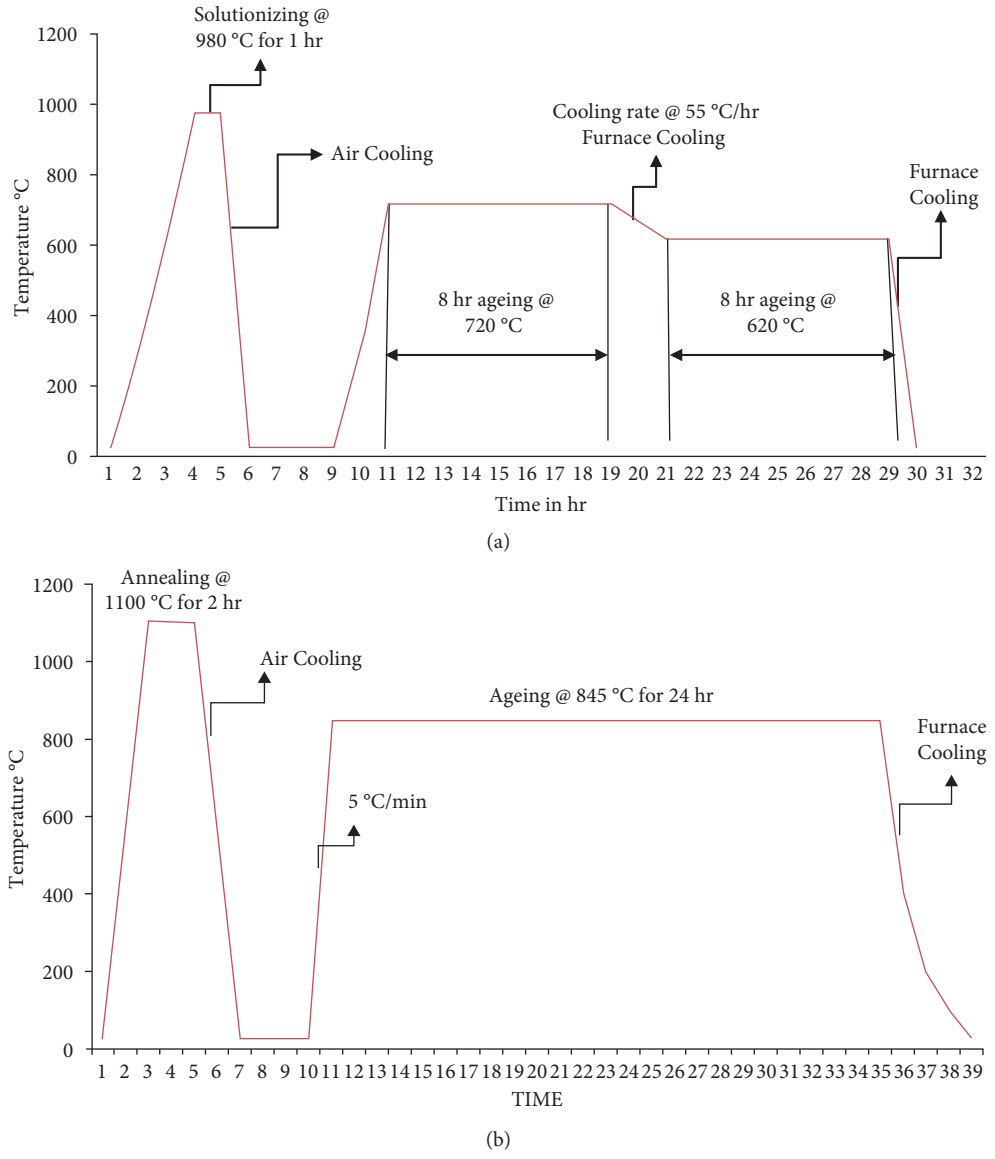

Figure 1: Heat treatment cycles for DMLS processed material: (a) HT 1 and (b) HT 2.

Table 3: Heat treatment variant.

Plan	Solutionizing	Cooling	Ageing	Cooling
HT 1	980°C/1 hr	Air cooling	720°C/8 hr and 620°C/8 hr	Furnace cooling
HT 2	1100°C/2 hr	Air cooling	845°C/24 hr	Furnace cooling

Table 4: Erosion test parameter for the proposed investigation.

Parameters	Range
Erodent material	Alumina
Particle size	50 micron
Particle velocity	250 m/sec
Erodent feed rate	5 g/min
Impact angle	90°
Nozzle diameter	1.5 mm
Test time	10 min

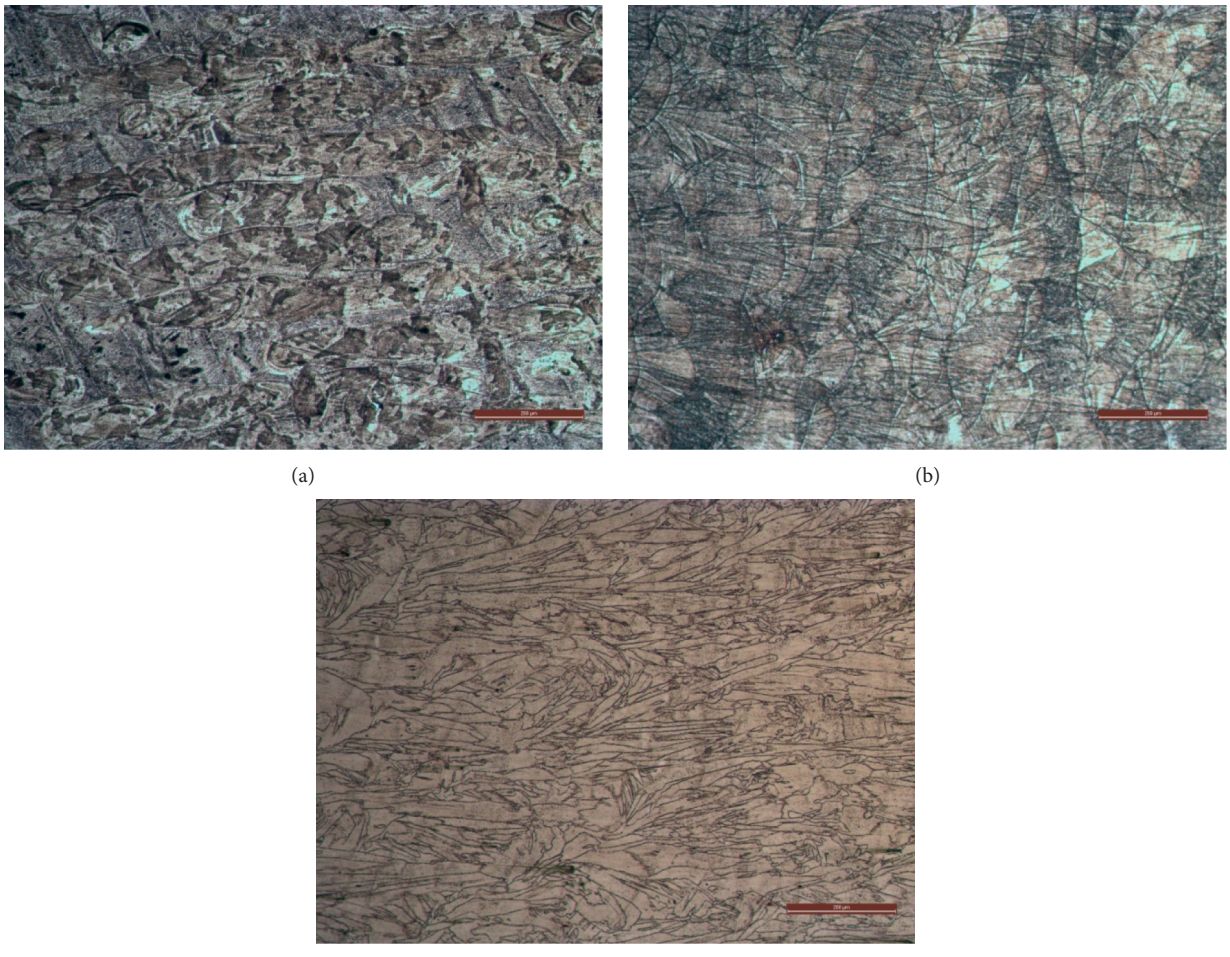

(a) (b) (c)

Figure 2: Optical microstructure of (a) as built, (b) HT 1, and (c) HT 2 DMLS alloy.

the segregation of Niobium elements in the form of BCT structure and γ' is formed due to the segregation of titanium and aluminum. In HT2 DMLS alloy, the δ phase is formed due to the segregation Niobium in the form of orthorhombic crystal structure; therefore, the γ" segregation is less which is clearly identified in the XRD graph. The effect of heat treatment on additive manufactured at 980°C has made metallurgical transformation by liquifying laves phase and releasing Nb atoms around the laves phase to improve the hardness [10]. Due to the uneven heat distribution and rapid cooling, the residual stress is caused. As a result of uneven heating and cooling process, distraction in metallurgical transformation may have an impact to pull down the strength in HT2 and base metal [11]. The reduction in γ'' and γ' phase and formation of δ phase lead to the reduction in hardness of alloy. Furthermore, Laves phase contains plenty of Mo, Ti, and Ni that may affect the strengthening of solid solution and decrease the number of γ'' and γ' phase which weakens the effect of precipitation. The presence of γ'', γ', and δ phase in the surface has increased the hardness with the HT1 sample. The metallurgical transformation of nickel alloy takes place at eutectic point (above 926°C), and it helps to form delta phase and their precipitates. In this research, it is evidently proved that the developed IN718 has completely

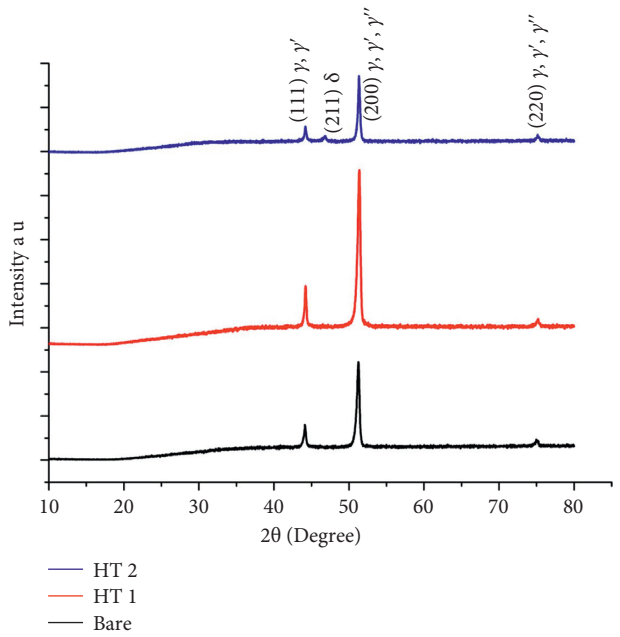

Figure 3: XRD peaks for the heat-treated sample and as built sample with phase diagram.

transformed into δ solvus during heat treatment (at 1100°C) and while ageing (at 845°C for 24 hours) the γ', γ'', and δ formation has taken place. In HT 1, the sample is double aged at 720°C and 620°C at 8 hours each, and the corresponding peak for the γ' and γ'' phase formation is strong. Therefore, the hardness of the alloy increased after heat treatment. The scale of Vickers hardness for bare, HT 1, and HT 2 DMLS alloy is 264.15, 385.55, and 352.43 Hv, respectively. The strength of the IN718 alloy mainly depends on the γ' and γ" of the alloy. The primary motive of the heat treatment is to fully solutionize the alloy and neglect the lave phase. During the fabrication process due to the rapid cooling, there is a formation of lave phase in the alloy which reduced the strength of the alloy. In HT 2 process, the sample is heat treated to 1100°C for 2 hrs which completely solutionized in the form of δ phase. In HT 1 process, the sample is heat treated to 980°C and double ageing at 720°C and 620°C where the lave phase is transformed in the form of γ' and γ" phase. Similar research in authentic phase transformation of additive built material is available in the literature for discussion [12].

Solid particle erosion test on metals mostly depends on the erosion test parameters such as flow rate of the erodent, velocity of the erodent, and impingement angle. In addition to the input process parameter, the quality of the erodent has also influenced over the erosion rate. Pure alumina is used an erodent having multiedges for the erosion study. Figure 4 shows the electron image of the alumina (erodent used for investigation) with similar dimensions and metallurgically qualified. The jet pressure used with high impact velocity strikes the surface of the DMLS processed alloy. Three samples per material grade are used for erosion studies. For a defined input process parameter, the erosion study is performed and weight loss is measured. Using the erosion rate formula for the recorded mass change, erosion rate is measured. Calculated erosion rate for the bare and the heat-treated DMLS alloy is given in Figure 5.

The sample tested at impact angle 90° exhibited the lowest erosion rate when compared with other impact angles. It is noted that the mass change in the erodent sample at perpendicular impingement is very meager. The mass change is in the range of 0.01 to 0.2 g for individual experiments. The bare DMLS sample exhibited the erosion rate of 5.02×10^{-4} Δg/g. The HT 1 and HT 2 DMLS alloy exhibited 3.81×10^{-4} Δg/g and 4.61×10^{-4} Δg/g rate of erosion. Heat-treated sample has good resistance towards erosion due to the metallurgical transformation. Presence of γ'', γ' and δ phase in the post processed alloy has increased bulk property. It has high strength to resist the erosion, and the intensity varies with respect the presence of precipitates (γ'', γ, and δ phase). The wear surface morphology and mechanism involved during the erosion are discussed in detail.

The erosion scar at the angle 90° for bare and heat-treated DMLS alloy is shown in Figure 6. The differences in the wear morphology due to impingement of the erodent over the surface of DMLS alloy for as built-bare, HT 1, and HT 2 (Figure 6(a)–6(c)) are elaborated in detail. The erosion scar diameter for the angle 90° impingement is very high for the HT 1 DMLS alloy and low in case of HT 2 DMLS alloy. The vertical force or normal force acts on the erodent which strikes the sample surface. The erosion resistance mainly depends on the hardness of the targeted surface, and the presence of hard precipitates resists the erosion. The similar results are obtained that the increase in hardness has increased the wear resistance of the material. To discuss in detail, the worn surface is investigated at higher magnifications.

The surface morphology of the worn surface is revealed with different wear mechanisms. Worn surface topography of the DMLS processed Inconel718 observed at higher magnification is given in Figure 7. The mechanical action of the solid particle erodent has impinged the surface and initiated plastic deformation on the bare DMLS alloy. Simultaneously, the repeated impingement of the erodent may strain harden the bare alloy, and when the strain hardening completed, the cracks are formed on the surface. The lip formation, crater, and ploughing are also observed on the surface of the heat-treated sample which is shown in Figures 7(c)–7(f). Fundamentally, the sliding of particle induces the surface to slide (shear) the surface, and the perpendicular impingement causes clinging effect. On the surface of heat-treated material, the crater and lip formation are noticed due to the continuous impact of erodent with multiedge which act as a spike during experimentation.

The improvement in the hardness of the heat-treated alloy improves the strain hardening of the sample and provides good resistance to erosion wear. It is also confirmed that the alumina solid particle after impingement found adhering to the worn surface. On continuous strike, the collision of alumina particle influences the erosion rate and the particle adheres to the surface with lip formation.

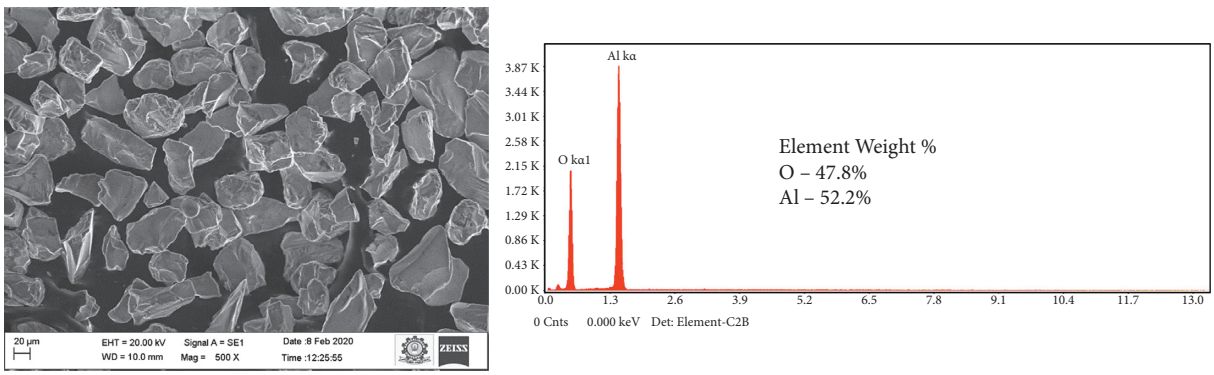

Figure 4: Electron image of the erodent particle with spectroscopic results.

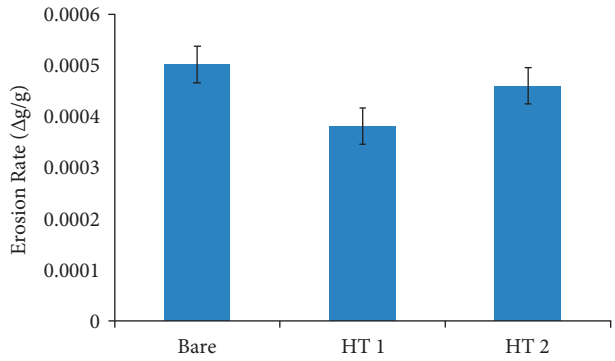

Figure 5: Erosion rate of the DMLS samples and hard particle impingement 90°.

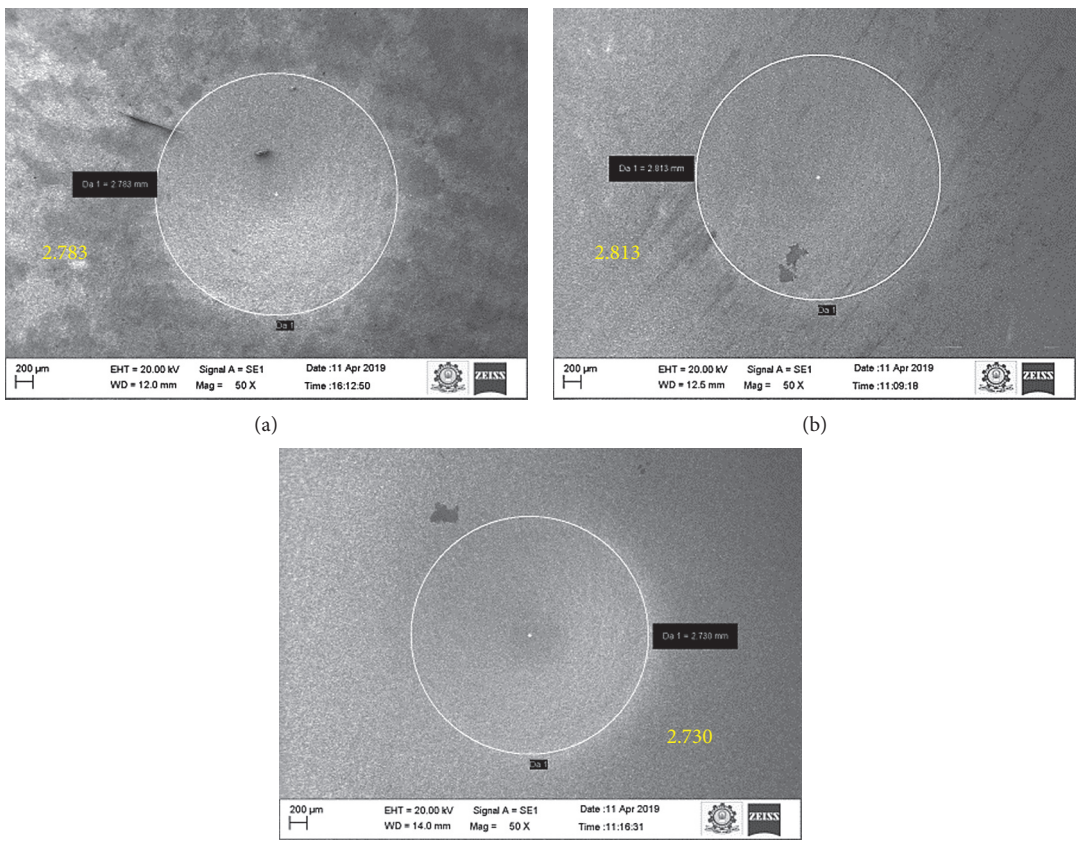

(a) (b)

(c)

Figure 6: The diameter of erosion scar: (a) bare, (b) HT 1, and (c) HT 2 DMLS alloy.

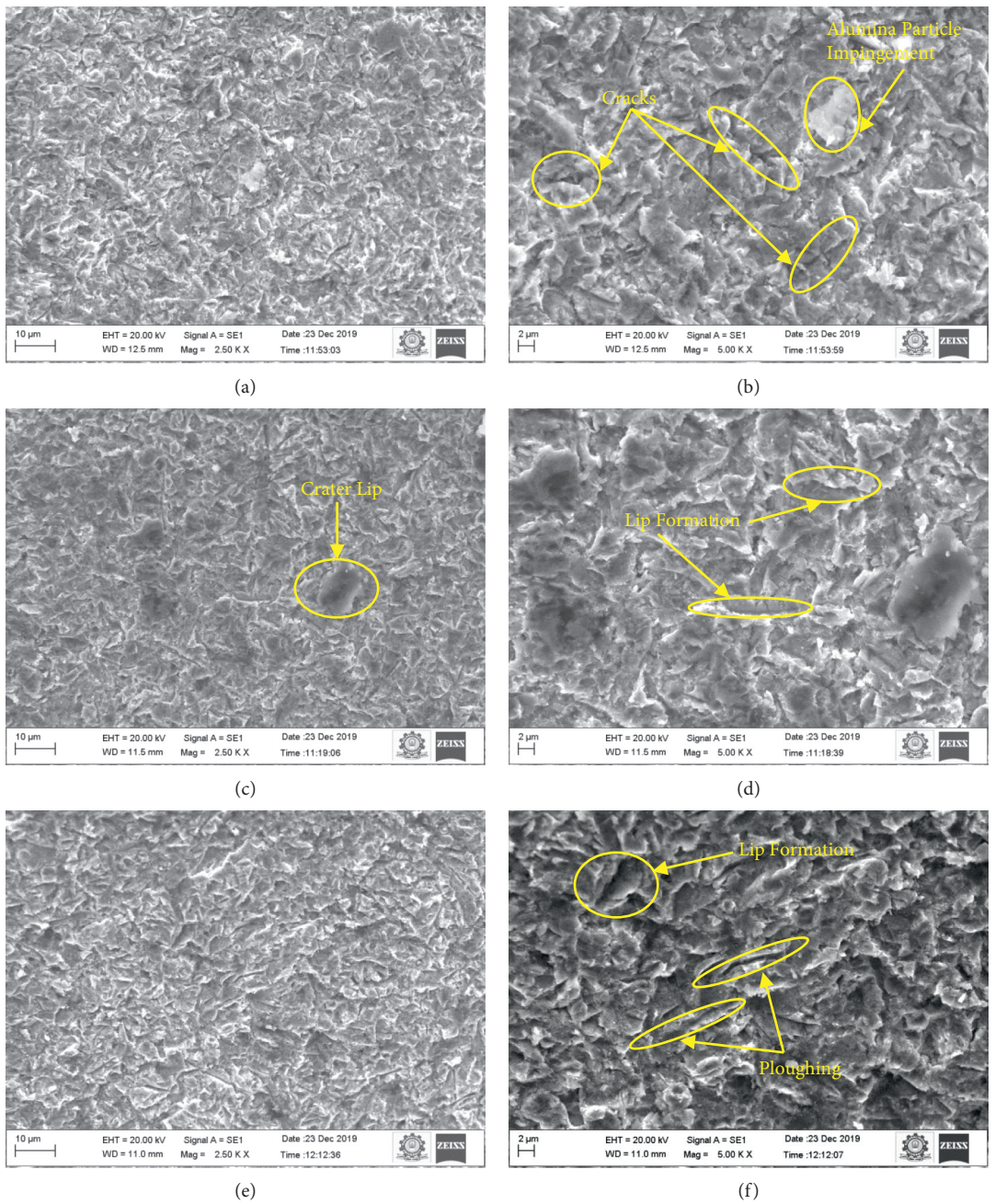

Figure 7: The higher and lower magnification of erosion morphology for the angle 90° for (a, b) Bare, (c, d) HT 1, and (e, f) HT 2.

Therefore, the metallurgical transformation due to isothermal heat treatment has highly influenced to increase the surface hardness of the DMLS processed alloy. In extension, the surface has high resistance towards erosion and controlled the material deterioration from severity in mechanical action of solid particle impingement.

4. Conclusions

The IN718 alloy is developed through DMLS process and followed by the different heat treatment plans. From investigation, following points found significant to justify the research findings:

(i) The heat treated DMLS alloy has significant changes in mechanical properties and metallurgical qualities. The wear resistance found increased with respect to increase in surface hardness. The built DMLS alloy has 264.15 Hv and expressively increased to 385.55 Hv for heat treated material. Vickers hardness found increased from 264.15 Hv to 385.55 Hv.

(ii) Concurrently, the built tracks found dissolved during heat treatment and the material revealed with austenitic phase. The carbides/dendrites in the built track reduced with annealing and complete phase transformation occurred with solutionizing.

It shows the metallurgical phase with achieved strength in change.

(iii) Indicating the erosion rate, annealed sample revealed with less in erosion rate (0.38 Δg/g) due to presence of partial carbide/dendrite structure. For the solutionized sample, erosion rate is average (0.46 Δg/g) compared with the as built DMLS alloy (0.5 Δg/g).

(iv) The common wear mechanism is revealed with lip formation and chipping due to hard particle impingement at perpendicular axis. However, the alumina particle striked on the surface found clinging with the as built material.

Therefore, it is recommended that the DMLS processed IN718 with annealing followed ageing has good mechanical properties, metallurgical strength, and high erosion resistance compared with solutionized sample and as built sample.

Data Availability

No data were used to support this study.

Conflicts of Interest

The authors declare that there are no conflicts of interest.

References

[1] I. Yadroitsev, L. Thivillon, P. Bertrand, and I. Smurov, "Strategy of manufacturing components with designed internal structure by selective laser melting of metallic powder," *Applied Surface Science*, vol. 254, no. 4, pp. 980–983, 2007.

[2] Ż. A. Mierzejewska, "Process optimization variables for direct metal laser sintering," *Advances in Materials Science*, vol. 15, no. 4, pp. 38–51, 2015.

[3] M. Ni, C. Chen, X. Wang et al., "Anisotropic tensile behavior of in situ precipitation strengthened Inconel 718 fabricated by additive manufacturing," *Materials Science and Engineering: A*, vol. 701, pp. 344–351, 2017.

[4] H. X. Hu, Y. G. Zheng, and C. P. Qin, "Comparison of Inconel 625 and Inconel 600 in resistance to cavitation erosion and jet impingement erosion," *Nuclear Engineering and Design*, vol. 240, no. 10, pp. 2721–2730, 2010.

[5] F. R. Caliari, N. M. Guimarães, D. A. P. Reis, A. A. Couto, C. De Moura Neto, and K. C. G. Candioto, "Study of the secondary phases in inconel 718 aged superalloy using thermodynamics modeling," in *Key Engineering Materials*vol. 553, pp. 23–28, Trans Tech Publications Ltd, 2013.

[6] C. Silva, M. Song, K. Leonard, M. Wang, G. Was, and J. Busby, "Characterization of alloy 718 subjected to different thermomechanical treatments," *Materials Science and Engineering: A*, vol. 691, pp. 195–202, 2017.

[7] H. Vasudev, P. Singh, L. Thakur, and A. Bansal, "Mechanical and microstructural characterization of microwave post processed Alloy-718 coating," *Materials Research Express*, vol. 6, no. 12, Article ID 1265f5, 2020.

[8] K. C. Wilson, G. R. Addie, A. Sellgren, and R. Clift, *Slurry Transport Using Centrifugal Pumps*, Springer Science & Business Media, Germany, 2006.

[9] Z. Li, J. Zhou, J. Han, and J. Chen, "Formation of cavitation-induced nanosize precipitates on the eroded surface for Inconel 718 alloy," *Materials Letters*, vol. 164, pp. 267–269, 2016.

[10] Z. Wang, K. Guan, M. Gao, X. Li, X. Chen, and X. Zeng, "The microstructure and mechanical properties of deposited-IN718 by selective laser melting," *Journal of Alloys and Compounds*, vol. 513, pp. 518–523, 2012.

[11] V. A. Popovich, E. V. Borisov, A. A. Popovich, V. S. Sufiiarov, D. V. Masaylo, and L. Alzina, "Impact of heat treatment on mechanical behaviour of Inconel 718 processed with tailored microstructure by selective laser melting," *Materials & Design*, vol. 131, pp. 12–22, 2017.

[12] D. Kong, C. Dong, S. Wei et al., "About metastable cellular structure in additively manufactured austenitic stainless steels," *Additive Manufacturing*, vol. 38, Article ID 101804, 2021.

Hindawi
Advances in Materials Science and Engineering
Volume 2022, Article ID 5625427, 8 pages
https://doi.org/10.1155/2022/5625427

Research Article

Post-Surface Processing and Virtual Simulation Analysis of Ball-Punch Test on CP-Ti Material

Ananda Mohan Vemula,[1] **G. Chandra Mohan Reddy**,[2] **M. Manzoor Hussain**,[3] **Atul Kumar**,[4] **Naresh Kumar**,[5] **and Haiter Lenin Allasi**[6]

[1]*Department of Mechanical Engineering, Guru Nanak Institutions Technical Campus, Hyderabad, Telangana, India*
[2]*Department of Mechanical Engineering, Chaitanya Bharathi Institute of Technology, Hyderabad, Telangana, India*
[3]*Department of Mechanical Engineering, Jawaharlal Nehru Technological University, Hyderabad, Telangana, India*
[4]*SET, Mody University of Science and Technology, Laxmangarh-332311, Sikar, Rajasthan, India*
[5]*Department of Mechanical Engineering, Manda Institute of Technology, Raisar, Bikaner, Rajasthan, India*
[6]*Department of Mechanical Engineering, WOLLO University, Kombolcha Institute of Technology, Post Box No: 208, Kombolcha, Ethiopia*

Correspondence should be addressed to Ananda Mohan Vemula; happymohan@yahoo.com and Haiter Lenin Allasi; drahlenin@kiot.edu.et

Received 11 November 2021; Accepted 20 February 2022; Published 11 March 2022

Academic Editor: J.T. Winowlin Jappes

Copyright © 2022 Ananda Mohan Vemula et al. This is an open access article distributed under the Creative Commons Attribution License, which permits unrestricted use, distribution, and reproduction in any medium, provided the original work is properly cited.

The titanium alloy is one of the prime materials for many engineering applications. It has been recommended for the components in automotive engines, power sector, biomedical industries, and more applications. It is due to the unique properties of the material with good strength and corrosion resistance. However, it is very challenging to handle Ti-based materials in manufacturing sectors without damaging the metallurgical quality. Thus, an attempt made to study the deformability of the CP-Ti material through ball–punch test to represent the stress, strain, and formability limit during mechanical loading and plastic deformation. The experiments are conducted following the ASTM E643 standards to study the material behavior. The maximum cupping reached to a height of 8.69 mm and got teared at the peak of doom. The separation has induced grain detachment due to tensile loading. The same condition is used to simulate with PAM STAMP™ software and 8.48 mm is the maximum cupping height achieved. The different is 0.21 mm. The results are interesting with similar observations and found acceptable to study the deformation.

1. Introduction

In the last two decades, demand for titanium alloy and its research are found increased in automobile components, biomedical engineering, and food processing industries [1–3]. These alloys are recommended for structural engineering and load bearing systems and widely used as alternate materials for biomedical components. The titanium alloy offers best performance in automobile components subjected to extreme load/suspension systems. Especially, the structure component should have high corrosion resistance, good formality, and high strength with low modulus to sustain reliable service period of the structure developed [4]. Literature is available to discuss about the processing of titanium alloys [5]. In general, the titanium alloys are widely used in aero jet engine components to make compressor disc, fan doom, and fan blades. It should possess high strength with less weight, less fatigue, and creep failures [6]. Jiang and Huang investigated and reported the grain replacement and effects on mechanical forming of Ti alloy. While processing the material through mechanical loading, the crystalline structure of alloy varies with respect to process condition. The commercial pure titanium (CP Ti) is HCP (hexagonal closely packed) structure below 800°C and

BCC (body centered cubic) above 800°C temperatures [7]. The CP Ti exhibits low elastic modulus limited plastic sag while deformation. While working with CP-Ti alloy, the deformed structure reveals with twinning effect due to the strength differential ratio with respect to direction of forming [8]. However, the studies on deformability and its process are yet to explore for titanium alloy. It has been reported that the plastic deformation of titanium and its alloys at room are found difficult [9]. The Ti and Ti-based alloys are induced to produce work hardening (rapidly) and strain leads to failure while cold working (mechanical loading and deformation at room temperature) [9, 10]. Since, there is a need for detailed studies deformation and its formability during mechanical processing.

In this study, the research has been focused on mechanical loading, plastic deformability, and structural analysis of the commercially pure titanium (CP-Ti) alloy. The ball-punch deformation test was performed on Cp-Ti alloy to forecast the formability limits and its strain during deep drawing. From the analysis the Erickson number, peak load, deformability, FLD, and its strain are calculated [11, 12]. In order to reduce the materials wastage, process time, and cost factor, the experimentations are performed through virtual systems, and the optimal results are verified through real-time instruments. The PAM STAMP™ is the commercially available simulation package used to study the deformation of engineering materials [13, 14]. The formability and deformability pressure of the material are the main components of the cupping test. The validation of the results from ball-punch analysis and FE simulation are inspiring in recent research situations [15, 16]. The highlight the research state of art is that there is no study to report on mechanical deformation of Ti alloys through ball-punch deformation test and simulated with PAM STAMP™ software. Therefore, an attempt is made to study the deformability of commercially pure titanium alloy through ball-punch deformation test and simulated with PAM STAMP™ software.

2. Materials and Method

The commercially pure titanium (Cp-Ti) alloy is chosen as a test material. The nomination composition and the physical dimension of the test sample are given in Table 1. The samples are cleaned with acetone to degrease and ensured the samples are ready to investigate. Investigations are performed in ball-punch (Erichsen Cupping) test (Sheet and Strip Metal Testing Machine Model 111) following standard procedure of ASTM E643 (equivalent to ISO 20482). The deformability of CP-Ti alloy is studied using ball-punch tester and the same was simulated with PAM STAMP™ simulation software. The pictorial representation of ball-punch test and proposed research plan is shown in Figure 1. The mechanical test parameters and the specifications for ball-punch instrument are given in Table 2. Figure 2 shows the detail sketch of ball-punch die arrangements following ASTM standards.

The estimation of forming limit diagram depends on the axial strain caused in major axis and minor axis. In addition, the dimension of the cup used for deformation is considered as a factor. It is also based on the tensile test results generated by testing the dog bone-shaped specimen and the details are given in Table 3. The fundamental sketch of FLD with different zones is shown in Figure 3.

Table 1: The nomination composition of Cp-Ti alloy and the physical dimension.

Input factors	Range
Thickness	1.20 mm
Size of sheet	90 mm × 90 mm ($l \times b$)
Density	4.51 g/cc
Brinell's hardness	120 BHN

Equation (1) represents the mathematical relation which is used to study the yield/fracture point of the material under cupping process [17]:

$$F|\sigma_2 - \sigma_3|a + G|\sigma_3 - \sigma_1|a + H|\sigma_1 - \sigma_2|a = 1. \quad (1)$$

It is assumed to be an anisotropy material having standard constants. On substitution of standard details, the relative equation is further given in

$$R_0|\sigma_2 - \sigma_3|a + R_{90}|\sigma_3 - \sigma_1|a + R_{90}R_0|\sigma_1 - \sigma_2|a = R_{90}\left(1 + R_0\right)Xa,$$
$$\sigma = K \cdot \left(\varepsilon_0 + \varepsilon_p\right)^n. \quad (2)$$

The above equations are related to Krupkowsky law. It is directly related to the stain components and its coefficient.

The mechanical boundary conditions for PAM STAMP TM are obtained by fixing the blank holder and die is fixed (all degrees of freedom); then, punch is allowed to indent on the CP-Ti sheet in Z direction till the crack appears.

3. Results and Discussion

The deformability of CP-Ti alloy is performed as per the ASTM standards and the results are discussed with reference to macroscopic (visual) analysis, microscopic analysis, simulated analysis, and FLD plots. The photo image of the mechanical deformed CP-Ti sample is shown in Figure 4. At the top of doom, the material deformed during cupping found stretched and the thickness got reduced. That is, the action of the metal atoms induced due to tensile loading and separation occurs. It is an action of sliding of metal atoms with respect to the mechanical force and so called as slipping. On continuous loading, the slipping persuades the metal thinning to cracking and the element cracking occurs. For better illustration, the traction-separation of the metal is illustrated in Figure 5. It is physically visible that the fracture is in the form of typical linear traction-separation response. The crack growth is analyzed over the fractured samples, and it is under two conditions. The crack is initiated in the perpendicular direction of the punch, and it depends on specimen thickness and maximum principal stress criterion. During continuous loading (in tensile loading), the continuous separation was noticed along the crack surface. When the stiffness (δ) of the material is greater than the crack stiffness (δ_o), the traction occurs. The traction is a

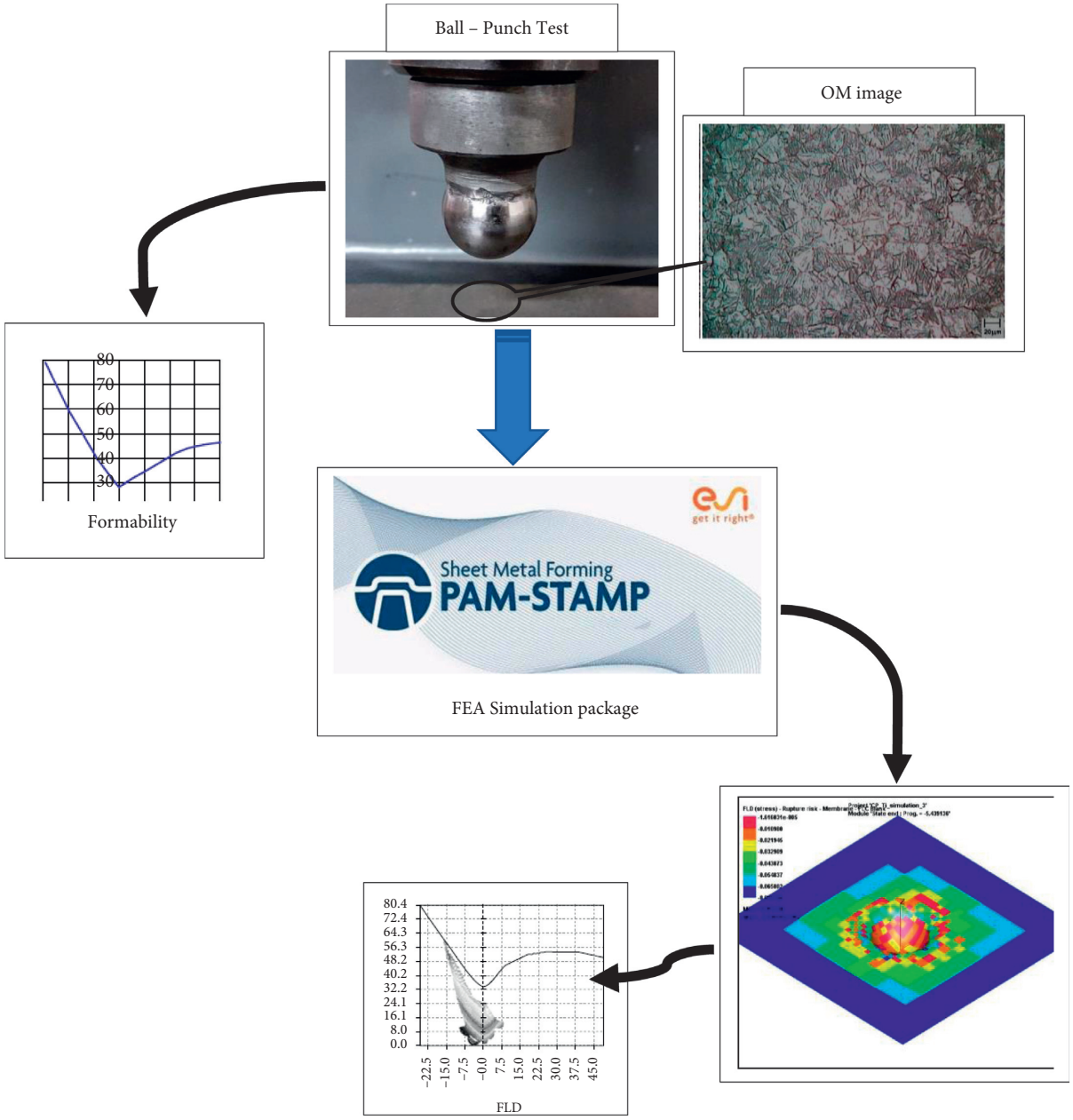

Figure 1: Work plan of the CP-Ti alloy formability study.

Table 2: The standard parameters and specifications for the ball-punch tester.

Sl. no.	Description	Value
1	Stroke of punch	5 mm/min to 20 mm/min
2	Diameter of the punch ($d1$)	20 mm
3	Inside corner radius of die ($R2$)	0.75 mm
4	Outside corner radius of die ($R1$)	0.75 mm

plastic deformation of a material in all coordinate (multi-direction) induced due to mechanical force. It has been reported that the doom fracture and the crack propagation depend on the materials properties [18].

Furthermore, the microstructural analysis is carried out on the fractured samples. The microstructure of the CP-Ti material before and after mechanical loading is recorded under a high-end metallurgical microscope and displayed in Figure 6. It is clear that the CP-Ti material used for the mechanical loading (ball-punch deformation test) is having an austenitic structure. At the same, on mechanical loading, the CP-Ti material has been deformed and the crack is initiated. The microstructure observed near to the separation (crack) is identified with the deformed grain structure. It has

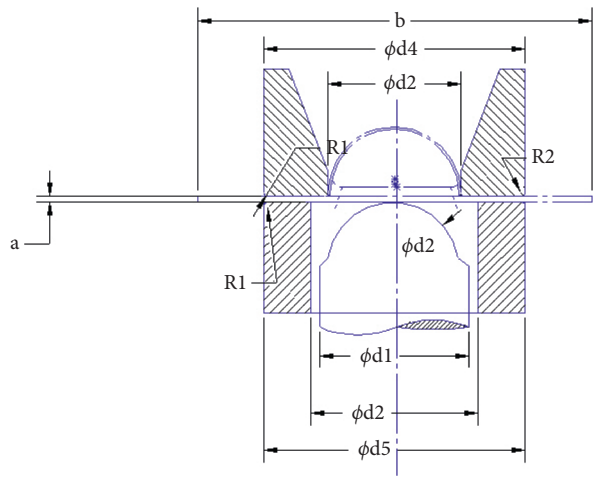

Figure 2: Schematic representation of ball-punch (Erichsen cupping) test methodology.

Table 3: Physical and mechanical properties of CP-Ti material.

Properties	Range	Units
Yield load	kN	3.2
Max. load	kN	4
Yield stress	MPa	269
U.T.S	MPa	336
% of elongation	%	52.28
Poisson's ratio	—	0.37
Modulus of elasticity	GPa	105
Coefficient of linear expansion		8.4×10^{-6}/K

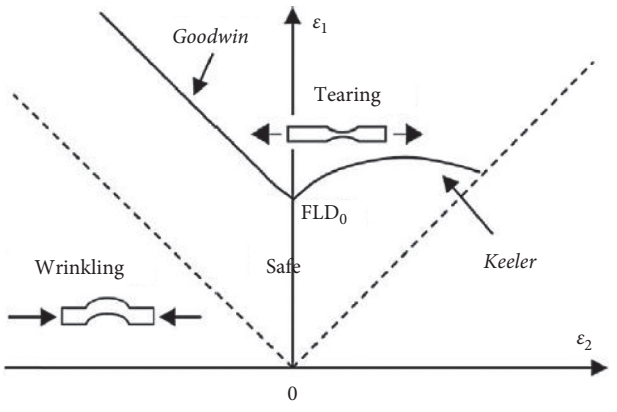

Figure 3: Fundamental representation sketch of forming limit diagram representing strains and different regimes.

also caused mechanical detachment between the grain traction. The rate of crack depends up on the ball-punch load coatings and the material thickness. During the loading, the material inclined to mechanical strain and further loading will induce the material to cracking. This is called tearing due to tension load and the deformed material with different regimes.

In continuation to metallurgical and mechanical observations on CP-Ti deformation, finite element analysis is carried out. To study the stress and strain rate on deformed material, the deformability diagram predicted through PAM STAMP™ numerical analysis software is used. With the same load condition, the material is simulated for stress and strain induced on ball-punch (cupping) test. The deformability of the material will indicate the major issues such as wrinkle, stretching, surface waviness, and insufficient formability from the analysis. Figure 7 illustrates the FLD graph plotted for strain developed from the simulation results and to locate points on different regimes for better understanding. The deformability rate of the material is recorded from the analysis and it is reported with respect to the axis coordinates. The results are as minor strain on abscissa (x-coordinate) and major strain on vertical axis (y-coordinate). From the cupping test, the fracture zone is indicated with dark spots over the deformed zone. The variations in the deformability is indicated with different color marks. The deformation of the material is as visualized in the photo image (Figures 4 and 5). Figure 8 shows the simulated ball-punch deformed area and strain distributed zone. It is clear to confirm that the center of the circular area has maximum strain and the rate recorded in the FLD diagram. Inset shows the maximum cupping height produced in the simulation. While comparing the results with standard FLD boundaries, the CP-Ti material is prone to some strain points above the Keeler line indicating material failure due to tearing. There are no spots around the Wrinkling or Good line regions. The test material has a major spot between the safe and Keeler line indicating the subregions are under safe

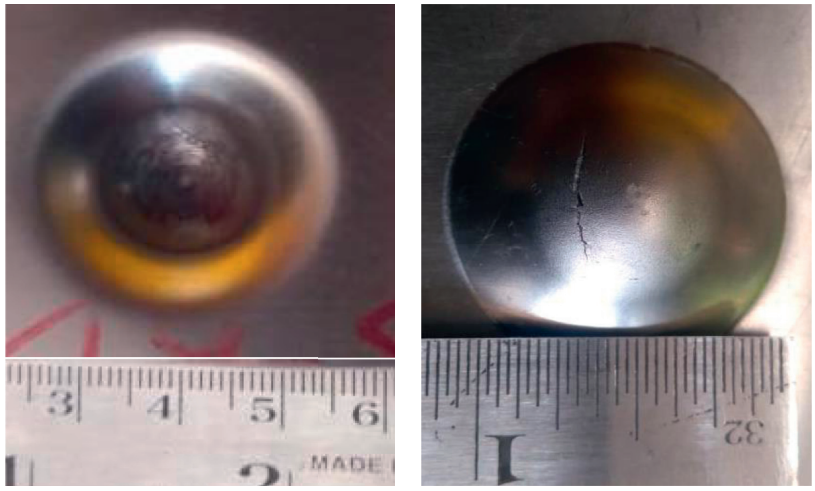

(a) (b)

Figure 4: Photo image of the CP-Ti material after ball-punch mechanical deformation. (a) Back view. (b) Front view.

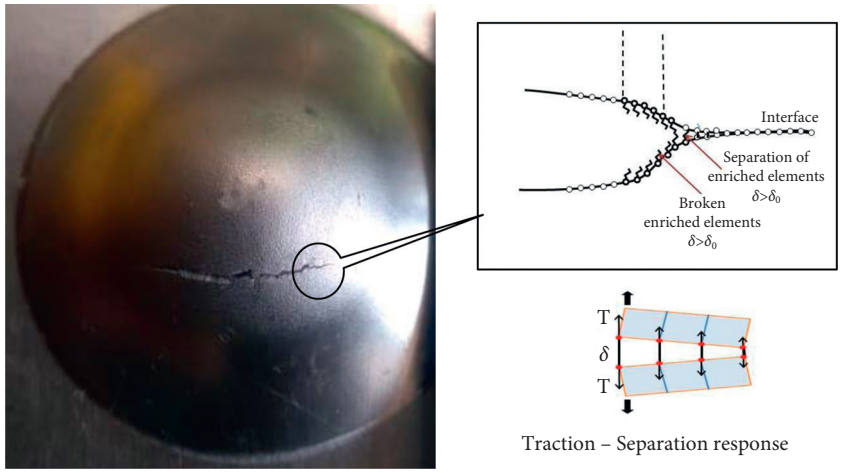

Figure 5: CP-Ti material to illustrate the traction-separation during mechanical loading.

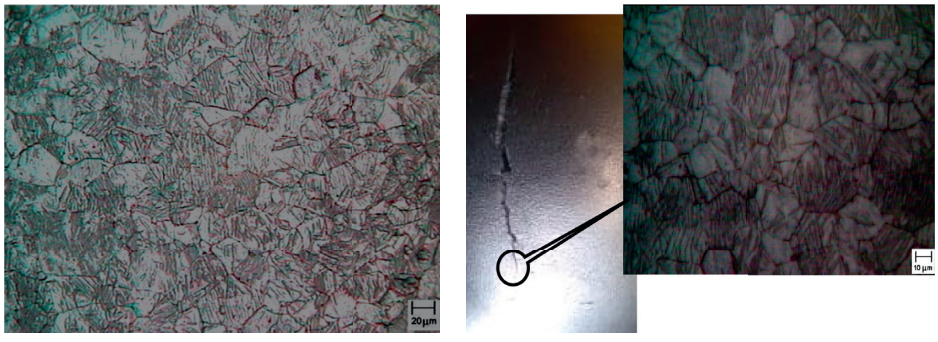

(a) (b)

Figure 6: Microstructural changes in CP-Ti sample before and after deformation. (a) Original microstructure. (b) Deformed microstructure.

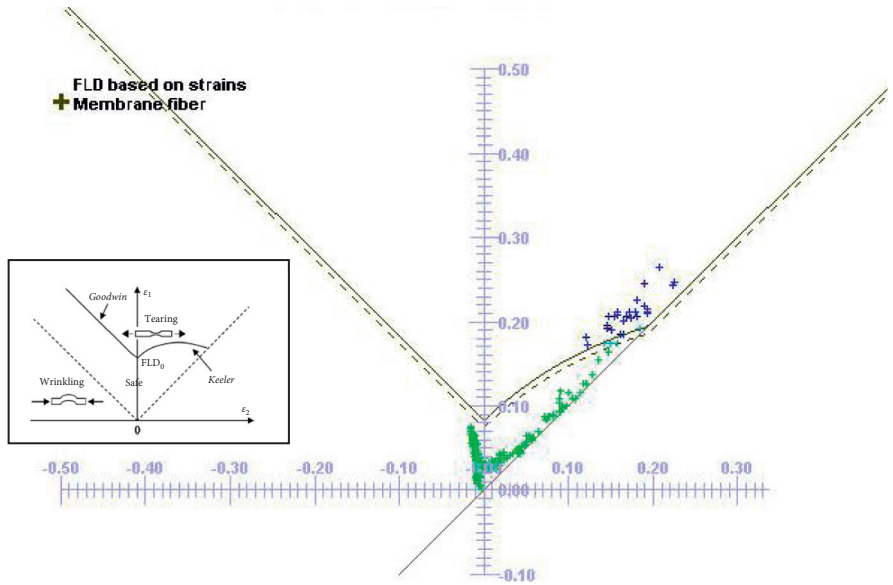

Figure 7: Graph to represent the strain developed on CP-Ti material induced while testing through formability limit diagram (FLD).

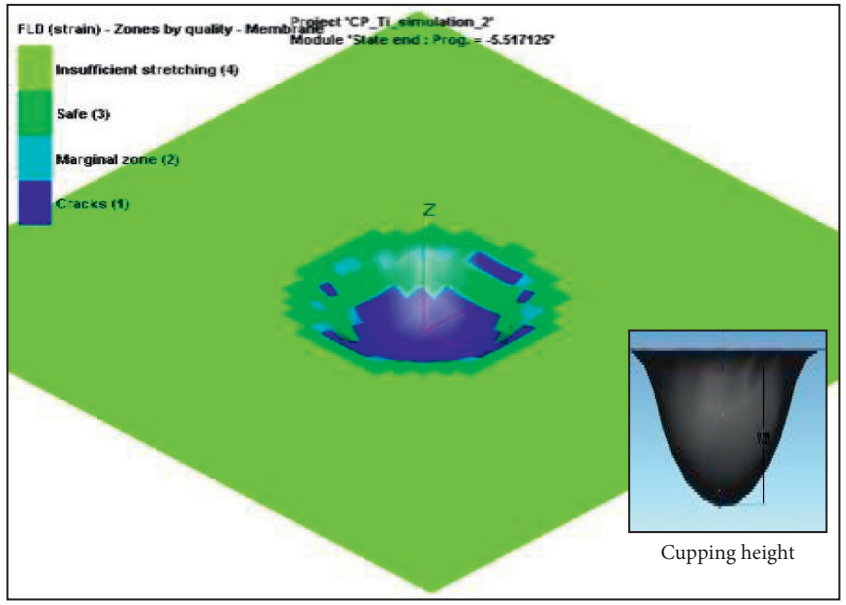

Figure 8: Simulated results indicating the FLD strain zones recorded after ball-punch test.

conditions. As a result, the numerical analysis of the material deformed and the tearing revealed to be similar with the experimental data.

Inference made on strain development: the simulation is also carried out to study the stress development during the same process. Figure 9 shows the FLD diagram with stress concentration of CP-Ti material during the ball-punch test. The spots are identified very close to Keeler line indicating the stress developed while material failure. During punching, the strain found more and continued to surface tear at the top of doom. At the same region, the FLD diagram indicates that the stress has been aggregated over the Keeler line with dense spots. Figure 10 shows the stress distribution on deformed area of ball-punch test sample results achieved through PAM STAMP™ simulation software. Red color indicates the maximum stress induced at the top of cup doom and found reducing in adjunct area of the sample with different colors of representation. As discussed above, the traction cum separation during tensile shear observed on the test sample is confirmed with the simulated results. From the experimental analysis and simulation method, the cupping height of the deformed material is measured for comparison. Three sets of experiments were done under the same test condition and simulation was carried out thrice for repeatability. The average results obtained for the analysis is tabulated in Table 4. The average cupping height of the deformed materials from the experiments and simulation are as 8.69 mm and 8.48 mm, respectively. The difference in

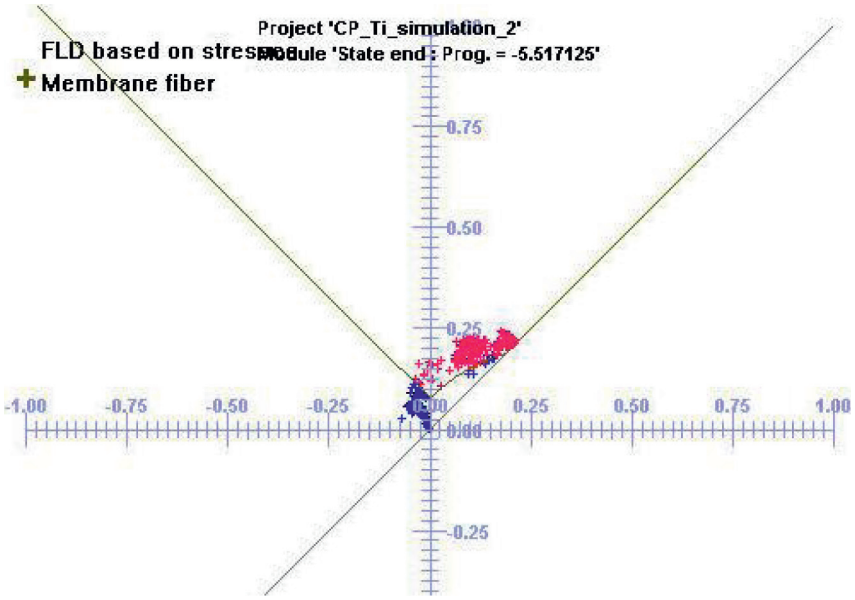

Figure 9: Graph to represent the stress developed on CP-Ti material induced while testing through formability limit diagram (FLD).

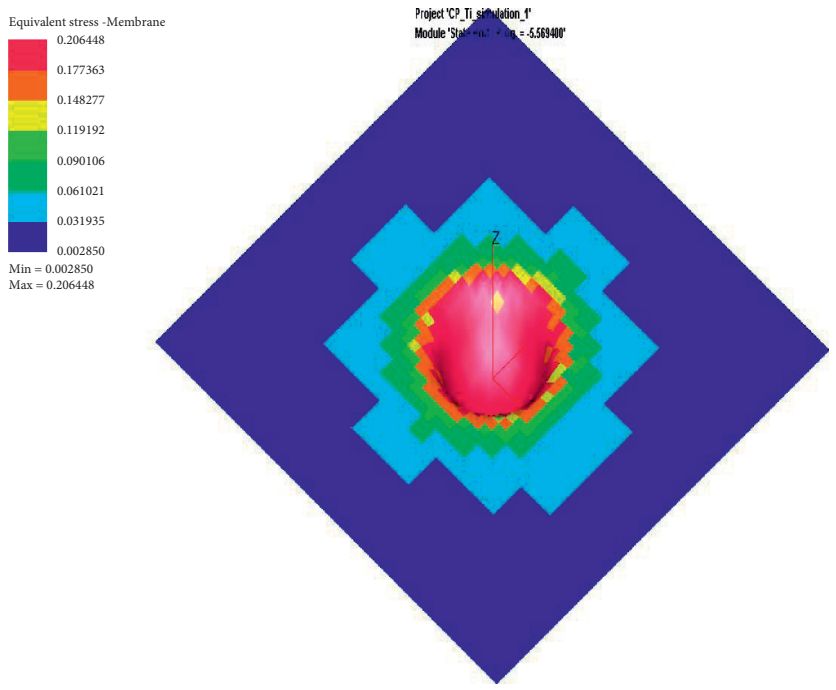

Figure 10: Simulated results indicating the stress distribution over the FLD zones recorded after the ball-punch test.

Table 4: Cupping test results from experiments and simulation.

Materials	Ball-punch test	Exp value (mm)	Sim value (mm)	Difference (mm)
CP-Ti	Cup height	8.69	8.48	0.21

cup height for experiments and simulation is 0.21 mm. It specifies that the formability value is similar in both the tests. Therefore, the same procedure can be used to study the deformation of the CP-Ti material with variation sections and materials composition.

4. Conclusions

The research presents the experimental investigation through the ASTM E643 ball-punch deformation test on CP-Ti material. Furthermore, for investigation, the results

are compared with simulation of the same experiments performed in PAM STAMP^{TM} simulation software. It has been confirmed that the CP-Ti alloy is perfect to deform under mechanical loading. During loading, the maximum height of the cupping found 8.69 mm in physical setups and surface fracture at the top of doom. The difference in cup height for experiments and simulation is 0.21 mm. The fracture is noticed perpendicular to ball-punch axis creating tensile load. The continuous tensile load has induced the grains to detach from each other and cause the adjunct layer to become vulnerable. The rate of stress and strain developed during deformation was found to be aggregated over the top of doom. The same has been confirmed from the simulation package, and FLD diagram has been drawn. The results achieved from mechanical and virtual analysis are similar to compare. Therefore, the proposed technique can support to study the behavior of the material using ball-punch deformation for different sections and is quite informative to report the quality of the material. [19].

Data Availability

No data were used to support the findings of the study.

Conflicts of Interest

The authors declare that they have no conflicts of interest.

Acknowledgments

The authors thank the MIDHANI management for providing commercially pure titanium (CP-Ti) material for this research work.

References

[1] M. Yamada, "An overview on the development of titanium alloys for non-aerospace application in Japan," *Materials Science and Engineering*, vol. 213, no. 1-2, pp. 8–15, 1996.

[2] M. J. Jackson and W. Ahmed, "Titanium and Titanium Alloy Applications in Medicine," *Surface Engineered Surgical Tools and Medical Devices*, pp. 533–576, Springer, Boston, MA, 2007.

[3] R. Hariharan, R. Raja, R. J. Golden Renjith Nimal, M. R. A. Refaai, S. Ravi, and L. A Haiter, "Characterization of TiZrN and TaZrN nano composite multilayer coating deposited via RF/DC magnetron sputtering on AISI4140 steel," *Advances in Materials Science and Engineering*, vol. 2021, Article ID 8273708, 10 pages, 2021.

[4] L.-C. Zhang and L.-Yu Chen, "A review on biomedical titanium alloys: recent progress and prospect," *Advanced Engineering Materials*, vol. 21, no. 1- 29, Article ID 1801215, 2019.

[5] A. K. Sachdev, K. Kulkarni, Z. Z. Fang, R. Yang, and V. Girshov, "Titanium for automotive applications: challenges and opportunities in materials and processing," *Journal of Occupational Medicine*, vol. 64, no. 5, pp. 553–565, 2012.

[6] M. Manish Kumar, S. Prakash Rao, and S. P. Jani, "Design and analysis of aero fin blades utilized in cargo aero plane," *Materials Today Proceedings*, vol. 45, pp. 1939–1944, 2021.

[7] C.-P. Jiang and Z. H. Huang, "Finite element modeling of grain size effect on the mechanical properties and deformability of titanium alloy in equal channel angular pressure," *Key Engineering Materials*, vol. 661, pp. 91–97, 2015.

[8] "Prediction of forming limit curve for pure titanium sheet," *Transactions of Nonferrous Metals Society of China*, vol. 28, no. 2, pp. 319–327, 2018.

[9] U. K. Ugurchiev and V. V. Stolyarov, "Deformability and microhardness of large-grain titanium alloys in rolling with pulsed current," *Journal of Machinery Manufacture and Reliability*, vol. 41, no. 5, pp. 404–406, 2012.

[10] L. Zhu, Y. D. Song, and J. Chen, "Modeling of multi-scale fatigue crack growth in titanium alloy TC4," *Iran J Sci Technol Trans Mech Eng*, vol. 45, 2020.

[11] R. Udaykumar, G. C. Reddy, and R Chandramohan, "Evaluation of erichsan number and peak load of sheet metals," *International Journal of Advanced Materials Manufacturing and Characterization*, vol. 3, no. 1, pp. 381–383, 2013.

[12] M. Singh, A. K. Choubey, and C. Sasikumar, "Formability analysis of aluminium alloy by erichsen cupping test method," *Materials Today Proceedings*, vol. 4, no. 2, pp. 805–810, 2017.

[13] M. A. Ablat and A. Qattawi, "Numerical simulation of sheet metal forming: a review," *International Journal of Advanced Manufacturing Technology*, vol. 89, no. 1-4, pp. 1235–1250, 2017.

[14] A. Wang, O. El Fakir, J. Liu et al., "Multi-objective finite element simulations of a sheet metal-forming process via a cloud-based platform," *International Journal of Advanced Manufacturing Technology*, vol. 100, no. 9-12, pp. 2753–2765, 2019.

[15] C. Schwindt, F. Schlosser, M. A. Bertinetti, M. Stout, and J. W. Signorelli, "Experimental and Visco-Plastic Self Consistent evaluation of forming limit diagrams for anisotropic sheet metals: an efficient and robust implementation of the M-K model," *International Journal of Plasticity xxx*, vol. 73, 2015.

[16] X. Ma, F. Li, J. Li, Q. Wang, Z. Yuan, and Y. Fang, "Analysis of forming limits based on a new ductile damage criterion in St14 steel sheets," *Materials and Design*, vol. 68, pp. 134–145, 2014.

[17] T. Altan and A. E. Tekkaya, *Sheet Metal Forming Fundamentals*, ASM International, Geauga, 2012.

[18] J. M. Sim and Y. S. Chang, "Crack growth evaluation by XFEM for nuclear pipes considering thermal aging embrittlement effect," *Fatigue and Fracture of Engineering Materials and Structures*, vol. 42, pp. 1–17, 2018.

Hindawi
Advances in Materials Science and Engineering
Volume 2022, Article ID 9349847, 9 pages
https://doi.org/10.1155/2022/9349847

Research Article

Experimental Investigation on Tribological Behaviour of AA6066: HSS-Cu Hybrid Composite in Dry Sliding Condition

T. Sathish,[1] **L. Natrayan**,[1] **S. Prasad Jones Christydass**,[2] **S. Sivananthan**,[3] **R. Kamalakannan**,[4] **V. Vijayan**,[5] **and Prabhu Paramasivam**[6]

[1]*Department of Mechanical Engineering, Saveetha School of Engineering, SIMATS, Chennai 602105, Tamilnadu, India*
[2]*Department of ECE, K. Ramakrishnan College of Technology, Trichy, Tamilnadu, India*
[3]*Department of Mechanical Engineering, K. Ramakrishnan College of Engineering, Samayapuram, Trichy 621112, Tamilnadu, India*
[4]*Department of Mechanical Engineering, M. Kumarasamy College of Engineering, Karur, Tamilnadu, India*
[5]*Department of Mechanical Engineering, K. Ramakrishnan College of Technology, Trichy, Tamilnadu, India*
[6]*Department of Mechanical Engineering, College of Engineering and Technology, Mettu University, Metu 318, Ethiopia*

Correspondence should be addressed to T. Sathish; sathish.sailer@gmail.com, L. Natrayan; natrayanphd@gmail.com, and Prabhu Paramasivam; prabhuparamasivam21@gmail.com

Received 8 November 2021; Revised 18 January 2022; Accepted 20 January 2022; Published 3 February 2022

Academic Editor: Temel Varol

Copyright © 2022 T. Sathish et al. This is an open access article distributed under the Creative Commons Attribution License, which permits unrestricted use, distribution, and reproduction in any medium, provided the original work is properly cited.

Aluminum is among the most preferred materials based on the desired properties. This investigation focused on to evaluate the wear rate of the AA6066 aluminium alloy composite by using pin-on-disc apparatus. The composites were created with three materials such as AA6066 alloy, high-speed steel, and copper which have a volume percentage variation of 92%, 5%, and 3%, respectively. These three parameters were considered for the experimental results of the wear rate such as load applied, sliding speed, and sliding distance. Experimental results of the composites were compared using an applied load of 20 N, a sliding velocity of 3.0 m/s and 1800 m of sliding distance with AAHSSCu reinforced composites offering a minimum wear rate. Similarly, using a 40 N applied load, the minimum wear rate is obtained. Further increasing the applied load to 60 N with 600 m of sliding distance provided a lower wear rate. The various graphical representations such as three-dimensional surface plots, contour plots, and bar charts were used for the experimental results. Wear rate consequences were expressed individually compared based on the considered parameters. Experimental results were having the reliability of nearly ninety-one percentage with only wear rate being focused. Finally, an optimized wear rate is obtained at the sliding distance of 1200 m with an applied load of 40 N and a spindle speed of 3 m/s.

1. Introduction

In recent days, composites have made major contributions in various regions of the world such as various industrial applications, different home appliance-based products, and different places of usage such as metal matrix composites, reinforcement composites, and fiber composites. In automobile industries, as well as any other industry, the wear rate properties are prepared in every material to increase their life and enhance the wear rate. Revankar et al. [1] absolutely explained about the augmentation of the wear resistance property in the titanium alloy with the aluminium alloy by using the process of ball burnishing. They use ANOVA and ANOM methods for the result comparison with the three different parameters. Various SEM images and comparative images were used to explain the results.

Guleryuz and Cimenoglu [2] described the modification of the surface for the wear resistance capacity with different experimental and result-orientated plots. Borgioli et al. [3] completely explained the various improvement techniques based on the wear resistance through thermal oxidation in the Ti-6Al-4V. Shibe and Chawla [4] undoubtedly reviewed, with the help of different articles from different time periods, about the enhancement of the wear rate through the hard

facing method. They completely provided the details about the different wear accruing reasons as a mechanism of the different types of wear and the various advantages and disadvantages based on their results. Bhushan and Gupta [5] explained that wear is the removal of the materials when the two different or the same materials are in solid contact together. This material removal rate is also known as the wear rate. There are so many factors that were considered for the wear rate, but decreasing the wear rate leads to an increase of the material life. High-speed steel and copper have higher wear resistance when compared with the aluminium alloy. So, some of the percentage of these materials were added to the composite specimens. Mishra and Srivastava [6] completely explained the wear property analysis in the Al 6061 aluminium alloy with the silicon carbide composites with different percentages of weights of both particles through the stir casting technique with the traditional standards. They also discussed about the working on the pin-on-disk wear tester with a neat sketch for the measurement of the wear rate on the specimens.

Umanath et al. [7] flatteringly discussed about the hybrid MMC participation in the recent reinforced MMC of various materials or alloys to influence both the materials merits and the desired properties of them in a greater manner. Das et al. [8] and Mishra et al. [9] evidently pointed out, commencing their investigation, that the distribution of the reinforcement phase, fraction of volume, positioning, shape, and sizes of composite elements have a considerable impact on the achievable development in the characteristics. Deuis et al. [10] reviewed a number of research articles on the composites of aluminium based on wear with respect to dry sliding in different ways. It gives a clear idea about the wear testing and the methods used for the testing depend on the composites and the various parameters and their influence on the experimental outcomes. Das and Das [11] gave details regarding the composite of the alumina reinforcement with the copper alloy and sand of zircon. They only focused about the abrasive wear-based parametric associate investigation with various diagrammatic representations with the experimental results. Similarly, Yilmaz and Butoz [12] discussed about the abrasive wear with various graphical and experimental results on the aluminium oxide reinforcement with the aluminium alloy composites. Uyyuru et al. [13] mainly focused regarding the wear behavior on the composites of Al-Si-SiCp and the system of automobile pads in the condition of dry sliding. They also expressed the impact of the dry sliding on the composite properties. Acilar and Gul [14] explained about the vacuum infiltration procedure to produce the composite and the dry sliding method is used for the experiments on the wear testing of the composites. Umanath et al. [15] clearly expressed the mechanical properties, specifically tensile strength, related investigations were performed with the composites of the aluminium alloy reinforcement by means of the silicon carbides in the same way Singla et al. [16] focused about the wear rate on the same composites. Panwar et al. [17] unobtrusively explained about the importance and the influence of lubrication on the wear testing in the reinforced aluminium alloy composites. Rao and Das [18] expressed the reliability of the wear rate and coefficient by testing on machines for the composites of the aluminium alloy. Sesharao et al. [19] focused on the impact of the sliding distance on the wear rate response for the heat-treated aluminium alloy composite materials by the casting method. Wu et al. [20] explained about the impact of the particle sizes used in the composites for the mechanical behaviour. Natrayan et al. [21] reviewed and concluded from the different research articles that stir casting is a suitable method for the aluminium composite. The pin-on-disc is a suitable testing method for the wear rate. The maximum inputs considered for the wear rate testing were load applied, sliding distance, and speed. Guler et al. [22] examined the minimum wear loss by influencing the reinforcement contents of 4 vol.% graphite and 4 vol.% alumina presents in the nanocomposites. These reinforcement particles are highly involved and dominant as the wear mechanism. Guler et al. [23] revealed that the higher corrosion resistance is achieved by using a 24 hour powder milling process. When compared to unmilled and milled powder hybrid nanocomposites, the corrosion rate is obtained as 29.068 and 4.033 mpy, respectively.

Metal matrix composites are termed as reinforcement of different materials into the base material for enhancing the strength of the base material. Normally, the base material is softer than the reinforcement material. This experimental work considered the base material of AA6066 aluminium alloy with reinforced particles of high-speed steel and copper. The various compositions of the AA6066 aluminium alloy with copper and high-speed steel were created. The wear rate of the composite specimens was measured by a wear tester such as the pin-on-disk method [24]. Similarly, the wear rate of the pure AA6066 alloy specimens was identified with the same experimental arrangement. Then, the comparison with both pure alloy and composite specimens was created to realize the impact of the composite and suitable machining parameters for the desired wear rate.

2. Experimental Procedure

Al 6066 has the compositions of 0.9–1.8% of silicon, 0.8 to 1.4% of magnesium, 0.7–1.2% of copper, 0.6–1.1% of manganese chromium have 0.4%, and the remaining was accompanied by pure aluminium alloy [25]. The AA6066 aluminium alloy was used as the microparticles. Similarly, the high-speed steel and the copper material were also used as the microparticles from the market. The taken materials were tested for the initial parameters of the material like microscopic testing for the material confirmation. Then, the particles were mixed in the propositions of volume as ninety-two percentage of the pure aluminium alloy of AA6066 with five percentage of high-speed steel and three percentage of copper.

The stir casting process is considered for this experimental work to prepare the hybrid composites. The base material and the reinforced particles are taken at different weight percentages (92% of AA6066, 5% of HSS, and 3% of Cu) and preheated in the furnace. Furthermore, the preheated reinforced particles are poured into the base material and maintained at 400 rpm of stirring speed to

achieve uniform mixing. Finally, the mixed molten material is poured into the selected die and given some time for cooling.

The specimen has a 20 mm diameter and a length of 110 mm. Similarly, the pure AA6066 alloy specimen was also prepared using the same method and same dimensions of the composite specimen preparation for the comparison perseverance [26–28].

The specimens were collected and cleaned manually, and then the specimens were visually inspected. The damaged and cracked specimens were rejected, and the specimens with a clear surface and without defects were selected for the investigation [29–31]. Then, the prepared composite specimen was named as AAHSS Cu based on the combinations of all the materials used in the composite. The pure AA6066 aluminium alloy specimen was mentioned as AA based on the material available on the composite. This flow of specimen preparation and testing is mentioned in Figure 1(a) as a flow chart. Then, the composite material and the pure aluminium material were tested in the traditional wear testing method as pin-on-disc, as referred to by the various references with high accuracy [32].

Specifications of the pin-on-disc equipment used are shown in Figure 1(b), in which the disc is 8 mm thick and 165 mm in diameter, 10 to 200 N of applied load range, 200 to 2000 rpm of rotation speed, and up to 2000 μm of wear measurement range with the lever system for the load. Initially, the AA6066 specimen is taken, and the weight is measured before the starting the experiment. Then, the specimen is fixed in the holder of the pin to strengthen the disc. Then, the load is applied on the load pan. The sliding distance is fixed by the adjustable sliding distance arrangement in the middle of the equipment. The sliding speed can be fixed using the digital meter. The time taken for the setup is fixed at 360 seconds for all the experiments by the timer.

There are three different parameters that were considered for the investigational comparison such as sliding distance, load applied, and the speed of sliding, as mentioned in Table 1. The applied load started from 20 N with a 20 N incremental value up to 60 N, the sliding distance started from 600 m with an incremental value of 600 m up to 1800 m, and the speed of sliding started from 1.5 m/s with 1.5 m/s incremental values. Then, the experiments were conducted, and the corresponding results from the digital output values such as wear rate were taken as per Table 1 and is performed for the AA6066 specimens. Twenty-seven specimens were created and tested under the conditions of these three parameters.

Similarly, the composite specimens of the AAHSSCu composite are taken in the pin holder and kept there to touch the disc. Then, the load is applied on the load pan with variations of 20 N, 40 N, and 60 N. Also, the sliding distance can be fixed at 600 m, 1200 m, and 1800 m by the adjustable sliding distance arrangement on the equipment. At last, the sliding speed is given as 1.5 m/s, 3.0 m/s, and 4.5 m/s by the digital input. The time taken for the testing is fixed at 360 seconds. Then, the wear rate of the AAHSSCu composites was measured as per the conditions mentioned in Table 1.

3. Results and Discussion

The experimental results from the traditional pin-on-disc method of wear rate were measured carefully and plotted for easy understanding. Figure 2 mentions the bar chart for the applied force of 20 N for both pure AA specimens and AAHSSCu composite specimens with respect to the three different sliding speeds. Wear rate variations start from a minimum range of 0.000003 mm^3/Nm and a maximum range of 0.00015 mm^3/Nm for the sliding distance of 600 to 1800 m. Figure 3 shows the contour plot for the applied force of 20 N for the pure AA specimens and the AAHSSCu composite specimens with respect to the three different sliding distances of 600 to 1800 m. Wear rate variations start from a minimum range of 0.000003 mm^3/Nm and a maximum range of 0.00014 mm^3/Nm for the sliding speeds from 1.5 m/s to 4.5 m/s. The maximum intensity of the wear rate is achieved at the 4.5 m/s of spindle speed of the AA specimen when compared to other conditions.

The measured wear rate can be represented as a bar chart with respect to the sliding distance for the applied load of 20 N for both AA specimens and AAHSSCu with three different spindle speeds were clearly mentioned. The minimum wear rate was achieved at 1800 m of sliding distance, at 1.5 m/s of the sliding speed at 20 N applied load of the AAHSSCu composite specimen.

For the applied force of 40 N for both pure AA specimens and AAHSSCu composite specimens with respect to the three diverse sliding speeds as shown in the bar chart in Figure 4. Wear rate variations start from a minimum range of 0.000002 mm^3/Nm and a maximum range of 0.00016 to 0.00018 mm^3/Nm for a sliding distance of 600 to 1800 m. Figure 5 expresses both pure AA specimens and AAHSSCu composite specimens' contour plots for the applied force of 40 N concerning the three diverse sliding distances of 600 to 1800 m. Wear rate variations started from a minimum range of 0.000003 mm^3/Nm and a maximum range of 0.00018 mm^3/Nm for the sliding speeds from 1.5 m/s to 4.5 m/s. The maximum intensity of the wear rate is achieved for the AA specimen at 4.5 m/s of spindle speed.

For both AA specimens and AAHSSCu, with three different spindle speed measured, the wear rate can be represented as a bar chart regarding the sliding distance for the applied load of 40 N, as clearly mentioned in Figure 5. The smallest wear rate was accomplished at a sliding distance of 1800 m, at a sliding speed of 1.5 m/s at a 40 N applied load of the AAHSSCu composite specimen.

Figure 6 demonstrates the bar chart for the applied force of 60 N for both pure AA specimens and AAHSSCu composite specimens with respect to the three different sliding speeds. For the sliding distance of 600 to 1800 m wear rate variations started from a minimum range of 0 to 0.000005 mm^3/Nm and a maximum range of 0.00035 to 0.00040 mm^3/Nm. For both pure AA specimens and AAHSSCu composite specimens, with respect to the three different sliding distances of 600 to 1800 m, is represented by the contour plot in Figure 7 for the applied force of 60 N. Wear rate variations started from a minimum range of 0.000003 mm^3/Nm and a maximum range of

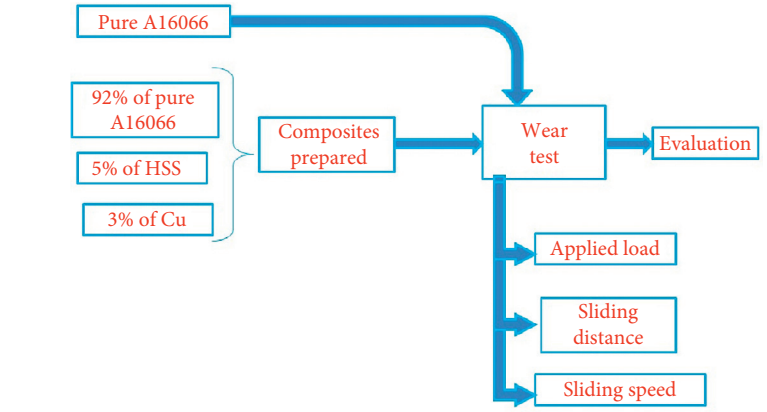

(a)

(b)

Figure 1: (a) Experimental methods for the comparison and (b) pin-on-disk wear tester.

Table 1: Factors considered for the experiments.

Sl. No.	Sliding distance (m)	Applied load (N)	Sliding speed (m/s)
1	600	20	1.5
2	1200	40	3
3	1800	60	4.5

0.00010 mm^3/Nm for the sliding speeds from 1.5 m/s to 4.5 m/s. The maximum intensity of the wear rate is achieved at the 1.5 m/s spindle speed of the AAHSSCu composite specimen when compared to other conditions. The smallest wear rate was obtained at the sliding distance of 600 m, at a sliding speed of 1.5 m/s at a 60 N applied load of the AAHSSCu composite specimen.

A minimum sliding speed of 1.5 m/s and a maximum sliding distance of 1800 m offered minimum wear rate. A minimum wear rate was recorded by a homogeneous mixture of base material and reinforced particles through the casting process. In the casting process, the reinforced particles were highly melted and blended uniformly. Even under the influence of the maximum level of load as well as sliding distance, the minimum wear rate was recorded.

Wear rate comparison based on the sliding distances with respect to the spindle speeds for the 20 N of the applied load, as shown in Figure 8. The maximum wear rate is reached at 4.5 m/s of spindle speed, and the minimum wear rate can be achieved at 1.5 m/s of spindle speed

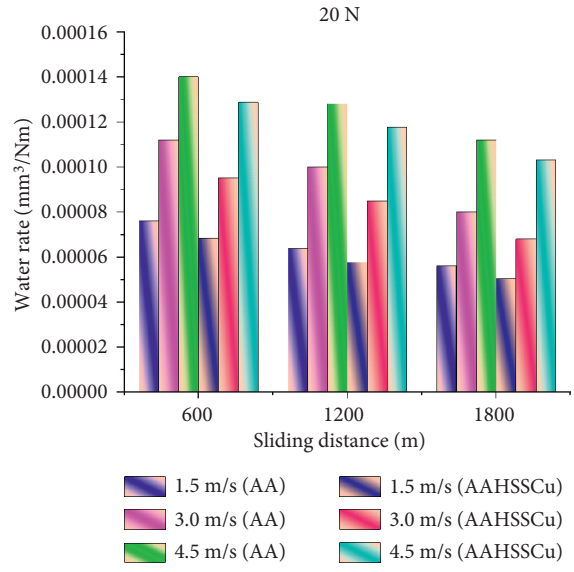

Figure 2: Wear rate (mm^3/Nm) comparison for a 20 N applied load impact as a bar chart.

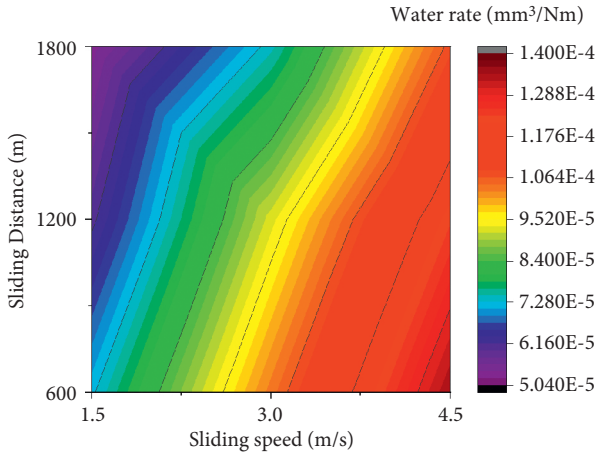

Figure 3: Wear rate (mm^3/Nm) comparison for a 20 N applied load impact as a contour plot.

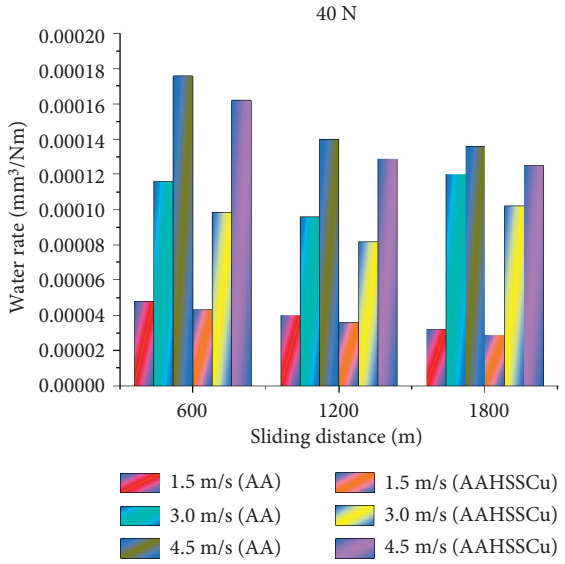

Figure 4: Wear rate (mm^3/Nm) comparison for a 40 N applied load impact as a bar chart.

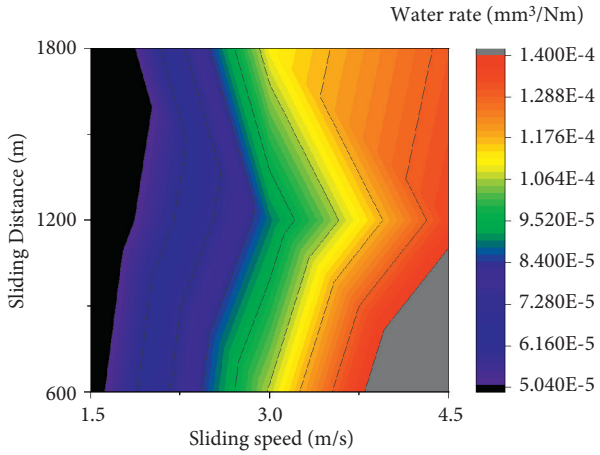

Figure 5: Wear rate (mm^3/Nm) comparison for a 40 N applied load impact as a contour plot.

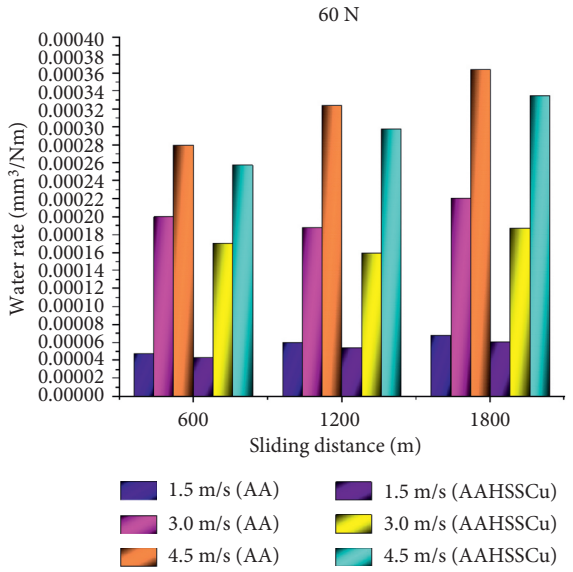

Figure 6: Wear rate (mm^3/Nm) comparison for a 60 N applied load impact as a bar chart.

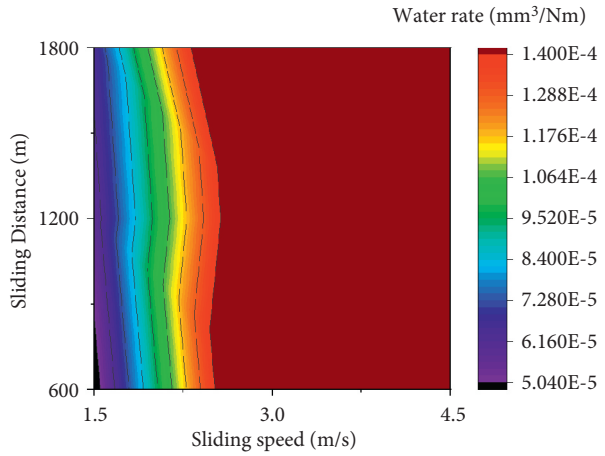

Figure 7: Wear rate (mm^3/Nm) comparison for a 60 N applied load impact as a contour plot.

at a sliding distance of 1800 m at 20 N of the applied load. The wear rate evaluation was constructed on the sliding distances with respect to the spindle speeds for the 40 N of the applied load mentioned in Figure 9. The supreme wear rate is reached at 4.5 m/s of spindle speed over 600 m of sliding distance, and the slightest wear rate can be attained at a sliding distance of 1800 m with 1.5 m/s of spindle speed at 40 N of the applied load. For the 60 N of the applied load-based wear rate evaluation based on the sliding distances with respect to the spindle speeds is plotted in Figure 10. 4.5 m/s of spindle speed and 1800 m of sliding distance reached the highest wear rate, and the smallest amount of wear rate can be attained at a sliding distance of 600 m with 1.5 m/s of spindle speed at a 60 N of the applied load. There is no separate comparison provided for the spindle speed because the abovementioned comparisons have the spindle speed relation included in the plot. All

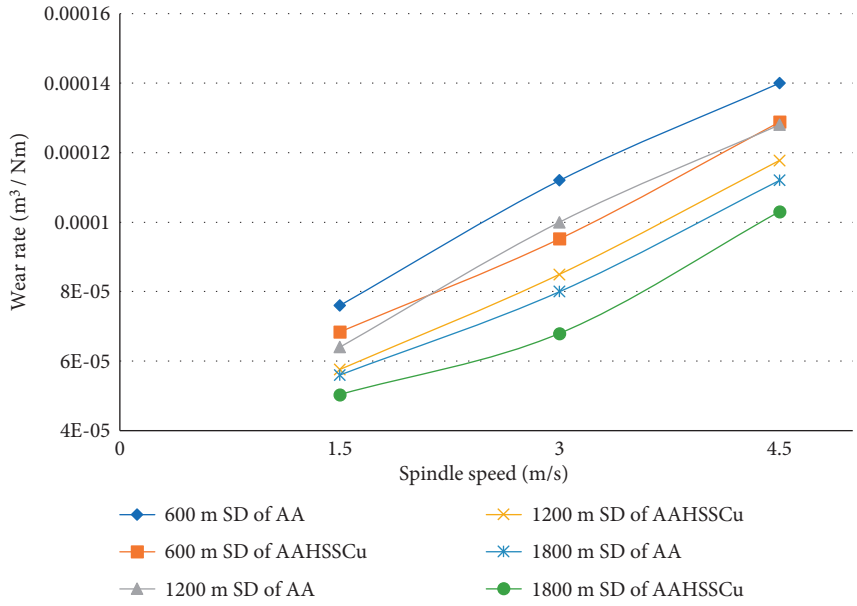

Figure 8: Sliding distance comparison on a 20 N applied load.

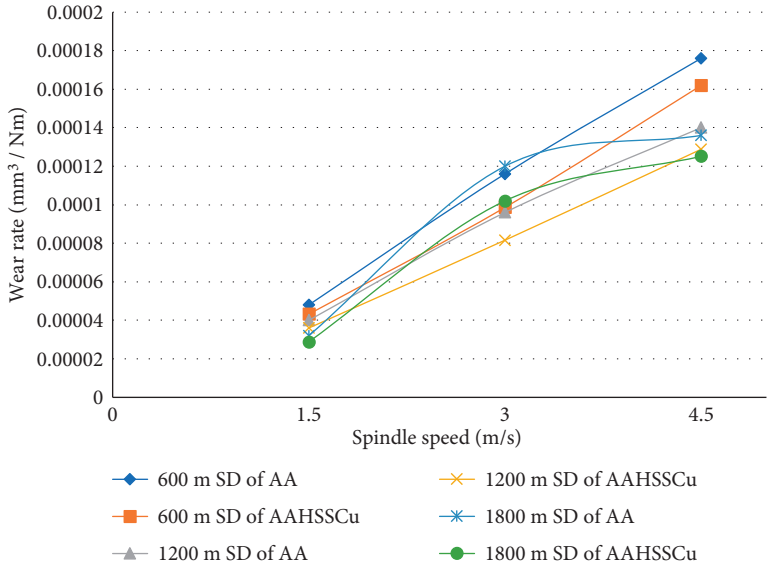

Figure 9: Sliding distance comparison on a 40 N applied load.

these figures show the relation that the wear rate of the composite has the greatest results when compared with the pure aluminium alloy. As the sliding distance increased, the coefficient of friction also increased uniformly. Compared to the hybrid composites, the base alloys possess a higher coefficient of friction. By increasing of the reinforcement percentage to the base material, the coefficient of friction was reduced moderately.

Figure 11 illustrates the SEM image of the wear test specimen under the load of 60 N. Figure 11(a) presents the before wear test specimen, which clearly shows the reinforced particles distributed to the base material such as aluminium alloy. Figure 11(b) shows after wear test specimen where some defects were present on the surface of the specimen such as delamination, groove, and cavity under involving of 60 N loads.

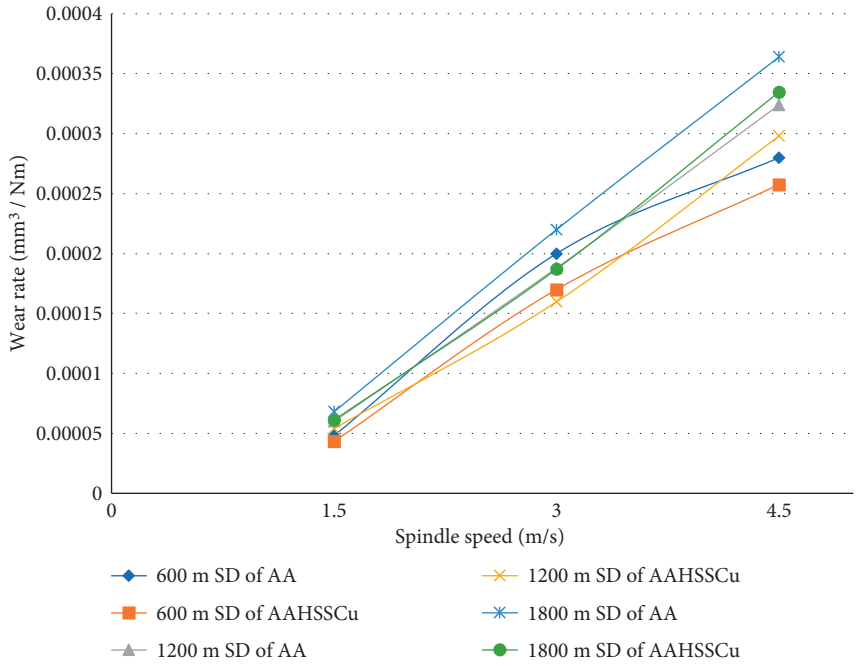

Figure 10: Sliding distance comparison on a 60 N applied load.

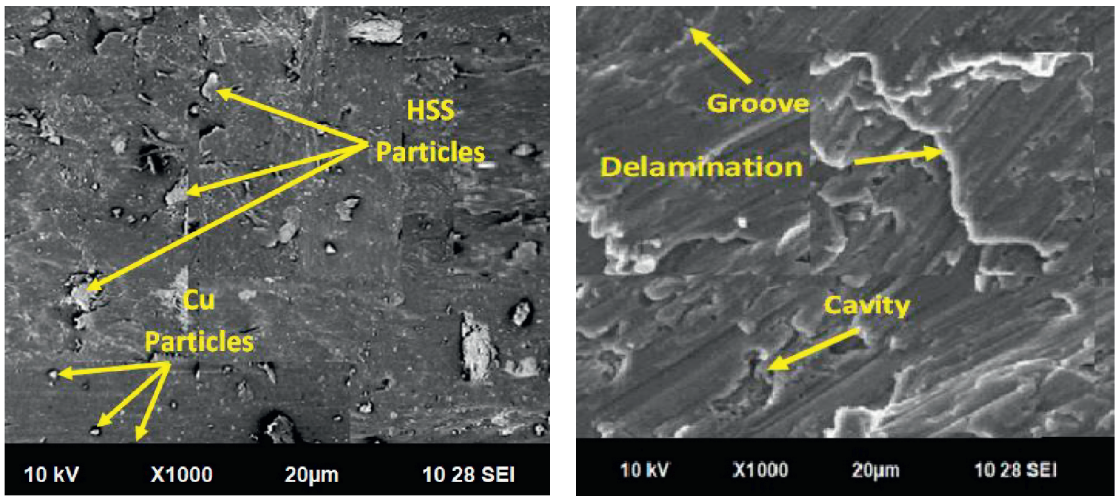

(a) (b)

Figure 11: SEM image of the worn out surface for wear specimen: (a) before the wear test specimen and (b) after the wear test on a 60 N applied load.

4. Conclusions

In this experimental study based on wear rate enhancement on high-speed steel and copper, AA6066 aluminium alloy composites were used, which produced the following results as conclusions:

(i) Enhancement of wear rate means reduction in the wear rate not augmentation in wear rate, because it should be reduced to develop the life of the material used product.

(ii) Aluminium alloy with HSS and Cu composite produced the minimum wear rate when compared with the pure aluminium specimens.

(iii) The aluminium alloy with HSS and Cu composite with a sliding distance of 1200 m and an applied load of 40 N at a spindle speed of 3 m/s produced

the minimum wear rate, so preferable parameters were studied from this investigation.

(iv) The maximum wear rate can be achieved at the AA specimens with 1800 m of sliding distance at 4.5 m/s of spindle speed at the applied load of 60 N.

(v) Wear rate variations are obtained from a minimum of 0.000002 mm^3/Nm and a maximum of 0.00016 to 0.00018 mm^3/Nm for the sliding distance of 600 to 1800 m under 20 N applied load.

(vi) In applied load, the 40 N wear rate was varied from a minimum of 0.000002 mm^3/Nm and a maximum of 0.00016 to 0.00018 mm^3/Nm for the sliding distance of 600 to 1800 m.

(vii) From an applied load 60N and a sliding distance of 600 to 1800 m, the wear rate was varied as a minimum range of 0 to 0.000005 mm^3/Nm and a maximum range of 0.00035 to 0.00040 mm^3/Nm.

Data Availability

The data used to support the findings of this study are included within the article. Should further data or information be required, request should be made to the corresponding author upon request.

Disclosure

It was performed as a part of the Employment of Mettu University, Ethiopia.

Conflicts of Interest

The authors declare that there are no conflicts of interest regarding the publication of this paper.

Acknowledgments

The authors thank Saveetha School of Engineering, SIMATS, Chennai, for the technical assistance. The authors appreciate the support from Mettu University, Ethiopia.

References

[1] G. D. Revankar, R. Shetty, S. S. Rao, and V. N. Gaitonde, "Wear resistance enhancement of titanium alloy (Ti-6Al-4V) by ball burnishing process," *Journal of Materials Research and Technology*, vol. 6, no. 1, pp. 13–32, 2017.

[2] H. Guleryuz and H. Cimenoglu, "Surface modification of a Ti–6Al–4V alloy by thermal oxidation," *Surface and Coatings Technology*, vol. 192, no. 2-3, pp. 164–170, 2005.

[3] F. Borgioli, E. Galvanetto, F. Iozzelli, and G. Pradelli, "Improvement of wear resistance of Ti-6Al-4V alloy by means of thermal oxidation," *Materials Letters*, vol. 59, no. 17, pp. 2159–2162, 2005.

[4] V. Shibe and V. Chawla, "Enhancement in wear resistance by hardfacing: a review," *Mechanica Confab*, vol. 2, no. 3, pp. 111–122, 2013.

[5] B. Bhushan and B. K. Gupta, *Handbook of Tribology: Materials, Coatings, and Surface Treatments*, McGraw-Hill, New York, NY, USA, 1991.

[6] A. K. Mishra and R. K. Srivastava, "Wear behaviour of Al-6061/SiC metal matrix composites," *Journal of the Institution of Engineers (India): Series C*, vol. 98, no. 2, pp. 97–103, 2017.

[7] K. Umanath, S. T. Selvamani, and K. Palanikumar, "Friction and wear behaviour of Al6061 alloy Al2O3P) hybrid composites," *International Journal of Engineering, Science and Technology*, vol. 3, no. 7, pp. 5441–5451, 2011.

[8] S. Das, R. Behera, A. Datta, G. Majumdar, B. Oraon, and G. Sutradhar, "Experimental investigation on the effect of reinforcement particles on the forgeability and the mechanical properties of Al MMCs," *Materials Sciences and Applications*, vol. 1, pp. 310–331, 2016.

[9] A. K. Mishra, R. Sheokand, and R. K. Srivastava, "Tribological behavior of Al6061/SiC MMCs by Taguchi's technique," *International Journal of Scientific and Research Publication*, vol. 2, pp. 1–8, 2012.

[10] R. L. Deuis, C. Subramanian, and J. M. Yellup, "Dry sliding wear of aluminium composites—a review," *Composites Science and Technology*, vol. 57, no. 4, pp. 415–435, 1997.

[11] S. Das and K. Das, "Abrasive wear of zircon sand and alumina reinforced Al-4.5wt% Cu alloy matrix composites—a comparative study," *Composites Science and Technology*, vol. 67, pp. 746–775, 2007.

[12] O. Yilmaz and S. Butoz, "Abrasive wear of Al_2O_3 reinforced aluminium based MMCs," *Composites Science and Technology*, vol. 61, pp. 2381–3239, 2001.

[13] R. K. Uyyuru, M. K. Surappa, and S. Brusethaug, "Tribological behavior of Al-Si-SiCp composites/automobile brake pad system under dry sliding conditions," *Tribology International*, vol. 40, no. 2, pp. 365–373, 2007.

[14] M. Acilar and F. Gul, "Effect of the applied load, sliding distance and oxidation on the dry sliding wear behaviour of Al-10Si/SiCp composites produced by vacuum infiltration technique," *Materials & Design*, vol. 25, no. 3, pp. 209–217, 2004.

[15] K. Umanath, S. T. Selvamani, and K. Natarajan, "Influence of silicon carbide particulate reinforcement on the tensile behaviour of Al6061 alloy composite produced by stir casting method," *Proceedings of Manufacturing*, vol. 2010, pp. 235–324, 2010.

[16] M. Singla, L. Singh, and V. Chawla, "Study of wear properties of Al-SiC composites," *Journal of Minerals and Materials Characterization and Engineering*, vol. 08, no. 10, pp. 813–821, 2009.

[17] N. Panwar, R. P. Poonia, G. Singh, R. Dabral, and A. Chauhan, "Effect of lubrication on sliding wear of red mud particulate reinforced aluminium alloy 6061," *Tribology in industry*, vol. 39, no. 3, 2017.

[18] R. N. Rao and S. Das, "Wear coefficient and reliability of sliding wear test procedure for high strength aluminium alloy and composite," *Materials & Design*, vol. 31, no. 7, pp. 3227–3233, 2010.

[19] Y. Sesharao, T. Sathish, P. Kumaran et al., "Optimization on operation parameters in reinforced metal matrix of AA6066 composite with HSS and Cu," *Advances in Materials Science and Engineering*, vol. 2021, Article ID 1609769, 12 pages, 2021.

[20] C. Wu, K. Ma, J. Wu et al., "Influence of particle size and spatial distribution of B4C reinforcement on the microstructure and mechanical behavior of precipitation strengthened Al alloy matrix composites," *Materials Science and Engineering: A*, vol. 675, pp. 421–430, 2016.

[21] L. Natrayan, M. Ravichandran, V. Dhinakaran, P. Sureshkumar, T. Jagadeesha, and W. D. Mammo, "Influence of nano graphite on dry sliding wear behaviour of novel encapsulated squeeze cast Al-Cu-Mg metal matrix composite using artificial neural network," *Journal of Nanomaterials*, vol. 2021, Article ID 4043196, 14 pages, 2021.

[22] O. Guler, H. Cuvalci, A. Canakci, and M. Celebi, "The effect of nano graphite particle content on the wear behaviour of ZA27 based hybrid composites," *Advanced Composites Letters*, vol. 26, no. 2, Article ID 096369351702600201, 2017.

[23] O. Guler, M. Celebı, R. Dalmıs, A. Canakci, and H. Cuvalci, "Novel ZA27/B_4C/graphite hybrid nanocomposite-bearing materials with enhanced wear and corrosion resistance," *Metallurgical and Materials Transactions A*, vol. 51, no. 9, pp. 4632–4646, 2020.

[24] P. Mukhopadhyay, "Alloy designation, processing, and use of AA6XXX series aluminium alloys, international scholarly research network," *ISRN Metallurgy*, vol. 2012, Article ID 165082, 15 pages, 2012.

[25] P. Samal, P. R. Vundavilli, A. Meher, and M. M. Mahapatra, "Recent progress in aluminum metal matrix composites: a review on processing, mechanical and wear properties," *Journal of Manufacturing Processes*, vol. 59, pp. 131–152, 2020.

[26] A. K. Singh, S. Soni, and R. S. Rana, "A critical review on synthesis of aluminum metallic composites through stir casting: challenges and opportunities," *Advanced Engineering Materials*, vol. 22, no. 10, Article ID 2000322, 2020.

[27] K. A. Novich, S. V. Pedersen, R. A. Borrelli, R. Christensen, and B. J. Jaques, "Synthesis of boron carbide reinforced aluminum castings through mechanical stir casting," *Journal of Composite Materials*, vol. 55, no. 16, pp. 2165–2177, 2021.

[28] S. Pan, T. Saso, N. Yu et al., "New study on tribological performance of AA7075-TiB_2 nanocomposites," *Tribology International*, vol. 152, Article ID 106565, 2020.

[29] N. K. Bhoi, H. Singh, and S. Pratap, "Developments in the aluminum metal matrix composites reinforced by micro/nano particles—a review," *Journal of Composite Materials*, vol. 54, no. 6, pp. 813–833, 2020.

[30] T. B. Rao, "Microstructural Mechanical, and wear properties characterization and strengthening mechanisms of AA7075/SiCnp composites processed through ultrasonic cavitation assisted stir-casting," *Materials Science and Engineering A*, vol. 805, Article ID 140553, 2021.

[31] P. Samal, R. K. Mandava, and P. R. Vundavilli, "Dry sliding wear behavior of AA 6082 metal matrix composites reinforced with red mud particles," *SN Applied Sciences*, vol. 2, no. 2, p. 313, 2020.

[32] K. L. Zheng, X. S. Wei, B. Yan, and P. F. Yan, "Ceramic waste SiC particle-reinforced Al matrix composite brake materials with a high friction coefficient," *Wear*, vol. 458–459, pp. 458-459, 2034.

Hindawi
Advances in Materials Science and Engineering
Volume 2022, Article ID 5144010, 9 pages
https://doi.org/10.1155/2022/5144010

Research Article

Investigation of Wear Behaviour and Mechanical Properties of Titanium Diboride Reinforced AMMC Composites

Madhan Prabhu Deva,[1] A. Parthiban,[2] B. Radha Krishnan,[3] Adisu Haile,[4] and Wubishet Degife[4]

[1]*Mechanical Engineering, Vels Institute of Science Technology and Advanced Studies, Chennai, Tamilnadu, India*
[2]*Mechanical Engineering, Vels Institute of Science Technology and Advanced Studies, Chennai, Tamilnadu, India*
[3]*Mechanical Engineering, Nadar Saraswathi College of Engineering and Technology, Theni, Tamilnadu, India*
[4]*Department of Mechanical Engineering, Wollo University, Kombolcha Institute of Technology, Ethiopia*

Correspondence should be addressed to Wubishet Degife; wubesvictory@kiot.edu.et

Received 18 September 2021; Revised 19 November 2021; Accepted 5 December 2021; Published 1 February 2022

Academic Editor: Waleed Fekry Faris

Copyright © 2022 Madhan Prabhu Deva et al. This is an open access article distributed under the Creative Commons Attribution License, which permits unrestricted use, distribution, and reproduction in any medium, provided the original work is properly cited.

The aluminium metal matrix composites (AMMCs) are preferred in automotive and aerospace industries for higher strength, weight ratio, good corrosion resistance, and also better tribological properties. This study proposed that the AA7075 alloy methodology was enhanced by stir casting with titanium diboride (TiB_2) particles at different percentages (5, 10, and 15 wt. %). The preheated titanium diboride powder is spread to the molten state AA7075 at 870°C to provide good weight resistance and delivery. The prepared composites are evaluated by wear analysis, tensile properties, hardness range, and microstructural behavior studies. Pin-on-disk and Rockwell hardness tester were used to analyze the wear behaviour and hardness level. The tensile strength and hardness have defined the strength of the proposed composite while the addition of TiB_2 particles improves the hardness and tensile stress. The findings showed that adding TiB_2 particles in the Al7075 matrix strengthened all properties compared to the Al7075 matrix. The scanning electron microscope and EDS were used to analyze the eroded surface and chemical composition of composites.

1. Introduction

The AMMCs have higher usage in the automotive and aerospace industries due to their enhanced strength and low wear. Enhanced mechanical and tribological characteristics of AMMCs are provided by adding reinforcements such as Al_2O_3, SiC, TiC, TiB_2, ZrO_2, and B_4C [1]. The AMMCs were made by the infiltration, powder metallurgy process, compocasting, and stir-casting method [2]. Many researchers used a stir-casting method to make AMMCs because of the maximum metal yield range, lower particle damage, and cost-efficiency. TiB_2 particles are highly stiff and hard and had better thermal stability range among the different ceramic strengthening particles.

The exothermic nature of the process, as well as the reduced oxidation, makes it a good candidate for wear-resistant composites [3]. Normally, the composites are made with oxide particles, carbide particles, boride particles, and nitride particles. While added, the ceramic particulate matter in different aluminium matrices significantly increased the matrix wear performance [4]. Matrix reinforcement fraction is the factor that influences the composite mechanical properties. The wear has been observed to be oxidative wear to a maximum of 800°C, and the oxidative wear has been found to dominate the wearing rate at higher temperatures. Certain scientists have found that the inhomogeneous distribution of reinforcement particles on a molten matrix results in low weight and low surface tension [5]. Preheating treatment is used to absorb gas and remove humidity and utilize any sort of surface protection, and inert gas-atmospheric alloying elements will improve the properties of the composites [6]. The particulate injection

avoided or minimised agglomeration and particulate clusters and enhanced the homogeneous atmosphere and distribution. A few researchers have prepared AA7075-TiB_2 composite and evaluated the mechanical properties. The AA7075-TiB_2 composites were synthesized by the stir-casting method with different percentages of TiB_2 (5%, 10%, and 15% wt.%), and then the quality of the composites was inspected by tribological characteristics. This paper investigated the tribological properties such as wear and microstructural characteristics of compounds AA7075-TiB_2 and investigated mechanical properties such as hardness.

2. Experimental Analysis

AA7075 alloy has been preferred as a matrix material in this study, and the chemical composition is illustrated in Table 1. An in situ reaction supported various amounts of TiB_2 (5, 10, and 15 wt.%).

The small pieces of Al7075 alloy are used for the composite's synthesis process. The quantity of matrix to be melted is measured with an additional 25% of slag. The induction crucible furnace was used to melt the aluminium alloy 7075 for 20 min with a temperature range of 850°C.

Meanwhile, TiB_2 was preheated up to 500 °C, and then, it was added uniformly into the furnace for avoiding agglomeration and clustering. The stirring process was carried out with the four-blade stirrer for 10 minutes at 500 rpm. Due to the stirring process, a vortex is formed [7].

The preheated TiB_2 particles have been fed into the furnace at proper timing intervals through a hopper which is shown in Figure 1. Approximately 750°C was regulated with continuous stirring to produce a uniform mixture. The molding mixture is formed by refreshing the mold at room temperature into rods and plates as shown in Figure 2 [8].

Figure 3 shows the processing methodology for AMMC and evaluation methods. The hardness and tensile tests were carried out for prepared specimens based on the ASTM E384-11 and ASTM E08 standards [9]. In this paper, the ASTM G99 standard was used as shown in Table 2 followed by wear test analysis of Al7075-TiB_2 composite. The surface morphological characteristics and microstructural views are analyzed to investigate how reinforced particles are mixing with matrix materials by using the scanning electron microscope (SEM) and energy dispersive spectroscopy (EDS) [10].

The components' weight was determined by density, and the theoretical densities have been obtained by the rule of mixture (ROM).

3. Results and Discussions

3.1. EDAX Testing. In Figures 4 to 6, the EDAX graph showed the aluminium and titanium peak values showing the particulate content of the composites made [11, 12]. The EDAX graph of Al7075/5% TiB_2, Al7075/10% TiB_2, and Al7075/15% TiB_2 composites shown in figures indicates the presence of aluminium and titanium particles.

3.2. Impact of Reinforcement on Tensile Strength. The tensile load is applied to create large internal tensions that can cause the material to break if they exceed its strength [13].

Table 1: Chemical constitutions of Al7075 alloy.

Constituents	Contribution
Al	90.60
Si	0.05
Fe	0.1
Cu	1.6
Mn	0.05
Mg	2.31
Cr	0.11
Zn	5.12
Ti	0.05
Ti + Zn	0.01

Figure 1: Titanium diboride.

Figure 2: Bottom pouring stir casting.

Reinforcement particle bonding will be the major focus of the internal stress distribution. The tensile strength of Al7075 composites is enhanced when the percentage of TiB_2 is increased, as shown in Figure 7.

Figure 7 shows that while adding TiB_2 particles, the tensile strength increases proportionally, increasing 242 MPa with 5% TiB_2. Therefore, it reached up to 250 MPa for 10% TiB_2. The tensile strength increases by 260 MPa at 15% TiB_2. The percentage is due to the improved linkage between the matrix TiB_2 and Al7075. The results show the TiB_2 particles can increase the tensile stress level, but it may

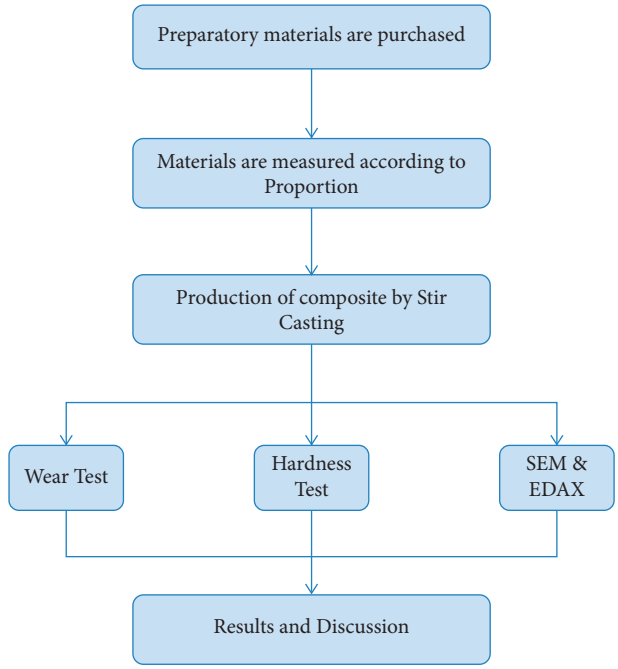

Figure 3: Processing methodology.

Table 2: Sample preparation.

Sample no.	Contribution	Aluminium (g)	TiB_2 (g)
1	Al7075 95% and TiB_2 5%	120.73	10.22
2	Al7075 90% and TiB_2 10%	114.38	20.44
3	Al7075 85% and TiB_2 15%	108.02	30.66

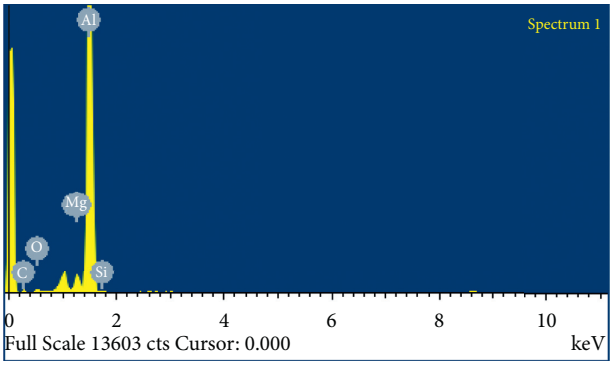

Figure 4: EDAX graph of Al 7075 95% and TiB_2 5%.

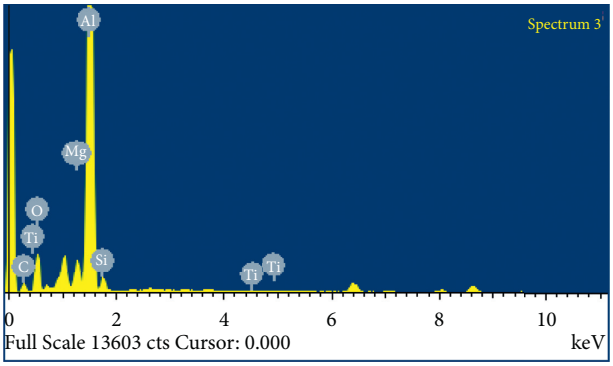

Figure 5: EDAX graph of Al7075 90% and TiB_2 10%.

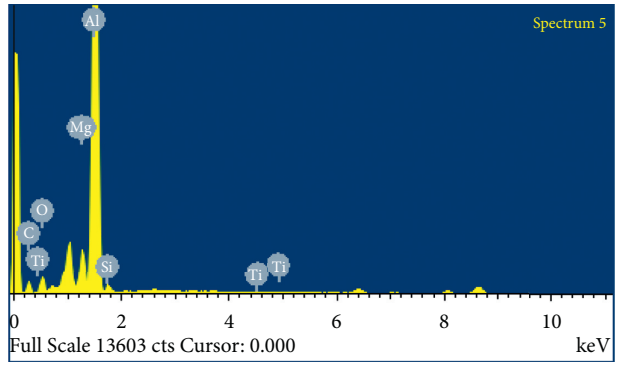

Figure 6: EDAX graph of Al7075 85% and TiB_2 15%.

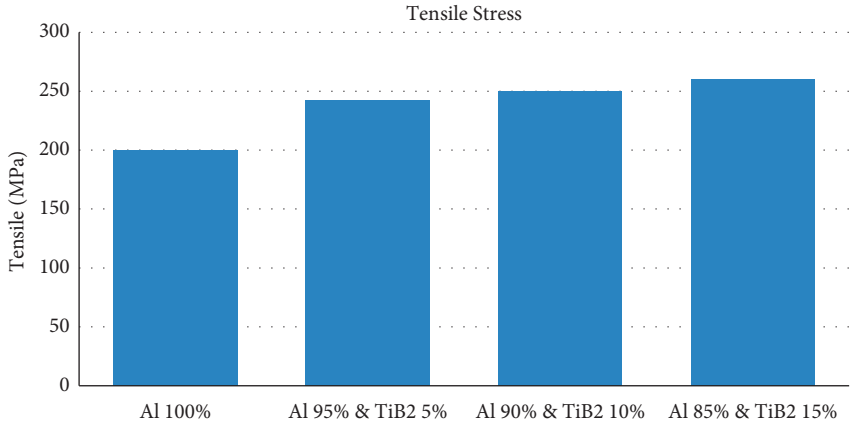

Figure 7: Tensile test report.

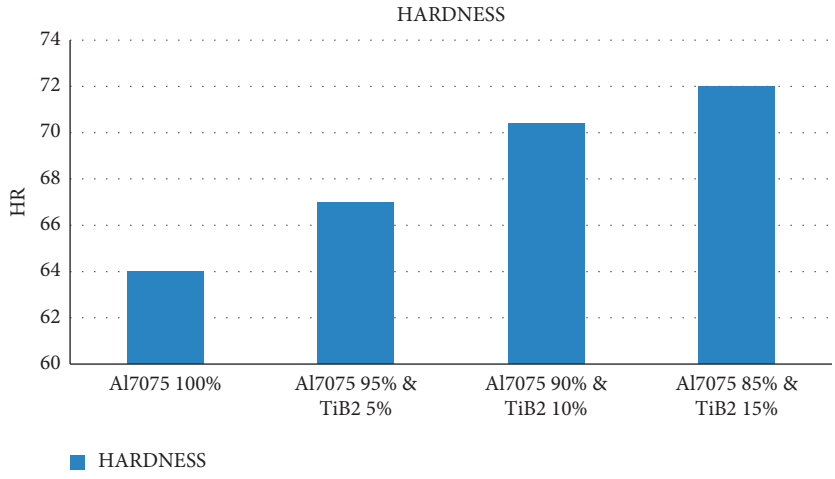

Figure 8: Hardness value report.

affect the ductile-brittle nature of the composite. Based on the problem mentioned above in this research, the TiB_2 was added at the range of 5% to 15%.

3.3. Impact of Reinforcement on Hardness. In general, hardness is defined as the resistance to indentation. Figure 8 depicts the Al7075 and TiB_2 composites. Figure 8 indicates a major change in the prepared sample's microhardness values was an increase in 5% TiB_2, 10% TiB_2, and 15% TiB_2. Table 3 shows the comparison of the pure Al7075 series and the hardness values such as Rockwell hardness number (RHN) enhanced with prepared samples.

TiB_2 particles are more resistant to plastic deformation due to the Al7075 matrix; when integrated into the molten matrix, the TiB_2 type preferred heterogeneous grain

Table 3: Hardness value for prepared samples.

S. no	Specimen	Intender	Load (kgf)	Rockwell hardness (HR)					Mean
				A	B	C	D	E	
1	Al7075 100%	Ball	100	B64	B64	B65	B63	B64	B64
2	Al7075 95% and TiB_2 5%	Ball	100	B65	B66	B70	B68	B66	B67
3	Al7075 90% and TiB_2 10%	Ball	100	B69	B68	B72	B73	B70	B70.4
4	Al7075 85% and TiB_2 15%	Ball	100	B70	B70	B73	B71	B75	B72

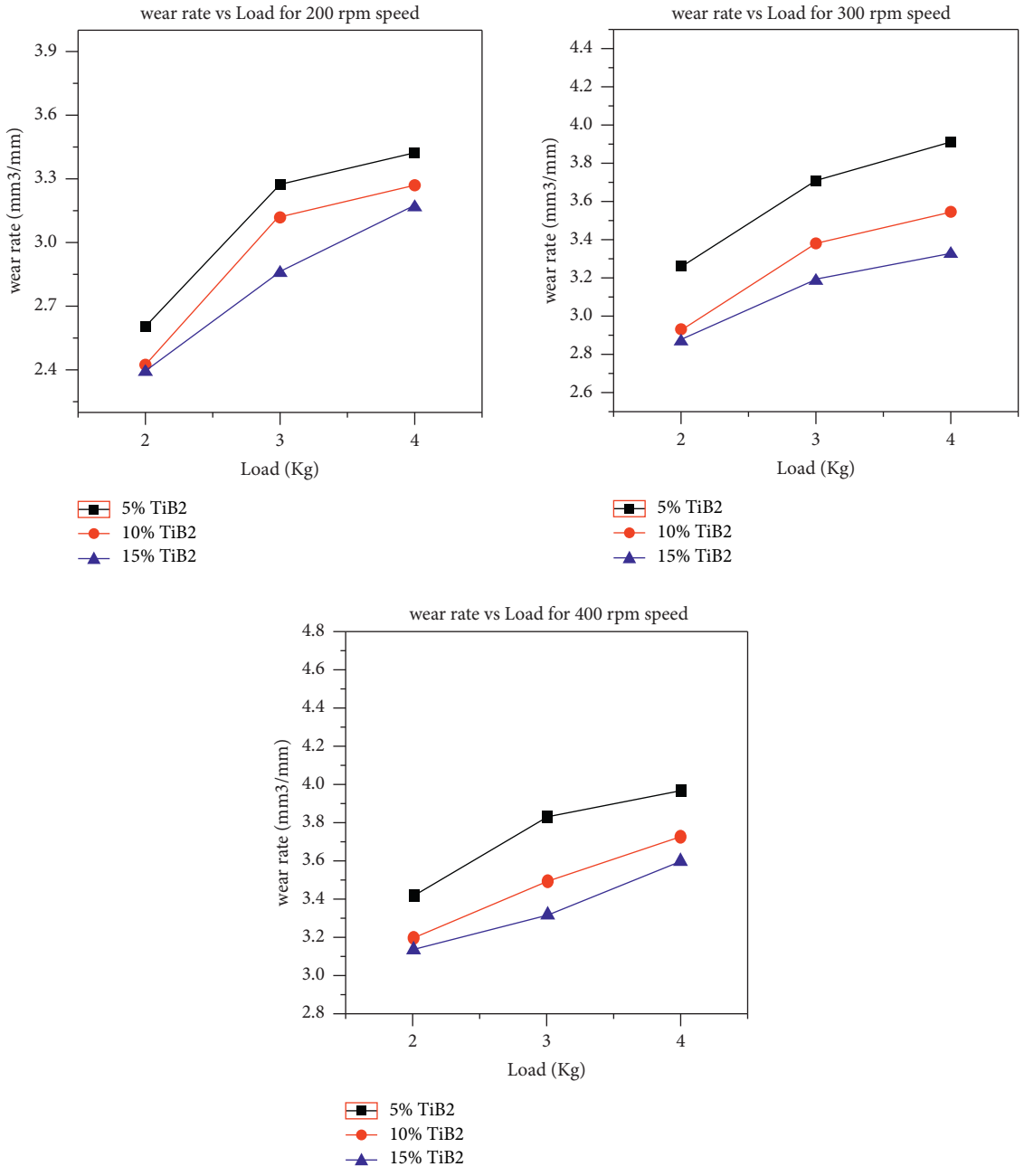

Figure 9: Wear rate load.

nucleation sites. Similarly, many researchers reported improving the value of Vickers hardness when TiB_2 particles were added to a metallic matrix in situ process [14].

3.4. Impact of Reinforcement on Wear Properties. As a function of the TiB_2 weight percentage, load, and speed, Figure 9 indicates Al7075 composite wear. Table 4 shows the wear rate at a constant sliding speed of different percentages

Table 4: Wear rate for prepared samples.

Speed (rpm)	Load (kg)	Wear rate (mm^3/min)		
		5%	10%	15%
200	2	2.61	2.42	2.4
	3	3.28	3.12	2.86
	4	3.43	3.27	3.17
300	2	3.27	2.93	2.87
	3	3.72	3.38	3.19
	4	3.92	3.55	3.33
400	2	3.42	3.19	3.13
	3	3.84	3.49	3.31
	4	3.97	3.72	3.59

Figure 10: SEM image of Al7075 95% and TiB_2 5%.

of TiB_2 refurbishments in the Al7075 matrix; therefore, the wear rate generally increases with the rising load. The wear loss of pure Al 7075 alloy is greater than that of other composites. When the amount of TiB_2 reinforcements in the Al7075 matrix was increased, the wear rate values began to drop. For all sliding speeds, the same trend was observed as shown in Table 4. As seen on the base alloy diagram, the wear rate gap is 30–35%, and the inclusion of both loads is 15% TiB_2.

The graph of wear rates is not aligned with the increase in TiB_2 strengthening due to the diverse wearing processes as shown in Figure 9. The wear rate at various loads at 200 rpm shows lower wear than that at the higher load. The wear rate is influenced by the reinforcement between the counterfeit and matrix. The adhesive phenomena are produced by contact asperity between the hard face (disk) and the soft surface (pin). Such touch is deformed by the effects of cold welding and is called adherence. This process leads to a loss of metal as sliding removes asperities from the surface, called adhesive wear. This is based on the applied load function, and TiB_2 particles have a constant sliding speed for 20 minutes.

Figure 9 indicates that the effect of TiB_2 on wear resistance at lower loads is high, and the wear resistance decreases as the load applied increases to 4 kg. The resulting graph is not linear, as improvements in adhesion and processing characteristics affect composite wear resistance.

As specified in the Archard wear equation act, "hardness is directly proportionate to the composite's volumetric wear resistance" [15]. The TiB_2% was similar, with a substantial increase in the applied load of 2 kg, but the resistance fell to 3 kg. Due to their major changes in intensity, the proportion of particulate strengthening TiB_2 is important to wear study.

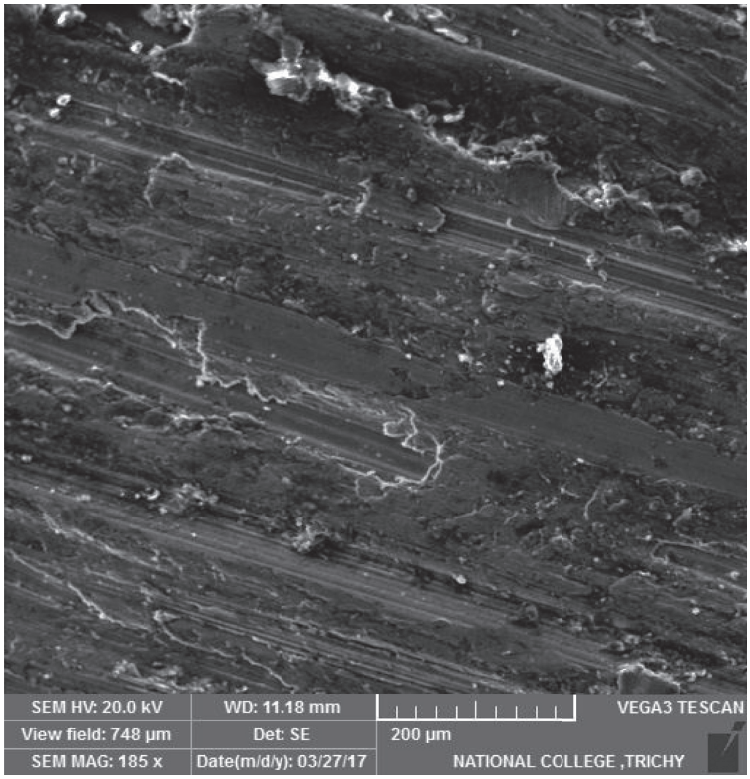

Figure 11: SEM image of Al7075 90% and TiB_2 10%.

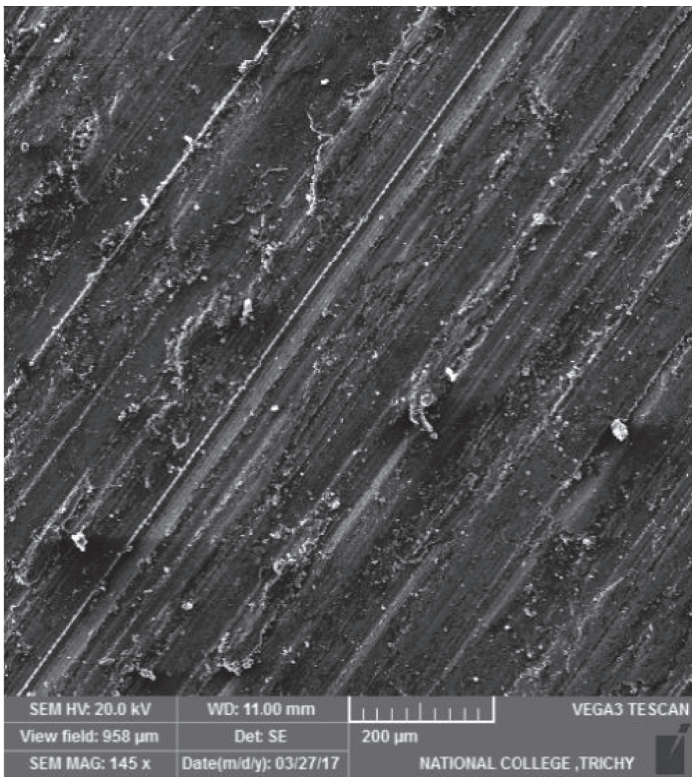

Figure 12: SEM image of Al7075 85% and TiB_2 15%.

An analysis of the worn surface and surface morphology is important to better understand the nonlinear graphs found in these specimens.

Figure 10 to 12 show the SEM image of the TiB_2 strengthened alliance Al7075 worn base, the specimen samples. The samples are fed on the different 2, 3, and 4 kg loads at room temperature. At first, chemical acetone was used to clean up the specimens and remove loose particles and dirt [16, 17]. The wear mechanism demonstrates the plastic surface's deformation due to relative contact motion, tension, asperities, and floor projections.

The wear rate inspection indicates that the grooves, scales, asperities, and ridges run in the sliding direction on the surface in parallel, as shown in Figure 12. The aggression of the grooves grows as the functional factor increases, becoming higher and lower than the regular arming grooves created on the low TiB2 strengthening matrix, which are greater than the 15% TiB_2 adding grooves. The vicinity of wear paths of a thin oxide film indicates the oxide waste surface layers [18]. The large craters were formed in the specimen, and the TiB_2 reinforcement particles adhered to the greater scrap due to the sliding conditions of larger scrap.

4. Conclusion

The stirring process was carried out with different percentages of TiB_2 enhancements applied to Al7075. The tensile stress, hardness range, and tribological characteristics were investigated in this research work; based on the investigation, the following findings have been reported:

(1) Upon melting, the preheating of the TiB_2 particles has a significant effect. The porosity is that indicating that the bonding is much better.

(2) When the inclusion of TiB_2 particles in the Al7075 matrix increases, microhardness values increase.

(3) The 2 kg load and 200 rpm sample processing with additional reinforcement of 15% at a rate of 200 rpm ensure optimum resistance to wear and minimum wear.

(4) Adding 15% of TiB_2 with Al7075 leads to an increase in wear behavior.

(5) In the tribological view, the high load sliding distance and reinforcement percentage of TiB_2 increase the wear rate.

Data Availability

No data were used to support this study.

Conflicts of Interest

The authors declare that they have no conflicts of interest.

References

[1] N. C. Kaushik and R. N. Rao, "High-stress abrasive wear behavior of Al–Mg–Si hybrid composites using regression analysis," *Industrial Lubrication & Tribology*, vol. 39, 2017.

[2] N. C. Kaushik and R. N. Rao, "Effect of applied load and grit size on wear coefficients of Al 6082-SiC-Gr hybrid composites under two body abrasion," *Tribology International*, vol. 103, pp. 298–308, 2016.

[3] N. C. Kaushik and R. N. Rao, "Effect of grit size on two body abrasive wear of Al 6082 hybrid composites produced by stir casting method," *Tribology International*, vol. 102, pp. 52–60, 2016.

[4] A. Atrian, G. H. Majzoobi, M. H. Enayati, and H. Bakhtiari, "A comparative study on hot dynamic compaction and quasi-static hot pressing of Al7075/SiCnp nanocomposite," *Advanced Powder Technology*, vol. 26, no. 1, pp. 73–82, 2015.

[5] M. Karbalaei Akbari, H. R. Baharvandi, and O. Mirzaee, "Nano-sized aluminum oxide reinforced commercial casting A356 alloy matrix: evaluation of hardness, wear resistance and compressive strength focusing on particle distribution in aluminum matrix," *Composites Part B: Engineering*, vol. 52, pp. 262–268, 2013.

[6] A. Kareem, J. A. Qudeiri, A. Abdudeen, T. Ahammed, and A. Ziout, "A review on AA 6061 metal matrix composites produced by stir casting," *Materials*, vol. 14, no. 1, Article ID 175, 2021.

[7] P. Raghuvaran, M. Suresh, J. Baskaran, S. Arun Prasadh, M. K. Charan, and T. Dhananjayan, "Investigation on characteristics of stir-casted aluminum matrix composites-a review," *Springer Proceedings in Materials*, vol. 5, pp. 841–851, 2021.

[8] Y. Pazhouhanfar and B. Eghbali, "Microstructural characterization and mechanical properties of TiB2 reinforced Al6061 matrix composites produced using stir casting process," *Materials Science and Engineering A*, vol. 710, pp. 172–180, 2018.

[9] J. Sundaram, J. Udaya Prakash, and H. Kagitha, "Wear properties on AA2014/Al2O3/TiB2 hybrid metal matrix composites," in *Innovative Design, Analysis and Development Practices in Aerospace and Automotive Engineering*, pp. 389–395, Springer, Berlin, Germany, 2021.

[10] D. Jianxin, A. Xing, and L. Zhaoqian, "Friction and wear behavior of Al 2O 3/TiB 2 composite against cemented carbide in various atmospheres at elevated temperature," *Wear*, vol. 195, no. 1-2, pp. 128–132, 1996.

[11] D. Jianxin and A. Xing, "SiC whisker reinforced Al2O3/TiB2 ceramic composites," *Chinese Ceramic Society*, vol. 23, no. 4, pp. 385–392, 1995.

[12] J. Hashim, L. Looney, and M. S. J. Hashmi, "Metal matrix composites: production by the stir casting method," *Journal of Materials Processing Technology*, vol. 92-93, pp. 1–7, 1999.

[13] Y. Han, X. Liu, and X. Bian, "In situ TiB2 particulate reinforced near eutectic Al-Si alloy composites," *Composites Part A: Applied Science and Manufacturing*, vol. 33, no. 3, pp. 439–444, 2002.

[14] S. Natarajan, R. Narayanasamy, S. P. Kumaresh Babu, G. Dinesh, B. Anil Kumar, and K. Sivaprasad, "Sliding wear behaviour of Al 6063/TiB2 in situ composites at elevated temperatures," *Materials & Design*, vol. 30, no. 7, pp. 2521–2531, 2009.

[15] A. Mandal, B. S. Murty, and M. Chakraborty, "Sliding wear behaviour of T6 treated A356–TiB2 in-situ composites," *Wear*, vol. 266, no. 7-8, pp. 865–872, 2009.

[16] A. Mandal, M. Chakraborty, and B. S. Murty, "Effect of TiB2 particles on sliding wear behaviour of Al–4Cu alloy," *Wear*, vol. 262, no. 1-2, pp. 160–166, 2007.

[17] A. Haiter Lenin, S. C. Vettivel, T. Raja, L. Belay, and S. C. E. Singh, "A statistical prediction on wear and friction

behavior of ZrC nano particles reinforced with Al Si composites using full factorial design," *Surfaces and Interfaces*, vol. 10, pp. 149–161, 2018.

[18] G. Robert Singh, S. Christopher Ezhil, M. Sivapragash, L. Anselm, R. S. Kumar, and A. Haiter Lenin, Tensile and compression behaviour, microstructural characterization on Mg-3Zn-3Sn-0.7Mn alloy reinforced with SiCp prepared through powder metallurgy method," *Materials Research Express*, vol. 9, 2020.

Hindawi
Advances in Materials Science and Engineering
Volume 2022, Article ID 4980291, 8 pages
https://doi.org/10.1155/2022/4980291

Research Article

Investigate the Process Parameter on the Friction Stir Welding of Dissimilar Aluminium Alloys

R. Raja,[1] **A. Parthiban**,[1] **S. Nandha Gopan**,[2] **and Derese Degefa**[3]

[1]*Department of Mechanical Engineering, Vels Institute of Science, Technology & Advanced Studies, Chennai, India*
[2]*Department of Mechanical Engineering, K.Ramakrishnan College of Engineering, Trichy, India*
[3]*Department of Mechanical Engineering, WOLLO University, Kombolcha Institute of Technology, Kombolcha, Post Box No: 208, Ethiopia*

Correspondence should be addressed to Derese Degefa; derese2013@kiot.edu.et

Received 9 September 2021; Accepted 4 December 2021; Published 22 January 2022

Academic Editor: Temel Varol

Copyright © 2022 R. Raja et al. This is an open access article distributed under the Creative Commons Attribution License, which permits unrestricted use, distribution, and reproduction in any medium, provided the original work is properly cited.

The welding of different materials with an acceptable quality range is an emerging study area; engineers and scientists worldwide have long been concerned with dissimilar welding materials. This study focuses on determining the friction stir welding of different aluminuim alloys; an experimental investigation was conducted (AA7475-T651 and AA2219-O). It also describes the FSW process parameters and response measurement for defining weld quality and the procedure for measuring them. Taguchi L27, orthogonal array method, is preferred for optimizing FSW parameters such as shoulder diameter, tool rotational speed, and traverse speed. The effect of welding parameters is investigated through the ANOVA table and graphs. The SEM analysis investigates the fracture and micrographic analysis in the heat-affected zone and thermo-mechanically affected zone.

1. Introduction

Dissimilar welding materials are vital for various goods used in automotive, shipbuilding, aerospace, and other industries. This can be such a difficult task that it is sometimes impossible to acquire a joint. In particular, this difficulty is caused by variations in the mechanical characteristics of the connected components (physical, chemical, and metallurgical). Even during welding, there may be failures at the weldments because of differences in melting point and thermal expansion coefficient. Aluminium alloys are used for structural components because of their fracture toughness, good corrosion resistance, and fatigue strength. Aluminium alloys are lightweight materials that minimize vehicle bulk, therefore reducing fuel consumption and hazardous emissions. As lightweight materials, many aluminium alloys meet the needs of the aircraft sector [1]. AA7475 outperforms numerous commercially available high-strength aircraft aluminium alloys such as AA7075 and AA7050 [2]. For connecting 6 mm AA6351-T6 and AA5083-H111, reseachers used HCHCr steel [3]. For connecting 8 mm different aluminium alloys, researchers employed H13 steel (AA7075-T6 and AA6082-T6) [4]. Khan et al. [5] utilised an HCHCr steel threaded pin tool to link 2.5 mm AA7475-T761 and AA2219-O.

There are some examples of aluminium alloys being joined, such as a ship's 5xxx aluminium alloy being joined to 6xxx aluminium and an aircraft's 2xx being joined to a 7xxx series aluminium alloy, due to extreme plastic deformation and low heat input [6]. This results in more minor pre-welding processing benefits and increased joint strength. To create the sound welded connection, FSW employs heat generated by friction between the tool and base material (BM), which softens materials that form the joint and causes plastic deformation of the base material, as shown in Figure 1. Al-A2219 and Al-7475 are frequently used in aircraft. It follows that research on connecting such alloys might be of both scholarly and industrial use. Conventional fusion welding methods are unable to fuse the aerospace aluminium alloys AA2219 and AA7475 adequately. As a result,

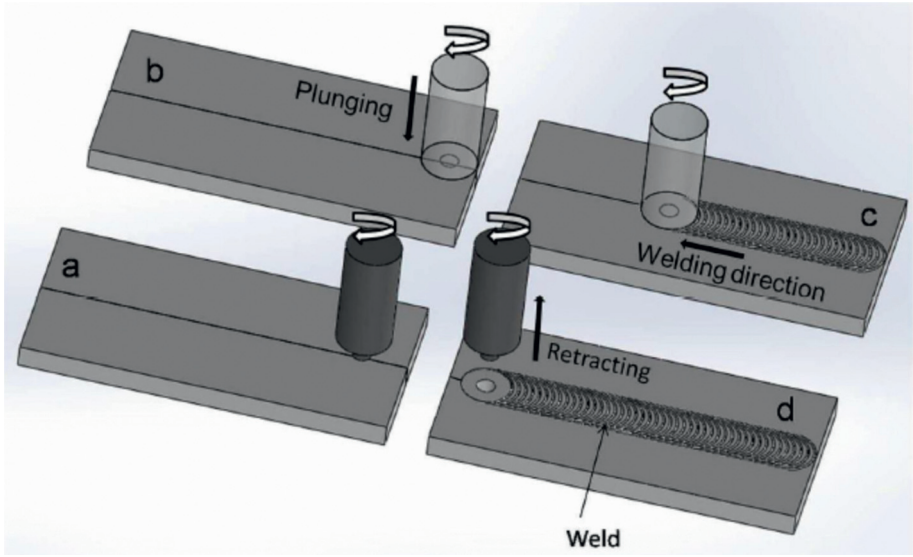

Figure 1: Steps of friction stir welding process.

joining such alloys requires the use of a different welding technique. Welding different aluminium alloys with FSW is a suitable option [7].

Three microstructural zones are visible in welded FS joints (Figure 2). Recrystallized grains appear in the stir zone (SZ). Plastically deformed grains appear in thermo-mechanically affected zone (TMAZ) [8]. Die Region SZ, in which dynamic recrystallization produced by the stirring action of the tool results in refined grains, is subjected to high deformation and high heat input. Plastic deformation occurs up to a lower level in the region next to SZ (TMAZ), which leads to partial dynamic recrystallization. The HAZ is exclusively subjected to a temperature influence [9].

Figure 2: Microstructural welding zones of friction stir-welded aluminium alloy.

2. Material Selection

This paper presents the methodology of dissimilar welding in aluminium alloys (2xxx and 7xxx) with prospective applications in important areas [10]. AA2219-O with AA7475-T761 (a combination usually utilised in aircraft construction) was FSW, and its microstructure and mechanical characteristics were studied and presented in this paper.

BMs used in the present research were hot rolled AA7475-T651 and AA2219-O plates of thickness 2.5 mm. The plates were sheared to nominal dimensions of 50 mm × 180 mm so that the grains aligned in the direction of the joint line. The experiments were performed on the plates in the rolling direction [11–13]. Figure 3 shows the geometric layout representation of HC steel for FSW. Table 1 lists the composition of BM alloys and the tool material HC steel. It is shown in Table 2 that BMs have mechanical and thermal characteristics.

In high-strength aluminium alloys, friction stir welding has shown to be a formidable welding method. An R. V. machine tools' limited friction stir welding machine was used for the tests (Figure 4). Two motors control the friction stir welding process: the spindle motor and feed motor. These motors are connected to driving controllers through a wire. Its spindle

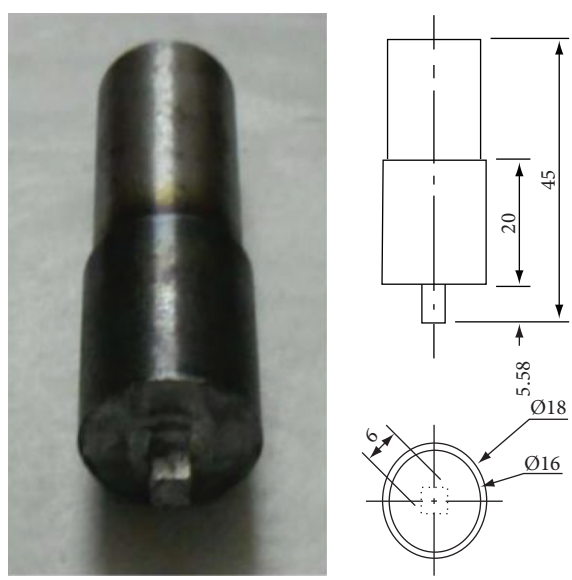

Figure 3: HC steel FSP tool and its geometric layout.

motor has a power rating of 22 kW, while its feed bed motor has a power rating of 1.5 kW. Motors with mechanical gearboxes are used in both cases to enhance torque at the output shaft. The spindle rotation is provided by a primary spindle motor, while the feed bed motor provides power for the bed's three-axis motions. With 24 V electromagnetic clutches, the different axes of the bed (X, Y, and Z) are locked into place. PCI boards are connected to limit switches and emergency stop

Table 1: AA7475, AA2219, and HC steel: chemical properties (wt. %).

Elements	Al	Cu	Mg	Sn	Mn	Fe	Si	Ti	Cr	Zn	Ni	Zr	C	V
AA2219	91.96	6.91	—	0.016	0.32	0.101	0.06	0.02	0.17	5.38	0.002	0.007	—	—
AA7475	90.99	1.34	1.93	0.016	0.32	0.156	0.044	0.06	—	0.06	0.034	0.293	—	0.147
HC steel (tool)	—	0.10	—	—	1.39	95.43	0.53	—	0.433	—	0.084	—	0.88	—

Table 2: AA7475 and AA2219: mechanical and thermal characteristics.

Materials	UTS (MPa)	Yield strength (MPa)	Percentage of elongation (%)	Material thermal conductivity (W/mK)	Incipient melting liquids' temperature (°C)
AA7475-T651	460–470	425–435	12–15	162–165	535–635
AA 2219-O	290–295	215–230	14–16	115–125	545–645

Figure 4: Friction stir welding.

buttons [14, 15]. Figure 4 shows the fixture set up on the FSW machine. By securing the plates to be stir-welded, all degrees of freedom are prevented, resulting in high-quality welding.

3. Taguchi Analysis

Many trail experiments were performed at different parameter combinations by varying process parameters to determine the feasible range of the selected parameters. Table 3 shows the FSW process parameter window with the specified parameters' minimum and maximum values.

The experiment plan shows the number of experiments and the order in which each experiment is required to be conducted. Three process parameters are selected in the present research along with three levels of each parameter, and 27 experiments are performed according to Taguchi's L27 orthogonal array (OA) [16]. Taguchi's L9 OA can also be used with the selected factors and levels, but this design does not allow the experimenter to investigate the effects of the interaction of the process parameters on the response variables. In order to investigate the effect of main factors and their interactions on the response variables, Taguchi's L27 OA was selected to perform the experiments, as shown in Table 4. The experimental plan based on Taguchi's L27 OA is presented with randomized order and date of experiment in Table 5.

3.1. Microstructural Investigation. In order to determine the location of internal flaws and defects, examine causes for poor strength, and comprehend the process of material flow, friction stir-welded samples were subjected to microstructural analysis. Optical microscopy was used to analyze microconstituent and grain structures and morphology, and advanced examination was done using scanning electron microscopes (SEM) [17].

Table 3: FSW process parameter window.

FSW process parameters	Levels		
	Level I	Level II	Level III
Parameter 1: rotational speed (A) (rpm)	710	900	1120
Parameter 2: traverse speed (mm/min) (B)	160	200	250
Parameter 3: shoulder diameter (mm) (C)	10	12	14

4. Results and Discussion

4.1. Traverse Force. Table 4 shows the experimentally measured traverse force data. Standard statistical software Minitab-17 was used to analyze experimental data. Traverse force was determined based on a "lower is better" (minimization) criterion because a lower value results in reduced tool wear (Figure 4), less load on the machine spindle and work fixture, etc. Table 4 shows the results of an analysis of the mean (ANOM) to identify the optimal parameter combination.

The impact of FSW parameters and their interplay on traverse force was assessed using ANOVA. Before executing an ANOVA, a diagnostic test is necessary to validate the assumptions stated in the ANOVA. The Minitab-17 program generated a normal probability plot (Figure 5). In Figure 5, it can be observed that the points (residuals) either lie on or are extremely close to the straight line. Thus, the residuals are normally distributed, and it validates the ANOVA assumption.

Figure 6 shows the normal probability plot for the values of traverse force. Furthermore, the results of ANOVA also indicate the significance of factors and their interactions defined in terms of percent contribution. Percent contribution gives the order of importance for each parameter and interaction affecting the traverse force in Table 6. Shoulder diameter (C) is identified as the most influencing factor because it directly affects the

Table 4: Response table for mean (traverse force).

FSW parameters	Level 1	Level 2	Level 3	Difference	Rank
Parameter 1	71.09	57.60	56.34	14.74	3
Parameter 1	49.43	62.06	73.54	24.11	2
Parameter 1	53.33	50.89	80.81	29.92	1

Table 5: Taguchi L27 OA showing 27 experiments.

Ex. no	Factors and their levels		
	Parameter 1	Parameter 2	Parameter 3
1	1	1	1
2	1	2	2
3	1	3	3
4	2	1	1
5	2	2	2
6	2	3	3
7	3	1	1
8	3	2	2
9	3	3	3
10	1	1	2
11	1	2	3
12	1	3	1
13	2	1	2
14	2	2	3
15	2	3	1
16	3	1	2
17	3	2	3
18	3	3	1
19	1	1	3
20	1	2	1
21	1	3	2
22	2	1	3
23	2	2	1
24	2	3	2
25	3	1	3
26	3	2	1
27	3	3	2

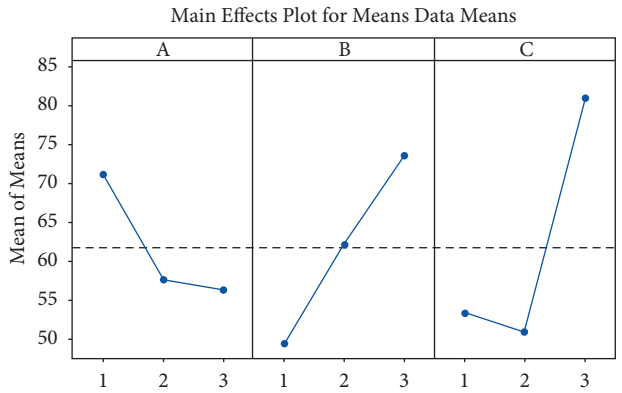

Figure 5: Main effect plot for the mean (traverse force).

traverse force with a higher percentage contribution of 32.45%, followed by interaction A × C with 18.72% contribution, traverse speed (B) with 17.22% contribution, interaction $A \times B$ with 13.82% contribution, interaction $B \times C$ with 7.13% contribution, and rotational speed with 6.90% contribution.

$$\text{Transverse Force}_{\text{avg}} = 1 - 0.020A + 0.883B - 12.1C - 0.000990A * B + 0.0155A * C + 0.0237\,B * C. \quad (1)$$

Equation (1) gives the following formula for predicting the traverse force in terms of factors.

The coefficient of determination is derived by the combinations of welding parameters and traverse force, i.e., $R2$. For the relationship shown in equation (1), a very high value of $R2 = 96.2\%$ is obtained, which indicates that 96.2% variation in the value of traverse force is explained by variation in the values of the FSW parameters and only a very small (3.8%) variation in the value of traverse force is not explained by variation in the values of the FSW parameters.

4.2. Effect of Rotational Speed on Traverse Force. Factor A variations affect traverse force, as seen in Figure 7 (i.e., rotational speed). When shown in Figure 7, the traverse force decreases sharply as the rotational speed increases from level 1 to 2. On the contrary, the traverse force decreases significantly less with an increase in rotational speed from level 2 to level 3.

This is because friction heat and strain rate are increased when rotational speed increases. An increase in frictional heat reduces the traverse force, while the increase in strain rate causes an increase in traverse force. An increase in rotational speed might significantly enhance the frictional heat compared to the strain rate. Thus, the effect of frictional heat takes over the effect of strain rate on traverse force, thereby reducing traverse force.

4.3. Effect of Traverse Speed on Traverse Force. Figure 8 shows the influence of traverse speed, or factor B, on traverse force. Level II traverse speed results in greater forces. When traverse speed is increased from level II to level III, the traverse force increases again. During welding, the traverse speed has a major impact on the distribution of the heat generated. Weld zone temperature rises with slower traverse speed, reducing flow stress. Higher traverse speed causes high flow stresses which increase the traverse force. Higher traverse speed increases the strain rate and decreases the weld temperature. Increased flow stress and increased traversal force are both enhanced by higher strain and lower temperature.

4.4. Effect of Shoulder Diameter on Traverse Force. The traversing force is reduced when the flow stress is low. However, an increase in shoulder diameter will result in more material being pushed under the shoulder, reducing tool travel and resulting in a greater force. As a result, when frictional heat is dominant, the shoulder diameter is increased the traverse force is reduced. When the moving material's resisting force is dominant, the shoulder diameter increases and the traverse force also increases (Figure 9). This may be expected that the effect of resisting force applied

Table 6: The ANOVA table for traverse force.

Source	Sum of squares	DF	Mean square	F value	Prob > F	% contribution
A	20.14	2	10.07	7.35	0.015	6.90
B	50.20	2	25.10	18.31	0.001	17.22
C	94.59	2	47.29	34.50	0.000	32.45
$A \times B$	40.28	4	10.07	7.35	0.009	13.82
$A \times C$	54.56	4	13.64	9.95	0.003	18.72
$B \times C$	20.78	4	5.19	3.79	0.052	7.13
Residual	10.97	8	1.37			3.76
Total	291.51	26				

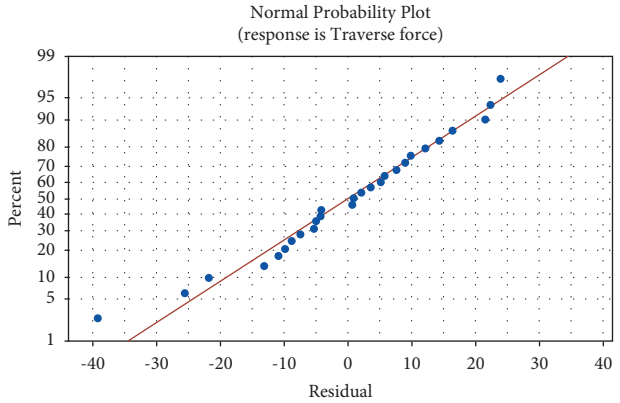

Figure 6: Normal probability plot for the values of traverse force.

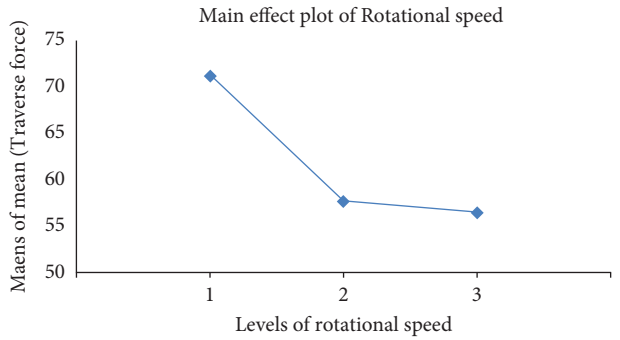

Figure 7: Main effect plot of rotational speed for means (traverse force).

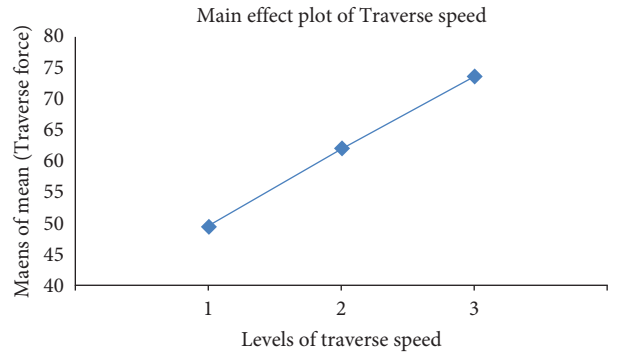

Figure 8: Main effect plot of traverse speed for means (traverse force).

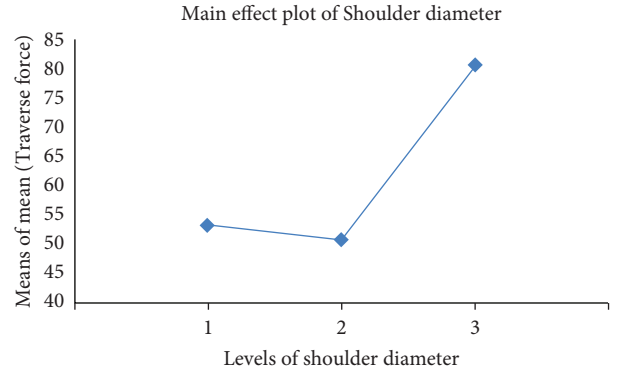

Figure 9: Main effect plot of shoulder diameter for means (traverse force).

by the moving material under the tool shoulder dominates over the effect of frictional heat and the effect is an increase in the traverse force on increasing shoulder diameter. Figure 10 denotes the interaction between rotational speed and traverse speed ($A \times B$) on average traverse force, and Figure 11 represents the interaction between rotational speed and shoulder diameter ($A \times C$) on average traverse force.

4.5. SEM Analysis. Figure 12 shows very few precipitates at RS, whereas a high density of precipitates is observed at AS of SZ. It might be due to sufficient temperature generated at SZ and dissolved strengthening precipitates at RS. While AS material was used in annealed conditions, and precipitates shown in SZ might be undissolvable Al_2Cu precipitates due to the presence of higher content of Cu in the Al matrix.

To achieve the desired shape and microstructure, the FSW process uses strain and heat. During FSW, many phenomena such as recovery, recrystallization, and grain growth occur depending on the kind of material, operating temperature, and degree of deformation. In FS welded materials, dynamic recovery and recrystallization occur, and these processes are responsible for grain refinement. The strain rate and available temperature dictate the degree of grain refining. With a higher strain rate and a lower temperature, grain size shrinks. FSW variables such as tool rotation speed, traverse speed, and tool shoulder diameter affect temperature and strain rate. Although tool rotational speed, traverse speed, and shoulder diameter are all linearly connected, temperature in the weld zone rises as tool rotational speed rises but declines as traverse speed grows. Increased shoulder diameter enhances the tool's heat-

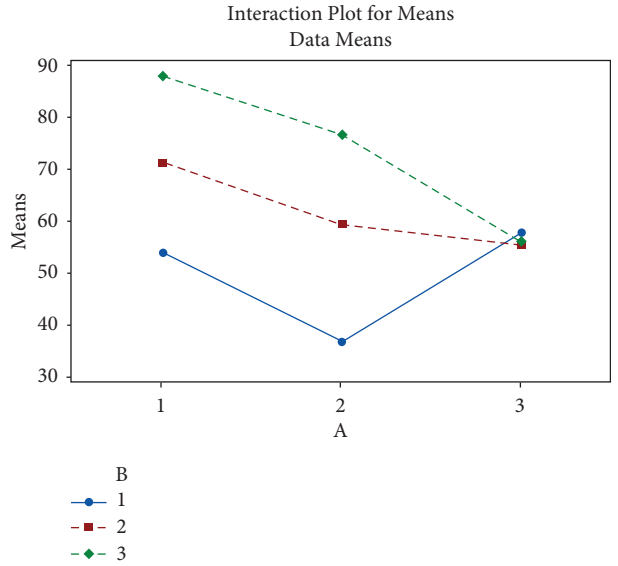

Figure 10: Effect of interaction between rotational speed and traverse speed ($A \times B$) on average traverse force.

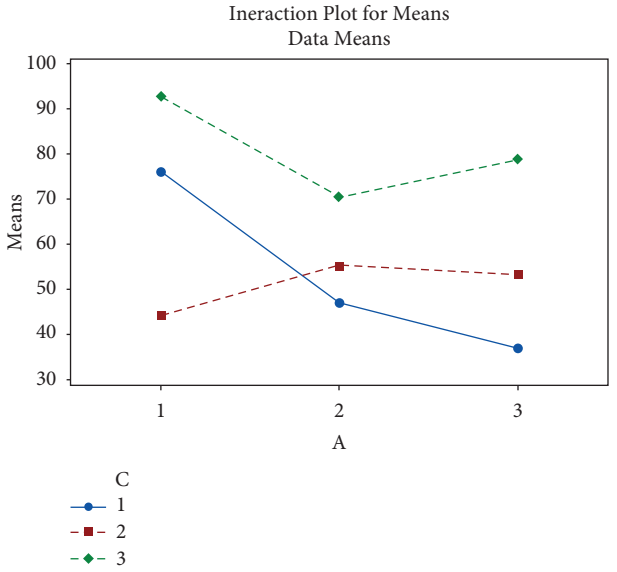

Figure 11: Effect of interaction between rotational speed and shoulder diameter ($A \times C$) on average traverse force.

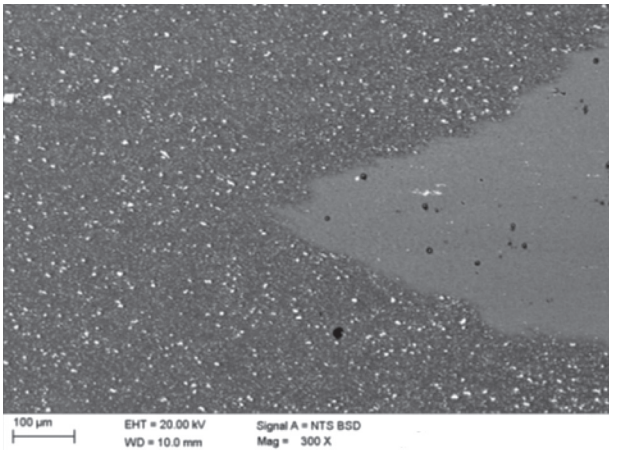

Figure 12: Micrograph for experiment no. 12 at SZ interface (RS on the right-hand side).

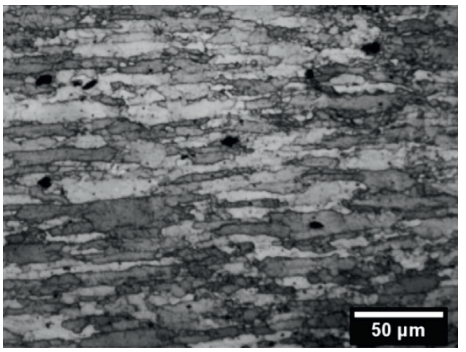

Figure 13: Micrograph of TMAZ in AS of the weld showing Cu-rich dark regions.

carrying capability while also increasing frictional heat. As a result, the impact of shoulder diameter on temperature is influenced by the interactions of other factors. Increased traversal speed raises the strain rate and lowers the temperature in the SZ, resulting in fine grain structure. After enduring intense plastic deformation and reaching higher temperatures, SZ may suffer dynamic recovery and dynamic recrystallization.

The grain structure of TMAZ is different depending upon the process parameter combination. Dark regions were found to be present at AS of the weld, as shown in Figure 13.

When examining broken specimens under a microscope, a variety of dimple characteristics can be seen. Some joints include a combination of shallow and deep dimples that are less densely packed, as seen in Figure 14. Here, large, deep dimples formed due to void development, indicating that more energy was used before fracture. We find deep dimples

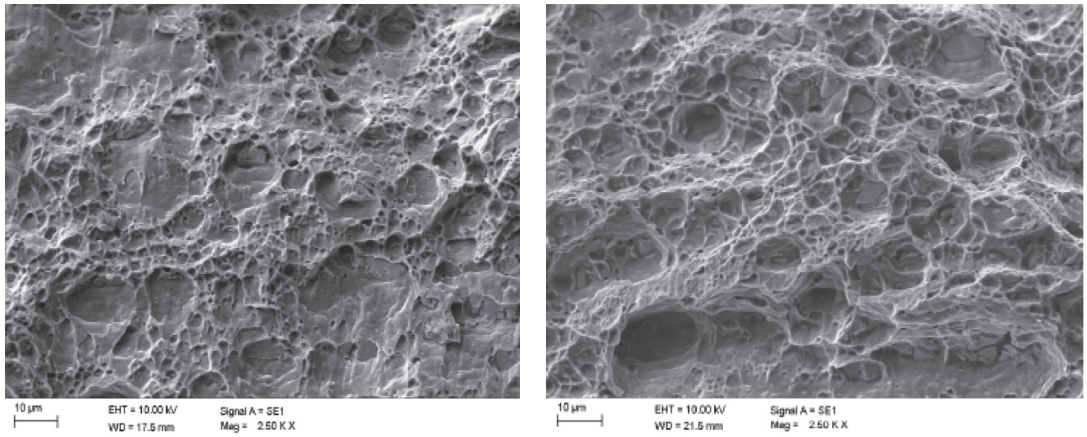

(a) (b)

Figure 14: SEM micrograph of fractured specimen for exp nos. (a) 4 and (b) 17.

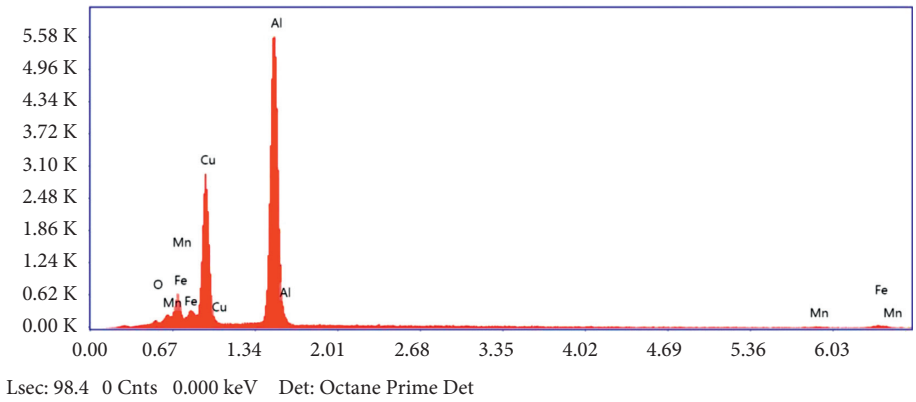

Figure 15: EDS spectrum of fractured specimen for exp no. 2.

that are densely populated, consistent with a typical ductile form of fracture.

The joint was fractured at the TMAZ is shown in Figure 14. The shallow dimples in the fractured sample are evidence of AS caused by cracking of the coagulated Al2Cu precipitates. Figure 15 shows the EDS of the fractured sample for exp. no. 2, showing the presence of Al_2Cu precipitates. Fe content in the EDS analysis might be due to fine Fe-rich precipitates present under the coagulated bigger Al_2Cu precipitates.

5. Conclusion

The weld joint quality and traverse force measurements were used to determine the efficacy of the proposed work fixture. Conclusions derived from many experiments done on dissimilar aluminium alloys include

(1) An FSW tool with a threaded cylindrical pin made of high-carbon steel can be used to manufacture joints free of defects and to obtain good mechanical and metallurgical weld on aluminium alloys.

(2) After a high initial rise in traversal force, the curve drops to a lower value and stabilizes. Continued tool movement generates a steady increase in the curve, stabilizing at a higher traverse force value after some distance.

(3) After experiencing a sharp increase in traverse force, the curve lowers to a lower value and stabilizes. Continued tool movement generates a steady increase in the curve, stabilizing at a higher traverse force value after some distance.

(4) For the smallest traverse force, the optimal combination of the FSW parameters is A3B1C1, which corresponds to the rotating speed of 1120 rpm, the travel speed of 160 mm/min, and shoulder diameter (C) of 10 mm.

(5) Shoulder diameter C (with 32.45 percent contribution), interaction $A \times C$ (with 18.72 percent contribution), traverse speed B (with 17.22 percent contribution), interaction $A \times B$ (with 13.82 percent contribution), interaction $B \times C$ (with 7.13 percent contribution), and rotational speed B (with 7.13

percent contribution) are the factors and their interactions in order of importance for traverse force (with 6.90 percent contribution).

(6) On investigation of the microstructure, grain refinement occurs in the stir and thermo-mechanically affected zones due to the dynamic recrystallization. The process parameters' effect is shown on the size of recrystallized grains. In SZ, partial dissolution occurs and reprecipitations occur in some welds.

Data Availability

No data were used to support the findings of the study.

Conflicts of Interest

The authors declare that they have no conflicts of interest.

References

[1] P. P. Raja and B. J. Raj, "Investigations on mechanical and metallurgical properties of friction welding of AlB2 reinforced aluminum matrix composites," *Silicon*, vol. 10, no. 4, pp. 1385–1391, 2018.

[2] R. K. Bhushan and D. Sharma, "Optimization of friction stir welding parameters to maximize hardness of AA6082/Si 3 N 4 and AA6082/SiC composites joints," *Silicon*, vol. 12, pp. 1–19, 2021.

[3] N. Gangil, A. N. Siddiquee, and S. Maheshwari, "Investigation on the in-process traverse force evolution during surface composites fabrication on Al-Zn-Mg-Cu alloy through friction stir processing," *Materials Today Proceedings*, vol. 25, pp. 686–690, 2020.

[4] M. Muthu Krishnan, J. Maniraj, R. Deepak, and K. Anganan, "Prediction of optimum welding parameters for FSW of aluminium alloys AA6063 and A319 using RSM and ANN," *Materials Today Proceedings*, vol. 5, no. 1, pp. 716–723, 2018.

[5] N. Z. Khan, A. N. Siddiquee, Z. A. Khan, and A. K. Mukhopadhyay, "Mechanical and microstructural behavior of friction stir welded similar and dissimilar sheets of AA2219 and AA7475 aluminium alloys," *Journal of Alloys and Compounds*, vol. 695, pp. 2902–2908, 2017.

[6] A. Sharma, V. K. Dwivedi, and Y. P. Singh, "Effect on ultimate tensile strength on varying rotational speed, plunge depth and welding speed during friction stir welding process of aluminium alloy AA7075," *Materials Today Proceedings*, vol. 26, pp. 2055–2057, 2020.

[7] P. Goel, A. K. Saxena, M. A. Wahid, S. Rathore, N. Sharma, and R. Kant Mishra, "Influence of friction stir welding parameters on mechanical properties of dissimilar AA 7475 to AISI 304," *IOP Conference Series: Materials Science and Engineering*, vol. 802, no. 1, Article ID 012010, 2020.

[8] R. Anand and V. G. Sridhar, "Effects of SiC and Al_2O_3 reinforcement of varied volume fractions on mechanical and micro structure properties of interlock FSW dissimilar joints AA7075-T6-AA7475-T7," *Silicon*, vol. 13, pp. 1–13, 2020.

[9] A. N. Siddiquee, S. Pandey, M. H. Abidi, A. Al-Ahmari, N. Z. Khan, and N. Gangil, "Microstructural characterization and in-process traverse force during friction stir welding of austenitic stainless steel," *Proceedings of the Institution of Mechanical Engineers-Part C: Journal of Mechanical Engineering Science*, vol. 234, no. 5, pp. 1031–1043, 2020.

[10] A. Haiter Lenin, S. C. Vettivel, T. Raja, L. Belay, and S. C. E. Singh, "A statistical prediction on wear and friction behavior of ZrC nano particles reinforced with Al Si composites using full factorial design," *Surfaces and Interfaces*, vol. 10, pp. 149–161, 2018.

[11] N. Z. Khan, A. N. Siddiquee, Z. A. Khan, D. Bajaj, and M. Ubaid, "Understanding the dissimilar friction stir welding through force and temperature evolution," *Materials Today Proceedings*, vol. 5, no. 9, pp. 17125–17131, 2018.

[12] O. Badran, N. Al-Kloub, A. M. Hassan, J. A. Al-Jarrah, and S. K. Khrais, "Effect of friction stir welding processing parameters on Abrasion wear Resistance of AA5083 welded joints," *Material Science Research India*, vol. 8, 2018.

[13] S. Pattnaik, P. K. Jha, and D. B. Karunakar, "A novel method of increasing ceramic shell permeability and optimizing casting shrinkage and tensile strength of the investment cast parts," *Proceedings of the Institution of Mechanical Engineers-Part B: Journal of Engineering Manufacture*, vol. 231, no. 3, pp. 377–388, 2017.

[14] M. Srivastava and S. Rathee, "A study on the effect of incorporation of SiC particles during friction stir welding of Al 5059 alloy," *Silicon*, vol. 13, pp. 1–11, 2020.

[15] R. K. Bhushan and D. Sharma, "Optimization of parameters for maximum tensile strength of friction stir welded AA6082/Si 3 N 4 and AA6082/SiC composite joints," *Silicon*, vol. 12, pp. 1–15, 2019.

[16] A. Goyal and R. K. Garg, "Establishing mathematical relationships to study tensile behavior of friction stir welded AA5086-H32 aluminium alloy joints," *Silicon*, vol. 11, no. 1, pp. 51–65, 2019.

[17] C. Kalangi, V. Bolleddu, and H. Lenin Allasi, "Tribological characteristics of carbon nanotubes-reinforced plasma-sprayed Al_2O_3-TiO_2 ceramic coatings," *Advances in Materials Science and Engineering*, vol. 2021, Article ID 8094640, 2021.

Hindawi
Advances in Materials Science and Engineering
Volume 2022, Article ID 3274672, 16 pages
https://doi.org/10.1155/2022/3274672

Research Article

Effect of Pin Geometry and Orientation on Friction and Wear Behavior of Nickel-Coated EN8 Steel Pin and Al6061 Alloy Disc Pair

Shiv Pratap Singh Yadav,[1] **Avinash Lakshmikanthan**,[1] **Siddappa Ranganath**,[2] **Manjunath Patel Gowdru Chandrashekarappa**,[3] **Praveena Bindiganavile Anand**,[1] **Vijay Kumar Shankar**,[1] **and Muralidhar Avvari**[4]

[1]*Department of Mechanical Engineering, Nitte Meenakshi Institute of Technology, Bangalore 560064, India*
[2]*Department of Mechanical Engineering, University Visvesvaraya College of Engineering, Bangalore 560001, India*
[3]*Department of Mechanical Engineering, PES Institute of Technology and Management, Shivamogga 577204, Visvesvaraya Technological University, Belagavi, India*
[4]*Faculty of Mechanical Engineering, Arba Minch Institute of Technology, Arba Minch University, Arba Minch, Ethiopia*

Correspondence should be addressed to Muralidhar Avvari; muralidhar.avvari@amu.edu.et

Received 1 November 2021; Revised 3 December 2021; Accepted 9 December 2021; Published 3 January 2022

Academic Editor: JT Winowlin Jappes

Copyright © 2022 Shiv Pratap Singh Yadav et al. This is an open access article distributed under the Creative Commons Attribution License, which permits unrestricted use, distribution, and reproduction in any medium, provided the original work is properly cited.

Most mechanical systems (in particular, gear transmission system) undergo relative motion which results in increased friction phenomenon (friction coefficient, stresses, and wear rate) and thereby results in loss of efficiency. Mechanical parts undergo relative motion in different geometry configurations and orientations that induce a different state of stress as a result of friction. Till date, attempts are being made to minimize the friction with full sphere pin geometry configuration. The present work focused to reduce the frictional and wear rate, and experiments are conducted with tribo-pairs. i.e., nickel-coated pin surface slide against Al6061 alloy disc. The friction studies are carried out at different loads and geometries of pin surfaces (sphere and hemisphere configured at different orientations such as full sphere and hemisphere configured at 0°, 45°, and 90°) to induce different stress states with reference to sliding directions. Change in the geometry of EN8 pin material and their orientation with reference to sliding direction resulted in a different state of stress. The resulting stress levels were examined under the scanning electron microscope, which revealed the mechanisms of adhesion, abrasion, and extrusion. At a lower magnitude of orientation and load, the extent of asperity breaking lessens and material removal from pin surface decreases. Abrasion wear mechanism was observed corresponding to full sphere configuration on Al 6061 disc, whereas adhesive wear mechanisms are seen with hemisphere pins. The amount of aluminum transfer on pin surface with a hemisphere pin is comparatively more than that of full sphere configuration. At a lower magnitude of state of stress, the mechanism of sliding was dominated by the adhesion effect. At a higher level of state of stress, the mechanism of sliding was dominated by abrasion and extrusion.

1. Introduction

Interface quality in moving parts is of practical significance to ensure proper function in the mechanical system [1, 2]. The drag and frictional forces are minimized due to their longitudinal ribs of shark, and tree frogs grip even on the smooth surface at wet environment due to their surface features (hexagonal cell separated by gaps observed in microstructure) [3, 4]. These observations ensure the study of surface properties, and their design for better performance in moving parts is of industrial relevance [5, 6].

Al alloys are extensively used in many industrial and household applications [7, 8]. Owing to excellent properties (high corrosion rate, good formability, and mechanical

properties) [9], Al 6061 finds major applications in automotive and marine applications [10]. Several attempts are being made to widespread the applications of Al6061 alloy by improving wear resistance with the addition of reinforcement materials [9–11]. The effect of reinforcement to Al6061 affects the machinability and formability and needs significant attention to bring back to optimal functioning conditions [12, 13]. Experimental study reveals that Al6061 composites exhibited better mechanical (tensile strength) and tribological (wear resistance) properties over Al7075 (high strength and high toughness) composites [10, 14]. Attempts are being made to enhance the tribological characteristics of two forge, and customary gear materials are evaluated [15]. Tests are conducted to examine the performance (friction coefficient, friction force, and wear rate) of planetary gear transmission (made of EN 24)-based CNC bending machine [16]. The tribological characteristic examination was performed on the pin-on-disc test rig against the different shaft materials (EN8 and EN24) with Al 6061 alloy under dry and wet conditions (SAE 20W50) [17]. The minimum coefficient of friction was observed with EN8-Al6061 tribo-pair [18]. It was observed that different geometric configuration (i.e., pin geometry: sphere-sphere, sphere-plane, block on ring, and piston ring-cylinder liner) induces different tribological characteristics (i.e., friction coefficient and wear rate) [18, 19]. Therefore, EN8-Al6061 tribo-pairs possess better tribological properties and require in-depth analysis (in terms of the state of stresses and friction developed, plastic deformation, and so on) at the different geometric configurations for further enhancement and widespread use of applications in industries.

A frictional phenomenon in moving parts brings loss in efficiency of the machine [20]. For example, spur gear efficiency was significantly affected by different frictional coefficients, load, velocity, and tooth profile [21]. Frictional parts subjected to periodic loading result in wear out of parts that causes increased clearances and losses of dimensional stability [22]. To minimize the frictional effects among moving parts, a series of experiments are conducted by distinguished researchers with material pairs, which are unlubricated, lubricated, and coatings [23, 24]. These techniques are basically employed to alter the displacement and velocity discontinuity across the contacting material pair [25, 26]. Therefore, significant attention is thus required to know the state of stress developed on sliding phenomenon for different tribo-pairs. The state of stress either a uniform or nonuniform is dependent on contacting surfaces (i.e., smooth surface results in steady state, whereas rough surface could result in the nonuniform state of stress) and load transfer between the mating element pairs [27]. It was confirmed that studying the different state of stress as a result of mating pairs are of practical significance. In spur gear applications, increased contact stresses are attributed to excessive load, which alter the gear tooth profile that causes wear on gear tooth [28, 29]. The contact stress can be minimized by altering the geometric parameters [30]. Excess wear on the tooth profile results in noise and vibration, which in turn reduces the efficiency [31, 32]. These phenomena are more common in mechanical transmission applications [28]. The effect of geometric parameters (gauge, gauge deficiency, cross-level, and longitudinal slope) on the wear phenomenon (lateral or vertical) of railway track was investigated [33]. It was observed that minimized wear with the right choice of geometric parametric conditions resulted in increased ride performance at reduced maintenance cost [34]. Creating artificial textures on the geometry of the cutting tools could help to minimize friction and wear [35]. These textures could help for better lubrication during the cutting phenomenon, thereby enhances the tool life and reduces workpiece surface roughness and power consumptions [20, 36]. Microtextures in the form of grooves, circle, rectangle, and hemisphere reduce the cutting temperature, friction, and wear that could enhance the tool life [37, 38]. The effect of pin geometries (flat and spherical) on the wear rate of low carbon steel material was investigated [39]. The results showed that the wear rate that corresponds to a flat pin is more than that of a spherical pin for a low load, whereas at higher loads, spherical pin quickly wears out. It was ascertained from the above literature review that changes in geometric parameters introduce different state of stress and help to control friction and wear. Therefore, the study of wear and friction phenomena as a result of geometric parameters and their orientations is of relative significance.

Coatings applied to substrate materials tend to improve the surface characteristics without affecting the properties of the parent material [40]. The application of coatings improves the hardness and surface integrity and reduces friction, wear, and corrosion [41–44]. Experiments are performed with EN8 carbon steel mating pair with ductile material Al6061 to know the wear phenomenon [45]. The magnetron deposition method was employed to coat aluminum oxide (Al_2O_3) on the aluminum substrate [46]. Compared to aluminum substrate, the coated samples resulted in reduced friction coefficient with enhanced strength and hardness were obtained. The friction and wear behaviors of hot-dip Al-Si and electroplated Zn-Ni alloy-coated steel blanks were investigated [47]. The coated Zn-Ni alloy resulted in better wear resistance at a reduced friction coefficient. The physical vapor deposition (PVD) technique was applied to coat the iron (Fe) nanoparticles on the flat surface of the pin on EN8 pin material, and the results are tested at room- and high-temperature applications [48]. The hard oxide layers are formed after sliding against pin material, which could help to sustain higher loads at elevated temperatures. Experiments are performed with Ni-P/bio-composite coating applied on EN 8 steel, which was subjected to friction and wear studies [49]. The coated samples resulted in a lower friction coefficient and wear rate than bare substrate material. The Mo-Ni-Cr coatings are applied on super-duplex stainless steel that resulted in better wear resistance and higher hardness than uncoated substrate material [43]. Nickel coatings are applied to H13 steel with the laser cladding technique that resulted in enhanced wear resistance and thermal fatigue characteristics [50]. The resistance to wear and corrosion, ductility, and microstructure characteristics are improved with nickel-based coatings [51, 52]. Nickel coatings find potential applications in

biomedical implants and automotive parts [53, 54]. Although coating technology improves the surface properties, the selection of the right choice of coating methods is often difficult as each technique possesses its own advantages and limitations. Electroplating is treated as a cost-effective technique compared to chemical vapor deposition and sputtering [55, 56]. In addition, electroplating coats materials in a single processing step (with faster, repeatable, control over the thickness of coating deposits and offers coating over a large surface area), which do not require costly equipment, materials, and nonhazardous method to deposit material on the substrates [57, 58]. There exists a significant scope to study the impact of electrodeposited nickel coatings on the substrate material for automotive applications. Most of the parts (prosthetic joint, crankshaft, connecting rod, brake pads, steering, chassis, axle housing, etc.) undergo either an individual or in the combination of sliding, reciprocating, and rotary actions [59–61]. Furthermore, tool wear occurred on die surface possessing sharp edges may not yield appropriate results with spherical or flat pin surfaces sliding against discs [39]. It was confirmed from the above literature review that applications of coatings increase the wear resistance. The said applications undergo wear with a different state of stress based on their contact movements and edge effects. Furthermore, not much research efforts have been made to examine worn surface morphology with different pin geometric configurations at different angles and applied loads to detail the insights of surface morphologies (plastic deformation and wear mechanism, i.e., adhesion, abrasion, and extrusion) relationship with friction and wear phenomenon.

To date, no studies have yet reported to study the field condition, which is arbitrary in terms of the state of stress concern. In this study, a cost-effective electrodeposited coating technique (widely employed with a growth rate of 15% per annum compared to other methods) [62] was used to apply nickel coating on the EN 8 steel pin. Nickel coatings are selected based on their properties, wide range of applications, and ability to withstand reduced wear loss both in oxidizing and nonoxidizing environments. The geometric parameters (spherical and hemispherical) of pin tip surface oriented at different angles are investigated to know the wear behavior and state of stress induced. Therefore, this study gives detailed insight into a different state of stress developed, friction induced, worn-surface morphologies (in terms of plastic deformation, abrasion, abrasive, and extrusion), and wear rate caused by different geometries and angle of orientation of pin surfaces with and without coatings.

2. Materials and Methods

EN 8 steel used in many mechanical parts due to better strength and toughness characteristics resulted in distinguished applications (connecting rod, spindles, axles, and so on) of automotive parts [63, 64]. Al 6061 alloy is used in commercial engineering and automotive applications due to better mechanical properties and ductility [9, 65]. The chemical composition of Al 6061 alloy disc and EN8 steel pin is presented in Table 1.

2.1. Electrodeposition Coatings. Nickel coatings based on electrodeposition technique were applied on the substrate material, i.e., EN8 steel. The dimensions of the pin specimens were equal to 9 mm × 35 mm (diameter and height), subjected to a nickel sulfate bath solution for coating applications as depicted in Figure 1. Prior to coating applications, the pins are cleaned (to remove the organic matter, present if any) after immersing in a dilute HCL acid bath solution. This process is referred to as the pickling process. After the acid pickling process, the pins are dipped in dilute sulfuric acid so as to improve the microroughness. This could help in better adhesion characteristics of coating on the substrate material. Note that, nickel coating was carried out by holding the pin as cathode and pure nickel as anode material in nickel sulfate solutions. The thickness of the coatings is about 100 μm and is decided after adjusting the duration of coating.

Pure nickel was selected to coat the substrate EN8 material due to their distinguished properties such as low friction and higher hardness with reduced wear and corrosion resistance properties [62]. Nickel electrodeposits are carried out, wherein nickel ion concentrations are varied subjected to 50–250 g/L, after maintaining Na_2SO_4 and boric acid fixed at 80 g/L and 10 g/L in the bath solution. It was observed that the bright deposits (without burnt) are attributed that correspond to the current density maintained equal to 3 Adm^{-2}. Note that during experimentation, the bath solution was maintained fixed that correspond to the potential of hydrogen equal to 3. Prior to electrodeposits, the solutions are subjected to agitation (say 500 rpm) for 24 hours at room temperature. From trial experimentations, it was clear that there is no presence of burnt appearance and uncoated regions when the pH value was maintained equal to 3. DC power source was used, and the depositions are carried out on substrate at the stagnant condition of bath solution. Schematic representation of electrodeposition technique used for coating nickel on EN8 substrate material is presented in Figures 2 and 3. Theoretically, the coating thickness was determined according to equations derived from the practical experiments.

$$\text{Thickness of coating} = \frac{\text{mass of deposit}}{\text{cross sectional area} \times \text{density of coating material}}. \quad (1)$$

Table 1: Chemical composition of EN8 steel and Al6061 alloy.

EN8 material	C	Si	Mn	Cr	Mo	Ni	P	S	Fe
wt. (%)	0.45	0.19	0.79	0.007	0.002	0.009	0.026	0.015	Balance
Al 6061 alloy	Mg	Si	Fe	Ca	Cu	Mn	Zn	Ti	Al
wt. (%)	0.92	0.6	0.33	0.20	0.18	0.06	0.03	0.02	Balance

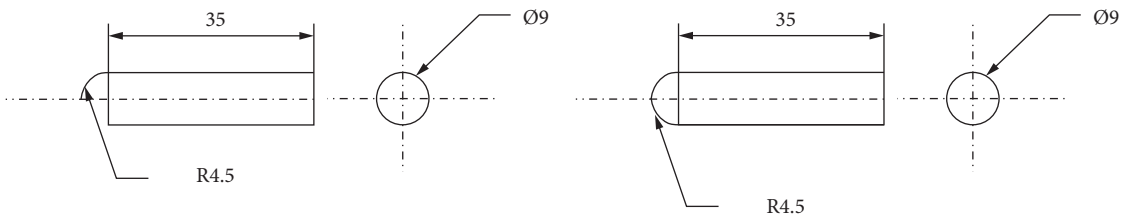

(a) (b)

Figure 1: Tipped EN8 pin surface with different configurations: (a) half-spherical shape and (b) spherical shape (all dimensions in mm).

(a) (b)

(c)

Figure 2: Nickel coating of EN8 pin. (a) Specimen preparation, (b) holding of specimens, and (c) nickel sulfate solution.

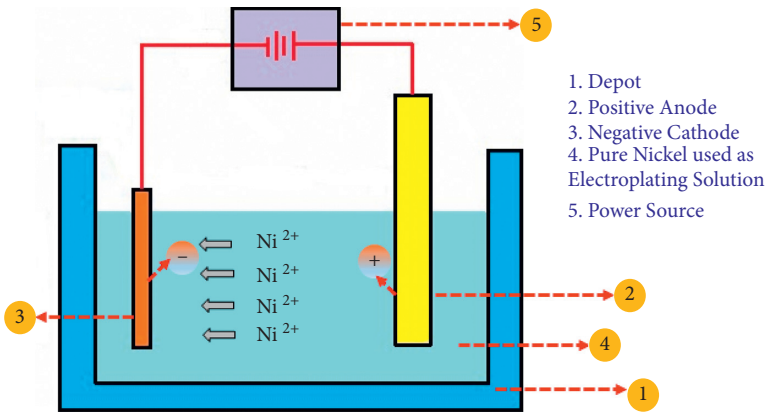

Figure 3: Schematic representation of electrodeposition coating.

2.1.1. XRD Characterization of Pin and Disc Materials. The XRD patterns of Al6061 are shown in Figure 4(a). The Al6061 XRD data show strong peaks at $2\theta = \sim 38.13^{\circ}$, $\sim 44.37^{\circ}$, followed by weaker peaks at $\sim 64.74^{\circ}$ and $\sim 77.88^{\circ}$, and $\sim 82.11^{\circ}$ due to the inherent Al content [66]. For Al 6061, the XRD pattern peak intensity is matched with JCPDS file card number 96-901-2004. In the case of Figure 4(b), i.e., EN8 steel pin (Peak 1), XRD data reveal sharp peaks at $2\theta = \sim 44.70^{\circ}$. Also, at $2\theta = \sim 65.09^{\circ}$ and $\sim 82.45^{\circ}$ dimmer peaks were detected owing to the intrinsic Fe content [66]. For EN8 steel pin, the XRD pattern peak intensity is matched with JCPDS file card number 96-900-6596. In the case of Figure 4(b), i.e., EN8 steel pin—Ni coated (Peak 2), the XRD data reveal sharp peaks at $2\theta = \sim 44.20^{\circ}$. The XRD pattern peak intensity of Ni-coated EN8 Pin is matched with JCPDS file card number no. 96-900-0658 and 96-901-2996. Similarly, at $2\theta = \sim 64.97^{\circ}$ and $\sim 82.28^{\circ}$ dimmer peaks were detected owing to the intrinsic Fe content. Also, the cause of a high broad peak at $\sim 44.20^{\circ}$ may be due to Ni-P coating [67, 68].

2.2. Experimental Details. The kinematic pair is treated as the building block in any mechanical system. The aluminum alloys are lightweight and possess excellent aesthetic qualities in any environment for a prolonged duration. Hot and cold extrusions are treated as the secondary route for processing aluminum parts. Tribo-phenomenon (i.e., mechanical interaction among stock and die) is of practical significance, as it decides the quality of parts. In the efforts of this research, understanding the tribo-phenomenon between die and aluminum stock is proposed to conduct laboratory experiments using a pin-on-disc test rig. The Al 6061 disc was used to simulate the stock in extrusion equipment. Electrodeposition of nickel material was performed to coat EN8 steel pin to a thickness of 100 μm.

The spherical (half and full) pin surface held at different angles against the rotating Al6061 disc could help to alter changes in the state of stress. The mating pair element in the disc form was precipitate hardened Al6061 alloy. Turning followed by facing operations ensures the dimensions of pin specimen possessing diameter and height equal to 9 and 35 mm, respectively. During experimentation (before and after), the pin and disc surfaces are ultrasonically cleaned with acetone. Figure 5 shows the pin-on-disc wear test rig, wherein the nickel-coated pin surfaces are subjected to three test loads (0.5, 3, and 5 kg or 4.9, 29.4, and 49.1 N). The wear tests are conducted at room temperature. Mechanical parts, namely, bearings, rotate smoothly at the speed of 100–250 rpm [69], wherein bearing supports gear parts, shafts, and so on. The test loads (0.5–5 kg) are selected in accordance with gear applications carried out earlier by authors [70, 71]. The wear parameters considered for examination on friction coefficient and wear rate are presented in Table 2. Three samples are separately prepared for each loading condition (0.5, 3, and 9 kg), and average values of three wear rate and coefficient of frictions are recorded to conduct analysis. The specimens are held on an aluminum disc, which is oriented at different configured stress state (full sphere and hemisphere configured at 0°, 45°, and 90°) with reference to sliding directions subjected to wear parameters (Figure 6). This could result in a different state of stress. Note that, after performing wear examination the surface topography of, namely, Al6061 and nickel-coated EN 8 steel is captured. SEM was performed to know the insight of wear mechanisms. The dimensions corresponding to Al 6061 disc are presented in Figure 7. Prior to wear examination, the pin and disc samples are examined for surface roughness and hardness. The surface roughness that corresponds to the uncoated pin, nickel-coated pin, and disc surface was maintained equal to 0.2 μm. The hardness values that correspond to uncoated pin, nickel-coated pin, and disc surfaces were found equal to 217.7 HV, 261.5 HV, and 98.1 HV.

3. Results and Discussion

The results of velocity discontinuity and state of stress caused by the sliding pair contact surfaces are discussed based on sliding mechanics. The EN8 pin surfaces coated with nickel for altering velocity discontinuity against the Al 6061 disc were also discussed. The state of stress altered by different pin tip-shaped surfaces (i.e., spherical and half-spherical) configured pin at different angles with reference to sliding direction. The state of stress as a result of different normal loads is discussed. Wear behavior and its mechanisms are examined with the help of scanning electron microscopic images.

3.1. Full Sphere Coated with Nickel Sliding against Al 6061 Disc. Figure 8 shows the coefficient of friction obtained for different loads with reference to time constraints. At 0.5 kg load, the friction coefficient increases from 0 to 0.18 for the duration of 5 seconds, and thereafter, a steady increase was observed till 110 seconds. Increased coefficient of friction with load might occur due to the plowing effect as a result of increased dislocation density, plastic deformation, and penetration depth [72]. Similarly, the coefficient of friction value tends to increase from 0 to ~0.5 till 10 seconds for 3 kg and 0 to ~0.56 till 8 seconds for 5 kg. The coefficient of friction remains at an almost steady state after crossing 10 seconds of duration. It was noted that at all loads the friction coefficient curves showed a similar trend, wherein the transient state was seen during the initial stage followed by a steady state (refer to Figure 8). The rate of increase in friction coefficient values was found to be of lesser magnitude after 10 seconds at all loads, compared to the time period of 0–5 seconds. This occurs because at the beginning of the experiments or sliding phenomenon, the soft disc (i.e., Al 6061 alloy) was plowed by the hard asperities of coating surfaces that resulted in the highest friction peaks. Similar observations are seen on friction performance of phosphate-coated brake materials [73]. A steady state with friction coefficient curves became flattened with the increased number of revolutions or time duration against sliding tests. As sliding continues, the hard asperities of coated pin surfaces slowly covered with accumulated transferred material (i.e., plowing mechanisms of

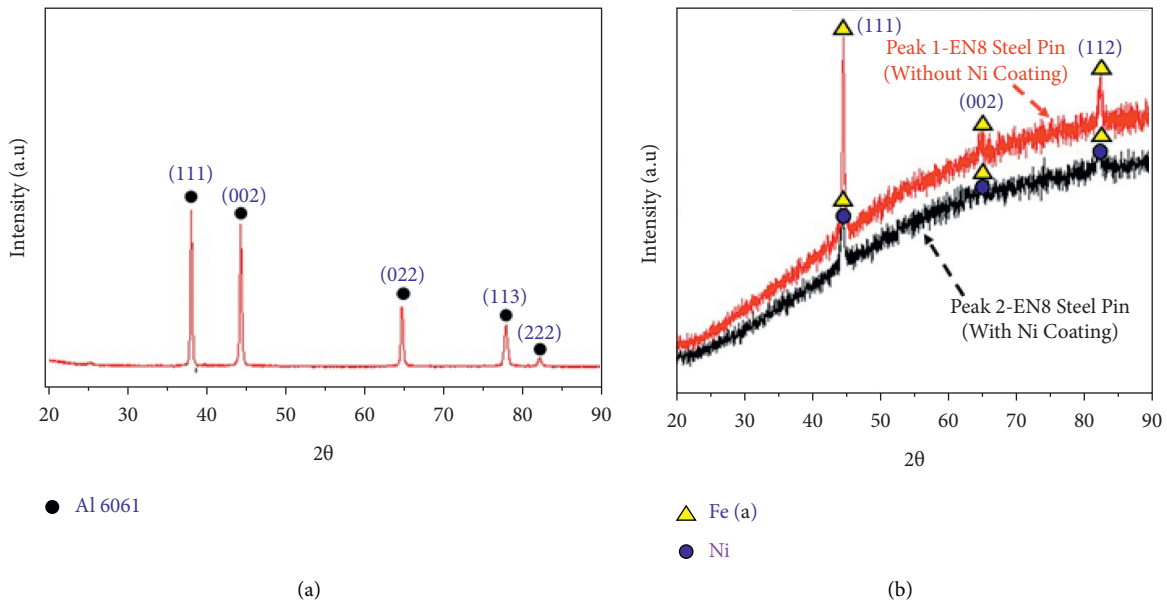

Figure 4: XRD analysis of (a) Al6061 disc and (b) EN8 steel pin (with and without Ni coating).

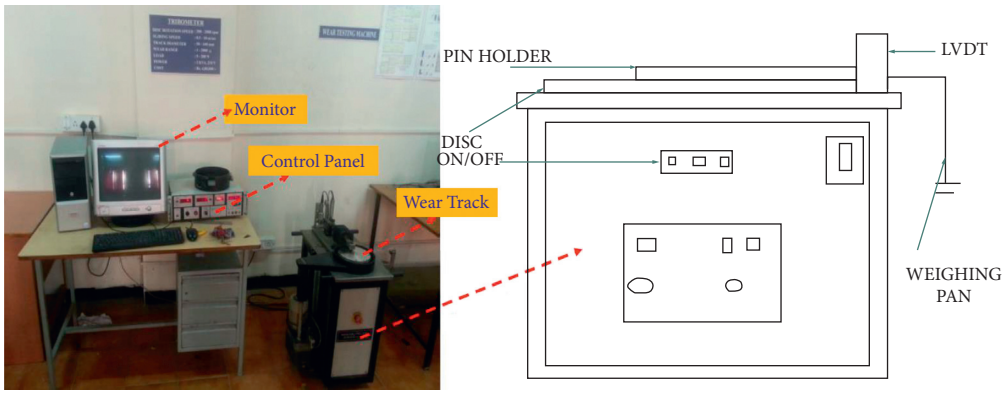

Figure 5: Schematic representations of pin-on-disc wear test rig with its line diagram.

Table 2: Experimental parameters for tribo-pairs: Al disc on EN8 steel pin (uncoated and coated).

S/No	Parameters	Aluminum disc on EN8 steel pin
1	Load (kg)	0.5, 3, and 5 kg
2	Track diameter (mm)	110 mm
3	Sliding time (seconds)	120 seconds
4	Speed (rpm)	250 rpm

hard asperities reduce, and in turn, friction coefficient becomes steady state), which was later deformed, and curves became flattened. The observations are similar to the friction behavior studies of titanium nickel coatings [74]. The average coefficient of friction tested at different loading conditions is presented in Table 3. The minimum and maximum friction coefficients were found equal to 0.3 for 0.5 kg and 0.48 for 3 kg loads, respectively. Interesting to note that, negligible change in friction coefficient values was attained after crossing the load from 3 kg to 5 kg. This is because more plastic deformation occurs at the sliding pairs as a result of compressive and shear forces [75].

3.2. Pin with Tip of the Hemisphere Coated with Nickel Configured 90° to the Sliding Directions against the Aluminum Disc. Figures 9(a)–9(c) show the variations of coefficient of friction for nickel-coated half-sphere configured at different orientations (0°, 45°, and 90°) sliding against Al6061 disc at different loads. For 0.5 kg load, the coefficient of friction rapidly increases from 0 to 0.33 up to 15 seconds at 90° orientation, 0 to 0.37 up to 35 seconds at 45° orientation, and 0 to 0.43 up to 8 seconds at 45° orientation, respectively. Similarly for 3 kg load, the coefficient of friction was found equal to 0.54 for 0°, 45°, and 90° orientations, respectively. However, for 5 kg load, the coefficient of friction steadily

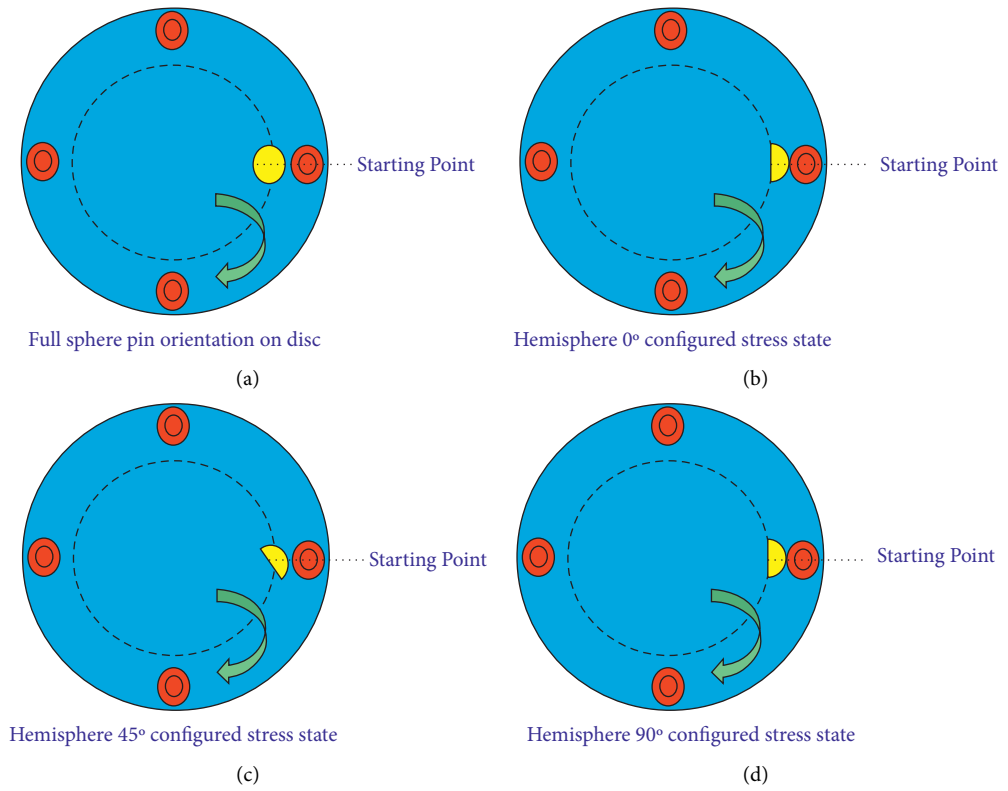

Figure 6: Schematic of aluminum disc with different orientations. (a) Full sphere pin orientation on disc; (b) hemisphere 0° configured stress state, (c) hemisphere 45° configured stress state, and (d) hemisphere 90° configured stress state.

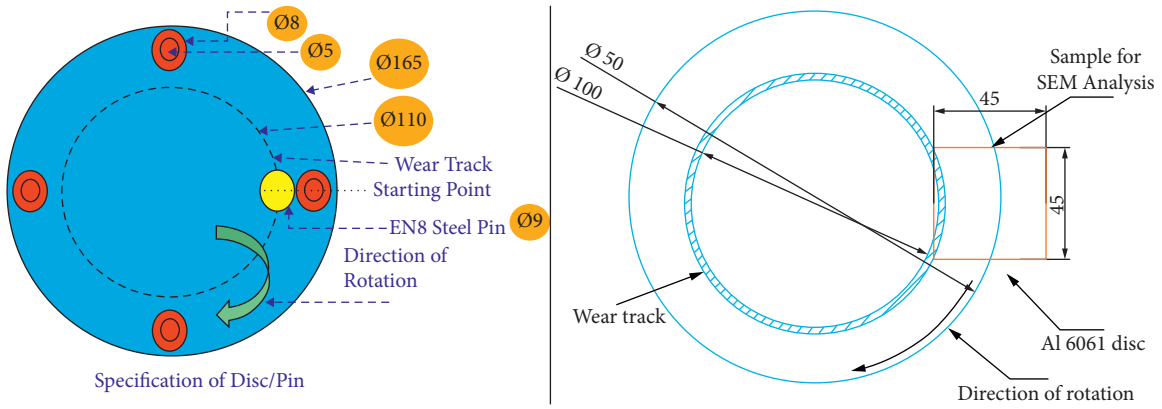

Figure 7: Schematic representations of Al6061disc.

increases to 0.6 for 0° and 45°, whereas 0.63 for 90° orientation of pin sample. It was clearly noted that comparatively stabilized friction curves were observed for 45° orientation than largest scatter (this occurrence might be due to stick-slip phenomenon) in friction values for 0° and 90°. It was clearly noticed from the friction curves that a rapid increase in friction at the initial stage of sliding due to soft aluminum disc was plowed by hard asperities of coatings. Thereafter, the surfaces are significantly altered such that original topographical orientation features (smooth surface ensures friction equalized to similar influenced values) possess minor variations showing that the friction curves remain flattened or steady for all orientations tested against different loads. Hard asperities of coatings tend to repeatedly indent the soft aluminum disc surfaces under stick-slip conditions, which results in increased sliding forces above the steady-state value during the beginning of experiments at all loads and orientations [76]. From Figures 9(a)–9(c), it was clear that the load at which both stick slips at start and amplitude oscillations are lower for 45° orientation than 0° and 90°. The average friction coefficients tested at different loads (0.5, 3, and 5 kg) against different pin configurations (0°, 45°, and 90°) are presented in Table 4. The coefficient of friction that increases with increasing load was clearly observed.

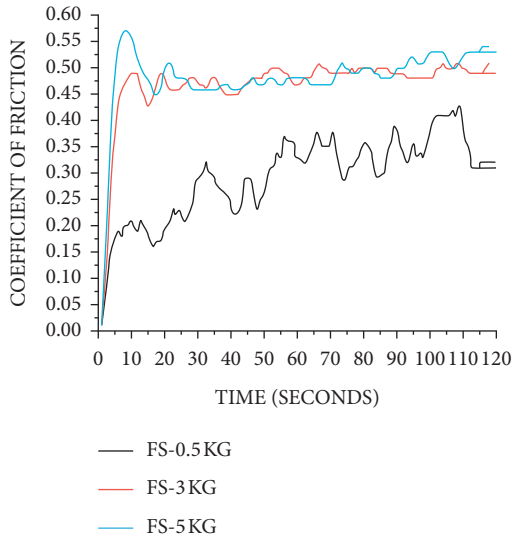

Figure 8: Coefficient of friction with sliding time at different normal loads.

Table 3: Average coefficient of friction for different load conditions.

Load (kg)	COF (μ) of sphere	
	With coating	Without coating
0.5	0.30 ± 0.031	0.55 ± 0.025
3.0	0.48 ± 0.035	0.68 ± 0.043
5.0	0.47 ± 0.038	0.70 ± 0.032

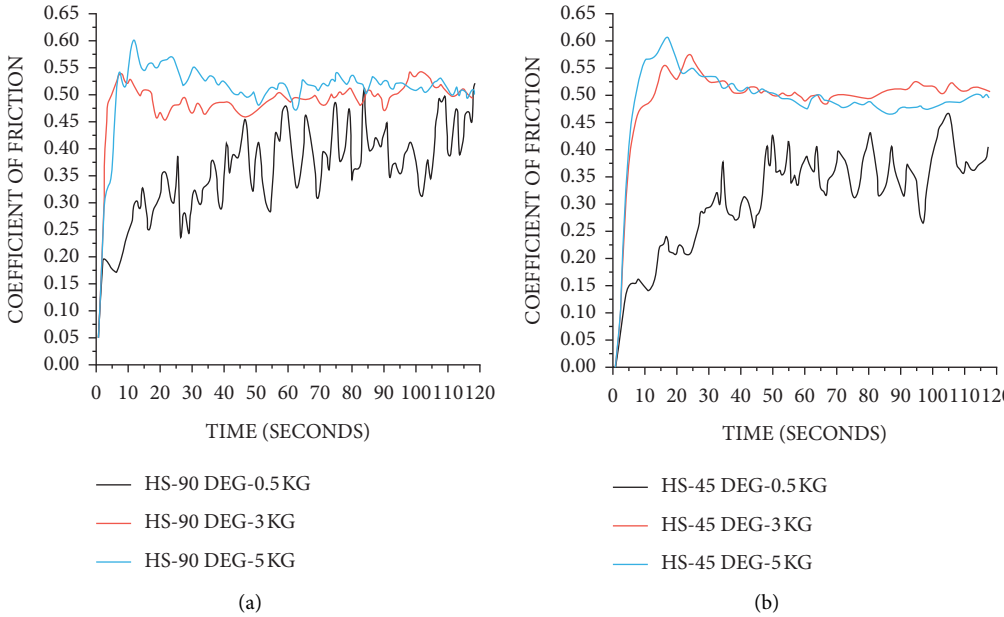

Figure 9: Continued.

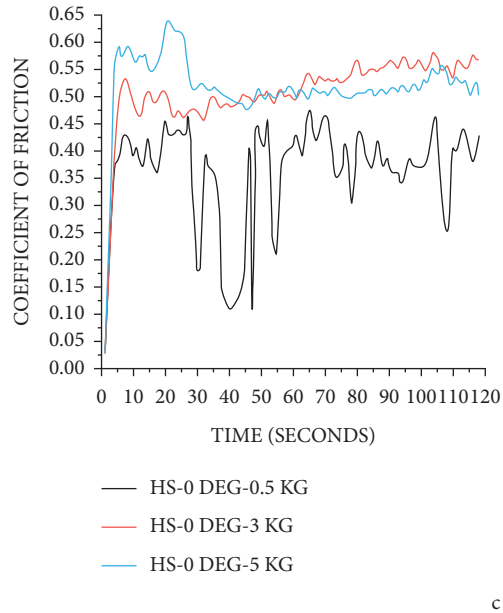

(c)

Figure 9: Coefficient of friction of nickel-coated half-sphere configured sliding against Al6061 disc with sliding time against different loads: (a) 90°, (b) 45°, and (c) 0°.

Table 4: Average coefficient of friction for different load conditions.

Load, kg	Coating samples: coefficient of friction, μ			Uncoated samples: coefficient of friction, μ		
	Pin configured at 90°	Pin configured at 45°	Pin configured at 0°	Pin configured at 90°	Pin configured at 45°	Pin configured at 0°
0.5	0.37 ± 0.025	0.33 ± 0.022	0.37 ± 0.028	0.61 ± 0.022	0.60 ± 0.012	0.62 ± 0.021
3.0	0.49 ± 0.045	0.51 ± 0.035	0.52 ± 0.031	0.68 ± 0.032	0.71 ± 0.025	0.71 ± 0.034
5.0	0.52 ± 0.052	0.50 ± 0.037	0.52 ± 0.028	0.71 ± 0.023	0.70 ± 0.017	0.72 ± 0.025

The surface topography orientation did not influence much on friction average friction coefficient for 0° and 90°, whereas comparatively lesser friction values were observed at 45° orientations. The plane strain conditions cause more amplitude of oscillations with higher frictions in the curves for 0° and 90° orientations. The reduced friction at 45° orientation is attributed to less continuous contact surface area. The behavior of pin geometry (full sphere and hemisphere) on frictional curves is presented in Figures 8 and 9. The mean values of coefficient of friction for spherical and hemispherical pins possess approximately similar magnitude values, with comparatively less friction for spherical pin surfaces (refer to Tables 3 and 4). The hemispherical pin friction curves showed that more fluctuations might be due to the damage that occurred at sliding or tribo-pairs, wherein the accumulated debris released from surface layers causes highly scattered variation in friction coefficients [77, 78]. However, full spherical pin surfaces are often smooth, which resulted in more stable friction. Similar observations are reported with different geometries of pin surfaces [79, 80]. Tables 3 and 4 clearly show that the nickel-coated pins resulted in a lesser coefficient of friction compared with uncoated or bare specimens. Increased hardness with nickel coating led to reducing the coefficient of friction values due to coating imparts, better oxide protection, and hot hardness properties. These observations are in good agreement with published literature [81].

3.3. Worn Surface Analysis of Al6061 Disc. Figure 10 depicts the wear surface morphology of Al6061 disc surfaces at different loads and orientations. From Figures 10(a)–10(h), the arrow mark represents sliding direction and the numbering 1, 2, and 3 represent flecks, slender abrasive furrows, and dense abrasive furrows, respectively. Figures 10(a)–10(b) show the SEM micrographs of track surface subjected to a load of 0.5 and 5 kg that correspond to the geometry of pin surface made of a full sphere. The track surface of a full sphere subjected to 5 kg load showed more abrasion than with 0.5 kg of load by pin material. Also, it is observed that a lesser extent of adhesions is observed on the track surfaces. Figures 10(c)–10(d) show the SEM micrographs and show the track of the hemispherical pin configured at 90° against sliding direction subjected to different loading conditions. Both figures showed more adhesion effects than that of abrasion. It can also be observed that the abrasion effects are comparatively larger than that obtained for Figure 9(a). Figure 9(c) shows more pronounced adhesion for 0.5 kg load compared to that obtained for 5 kg of load.

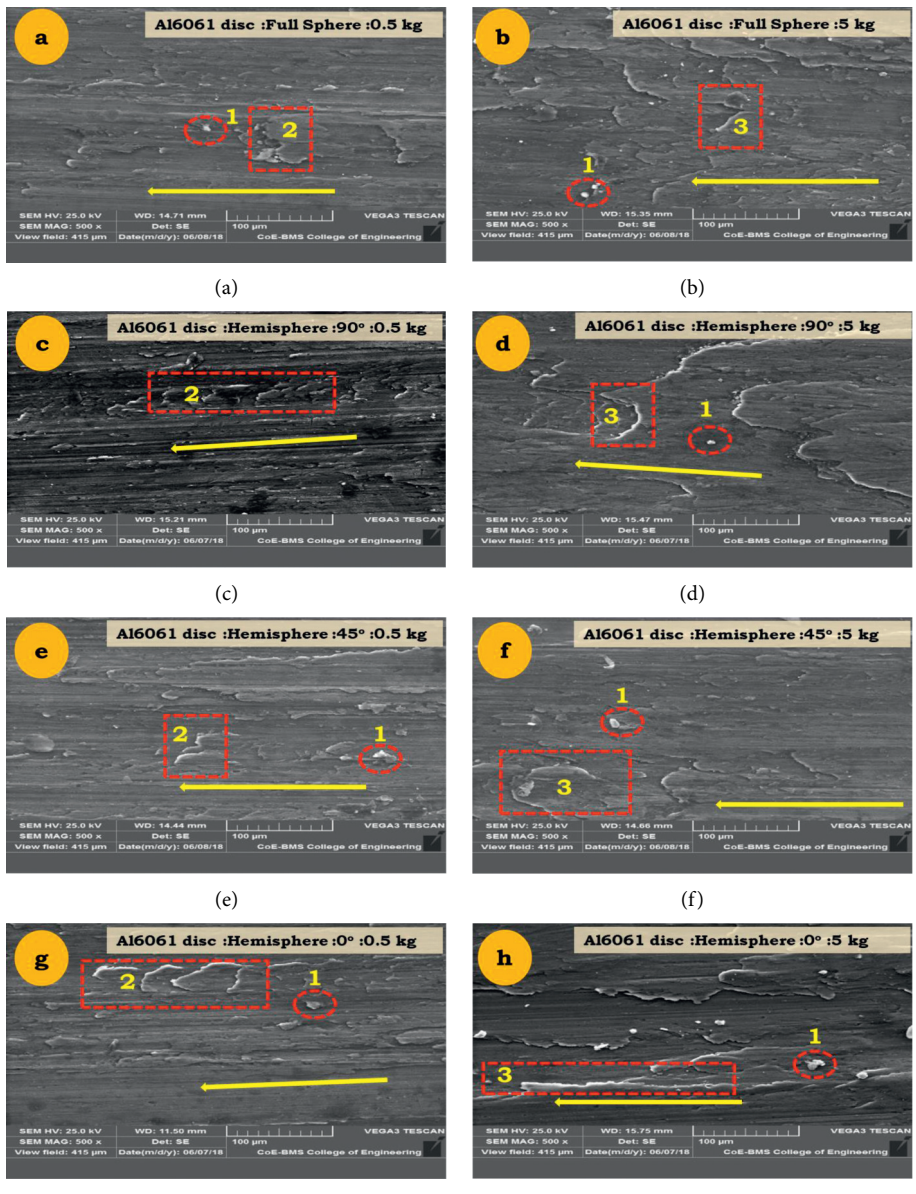

(a) (b) (c) (d) (e) (f) (g) (h)

Figure 10: SEM wear tracks of Al6061 disc surfaces for different load conditions and orientations.

Figure 10(d) clearly shows that there exists a larger extent of extrusion compared to the micrographs of Figures 10(a)–10(c). Figure 10(e) shows the track surface that corresponds to a pin configured to 45° against sliding direction subjected to different loads. The said figures clearly show that there is an extrusion phenomenon coupled with traces of abrasion. Figure 10(g) shows the small extent of abrasion, and the amount of extrusion was more pronounced for 5 kg normal load than that obtained for 0.5 kg against sliding direction. Under dry sliding conditions, there is a significant level of iron layer transfer from the EN8 steel pins to the surface of the aluminum disc plate. The amount of transferred layer was also found to increase load from 0.5 kg to 5 kg. Analogous remarks were made by quite a few researchers [76, 80, 82].

3.4. Worn Surface Analysis of the Nickel-Coated Pin. Figure 11 depicts the wear surface morphology of EN8 steel pin coated with nickel at different loads and orientations. From Figures 11(a)–11(h), the arrow mark represents cracks and the numbering 1, 2, and 3 represent slender abrasive furrows, material transfer area, and dense abrasive furrows, respectively. Figure 11(a) shows the SEM micrograph of pin surface for the full sphere at 0.5 kg load depicting the transfer of aluminum layer on the pin surface at a leading edge. Figure 11(b) presents the hemispherical pin configured to 90° that showed the aluminum layer transferred on the pin surface at the leading edge. Interesting to note that, the amount of aluminum transfer on the pin surface is comparatively more than that of the full sphere configuration seen in Figure 11(a). Similar observations were recorded for

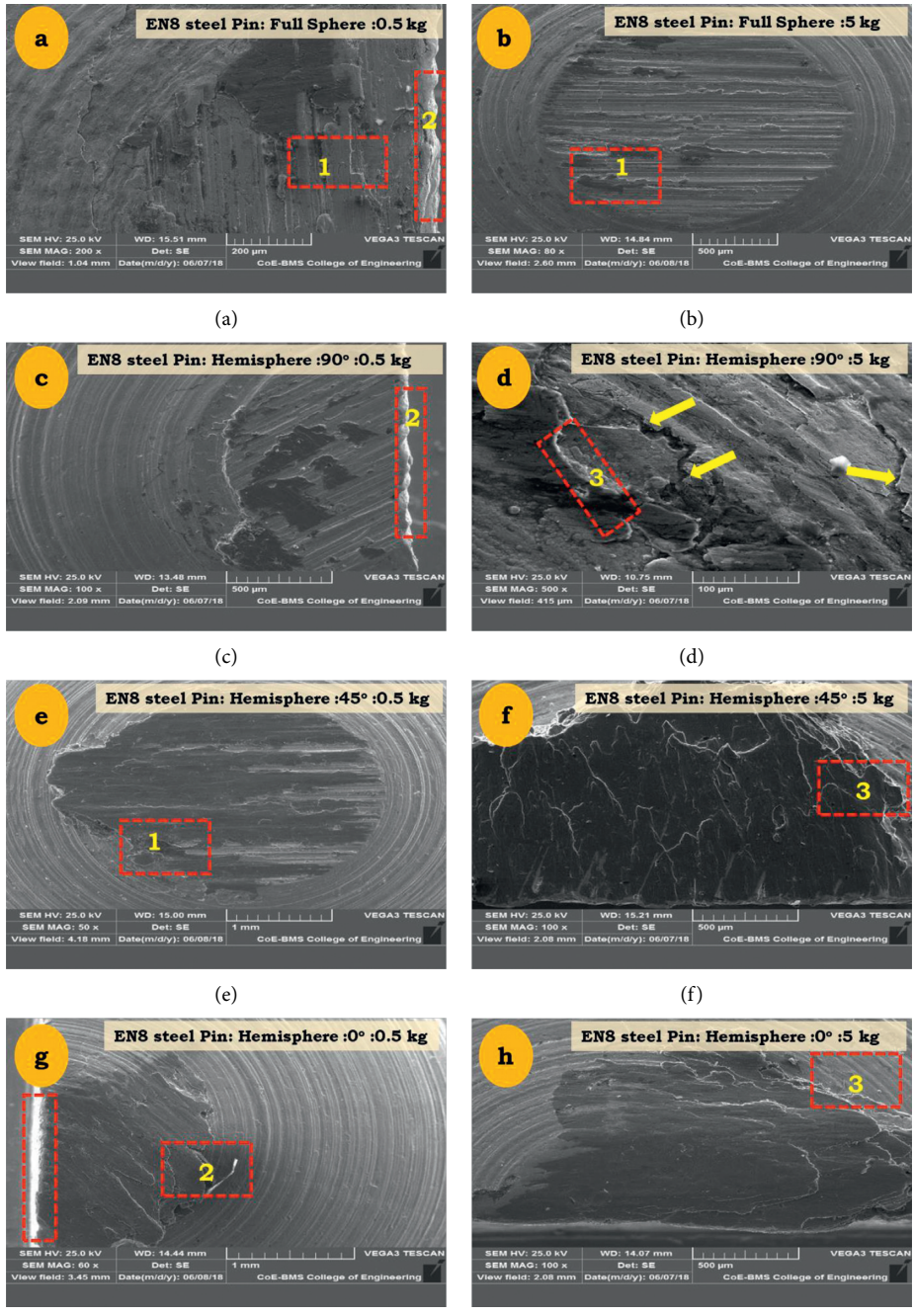

(a) (b) (c) (d) (e) (f) (g) (h)

FIGURE 11: SEM micrograph of nickel-coated pin surfaces for different load conditions and orientations.

a hemispherical pin configured to 45° and 0° as shown in Figures 11(c) and 11(d). Figures 11(e)–11(h) show the pin surface for all configurations at 5 kg load depicting aluminum transfer layer at the leading edge. Compared to 0.5 kg, the amount of aluminum transfer is quite large at 5 kg. Furthermore, as the steel pins slid across the aluminum plate, a few of the relatively weak asperities with poorer Al plate areas will indeed crack and then abide by the steel pin. The level of severity is such that these weaken the crack and relocate to the steel pin surface that is determined by oriented angle. While EN8 steel is slid tangential to the abrasion track rather than parallel to the sliding direction, the chances of breakdown of plate severities will surge. This is due to the asperities being aligned across the sliding direction when the oriented angle is 90° but along the sliding direction when the oriented angle is 0°. As the oriented angle and load are reduced, the extent of asperity breaking lessens, and thus, the extent of iron removal from the pin also decreases. Similar observations were made by several researchers [45, 76, 80, 83].

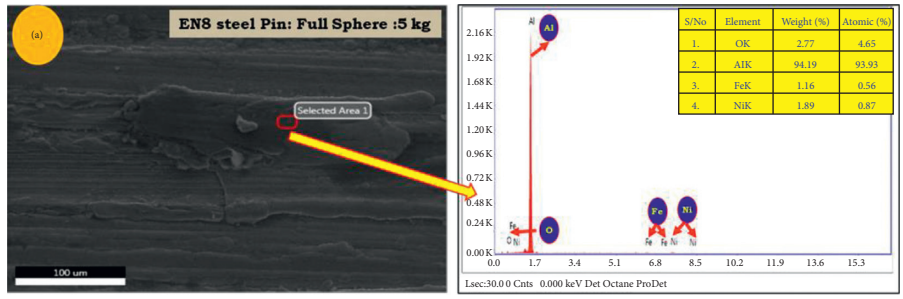

(a)

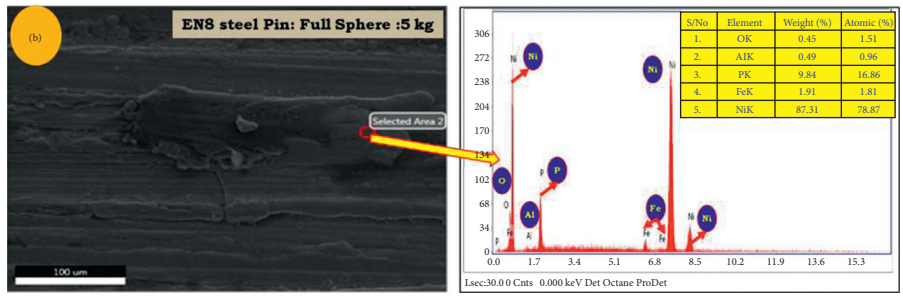

(b)

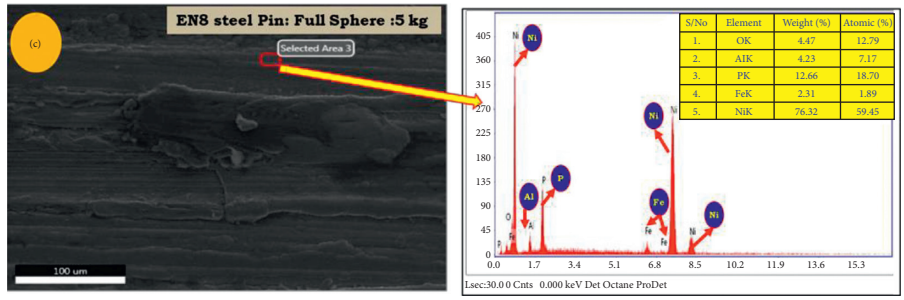

(c)

Figure 12: EDAX analysis of nickel-coated pin surfaces for different locations.

3.5. EDAX Analysis of the Nickel-Coated Pin. EDAX studies have been conducted for identifying elements present in worn surface and debris of nickel-coated spherical tipped pin surface at a load of 5 kg at different selected areas. The elemental analysis on transferred aluminum on pin surface was carried out at different locations and is shown in Figures 12(a)–12(c), respectively. From Figure 12(a), it was revealed that aluminum is 94.19 in weight percentage and the transfer layer is aluminum. Figure 12(b) reveals that nickel is 87.31 in weight percentage. The nickel coating is found to be intact. Figure 12(a) reveals that nickel is 76.32 in weight percentage. The nickel coating is found to be intact. From Figures 12(a)–12(c), the commonly observed elements were Al, Fe, Ni, and O. The occurrence of Fe implies that Fe has been transferred from the pin (EN8) to the disc surface, confirming the formation of an oxide layer on the disc, which protects the disc. The existence of thick oxides aids in the formation of wear protective layers.

4. Conclusions

The friction and wear behavior of tribo-pairs such as nickel-coated EN8 steel pin and Al6061 alloy disc was investigated at different loads and pin surface that configured to different geometries and orientations. The following conclusions that are drawn from this study are discussed in the following:

(1) Electrodeposition technique was applied to coat the nickel material onto the EN8 steel pin surfaces to a thickness of 100 μm. To induce a different state of stress, the geometry of pin surfaces is configured to full sphere and hemisphere with a different orientation (0°, 45°, and 90°) and load (0.5, 3, and 5 kg load).

(2) In full sphere configuration, the minimum and maximum friction coefficients were found equal to 0.3 for 0.5 kg, 0.48 for 3 kg loads, and 0.47 for 5 kg,

respectively. The plastic deformation that occurs at sliding pairs initiates at 3 kg load (as a result of compressive and shear forces), which resulted in a negligible change in friction coefficient values.

(3) The hemispherical pin friction curves showed that more fluctuations might be due to the damage that occurred at sliding or tribo-pairs, wherein the accumulated debris released from surface layers causes highly scattered variation in friction coefficients. However, full spherical pin surfaces are often smooth, which resulted in more stable friction.

(4) At higher load (say 5 kg), the abrasion and extrusion were more pronounced than 0.5 kg against sliding direction on the wear tracks of Al6061 disc surfaces.

(5) The amount of aluminum transfer on the hemisphere pin surface is comparatively more than that of full sphere configuration. As the oriented angle and load are reduced, the extent of asperity breaking lessens, and thus, the extent of iron removal from the pin also decreases.

(6) From COF vs. time plot, the coating studies are described by the transient state seen during the initial stage, followed by a steady state at all loads.

(7) Hard asperities of coatings tend to repeatedly indent the soft aluminum disc surfaces under stick-slip conditions, which results in increased sliding forces above the steady-state value during the beginning of experiments at all loads and orientations.

(8) From the wear surface morphology and surfaces at different loads and orientations, it is observed that a lesser extent of adhesion effects is observed than that of abrasion on the track surface effects [84].

Data Availability

Data used to support the findings of this study are available from the corresponding author upon request.

Conflicts of Interest

The authors declare that they have no conflicts of interest.

References

[1] C. J. Evans and J. B. Bryan, ""Structured," "textured" or "engineered" surfaces," *CIRP Annals*, vol. 48, no. 2, pp. 541–556, 1999.

[2] W. Huang, L. Jiang, C. Zhou, and X. Wang, "The lubricant retaining effect of micro-dimples on the sliding surface of PDMS," *Tribology International*, vol. 52, pp. 87–93, 2012.

[3] W. Federle, W. J. P. Barnes, W. Baumgartner, P. Drechsler, and J. M. Smith, "Wet but not slippery: boundary friction in tree frog adhesive toe pads," *Journal of The Royal Society Interface*, vol. 3, no. 10, pp. 689–697, 2006.

[4] D. W. Bechert, M. Bruse, W. Hage, and R. Meyer, "Fluid mechanics of biological surfaces and their technological application," *Naturwissenschaften*, vol. 87, no. 4, pp. 157–171, 2000.

[5] A. Parthasarathy, L. Avinash, K. N. Varun Kumar, B. Sajjan, and S. Varun, "Fabrication and characterization of Al-0.4% Si-0.5% Mg-SiCp using permanent mould casting technique," *Applied Mechanics and Materials*, vol. 867, pp. 34–40, 2017.

[6] L. Avinash, T. Ram Prabhu, A. Parthasarathy, K. N. Varun Kumar, and B. Sajjan, "Wear and mechanical behaviour of Hypo-eutectic Al-7% Si-0.5% Mg alloy (A357) reinforced with Al2O3 particles," *Applied Mechanics and Materials*, vol. 829, pp. 66–72, 2016.

[7] R. E. Melchers, "Time dependent development of aluminium pitting corrosion," *Advances in Materials Science and Engineering*, vol. 2015, no. 12, 10 pages, Article ID 215712, 2015.

[8] S. Jayaprakash, S. Siva Chandran, T. Sathish et al., "Effect of tool profile influence in dissimilar friction stir welding of aluminium alloys (AA5083 and AA7068)," *Advances in Materials Science and Engineering*, vol. 2021, Article ID 7387296, 7 pages, 2021.

[9] T. V. Christy, N. Murugan, and S. Kumar, "A comparative study on the microstructures and mechanical properties of Al 6061 alloy and the MMC Al 6061/TiB2/12p," *Journal of Minerals and Materials Characterization and Engineering*, vol. 9, no. 1, pp. 57–65, 2010.

[10] G. V. Kumar, C. S. P. Rao, N. Selvaraj, and M. S. Bhagyashekar, "Studies on Al6061-SiC and Al7075-Al2O3 metal matrix composites," *Journal of Minerals and Materials Characterization and Engineering*, vol. 9, no. 1, pp. 43–55, 2010.

[11] T. B. Rao and G. R. Ponugoti, "Characterization, prediction, and optimization of dry sliding wear behaviour of Al6061/WC composites," *Transactions of the Indian Institute of Metals*, vol. 74, no. 1, pp. 159–178, 2021.

[12] V. Anandakrishnan and A. Mahamani, "Investigations of flank wear, cutting force, and surface roughness in the machining of Al-6061–TiB 2 in situ metal matrix composites produced by flux-assisted synthesis," *International Journal of Advanced Manufacturing Technology*, vol. 55, no. 1, pp. 65–73, 2011.

[13] H. Karakoç, S. Karabulut, and R. Çıtak, "Study on mechanical and ballistic performances of boron carbide reinforced Al 6061 aluminum alloy produced by powder metallurgy," *Composites Part B: Engineering*, vol. 148, pp. 68–80, 2018.

[14] J. G. Kaufman, *Properties of Aluminum Alloys; Tensile, Creep, and Fatigue Data at High and Low Temperatures*, ASM International: Almere, Geauga, OH, USA, 2002.

[15] X. Li, M. Sosa, and U. Olofsson, "A pin-on-disc study of the tribology characteristics of sintered versus standard steel gear materials," *Wear*, vol. 340-341, pp. 31–40, 2015.

[16] N. H. Dhanvij, S. H. Gawande, and P. S. Gajjal, "Performance evaluation of EN24 for planetary gear transmission of CNC bending machine," *Journal of the Brazilian Society of Mechanical Sciences and Engineering*, vol. 42, pp. 1–17, 2020.

[17] M. Charool, M. Wani, M. Hanief, A. Chetani, and M. Rather, "Tribological characteristics of EN8 and EN24 steel against aluminium alloy 6061 under lubricated condition," *Advanced Materials Proceedings*, vol. 2, no. 7, pp. 445–449, 2017.

[18] W. K. Shafi and M. S. Charoo, "An overall review on the tribological, thermal and rheological properties of nano-lubricants," *Tribology: Materials, Surfaces & Interfaces*, vol. 15, no. 1, pp. 20–54, 2021.

[19] J. Takadoum, *Materials and Surface Engineering in Tribology*, Wiley, Hoboken, NJ, USA, 2013.

[20] C. Gachot, S. M. Hsu, H. L. Costa, and H. L. Costa, "A critical assessment of surface texturing for friction and wear improvement," *Wear*, vol. 372, pp. 21–41, 2017.

[21] D. Žeželj, A. Lončar, and K. Vučković, "Multi-objective spur gear pair optimization focused on volume and efficiency," *Mechanism and Machine Theory*, vol. 372-373, pp. 185–195, 2018.

[22] S. Baglioni, F. Cianetti, and L. Landi, "Influence of the addendum modification on spur gear efficiency," *Mechanism and Machine Theory*, vol. 49, pp. 216–233, 2012.

[23] L. Zemanová and P. Rudolf, "Flow inside the sidewall gaps of hydraulic machines: a review," *Energies*, vol. 13, no. 24, p. 6617, 2020.

[24] S. H. Adsul, K. R. C. Soma Raju, B. V. Sarada, S. H. Sonawane, and R. Subasri, "Evaluation of self-healing properties of inhibitor loaded nanoclay-based anticorrosive coatings on magnesium alloy AZ91D," *Journal of Magnesium and Alloys*, vol. 6, no. 3, pp. 299–308, 2018.

[25] S. Arulvel, A. Elayaperumal, and M. S. Jagatheeshwaran, "Controlling adhesive wear failure of nickel-phosphorus coating at high load condition using crab shell particle as reinforcement," *Engineering Failure Analysis*, vol. 90, pp. 310–323, 2018.

[26] T. He, Q. J. Wang, X. Zhang et al., "Visco-elastohydrodynamic lubrication of layered materials with imperfect layer-substrate interfaces," *International Journal of Mechanical Sciences*, vol. 189, Article ID 105993, 2020.

[27] V. Gurey, H. Shynkarenko, and I. Kuzio, "Mathematical model of the thermoelasticity of the surface layer of parts during discontinuous friction treatment," in *Design, Simulation, Manufacturing: The Innovation Exchange, Lecture Notes in Mechanical Engineering*, pp. 12–22, Springer International Publishing, Berlin, Germany, 2021.

[28] P. Põdra and S. Andersson, "Finite element analysis wear simulation of a conical spinning contact considering surface topography," *Wear*, vol. 224, no. 1, pp. 13–21, 1999.

[29] R. Prabhu Sekar and R. Sathishkumar, "Enhancement of wear resistance on normal contact ratio spur gear pairs through non-standard gears," *Wear*, vol. 380-381, pp. 228–239, 2017.

[30] W. J. Qin and C. Y. Guan, "An investigation of contact stresses and crack initiation in spur gears based on finite element dynamics analysis," *International Journal of Mechanical Sciences*, vol. 83, pp. 96–103, 2014.

[31] L. Ivanović, "Reduction of the maximum contact stresses by changing geometric parameters of the trochoidal gearing teeth profile," *Meccanica*, vol. 51, no. 9, pp. 2243–2257, 2016.

[32] J. H. Kuang and A. D. Lin, "The effect of tooth wear on the vibration spectrum of a spur gear pair," *Journal of Vibration and Acoustics*, vol. 123, no. 3, pp. 311–317, 2001.

[33] A. Lakshmikanthan, V. Mahesh, R. T. Prabhu, M. G. C. Patel, and S. Bontha, "Free vibration analysis of A357 alloy reinforced with dual particle size silicon carbide metal matrix composite plates using finite element method," *Archives of Foundry Engineering*, vol. 21, no. 1, pp. 101–112, 2021.

[34] J. Sadeghi and B. Akbari, "Field investigation on effects of railway track geometric parameters on rail wear," *Journal of Zhejiang University - Science*, vol. 7, no. 11, pp. 1846–1855, 2006.

[35] J. Sadeghi, "Sufficient experimental methods in investigation of dynamic behavior of track components and track system," in *Proceedings of the 7th International Conference on Mechanics of Systems*, pp. 71–79, University of Wollongong, Wollongong, Australia, June 2002.

[36] M. A. Khan and K. Gupta, "A study on machinability of nickel based superalloy using micro-textured tungsten carbide cutting tools," *Materials Research Express*, vol. 7, no. 1, Article ID 016537, 2020.

[37] M. Adam Khan and K. Gupta, "Optimization of machining parameters for material removal rate and machining time while cutting inconel 600 with tungsten carbide textured tools," in *Intelligent Manufacturing*, pp. 37–56, Springer, Berlin, Germany, 2021.

[38] A. Arslan, H. H. Masjuki, M. A. Kalam et al., "Surface texture manufacturing techniques and tribological effect of surface texturing on cutting tool performance: a review," *Critical Reviews in Solid State and Materials Sciences*, vol. 41, no. 6, pp. 447–481, 2016.

[39] S. Durairaj, J. Guo, A. Aramcharoen, and S. Castagne, "An experimental study into the effect of micro-textures on the performance of cutting tool," *International Journal of Advanced Manufacturing Technology*, vol. 98, no. 1, pp. 1011–1030, 2018.

[40] M. Mart'nez, A. Massetti, and H. Svoboda, "Effect of the pin geometry on the wear behavior of weld-deposited hardfacing," *Procedia Materials Science*, vol. 1, pp. 305–312, 2012.

[41] K. Holmberg and A. Matthews, *Coatings Tribology: Properties, Mechanisms, Techniques and Applications in Surface Engineering*, Elsevier, Amsterdam, Netherlands, 2009.

[42] C. M. P. Kumar, M. P. G. Chandrashekarappa, R. M. Kulkarni, D. Y. Pimenov, and K. Giasin, "The effect of Zn and Zn-WO3 composites nano-coatings deposition on hardness and corrosion resistance in steel substrate," *Materials*, vol. 14, no. 9, p. 2253, 2021.

[43] C. M. P. Kumar, A. Lakshmikanthan, M. P. G. Chandrashekarappa, D. Y. Pimenov, and K. Giasin, "Electrodeposition based preparation of Zn-Ni alloy and Zn-Ni-wc nano-composite coatings for corrosion-resistant applications," *Coatings*, vol. 11, no. 6, p. 712, 2021.

[44] G C Manjunath Patel, N B Pradeep, Girisha Lakhman Naik, H M Harsha, and A. K. Shettigar, "Experimental analysis and optimization of plasma spray parameters on microhardness and wear loss of Mo-Ni-Cr coated super duplex stainless steel," *Australian Journal of Mechanical Engineering*, vol. 2020, pp. 1–13, Article ID 1808760, 2020.

[45] H. A. Ching, D. Choudhury, M. J. Nine, and N. A. Abu Osman, "Effects of surface coating on reducing friction and wear of orthopaedic implants," *Science and Technology of Advanced Materials*, vol. 15, no. 1, Article ID 014402, 2014.

[46] S. Yadav, S. Ranganath, S. Sharieff, R. Suresh, and L. Avinash, "Investigations on the change in state of stress with respect to the sliding direction in dry sliding wear of hard elastic material with different geometry and orientation on ductile flat surface," *FME Transactions*, vol. 48, no. 3, pp. 716–723, 2020.

[47] A. D. Pogrebnyak, V. M. Beresnev, A. S. Kaverina et al., "Adhesive strength and physical, mechanical, and triboengineering properties of nano- and microstructural Al2O3 coatings," *Journal of Friction and Wear*, vol. 33, no. 3, pp. 195–202, 2012.

[48] G. Quercia, I. Grigorescu, H. Contreras, C. Di Rauso, and D. Gutierrez-Campos, "Friction and wear behavior of several hard materials," *International Journal of Refractory Metals and Hard Materials*, vol. 19, no. 4–6, pp. 359–369, 2001.

[49] J. C. Walker, S. R. Saranu, A. H. Kean, and R. J. K. Wood, "Fe nano-particle coatings for high temperature wear resistance," *Wear*, vol. 271, no. 9-10, pp. 2067–2079, 2011.

[50] M. S. Jagatheeshwaran, A. Elayaperumal, and S. Arulvel, "Wear characteristics of electroless NiP/bio-composite coatings on En8 steel," *Journal of Manufacturing Processes*, vol. 20, pp. 206–214, 2015.

[51] F. Yao and L. Fang, "Thermal stress cycle simulation in laser cladding process of Ni-based coating on H13 steel," *Coatings*, vol. 11, no. 3, p. 203, 2021.

[52] C. P. Paul, S. K. Mishra, P. Tiwari, and L. M. Kukreja, "Solid-particle erosion behaviour of WC/Ni composite clad layers with different contents of WC particles," *Optics & Laser Technology*, vol. 50, pp. 155–162, 2013.

[53] P. Farahmand, S. Liu, Z. Zhang, and R. Kovacevic, "Laser cladding assisted by induction heating of Ni-WC composite enhanced by nano-WC and La2O3," *Ceramics International*, vol. 40, no. 10, pp. 15421–15438, 2014.

[54] T. Ruthradevi, J. Akbar, G. Suresh Kumar et al., "Investigations on nickel ferrite embedded calcium phosphate nanoparticles for biomedical applications," *Journal of Alloys and Compounds*, vol. 695, pp. 3211–3219, 2017.

[55] A. Y. Cheng, H. H. Sheu, Y. M. Liu, K. H. Hou, P. Y. Hsieh, and M. D. Ger, "Effect of pretreatment process on the adhesion and corrosion resistance of nickel-boron coatings deposited on 8620H alloy steel," *International Journal of Electrochemical Science*, vol. 15, pp. 61–89, 2020.

[56] M. Schlesinger, *Modern Electroplating*, John Wiley & Sons, Hoboken, NJ, USA, 2011.

[57] N. Lotfi, M. Aliofkhazraei, H. Rahmani, and G. B. Darband, "Zinc-nickel alloy electrodeposition: characterization, properties, multilayers and composites," *Protection of Metals and Physical Chemistry of Surfaces*, vol. 54, no. 6, pp. 1102–1140, 2018.

[58] X. She, J. Wu, H. Xu et al., "Enhancing charge density and steering charge unidirectional flow in 2D non-metallic semiconductor-CNTs-metal coupled photocatalyst for solar energy conversion," *Applied Catalysis B: Environmental*, vol. 202, pp. 112–117, 2017.

[59] G. Barati Darband, M. Aliofkhazraei, S. Khorsand, S. Sokhanvar, and A. Kaboli, "Science and engineering of superhydrophobic surfaces: review of corrosion resistance, chemical and mechanical stability," *Arabian Journal of Chemistry*, vol. 13, no. 1, pp. 1763–1802, 2020.

[60] Z. Wang, B. Huang, H. Chen, C. Wang, J. Ma, and X. Zhao, "The effect of quenching and partitioning heat treatment on the wear resistance of ductile cast iron," *Journal of Materials Engineering and Performance*, vol. 29, no. 7, pp. 4370–4378, 2020.

[61] A. Borjali, K. Monson, and B. Raeymaekers, "Predicting the polyethylene wear rate in pin-on-disc experiments in the context of prosthetic hip implants: deriving a data-driven model using machine learning methods," *Tribology International*, vol. 133, pp. 101–110, 2019.

[62] B. Swain, S. Bhuyan, R. Behera, S. S. Mohapatra, and A. Behera, "Wear: a serious problem in industry," in *Tribology In Materials And Manufacturing-Wear, Friction And Lubrication*IntechOpen, London, UK, 2020.

[63] C. A. Loto, "Electroless nickel plating - a review," *Silicon*, vol. 8, no. 2, pp. 177–186, 2016.

[64] M. Ramesh, K. Marimuthu, P. Karuppusamy, and L. Rajeshkumar, "Microstructure and properties of YSZ-Al2O3 functional ceramic thermal barrier coatings for military applications," *Boletin de la Sociedad Espanola de Ceramica y Vidrio*, vol. 60, no. 6, 2021.

[65] D. Umapathi, A. Devaraju, C. Rathinasuriyan, and A. Raji, "Mechanical and tribological properties of electroless nickel phosphorous and nickel Phosphorous-Titanium nitride coating," *Materials Today Proceedings*, vol. 22, pp. 1038–1042, 2020.

[66] L. L. Natrayan, L. N. Singh, and M. S. Kumar, "An experimental investigation on mechanical behaviour of SiCp reinforced Al 6061 MMC using squeeze casting process," *International Journal of Mechanical and Production Engineering Research and Development*, vol. 7, no. 6, pp. 663–668, 2017.

[67] B. D. Cullity, *Elements of X-rays diffraction*, Addison-Wesley Publishing Co. Inc., Reading, MA, USA., 1956.

[68] S. Ankita and A. K. Singh, "Corrosion and wear resistance study of Ni-P and Ni-P-PTFE nanocomposite coatings," *Central European Journal of Engineering*, vol. 1, no. 3, pp. 234–243, 2011.

[69] J. N. Balaraju and K. S. Rajam, "Influence of particle size on the microstructure, hardness and corrosion resistance of electroless Ni–P–Al2O3 composite coatings," *Surface and Coatings Technology*, vol. 200, no. 12-13, pp. 3933–3941, 2006.

[70] A. Choudhury and N. Tandon, "Application of acoustic emission technique for the detection of defects in rolling element bearings," *Tribology International*, vol. 33, no. 1, pp. 39–45, 2000.

[71] A. Kumar, A. Patnaik, and I. K. Bhat, "Dry sliding wear behavior of Titanium metal powder filled aluminum alloy composites for gear application," *Applied Mechanics and Materials*, vol. 877, pp. 118–136, 2018.

[72] A. Kumar, A. Patnaik, and I. K. Bhat, "Tribology analysis of cobalt particulate filled Al 7075 alloy for gear materials: a comparative study," *Silicon*, vol. 11, no. 3, pp. 1295–1311, 2019.

[73] C. Gao and M. Liu, "Effects of normal load on the coefficient of friction by microscratch test of copper with a spherical indenter," *Tribology Letters*, vol. 67, no. 1, pp. 1–12, 2019.

[74] S. Fan, C. Yang, L. He, J. Deng, L. Zhang, and L. Cheng, "The effects of phosphate coating on friction performance of C/C and C/SiC brake materials," *Tribology International*, vol. 114, pp. 337–348, 2017.

[75] N. Thiyaneshwaran, C. P. Selvan, A. Lakshmikanthan, K. Sivaprasad, and B. Ravisankar, "Comparison based on specific strength and density of in-situ Ti/Al and Ti/Ni metal intermetallic laminates," *Journal of Materials Research and Technology*, vol. 14, pp. 1126–1136, 2021.

[76] J. Li, H. Liao, and C. Coddet, "Friction and wear behavior of flame-sprayed PEEK coatings," *Wear*, vol. 252, no. 9-10, pp. 824–831, 2002.

[77] P. L. Menezes and S. V. Kailas, "On the effect of surface texture on friction and transfer layer formation-a study using Al and steel pair," *Wear*, vol. 265, no. 11-12, pp. 1655–1669, 2008.

[78] P. J. Blau, "The significance and use of the friction coefficient," *Tribology International*, vol. 34, no. 9, pp. 585–591, 2001.

[79] O. Barrau, C. Boher, R. Gras, and F. Rezai-Aria, "Wear mechanisms and wear rate in a high temperature dry friction of AISI H11 tool steel: influence of debris circulation," *Wear*, vol. 263, no. 1-6, pp. 160–168, 2007.

[80] J. A. Williams, "Wear and wear particles-some fundamentals," *Tribology International*, vol. 38, no. 10, pp. 863–870, 2005.

[81] A. Lakshmikanthan, S. Bontha, M. Krishna, P. G. Koppad, and T. Ramprabhu, "Microstructure, mechanical and wear properties of the A357 composites reinforced with dual sized SiC particles," *Journal of Alloys and Compounds*, vol. 786, no. 25, pp. 570–580, 2019.

[82] S. Kumar, S. R. Maity, and L. Patnaik, "Friction and tribological behavior of bare nitrided, TiAlN and AlCrN coated MDC-K hot work tool steel," *Ceramics International*, vol. 46, no. 11, pp. 17280–17294, 2020.

[83] A. Lakshmikanthan, S. B. Udayagiri, P. G. Koppad, M. Gupta, K. Munishamaiah, and S. Bontha, "The effect of heat treatment on the mechanical and tribological properties of dual size SiC reinforced A357 matrix composites," *Journal of Materials Research and Technology*, vol. 9, no. 3, pp. 6434–6452, 2020.

[84] N. Vinayaka, A. Lakshmikanthan, G. C. M. Patel, and C. Pon, "Mechanical, microstructure and wear properties of Al 6113 fly ash reinforced composites: comparison of as-cast and heat-treated conditions," *Advances in Materials and Processing Technologies*, vol. 2021, Article ID 1927649, 2021.

Hindawi
Advances in Materials Science and Engineering
Volume 2021, Article ID 3551097, 8 pages
https://doi.org/10.1155/2021/3551097

Research Article

Effects of Diode, CO_2, Er : YAG, and Er and Cr : YSGG on Titanium Implant Surfaces by Scanning Electron Microscopy

Amir Moeintaghavi,[1] **Hossein Bagheri**,[2] **Mahdie Yavari Pour**,[3] **Shervin Shafiei**,[4] **Hamidreza Moslemi**,[4] **Kamyar Abbasi**,[5] **Behrad Rahbani Nobar**,[6] **Amirreza Mehdizadeh**,[3] **Farzaneh Ahrari**,[1] **and Mostafa Alam**[4]

[1]*Dental Research Center, School of Dentistry, Mashhad University of Medical Sciences, Mashhad, Iran*
[2]*Dental Materials Research Center, School of Dentistry, Mashhad University of Medical Sciences, Mashhad, Iran*
[3]*Department of Oral and Maxillofacial Radiology, School of Dentistry, Islamic Azad University, Tehran, Iran*
[4]*Department of Oral and Maxillofacial Surgery, School of Dentistry, Shahid Beheshti University of Medical Sciences, Tehran, Iran*
[5]*Department of Prosthodontics, School of Dentistry, Shahid Beheshti University of Medical Sciences, Tehran, Iran*
[6]*Private Practice, Tehran, Iran*

Correspondence should be addressed to Mostafa Alam; mostafa_alam1@yahoo.com

Received 23 September 2021; Revised 31 October 2021; Accepted 3 December 2021; Published 23 December 2021

Academic Editor: Adam Khan M

Copyright © 2021 Amir Moeintaghavi et al. This is an open access article distributed under the Creative Commons Attribution License, which permits unrestricted use, distribution, and reproduction in any medium, provided the original work is properly cited.

This study aimed to determine the effects of various lasers on dental implants' surface characteristics. Nine explanted dental implants were included. Two implants were randomly allocated to four intervention groups, namely, diode (2 W, 810 nm, 10 s), CO_2 (2 W, 10600 nm, 10 s), Er : YAG (200 mJ/20 Hz, 2940 nm, 10 s), and Er, Cr : YSGG (200 mJ/20 Hz, 2780 nm, 10 s) groups and one control group. After laser irradiation, all implants were imaged with scanning electron microscopy. Qualitative changes on the surface of implants were evaluated. Quantitative surface changes at the threads and between the threads were assessed by software using depression and prominence plots. The paired *t*-test was used for statistical analysis. Diode laser irradiation showed the least surface changes while the Er : YAG group showed the greatest surface changes. Furthermore, CO_2 and Er : YAG laser irradiation significantly altered the mean profile area at the threads ($p < 0.05$), while CO_2 and Er, Cr : YSGG laser irradiation significantly altered the mean profile area between the threads ($p < 0.05$). Diode laser irradiation does not alter the implant surface characteristics. However, the use of CO2, Er : YAG, and Er, Cr : YSGG lasers on titanium implant surfaces is discouraged as they damage the titanium implant surfaces.

1. Introduction

Peri-implantitis is defined as the inflammation of the tissues surrounding the dental implant, including soft tissues and bone, which results in progressive peri-implant bone loss [1]. It has been reported that this condition may affect 8–25% of the population which may subsequently lead to the intentional explanation of 10% of the implants [2–7]. Various nonsurgical and surgical treatment methods have been proposed for peri-implantitis treatment. However, due to differences in study designs such as patient criteria, length of follow-up, disease severity in the studied groups [8], lack of high-quality evidence [9], and long-term randomized controlled trials [10], no specific therapy has ever been described as the most effective for this condition. Recently, laser therapy has shown promising results in

reducing peri-implant inflammation compared to other nonsurgical methods [11].

The aim of therapy for peri-implantitis is complete and thorough removal of microbial biofilm and calculus from the implant surface and the inner pocket epithelium. Besides, modern dental implants possess numerous morphological and topographical characteristics which can complicate complete surface detoxification by conventional methods [12–17]. Also, conventional nonsurgical therapy may also damage the implant surface [18, 19] which can further complicate subsequent epithelial attachment and may also lead to increased bacterial aggregation [20–25]. Laser therapy, with its bactericidal action, may well enhance debridement and may also prevent implant surface alteration due to its selective action [26]. However, the effects of various laser types and settings on implant surface topography have also been controversial.

While the literature supports the use of diode [27, 28] and CO_2 [28, 29] lasers on implant surface without significant topographical compromise, conflicting results have been obtained for Er : YAG(12, 28, 30) and Nd : YAG [27, 29] lasers. Additionally, to the best of our knowledge, we only found one study which had described the effects of Er, Cr : YSGG laser on implant surfaces [30]. While the conflicting results may be attributed to different implant systems used, laser energy settings, in vivo or in vitro laser applications, overall different study designs, and direct comparisons of the aforementioned lasers in identical settings are scarce throughout the literature [31]. Additionally, recent reviews on the effects of various lasers on implant surface decontamination have been inconclusive [31, 32]. Thus, in order to determine which laser type can better preserve the surface characteristics of dental implants, we aimed to investigate the effects of diode, CO_2, Er : YAG, and Er, Cr : YSGG lasers on the surface topography of dental implants via an ex vivo experimental study.

2. Materials and Methods

2.1. Design the Experimental. In this ex vivo experimental study, nine explanted titanium dental implants (Biohorizons®, Birmingham, AL, USA) with surfaces prepared with resorbable blasting media (RBM) and possessed Laser-Lok microchannels which had failed due to peri-implantitis were included. Peri-implantitis was diagnosed by observing recurrent gingival bleeding from the affected site, bleeding on probing, suppuration, and increasing pocket depth since insertion [33]. This diagnosis was also confirmed by radiographic examination by observing bone loss around the implant shoulder and the presence of radiolucencies around the implant. All dental implants were previously inserted by one surgeon. For explantation procedures, the same surgeon used the method described by Shibli et al. [34] which consisted of the removal of the implants under local anesthesia. Steel forceps were used to grab the implants by the cover screw and remove them from the bone. Subsequently, each implant was copiously irrigated with saline solution (DarouPakhsh Pharmaceutical, Tehran, Iran) until no visible organic remnants such as blood or saliva remained on the implant surface. Additionally, titanium tweezers were used to remove any possible soft tissue remnants on the implant surface. Thereafter, each implant was placed in a separate previously sterilized plastic bag. Based on the acquired data from the pilot study, a number of two implants per group would be necessary in order to conduct statistical analysis as later described in this section. Out of nine implants, eight of them were allocated to four groups, namely, diode, CO_2, Er : YAG, and Er, Cr : YSGG groups. The one remaining implant was determined as the control group. Sample size calculation was based on a pilot study which had been conducted before the actual study was conducted. The aim and design of the study and the surgical procedure were thoroughly explained to patients, and a written informed consent was obtained from all participants.

2.2. Preparing the Groups. In order to prepare the samples for laser treatment, every implant's surface was painted with an oil ink while leaving two 4×3 mm rectangular windows on the implant surface unpainted. The windows on all implants began from the second thread and ended on the sixth thread. One of the windows would serve as the laser treatment group while the other would serve as the untreated surface which was also protected by an aluminum foil covering. Each implant was carefully handled in this process so as not to contaminate the implant surface. Subsequently, each implant was mounted on an acrylic resin jig for subsequent procedures. The implants were randomly allocated to five groups which consisted of four intervention groups and one control group. Each group received different laser treatments.

In the first group, the specified window was irradiated using diode laser (2W, 810 nm) (FOX IV, A.R.C Laser, Nuremberg, Germany) using a 400 μm sized tip with a sweeping motion in a continuous wave [35] mode from a one-millimeter distance with a 90-degree angulation with the implant surface for 10 seconds.

In the second group, the specified window was irradiated using CO_2 laser (2W, 10600 nm) (Smart US-20, Deka, Florence, Italy) using a 400 μm-sized tip with a sweeping motion in the CW mode from a one-millimeter distance with a 90-degree angulation with the implant surface for 10 seconds.

In the third group, the specified window was irradiated using Er : YAG laser (200 mJ/20 Hz, 2940 nm) (Key3, KaVo, Biberach, Germany) using a 400 μm-sized tip with a sweeping motion in the pulsed mode from a one-millimeter distance with a 90-degree angulation with the implant surface for 10 seconds. The spray was set at 50% of the maximum and saline solution was used for the spray.

In the fourth group, the specified window was irradiated using Er, Cr : YSGG laser (200 mJ/20 Hz, 2780 nm) (WATERLASE IPLUS®, BIOLASE Inc., Irvine, CA, USA) using a 400 μm-sized tip with a sweeping motion in the pulsed mode from a one-millimeter distance with a 90-degree angulation with the implant surface for 10 seconds. The spray was set at 50% of the maximum, and saline solution was used for the spray.

The fifth group served as the control group. No laser interventions were conducted on this group so as to exclude any irradiation effects such as transmission.

2.3. Scanning Electron Microscope (SEM) Analysis. The specimens were subsequently prepared for scanning electron microscope (SEM) evaluation. Firstly, the specimens were fixed in 2% paraformaldehyde solution (Sorenchem, Mashhad, Iran) and then subjected to progressive dehydration in increasing concentrations of ethanol (Kimiaalcoholzanjan, Tehran, Iran). Then, the specimens were sputter-coated with a 50 nm layer of gold due to the higher backscattering coefficient of gold than other elements which prevents microscope beam damage. This thin layer of gold does not alter the topographical characteristics of the specimens. Thereafter, the specimens were placed in a vacuum container and SEM images were subsequently obtained (SEM; S-4700, Hitachi, Japan). The SEM images were qualitatively evaluated for signs of damage by two blinded assessors. For quantitative analyses, images with equal magnification were selected and imported into ImageJ software (National Institutes of Health, Bethesda, MD) by a blinded assessor [22, 36]. Six segments with the length of 100 pixels were drawn on the implant threads and also between the implant threads. Analyses of the surface characteristics at the threads and between the threads were conducted separately. Subsequently, the profile area plugin was used to develop the depression and prominence plot based on the numerical value of each grey shade of every pixel. The grey values ranged from 0 to 1000, i.e., completely white pixels were assigned a value of 1000, while completely black pixels were assigned a value of 0. Subsequently, the area under the curve of each profile area was calculated and the means of all the six segments were obtained. The values obtained for each profile area was used to determine quantitative surface changes before and after laser irradiation. Analysis was carried out by one experienced oral and maxillofacial radiologist. All assessments were carried out by one experienced and blinded operator.

We used the paired *t*-test for the quantitative surface changes' analyses using a software package (SPSS 11.0, SPSS Inc., and Chicago, IL, USA). A p-value of less than 0.05 was considered as statistically significant in all analyses.

3. Results

3.1. Qualitative Changes. This study was done to determine the effects of various lasers on the surface topography of titanium dental implants which were explanted because they were affected by peri-implantitis. The resultant changes could be classified as qualitative and quantitative. Figure 1 shows the SEM image of the control group (Figure 1). Figures 2–5 are the SEM images of the laser groups. The least amount of surface changes were observed in the diode laser group, while the highest amount of surface changes were observed in the Er : YAG laser group. The diode laser SEM images exhibited the least amount of surface alterations between the threads (Figure 2). Likewise, CO_2 laser irradiation melted both the threads and surfaces between the threads. Additionally, this laser also increases the surface roughness (Figure 3). It was shown that the Er : YAG laser completely alters the implant surface topography both at the thread level and between the threads (Figure 4). Er, Cr : YSGG laser irradiation increased the surface roughness both at the thread level and between the threads. Additionally, it also melted the implant surface between the threads and changes the surface topography at the thread level (Figure 5).

3.2. Quantitative Changes. Table 1 summarizes the mean profile area before and after laser irradiation at the thread level (Table 1). Table 2 summarizes the same values before and after laser irradiation for the surfaces located between the threads (Table 2). Er : YAG and CO_2 lasers significantly changed the mean profile area at the threads. Er, Cr : YSGG and CO_2 lasers significantly changed the mean profile area between the threads.

4. Discussion

This ex vivo experimental study aimed to evaluate the effects of various laser wavelengths' irradiation on titanium implants' surface topographies. It was found that diode laser irradiation produced the least amount of surface changes, while CO_2, Er : YAG, and Er, Cr : YSGG lasers produced significant surface alterations. As mentioned before, one of the main limitations of the previous studies on implant surface decontamination strategies has been their limited comparability. Factors such as power output, operation mode, irradiation time, and distance from the specimens, irradiation angles, specimen types, and preparation can confound the results of these strategies' comparisons [31, 34]. This study provided a setting in which the comparison of the four types of lasers became feasible.

In order to replicate the clinical situation as much as possible, we used explanted implants from human subjects as opposed to titanium disks [27, 28, 30, 35] or unused implants [37–39]. This approach helps simulate the clinical situation as much as possible where the chemical composition of the implant surface may be altered due to deposition of human or bacterial remnants which may alter the titanium dissolution rate due to blockage of oxygen cathodic reaction [34]. Furthermore, the power settings for each of the lasers used were based on the works of previous studies with regards to temperature elevations due to laser irradiation so that the results of our study would not be confounded by excessive temperature rises, i.e., more than 10 degrees Celsius [40] within the specimens [27, 35, 38]. Thus, excessive temperature increases in the implant body was ruled out as a confounding factor.

According to the qualitative and quantitative results, the Er : YAG and Er, Cr : YSGG groups demonstrated significant surface alterations which are also in line with the results of previous studies [28, 38, 39]. These alterations may be due to microexplosions associated with the effect of these lasers on the water which was sprayed during irrigation, thus damaging the nearby surface in addition to irradiation

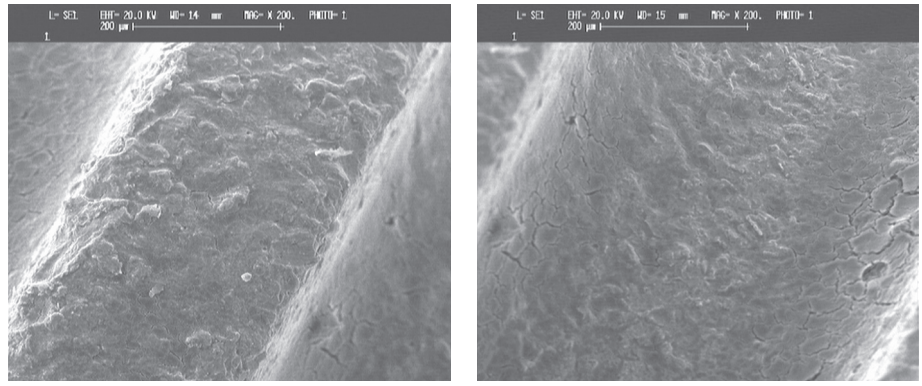

(a) (b)

Figure 1: Scanning electron micrograph of the control group. (a) Thread surface (×200). (b) Between thread surfaces (×200).

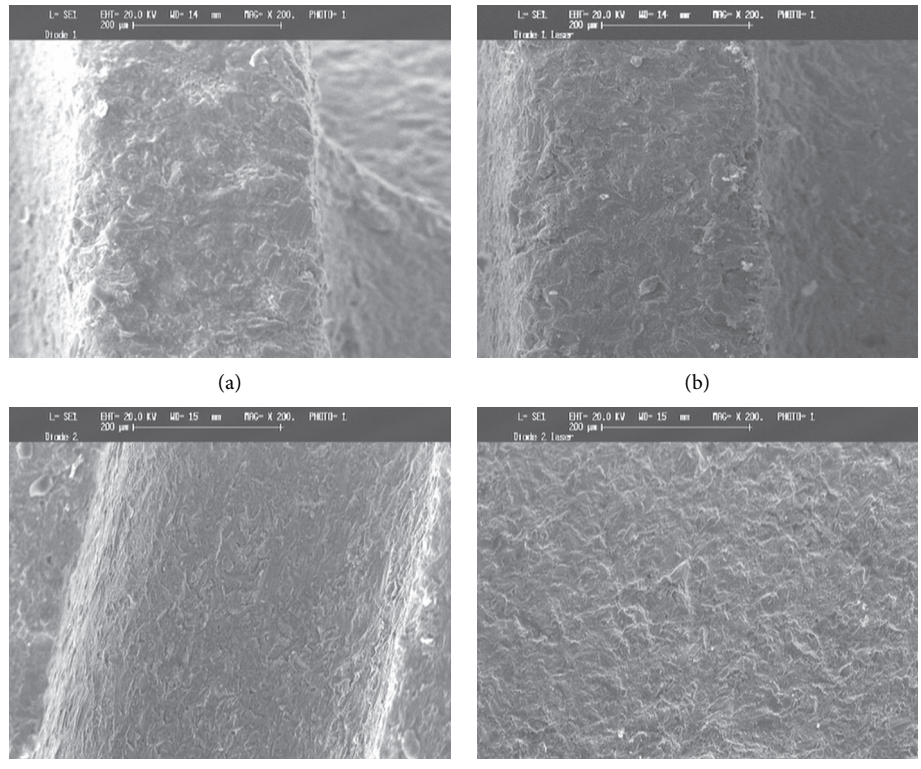

(a) (b)

(c) (d)

Figure 2: SEM image of the diode laser group. (a) Thread surface before laser irradiation (×200). (b) Thread surface after laser irradiation (×200). (c) Between thread surfaces before laser irradiation (×200). (d) Between thread surfaces after laser irradiation (×200).

absorption at the implant surface. Additionally, CO_2 laser application also altered the implant surfaces. We only found one study which supported our results about CO_2 irradiation-related damage [41]. The diode laser did not show any significant surface changes. This finding was also in line with the results of the previous studies [27, 28, 42].

It has been stated in the literature that, due to the higher spectral reflectance values of titanium for lower wavelengths, lasers with longer wavelengths can produce lesser damage, while lasers with shorter wavelengths can produce more damage [43]. Although CO_2 laser damage was lower compared to Er : YAG laser, it still did inflict significant damage to the implant surface. This shows that although CO_2 laser irradiation is reflected off the implant surface to a higher degree, surface alterations by CO_2 laser irradiation are still possible. As previously stated, the chemical composition of the implant surface might have been altered. Thus, CO_2 laser irradiation might not have been so readily reflected as previously thought.

Inevitably, this study also had some limitations. In order to minimize the confounding effects of beam angulation on the amount of energy transfer to the specimens, we opted for an

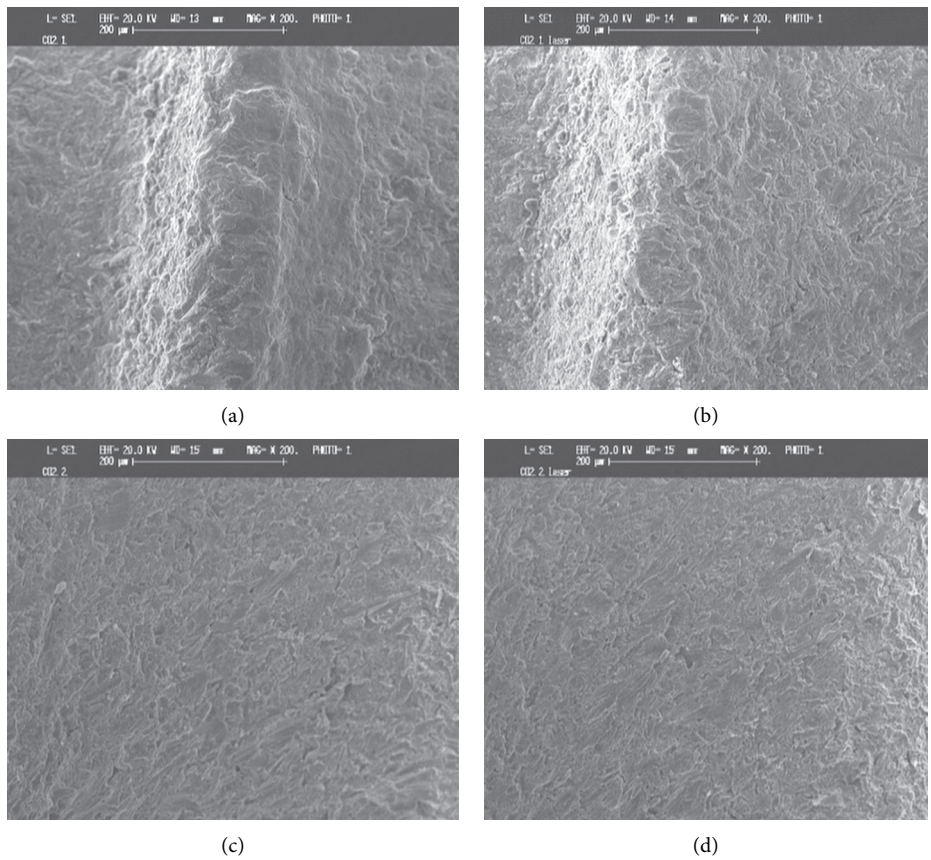

(a) (b)

(c) (d)

Figure 3: SEM image of the CO_2 laser group. (a) Thread surface before laser irradiation (×200). (b) Thread surface after laser irradiation (×200). (c) Between thread surfaces before laser irradiation (×200). (d) Between thread surfaces after laser irradiation (×200).

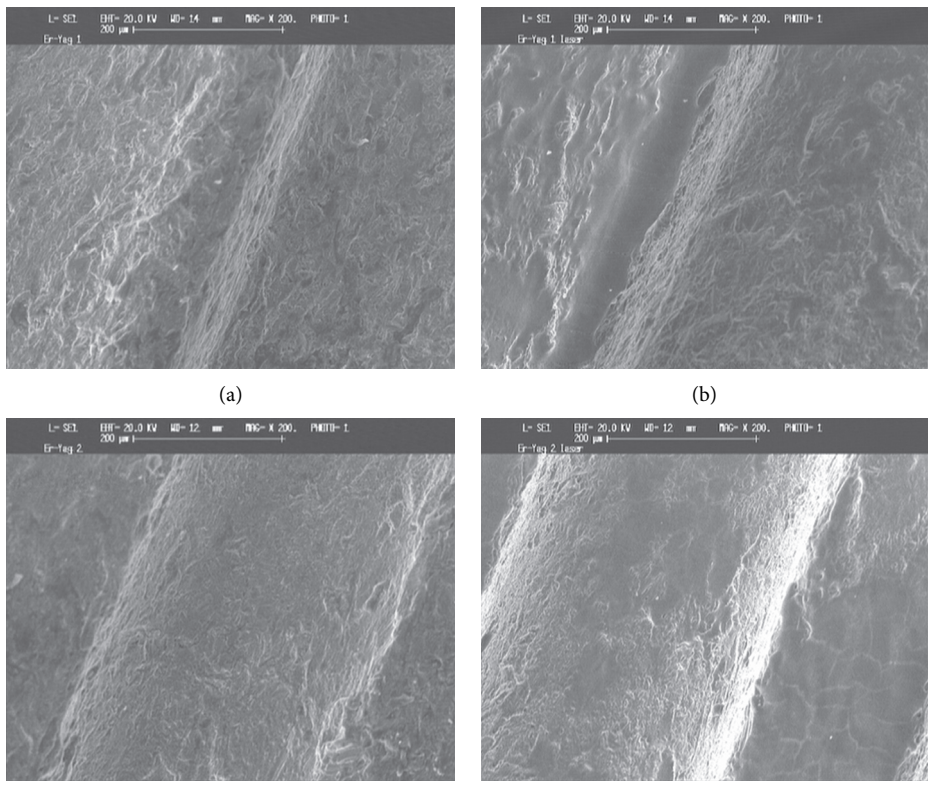

(a) (b)

(c) (D)

Figure 4: SEM image of the Er : YAG laser group. (a) Thread surface before laser irradiation (×200). (b) Thread surface after laser irradiation (×200). (c) Between thread surfaces before laser irradiation (×200). (D) Between thread surfaces after laser irradiation (×200).

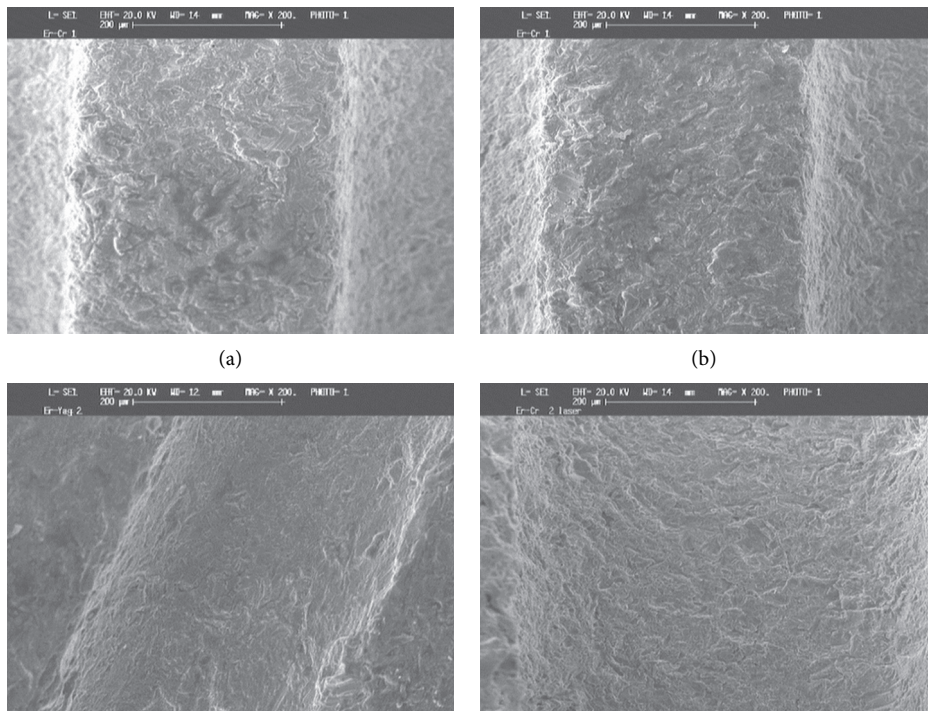

(a) (b) (c) (d)

Figure 5: SEM image of the Er, Cr : YSGG laser group. (a) Thread surface before laser irradiation (×200). (b) Thread surface after laser irradiation (×200). (c) Between thread surfaces before laser irradiation (×200). (d) Between thread surfaces after laser irradiation (×200).

Table 1: Mean profile area before and after laser irradiation at the thread level.

Laser type	Mean profile area before laser irradiation	Mean profile area after laser irradiation	p value
Diode	3749/20 ± 840/36	3196/96 ± 450/59	0.186
CO_2	2802/47 ± 328/55	4832/45 ± 1095/37	0.001
Er : YAG	2495/75 ± 522/48	920/73 ± 189/27	$p < 0.001$
Er,Cr : YSGG	2842/93 ± 579/52	3342/10 ± 1314/93	0.415

Table 2: Mean profile area before and after laser irradiation between threads.

Laser type	Mean profile area before laser irradiation	Mean profile area after laser irradiation	p value
Diode	3154/24 ± 620/93	3226/47 ± 378/21	0.813
CO_2	2227/90 ± 484/65	3673/34 ± 1241/76	0.024
Er : YAG	2431/21 ± 475/10	3072/03 ± 565/78	0.060
Er,Cr : YSGG	5089/38 ± 1627/58	4493/25 ± 679/92	0.042

approximate 90-degree angle of irradiation in all intervention groups using a free-hand technique. This angulation can readily be achieved in clinical situations such as open flap debridement but may not be possible when conducting nonsurgical periodontal therapy. Nonsurgical therapy may require a more parallel irradiation angle, the effects of which should be investigated in future studies. Furthermore, successful implant surface decontamination must also ensure suitable chemical composition and biocompatibility of the irradiated surface which should also be evaluated in future studies.

5. Conclusions

Diode laser irradiation does not change the implant surface characteristics and can therefore be a safe option for implant surface decontamination. However, the use of CO_2, Er : YAG, and Er, Cr : YSGG lasers can damage the surface properties of titanium implants, and therefore, they should be used with caution. Moreover, further studies regarding different lasers' setting and other confounding factors are suggested by this article.

Data Availability

The data used to support the findings of the research are available from the corresponding author upon reasonable request.

Ethical Approval

Considering the ex vivo design of this study, no ethical objections to the design and process of this study were made at the time of conducting this research.

Conflicts of Interest

The authors have no conflicts of interest.

Acknowledgments

The authors would like to thank the colleagues for supporting the research.

References

[1] F. Schwarz, J. Derks, A. Monje, and H.-L. Wang, "Peri-implantitis," *Journal of Clinical Periodontology*, vol. 45, pp. S246–S266, 2018.

[2] M. Krebs, N. Kesar, A. Begić, N. Krockow, G. H. Nentwig, and P. Weigl, "Incidence and prevalence of peri-implantitis and peri-implant mucositis 17 to 23 (18.9) years postimplant placement," *Clinical Implant Dentistry and Related Research*, vol. 21, no. 6, pp. 1116–1123, 2019.

[3] K. Kordbacheh Changi, J. Finkelstein, and P. N. Papapanou, "Peri-implantitis prevalence, incidence rate, and risk factors: a study of electronic health records at a U.S. dental school," *Clinical Oral Implants Research*, vol. 30, no. 4, pp. 306–314, 2019.

[4] E. Papathanasiou, M. Finkelman, J. Hanley, and A. O. Parashis, "Prevalence, etiology and treatment of peri-implant mucositis and peri-implantitis: a survey of periodontists in the United States," *Journal of Periodontology*, vol. 87, no. 5, pp. 493–501, 2016.

[5] M. Yazdanian, A. Rahmani, E. Tahmasebi, H. Tebyanian, A. Yazdanian, and S. A. Mosaddad, "Current and advanced nanomaterials in dentistry as regeneration agents: an update," *Mini Reviews in Medicinal Chemistry*, vol. 21, no. 7, pp. 899–918, 2021.

[6] M. Yazdanian, A. H. Arefi, M. Alam et al., "Decellularized and biological scaffolds in dental and craniofacial tissue engineering: a comprehensive overview," *Journal of Materials Research and Technology*, vol. 15, pp. 1217–1251, 2021.

[7] E. Tafazoli Moghadam, M. Yazdanian, M. Alam et al., "Current natural bioactive materials in bone and tooth regeneration in dentistry: a comprehensive overview," *Journal of Materials Research and Technology*, vol. 13, pp. 2078–2114, 2021.

[8] L. J. Heitz-Mayfield and A. Mombelli, "The therapy of peri-implantitis: a systematic review," *The International Journal of Oral & Maxillofacial Implants*.vol. 29, pp. 325–345, 2014.

[9] H.-L. Chan, G.-H. Lin, F. Suarez, M. MacEachern, and H.-L. Wang, "Surgical management of peri-implantitis: a systematic review and meta-analysis of treatment outcomes," *Journal of Periodontology*, vol. 85, no. 8, pp. 1027–1041, 2014.

[10] M. Muthukuru, A. Zainvi, E. O. Esplugues, and T. F. Flemmig, "Non-surgical therapy for the management of peri-implantitis: a systematic review," *Clinical Oral Implants Research*, vol. 23, pp. 77–83, 2012.

[11] M. Chala, E. Anagnostaki, V. Mylona, A. Chalas, S. Parker, and E. Lynch, "Adjunctive use of lasers in peri-implant mucositis and peri-implantitis treatment: a systematic review," *Dentistry Journal*, vol. 8, no. 3, 2020.

[12] R. Nejem Wakim, M. Namour, H. Nguyen et al., "Decontamination of dental implant surfaces by the Er:YAG laser beam: a comparative in vitro study of various protocols," *Dentistry Journal*, vol. 6, no. 4, p. 66, 2018.

[13] A. Soudi, M. Yazdanian, R. Ranjbar et al., "Role and application of stem cells in dental regeneration: a comprehensive overview," *EXCLI Journal*, vol. 20, pp. 454–489, 2021.

[14] M. N. Motallaei, M. Yazdanian, H. Tebyanian et al., "The current strategies in controlling oral diseases by herbal and chemical materials," *Evidence-based Complementary and Alternative Medicine: eCAM*, vol. 2021, Article ID 3423001, 2021.

[15] S. A. Mosaddad, K. Beigi, T. Doroodizadeh et al., "Therapeutic applications of herbal/synthetic/bio-drug in oral cancer: an update," *European Journal of Pharmacology*, vol. 890, Article ID 173657, 2021.

[16] E. Hajmohammadi, T. Molaei, S. H. Mowlaei et al., "Sonodynamic therapy and common head and neck cancers: in vitro and in vivo studies," *European Review for Medical and Pharmacological Sciences*, vol. 25, no. 16, pp. 5113–5121, 2021.

[17] E. Tahmasebi, M. Alikhani, A. Yazdanian, M. Yazdanian, H. Tebyanian, and A. Seifalian, "The current markers of cancer stem cell in oral cancers," *Life Sciences*, vol. 249, Article ID 117483, 2020.

[18] O. I. Larsen, M. Enersen, A. K. Kristoffersen et al., "Antimicrobial effects of three different treatment modalities on dental implant surfaces," *Journal of Oral Implantology*, vol. 43, no. 6, pp. 429–436, 2017.

[19] O. Unursaikhan, J.-S. Lee, J.-K. Cha et al., "Comparative evaluation of roughness of titanium surfaces treated by different hygiene instruments," *Journal of Periodontal & Implant Science*, vol. 42, no. 3, pp. 88–94, 2012.

[20] P. M. Duarte, A. F. Reis, P. M. de Freitas, and C. Ota-Tsuzuki, "Bacterial adhesion on smooth and rough titanium surfaces after treatment with different instruments," *Journal of Periodontology*, vol. 80, no. 11, pp. 1824–1832, 2009.

[21] R. Xing, S. P. Lyngstadaas, J. E. Ellingsen, S. Taxt-Lamolle, and H. J. Haugen, "The influence of surface nanoroughness, texture and chemistry of TiZr implant abutment on oral biofilm accumulation," *Clinical Oral Implants Research*, vol. 26, no. 6, pp. 649–656, 2015.

[22] M. Yazdanian, H. Tabesh, B. Houshmand et al., "Fabrication and properties of βTCP/Zeolite/Gelatin scaffold as developed scaffold in bone regeneration: in vitro and in vivo studies," *Biocybernetics and Biomedical Engineering*, vol. 40, no. 4, pp. 1626–1637, 2020.

[23] R. S. Soufdoost, S. A. Mosaddad, Y. Salari et al., "Surgical suture assembled with tadalafil/polycaprolactone drug-delivery for vascular stimulation around wound: validated in a preclinical model," *Biointerface Res Appl Chem*, vol. 10, no. 5, pp. 6317–6327, 2020.

[24] S. A. Mosaddad, M. Yazdanian, H. Tebyanian et al., "Fabrication and properties of developed collagen/strontium-doped bioglass scaffolds for bone tissue engineering," *Journal of Materials Research and Technology*, vol. 9, no. 6, pp. 14799–14817, 2020.

[25] E. T. Moghadam, M. Yazdanian, E. Tahmasebi et al., "Current herbal medicine as an alternative treatment in dentistry: in vitro, in vivo and clinical studies," *European Journal of Pharmacology*, vol. 889, Article ID 173665, 2020.

[26] F. Suarez, A. Monje, P. Galindo-Moreno, and H.-L. Wang, "Implant surface detoxification," *Implant Dentistry*, vol. 22, no. 5, pp. 465–473, 2013.

[27] G. E. Romanos, H. Everts, and G. H. Nentwig, "Effects of diode and Nd:YAG laser irradiation on titanium discs: a scanning electron microscope examination," *Journal of Periodontology*, vol. 71, no. 5, pp. 810–815, 2000.

[28] S. Stubinger, C. Etter, M. Miskiewicz et al., "Surface alterations of polished and sandblasted and acid-etched titanium implants after Er : YAG, carbon dioxide, and diode laser irradiation," *The International Journal of Oral & Maxillofacial Implants*, vol. 25, no. 1, pp. 104–11, 2010.

[29] C.-Y. Park, S.-G. Kim, M.-D. Kim, T.-G. Eom, J.-H. Yoon, and S.-G. Ahn, "Surface properties of endosseous dental implants after NdYAG and CO_2 laser treatment at various energies," *Journal of Oral and Maxillofacial Surgery*, vol. 63, no. 10, pp. 1522–1527, 2005.

[30] A. S. Alagl, M. Madi, S. Bedi, F. Al Onaizan, and Z. S. Al-Aql, "The effect of Er,Cr:YSGG and diode laser applications on dental implant surfaces contaminated with acinetobacter baumannii and *Pseudomonas aeruginosa*," *Materials*, vol. 12, no. 13, p. 2073, 2019.

[31] M. S. Kamel, A. Khosa, A. Tawse-Smith, and J. Leichter, "The use of laser therapy for dental implant surface decontamination: a narrative review of in vitro studies," *Lasers in Medical Science*, vol. 29, no. 6, pp. 1977–1985, 2014.

[32] A. Mellado-Valero, P. Buitrago-Vera, M. Sola-Ruiz, and J. Ferrer-Garcia, "Decontamination of dental implant surface in peri-implantitis treatment: a literature review," *Medicina Oral, Patología Oral y Cirugía Bucal*, vol. 18, no. 6, pp. e869–e876, 2013.

[33] S. Renvert, G. R. Persson, F. Q. Pirih, and P. M. Camargo, "Peri-implant health, peri-implant mucositis, and peri-implantitis: case definitions and diagnostic considerations," *Journal of Clinical Periodontology*, vol. 45, pp. S278–S285, 2018.

[34] J. A. Shibli, L. H. Theodoro, P. Haypek, V. G. Garcia, and E. Marcantonio Jr., "The effect of CO2 laser irradiation on failed implant surfaces," *Implant Dentistry*, vol. 13, no. 4, pp. 342–351, 2004.

[35] J. Strever, J. Lee, W. Ealick, M. Peacock, D. Shelby, C. Susin et al., "Er, Cr : YSGG laser effectively ablates single-species biofilms on titanium disks without detectable surface damage," *Journal of Periodontology*, vol. 88, pp. 484–492, 2016.

[36] H. Tebyanian, A. Karami, E. Motavallian, A. Samadikuchaksaraei, B. Arjmand, and M. R. Nourani, "Rat lung decellularization using chemical detergents for lung tissue engineering," *Biotechnic & Histochemistry*, vol. 94, no. 3, pp. 214–222, 2019.

[37] A. Saffarpour, A. Nozari, R. Fekrazad, A. Saffarpour, M. N. Heibati, and K. Iranparvar, "Microstructural evaluation of contaminated implant surface treated by laser, photodynamic therapy, and chlorhexidine 2%," *The International Journal of Oral & Maxillofacial Implants*, vol. 33, no. 5, 2018.

[38] S.-I. Shin, E.-K. Lee, J.-H. Kim et al., "The effect of Er : YAG laser irradiation on hydroxyapatite-coated implants and fluoride-modified TiO_2-blasted implant surfaces: a microstructural analysis," *Lasers in Medical Science*, vol. 28, no. 3, pp. 823–831, 2013.

[39] S.-W. Kim, Y.-H. Kwon, J.-H. Chung, S.-I. Shin, and Y. Herr, "The effect of Er : YAG laser irradiation on the surface microstructure and roughness of hydroxyapatite-coated implant," *Journal of Periodontal & Implant Science*, vol. 40, no. 6, pp. 276–282, 2010.

[40] A. R. Eriksson and T. Albrektsson, "Temperature threshold levels for heat-induced bone tissue injury: a vital-microscopic study in the rabbit," *The Journal of Prosthetic Dentistry*, vol. 50, no. 1, pp. 101–107, 1983.

[41] C. F. Ferreira, J. Babu, E. K. Migliorati, S. Stein, and F. Garcia-Godoy, "Assessment of the effect of CO2 laser irradiation on the reduction of bacteria seeded on commercially available sandblasted acid-etched titanium dental implants: an in vitro study," *The International Journal of Oral & Maxillofacial Implants*, vol. 30, no. 3, pp. 588–95, 2015.

[42] M. Lollobrigida, L. Fortunato, G. Serafini et al., "The prevention of implant surface alterations in the treatment of peri-implantitis: comparison of three different mechanical and physical treatments," *International Journal of Environmental Research and Public Health*, vol. 17, no. 8, p. 2624, 2020.

[43] P. Rechmann, H. M. Sadegh, D. S. Goldin, and T. Hennig, Eds., *Lasers in Dentistry V*, International Society for Optics and Photonics, Bellingham, WA, USA, 1999.

Hindawi
Advances in Materials Science and Engineering
Volume 2021, Article ID 1364423, 6 pages
https://doi.org/10.1155/2021/1364423

Research Article

Analyzing the Cooling Rate and Its Effect on Distribution of Pattern and Size of the Titanium Diboride Particles Formed

P. Senthil Kumar,[1] **Pon Selvan Chithirai**,[2] **D. Antony Prabu**,[3] **G. Surya Prakash**,[4] **V. Murali Krishna**,[1] **and Jemal Yimer Mohammed**[5]

[1]*Department of Mechanical Engineering, B. V. Raju Institute of Technology, Narsapur, Telangana, India*
[2]*Head of School, Science and Engineering, Curtin University Dubai, Dubai, UAE*
[3]*Department of Mechanical Engineering, Loyola-ICAM College of Engineering and Technology, Chennai, India*
[4]*Department of Mechanical Engineering, Marri Laxman Reddy Institute of Technology and Management, Hyderabad, India*
[5]*Department of Mechanical Engineering, WOLLO University, Kombolcha Institute of Technology, Kombolcha, Ethiopia Post Box No: 208*

Correspondence should be addressed to Jemal Yimer Mohammed; jemalm@kiot.edu.et

Received 7 October 2021; Revised 3 November 2021; Accepted 6 November 2021; Published 10 December 2021

Academic Editor: Adam Khan M

Copyright © 2021 P. Senthil Kumar et al. This is an open access article distributed under the Creative Commons Attribution License, which permits unrestricted use, distribution, and reproduction in any medium, provided the original work is properly cited.

In this work, we synthesize Al/TiB_2 metal matrix composites (MMC) based on the effect of cooling rate in the melt while pouring into the permanent mold condition. The objective of this paper is to achieve the desired distribution pattern and increased TiB_2 particles' size in the Al/TiB_2 MMC ingot. Two halide salts, viz., potassium hexafluorotitanate (K_2TiF_6) and potassium tetrafluoroborate (KBF_4), are procured and measured. The two salts were mixed with the aluminium melt in the crucible, and it is stirred manually with help of a graphite rod. Because of the exothermic reaction, the melt reacts very quickly and that is what dropped the salts slowly. The salt particles were synthesized because of the exothermic reaction, and it will allow the particles to grow. The size and distribution of particles differ at different place in the MMC. An FEA tool ProCAST was used to analyze the cooling rate of the melt, and SEM is used to study the microstructure of the ingot at different places. The microstructures helped to identify the size of reinforcement in the MMC. The TiB_2 particles are distributed more at this location at 810°C, and the TiB_2 particles formed various clusters in this zone as 70%–80%. Also, the tribological characteristics are analyzed with the help of the results.

1. Introduction

The cast aluminium components are used in automotive industries due to its more strength-weight ratio, outstanding castability, and corrosion resistance [1, 2]. The *ex situ* method is involved for the fabrication of particulate matter reinforced metal matrix composites (PRMMCs) by conventional *ex situ* method due to its isotropic properties, ease of fabrication, and the lower cost. The reinforcement is added directly to fabricate the *ex situ* composites [3, 4]. In *in situ* method, a chemical reaction of reinforcements inside the composites takes place to synthesize the composites. To identify the behavior of *in situ* particles, a small work was carried out in the aluminium matrix composites [5].

The *in situ* metal matrix composites have a good attraction characteristic because of their good bonding strength and well distribution of fine reinforcement [6, 7]. It was found that the study was concentrated on fabrication and the mechanical properties of the reinforcement such as SiC, Al_2O_3, TiC, and B_4C. Various researchers have performed high-performance applications focusing on TiB2 as the reinforcement as of its high elastic modulus and high thermal conductivity [8, 9]. Also, it does not react with the molten aluminium. The casting defects such as oxide films, porosity, and other inclusions will strongly disturb the mechanical behavior of the cast aluminium alloys [10, 11]. However, because of the stiffness, hardness, and improved tensile strength, the aluminium-based MMCs are preferred

compared to the base matrix alloy [12–14]. The fabrication of aluminium-based MMCs is done by addition of SiC, Al_2O_3, TiC, CBN, and TiB_2. Out of these ceramic-based reinforced particles, TiB_2 is used mostly because they possess hardness, maximum tensile strength, and compressive strength [15, 16].

Because of the very clean and size of particles in the interface of the *in situ* method, the fabrication of Al/TiB_2 MMCs is preferred. Also, the increased tensile strength and fatigue strength is due to the very fine particles [17].

In the *in situ* fabrication method, two salt powders such as K_2TiF_6 and KBF_4 were used as reinforcement. They were mixed in measured proportion and then poured to the aluminium melt slowly. The mixture was stirred manually to endorse the reaction between salts with the help of a manual graphite rod. The floron gas was inserted in the melt to avoid formation of gases which will create the casting defects such as blow holes [18, 19]. Later, the melt was kept in hold to synthesize TiB_2 particles that grow in size with holding time [20, 21].

The Al/TiB_2 melt was poured into the mould, so the falling elevation will be the possible turbulence that occurs during filling. The fragmented TiB_2 particles are created due to the turbulence, and also a variation in distribution occurred at different locations. It occurs because the cooling rate and turbulence were attributed and also due to the influence of melt fluidity [22, 23]. The above parameters were analyzed, and their effects are understood clearly from the SEM micrographs captured from the cast ingot at six different locations.

2. Experimental Work

An *in situ* method was used to fabricate Al/TiB_2 MMCs through salt metal reaction. Three different melt temperatures were maintained, such as 750°C, 780°C, and 810°C. Also, three dissimilar holding times were maintained after mixing of entire salt such as ten minutes, twenty minutes, and thirty minutes before pouring into the permanent molds. Through the same procedure, totally nine ingots were fabricated with different combinations, pouring temperature, and holding time [24]. The size of the reinforced particle is not the same as in the melt because of the parameters' fluidness and disorder at different places of the ingot and the local cooling rate of the casting [25].

Figure 1(a) shows the twenty-four various locations in cast ingots from top to bottom, and based on variation of local conditions of ingot, six locations were selected from twenty-four various locations. The distribution of TiB_2 particles and size were compared for all nine ingots through the SEM micrographs; Figures 1(b)–1(d) show the SEM micrographs.

2.1. Finite Element Analysis. Figure 2(a) shows the simulation model, and Figure 2(b) describes the mesh diagrams of ingot. The temperature vs. time curves were generated at twenty-four different locations of each ingot by using the FEA tool. Out of the twenty-four different locations, selected six locations were shortlisted for simulation. From the simulation, a drastic variation occurred in the melt due to the turbulence of melt, cooling rate, and fluidness.

Figures 3(a)–3(f) show the temperature vs. time curves at selected six different locations.

3. Results and Discussions

At location 23, the temperature-time curve indicates maximum cooling rate and turbulence during filling out of twenty-four different locations. Also, it was found that the fluidness reaches its maximum range at the maximum pouring temperature.

Also, here we discuss the effect of cooling rate at location 23. This location is marked in the bottom surface of the ingot, and the cooling rate and the fluidity are maximum at this location at 810°C pouring temperature. Additionally, the falling height of the melt during the filling process is considered to be maximum. Because of the abovementioned reasons, at location 23, the turbulence will be maximum. Because of these reasons, the circulation will be maximum at 810°C, and it will cause the TiB_2 particles to fragment. Hence, the TiB_2 particles get entrapped quickly because of maximum cooling rate, and the casting at this location is freezed [26].

Moreover, more TiB_2 particles are distributed at this location at 810°C and the TiB_2 particles formed various clusters in this zone as 70%–80%.

Here, we discuss the effect of cooling rate at location 21. This location is marked in the middle surface of the ingot; the cooling rate and the fluidity are modest at this location at 810°C pouring temperature. Additionally, the falling height of the melt during the filling process is considered to be average. Because of the abovementioned reasons, at location 21, the turbulence will be average. Because of these reasons, the circulation will be maximum at 810°C, and it will cause the TiB_2 particles to fragment. Hence, the TiB_2 particles get entrapped quickly because of maximum cooling rate, and the casting at this location is freezed [27, 28].

Moreover, more TiB_2 particles are distributed at this location at 810°C and the TiB_2 particles formed various clusters in this zone as 60%–70%.

In this paragraph, we discuss the effect of cooling rate at location 19. This location is marked in the top surface of the ingot; the cooling rate and the fluidity are very low at this location at 810°C pouring temperature. Additionally, the falling height of the melt during the filling process is considered to be very less. Because of the abovementioned reasons, at location 19, the turbulence will be average. Because of these reasons, the circulation will be maximum at 810°C, and it will cause the TiB_2 particles to fragment. Hence, the TiB_2 particles get entrapped quickly because of very minimum cooling rate, and the casting at this location is freezed. Most of the TiB_2 particles were trapped at locations 23 and 21 already. Hence, very small particles settled down in this particular location.

Analyzing at location 1, the falling height and the cooling rate were minimum. Due to the effect, most of the particles

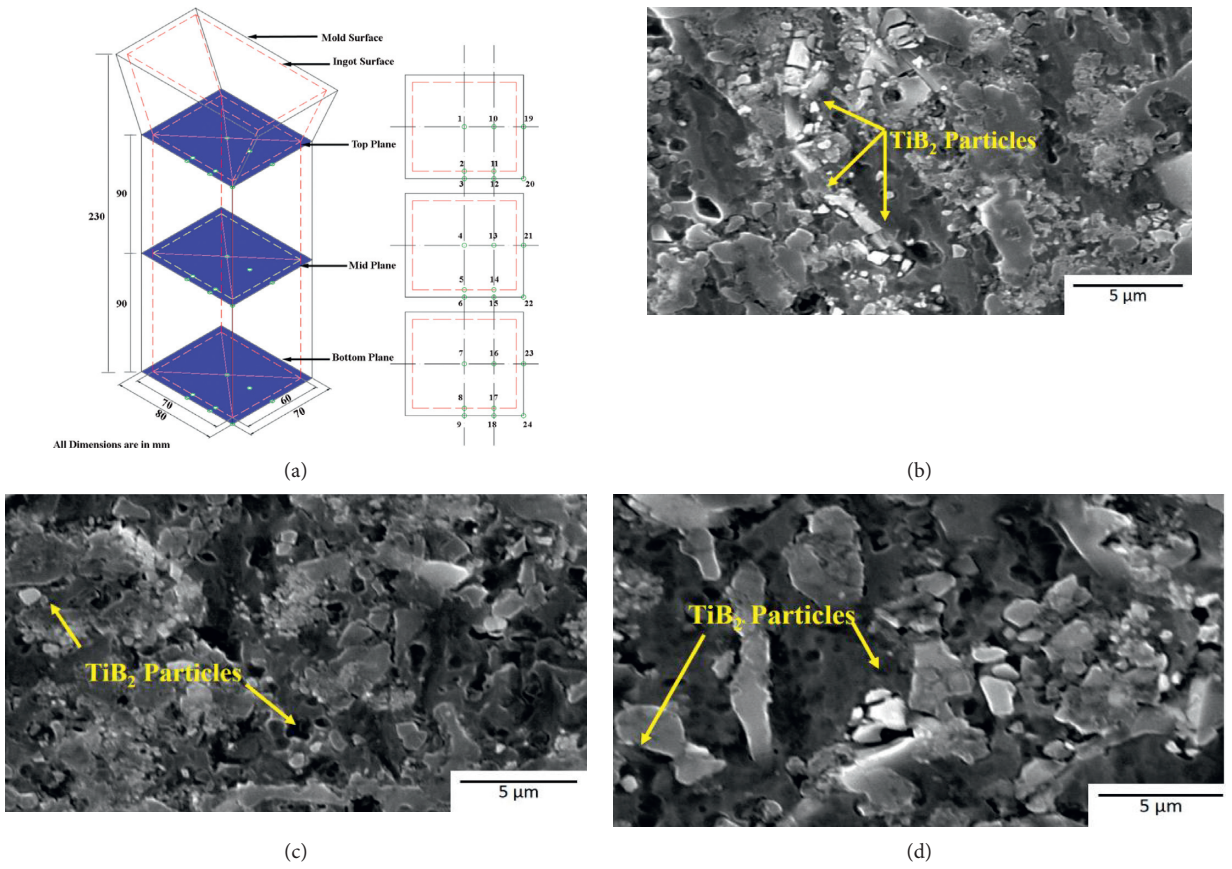

Figure 1: (a) Ingot drawing showing locations considered. SEM micrograph at location 1 of the ingot for (b) 750°C pouring temperature and 10-min holding time, (c) 750°C pouring temperature and 20-min holding time, and (d) 750°C pouring temperature and 30-min holding time.

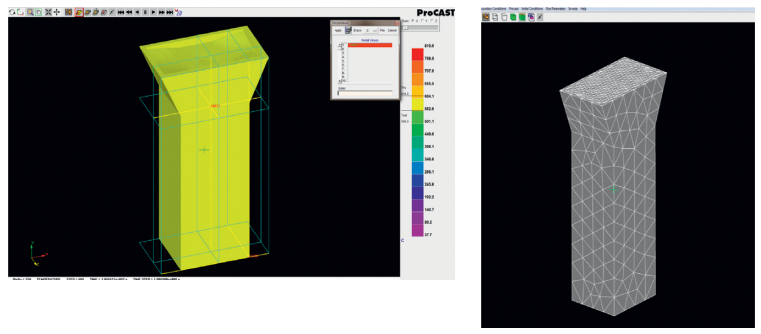

Figure 2: (a) Mold model. (b) Mold meshing.

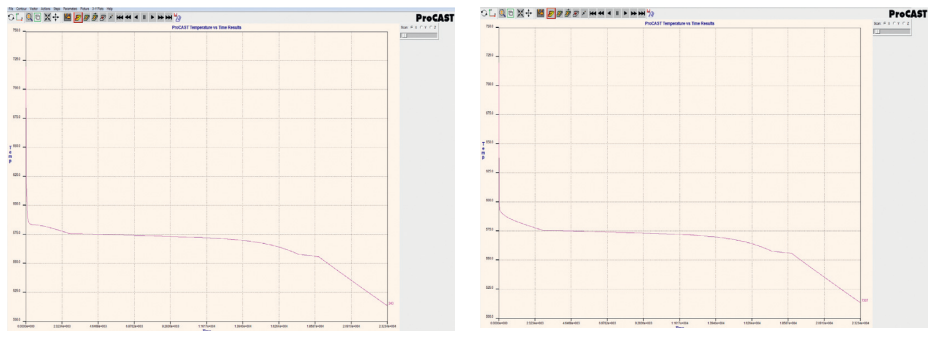

Figure 3: Continued.

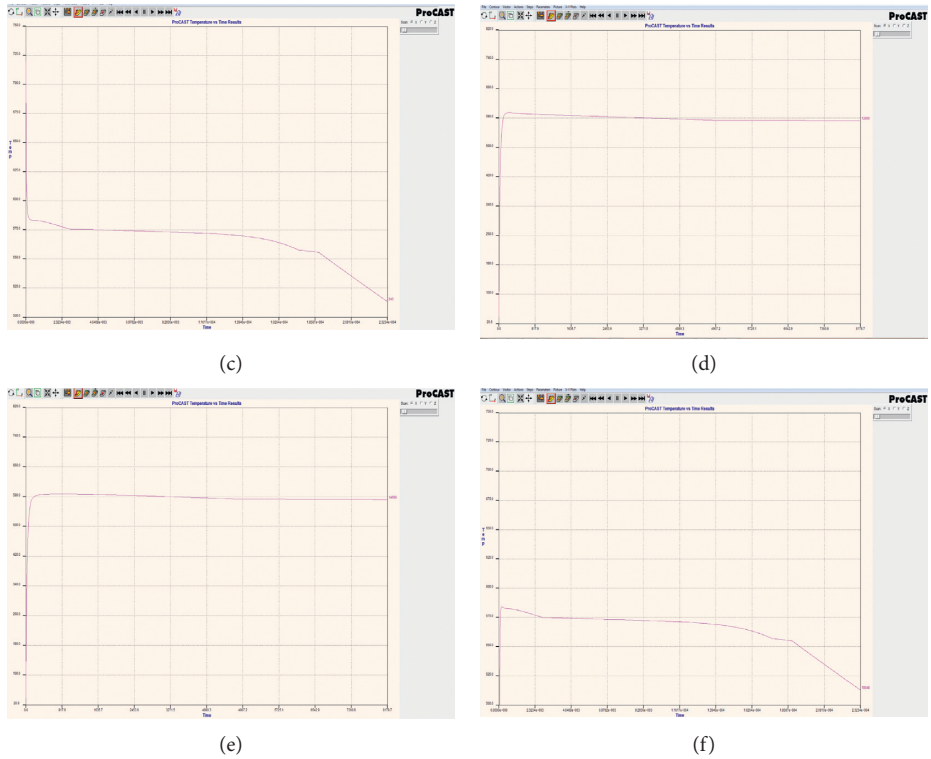

Figure 3: (a) T vs. t at point 1 for 750°C. (b) T vs. t at point 4 for 780°C. (c) T vs. t at point 7 for 780°C. (d) T vs. t at point 19 for 780°C. (e) T vs. t at point 21 for 780°C. (f) T vs. t at point 23 for 780°C.

Table 1: TiB2% of different places in micrographs.

Location	Pouring temperature (in degree Celsius)	Percentage area of TiB_2		
		10 min	20 min	30 min
1	750	10–20	30–40	35–40
	780	20–30	30–40	35–40
	810	20–30	30–40	40–50
4	750	30–35	30–35	35–40
	780	20–30	25–35	30–40
	810	25–30	30–35	40–50
7	750	10–20	30–40	25–35
	780	20–30	35–45	40–50
	810	20–30	40–50	60–70
19	750	20–30	20–30	30–40
	780	20–30	40–50	40–50
	810	20–30	50–60	50–60
21	750	30–40	20–30	40–50
	780	10–20	30–40	30–40
	810	30–40	50–60	60–70
23	750	30–35	35–40	40–50
	780	35–40	45–50	50–60
	810	40–50	60–70	70–80

were trapped at the bottom of the ingot at location 1, which was found to have fewer TiB2 particles through SEM micrographs. Also, it covers 40%–50% area in the SEM micrograph.

The friction between the aluminium matrix and TiB2 particles was analyzed. The tribological characteristics showed better performance than conventional material.

Table 2: TiB2% particle size for holding time.

Position	Temperature (°C)	Particle size for holding time (μm)		
		10 minutes	20 minutes	30 minutes
1	750	1–1.5	1–1.5	2–2.5
	780	1–1.5	1.5–2	2–2.5
	810	1.5–2	2–2.5	2.5–3
4	750	1–1.5 *L*–5, *D*–1	1.5–2	2.5–3
	780	1–1.5	1–1.5	2–3
	810	1–1.5	1–1.5	2–2.5 *L*–12, *D*–1
7	750	1–1.5	1.5–2	2.5–3
	780	1.5–2	2–2.5	2–2.5
	810	1–1.5 *L*–8, *D*–1.5	1–1.5	2–2.5
19	750	1–1.5	1–1.5	1.5–2
	780	1–1.5	1.5–2	2–2.5
	810	1–1.5	1–1.5	2–2.5
21	750	1–1.5	1.5–2	2–2.5
	780	1–1.5	1–1.5	1.5–2
	810	1–1.5 *L*–10, *D*–1.5	1–1.5	2–2.5
23	750	1.5–2	2–2.5	2–2.5
	780	1–1.5	1.5–2	2–2.5
	810	1–1.5	1–1.5	2–2.5 *L*–5, *D*–1

L = length of needle-shaped TiB_2 particles. D = diameter of needle-shaped TiB_2 particles.

Also, the distribution of TiB_2 particles at different locations for less holding times and pouring temperatures was found to be low, which is tabulated in Tables 1 and 2.

4. Conclusions

The TiB_2 particles were found to be more at location 23 because of the very high cooling rate.

The TiB_2 particles were found more at locations 23 and 21 due to the very high turbulence. When the circulation of the fluid is more, the fluidity is also more.

Also, the tribological characteristics showed significant improvement on the basis of hardness. However, the reinforced particles get trapped quickly when the cooling rate was very high at these locations.

Data Availability

No data were used to support this study.

Conflicts of Interest

The authors declare that they have no conflicts of interest.

References

[1] S. Parasuraman, I. Elamvazuthi, G. Kanagaraj, E. Natarajan, and A. Pugazhenthi, "Assessments of process parameters on cutting force and surface roughness during drilling of AA7075/TiB2 in situ composite," *Materials*, vol. 14, no. 7, Article ID 1726, 2021.

[2] G. Li, Y. Qu, Y. Yang, Q. Zhou, X. Liu, and R. Li, "Improved multi-orientation dispersion of short carbon fibers in aluminum matrix composites prepared with square crucible by mechanical stirring," *Journal of Materials Science & Technology*, vol. 40, pp. 81–87, 2020.

[3] G. F. Aynalem, "Processing methods and mechanical properties of aluminium matrix composites," *Advances in Materials Science and Engineering*, vol. 2020, Article ID 3765791, 19 pages, 2020.

[4] R. Purohit, M. M. U. Qureshi, and B. Kumar, "Effect of forging on aluminum matrix nano composites: a review," *Materials Today: Proceedings*, vol. 4, no. 4, pp. 5357–5360, 2017.

[5] C. Prakash, S. Singh, S. Sharma et al., "Fabrication of aluminium carbon nano tube silicon carbide particles based hybrid nano-composite by spark plasma sintering," *Materials Today: Proceedings*, vol. 21, no. 1, pp. 1637–1642, 2020.

[6] P. Senthil Kumar, V. Kavimani, K. Soorya Prakash, V. Murali Krishna, and G. Shanthos Kumar, "Effect of TiB2 on the corrosion resistance behavior of in situ Al composites," *International Journal of Metalcasting*, vol. 14, no. 1, pp. 84–91, 2020.

[7] M. Hadian, H. Shahrajabian, and M. Rafiei, "Mechanical properties and microstructure of Al/(TiC+TiB2) composite fabricated by spark plasma sintering," *Ceramics International*, vol. 45, no. 9, pp. 12088–12092, 2019.

[8] C. Mallikarjuna and S. M. Shashidhara, *Proceedings of the World Congress on Engineering and Computer Science*, San Francisco, CA, USA, 2007.

[9] Y. Shadangi, S. Sharma, V. Shivam et al., "Fabrication of Al-Cu-Fe quasicrystal reinforced 6082 aluminium matrix nanocomposites through mechanical milling and spark plasma sintering," *Journal of Alloys and Compounds*, vol. 828, Article ID 154258, 2020.

[10] I. Dinaharan and E. T. Akinlabi, "Low cost metal matrix composites based on aluminum, magnesium and copper reinforced with fly ash prepared using friction stir processing," *Composites Communications*, vol. 9, pp. 22–26, 2018.

[11] K. Niranjan and P. R. Lakshminarayanan, "Optimization of process parameters for in situ casting of Al/TiB2 composites through response surface methodology," *Transactions of Nonferrous Metals Society of China*, vol. 23, no. 5, pp. 1269–1274, 2013.

[12] P. S. Kumar, P. R. Lakshminarayanan, and R. Varahamoorthi, "Effect of holding time of the Al/TiB2 melt at the pouring temperature on the formation and size of TiB2 particles formed," *Journal of Advanced Microscopy Research*, vol. 11, no. 2, pp. 140–144, 2016.

[13] S. Suresh, N. Shenbag, and V. Moorthi, "Aluminium-Titanium diboride (Al-TiB2) metal matrix composites: challenges and opportunities," *Procedia Engineering*, vol. 38, pp. 89–97, 2012.

[14] G. Elango and B. K. Raghunath, "Tribological behavior of hybrid (LM25Al + SiC+ TiO2) metal matrix composites," *Procedia Engineering*, vol. 64, pp. 671–680, 2013.

[15] V. Mohanavel, K. Rajan, S. Arul, and P. V. Senthil, "Study on microstructure and mechanical behavior of particulate reinforced aluminum matrix composites (PRAMCS)," *International Journal of Advances in Engineering & Technology*, vol. VII, no. 1, p. 253, 2016 -March 252.

[16] M. R. Roshan, T. Mousavian, H. Ebrahimkhani, and A. Mosleh, "Fabrication of Al-based composites reinforced with Al2O3-Tib2 ceramic composite particulates using

vortex-casting method," *Journal of Mining and Metallurgy, Section B: Metallurgy*, vol. 49, no. 3, pp. 299–305, 2013.

[17] X. Huang, Z. Zhao, L. Zhang, and J. Wu, "The effects of ultra-high-gravity field on phase transformation and microstructure evolution of the TiC-TiB2 ceramic fabricated by combustion synthesis," *International Journal of Refractory Metals and Hard Materials*, vol. 43, pp. 1–6, 2014.

[18] M. Selvaganesan and S. Suresh, "Production and characterization of Al 6061-TiB_2 metal matrix composites," *International Journal of Engineering Research and Technology*, vol. 2, no. 11, 2013.

[19] H. B. Michael Rajan, S. Ramabalan, I. Dinaharan, and S. J. Vijay, "Synthesis and characterization of in situ formed titanium diboride particulate reinforced AA7075 aluminum alloy cast composites," *Materials & Design*, vol. 44, pp. 438–445, 2013.

[20] D. Yadav and R. Bauri, "Friction stir processing of Al-TiB2 in situ composite: effect on particle distribution, microstructure and properties," *Journal of Materials Engineering and Performance*, vol. 24, no. 3, pp. 1116–1124, 2015.

[21] H. Itoh, S. Naka, T. Matsudaira, and H. Hamamoto, "Preparation of TiB2 sintered compacts by hot pressing," *Journal of Materials Science*, vol. 25, no. 1, pp. 533–536, 1990.

[22] L. Lu, M. O. Lai, and F. L. Chen, "Al-4 wt% Cu Composite reinforced with in-situ TiB_2 particles," *Acta Materialia*, vol. 45, pp. 4297–4309, 1997.

[23] A. R. Kennedy, A. E. Karantzalis, and S. M. Wyatt, "The microstructure and mechanical properties of TiC and TiB_2-reinforced cast metal matrix composites," *Journal of Materials Science*, vol. 34, no. 5, pp. 933–940, 1999.

[24] J. H. Abboud and D. R. F. West, "Microstructure of Ti-TiB2 surface layers produced by laser particle injection," *Journal of Materials Science Letters*, vol. 13, no. 6, pp. 457–461, 1994.

[25] M. Wang, D. Chen, Z. Chen et al., "Mechanical properties of in-situ TiB2/A356 composites," *Materials Science and Engineering A*, vol. 590, pp. 246–254, 2014.

[26] A. Haiter Lenin, S. C. Vettivel, T. Raja, L. Belay, and S. C. E. Singh, "A statistical prediction on wear and friction behavior of ZrC nano particles reinforced with Al Si composites using full factorial design," *Surfaces and Interfaces*, vol. 10, pp. 149–161, 2018.

[27] J. S. Park, J. H. Yun, Y. D. Park, Y. H. Park, K. M. Cho, and I. M. Park, "Effect of cooling rate on mechanical and electrical properties of Cu-TiB_2 by turbulent in-situ mixing process," *Solid State Phenomena*, Trans Tech Publications, vol. 119, Zurich, Switzerland, 2007.

[28] P. Senthilkumar, R. Manimaran, and Y. Krishna Reddy, "Evaluation of mechanical properties of hybrid Al7009 nanocomposite," *Energy Sources, Part A: Recovery, Utilization, and Environmental Effects*, vol. 43, no. 2, pp. 216–224, 2018.

Hindawi
Advances in Materials Science and Engineering
Volume 2021, Article ID 9078702, 11 pages
https://doi.org/10.1155/2021/9078702

Research Article

Studies on Dry Sliding Wear and Solid Particle Erosive Wear Behaviours of Natural Fibre Composite Developed from Water Hyacinth Aquatic Plant for Automotive Application

A. Ajithram,[1] **Jappes J. T. Winowlin**,[1] **Khan M. Adam**,[1] **N. C. Brintha**,[2] **and Faris Waleed Fekry**[3]

[1]*Department of Mechanical Engineering and Centre for Surface Engineering, Kalasalingam Academy of Research and Education, Virudhunagar, Tamil Nadu, India*
[2]*Department of Computer Science Engineering and Centre for Surface Engineering, Kalasalingam Academy of Research and Education, Virudhunagar, Tamil Nadu, India*
[3]*Department of Mechanical & Aerospace Engineering, College of Engineering, International Islamic University Malaysia, Gombak, Selangor, Malaysia*

Correspondence should be addressed to Khan M. Adam; adamkhanm@gmail.com

Received 30 October 2021; Accepted 16 November 2021; Published 2 December 2021

Academic Editor: Veronica Calado

Copyright © 2021 A. Ajithram et al. This is an open access article distributed under the Creative Commons Attribution License, which permits unrestricted use, distribution, and reproduction in any medium, provided the original work is properly cited.

In this research, an attempt is made to investigate the abrasive and erosion wear resistance of aquatic waste plant water hyacinth converted fibre-reinforced polymer composites. From a novel approach, the new fibre extraction machine is designed to extract the hyacinth fibre from the parent plant and reinforce it to the epoxy matrix material to produce a natural fibre composite for frictional applications. The extracted fibre is dried in the open sunlight area for 22 to 35 days to remove moisture and external dust particles. Then, different weight percentages (15, 20, 25, 30, and 35) of composite samples are produced with the help of the hot press compression moulding technique. Improved hyacinth composite tribology properties are tested by utilizing the pin on the disk machine. This setup included various processing parameters like load (10, 20, and 30 N), velocities (1, 2, and 3 m/s), speed (160, 320, and 479 rpm), and constant sliding distance condition, and the erosion setup also influences the essential parameters like impact angle (30, 45, and 60°), erodent velocity (1, 2.5, and 3.3 m/s), and discharge rate (28, 41, and 72 g/m). The factorial techniques are used to identify the important design factors. The final results represent the weight loss, volume loss, and erosion rate of hyacinth fibre composite. By utilizing the SEM (scanning electron microscope), the worn surface morphology of different weight percentages of hyacinth fibre samples are analysed. To upgrade the usage of hyacinth reinforced composites for different industrial applications, wear and erosion studies are conducted with different parameter conditions.

1. Introduction

In recent years, researchers are focusing on recycling of material concepts in the aspect of global impact because of environmental problems. Previously, in polymer composite fields, the synthetic fibres glass, carbon, and some of the other fibres were used. But all synthetic fibres have some disadvantages like being non-recyclable and non-degradable and having higher cost and high amount of energy consumption aspects. Nowadays, the demand for biodegradable materials is increasing [1]. Normally, the usage of natural fibres in the polymer composite material field has enormously increased and created a huge impact. All over the world, so many researchers and industrial experts used natural fibre as a reinforcement material because of so many positive advantages and applications compared to synthetic fibres. Generally, natural fibres have low cost and are biodegradable, very cheap, easily available, and ecofriendly. The natural fibre reinforced composites have very good mechanical strength and good thermal stability [2]. The sisal, coir, banana, hemp, jute, flax, and kenaf fibres are used as a reinforcement in the conventional polymer composites. The

aspect of tribology behaviour in natural composites has not been properly covered and elaborated. These composite materials are used in building materials, commercial applications, and automotive and construction industries. Main disadvantage of natural fibre is the presence of external dust particles on the fibre surfaces, poor primary and secondary phase adhesions like reinforcement and matrix material phase, and dimensional stability [3]. However, composite developed with fibres and fillers as reinforcement in the matrix is the good combination for product development. Both natural and synthetic fibres have serious disadvantages [4]. Conventionally, fibres' primary phase and matrix material phase bonding is the main reason to increase and decrease the sample properties. But few surface treatments to the fibres slightly increase the bond between the reinforcement and matrix phase and this bonding surely expands the strength of the materials. From the interlocking bonding aspect, alkali treatment is one of the effective methods [5]. Based on the chemical structure and effect of the alkaline solutions, it dissolves the cellulose and hemicellulose contents on the surface of the fibre. This treatment increases the fibrillation process to remove the outer layer of the fibre. At the same time, the seawater treatment also improves the interfacial bonding of fibre composites. It leads to improving the mechanical property. In terms of tribology behaviours, most of the literature surveys cover the synthetic composite majorly. Fewer kinds of literature are only available to give the details in tribology behaviour of natural fibre composites. Generally, the BOR machine (block on ring) is used for the dry sliding test of the composite. The final results indicate the natural fibre's composite wear behaviour. Some of the authors studied and evaluated the natural fibre composite wear and erosion behaviours like sisal, coir, and palm fibre reinforced composite.

Mechanical degradation refers to solid particle erosion with the usage of different erodents [6]. Many industries reported material damages because of this erosion behaviour. Solid particle erosion is the conventional process to find out the progressive loss of a material's solid particles. Very few literature surveys are conducted in the aspect of natural fibre composite erosion studies. Mostly, the erosion rate of fibre composites is higher than that of the metals. The erosion behaviour is related to the velocity, impact angle, erodent type, and particle size parameters [7].

In this work, water hyacinth natural fibre is extracted from the parent plant and then the fibre is reinforced with epoxy matrix materials with different weight percentages, and a hyacinth fibre composite sample is produced with the help of a hot press compression moulding machine. Water hyacinth is a free-floating aquatic plant, mainly available in a local water body especially in a tropical and subtropical region [8]. Temperature plays a very important role in water hyacinth plant growth life. 15°C is the minimum, 20–28°C is an optimum level, and above 36°C is the maximum temperature of the water hyacinth plant [9]. The water hyacinth has a good character that it can grow fast over surface of any water bodies. So, even the Sun's rays will not penetrate below the water. The behaviour of the hyacinth plant is a serious threat to the entire environment [10]. All the countries invested huge amounts of money to remove hyacinth plants from the water bodies. Present work will encourage the researchers to use natural (waste) material as a useful material for effective utilization.

2. Materials

The water hyacinth plants are found in the water bodies of Trichy District, Tamil Nadu, India. After cultivating the plant, the separation process is done. The plant stem is separated from the parent plant. Normally, all the aquatic plant fibres are extracted by retting. Water hyacinth plant fibre cannot be effectively extracted from retting. By utilizing the mechanical way of the extraction process, hyacinth plant fibres are extracted. To remove the impurities and external dust particles, hyacinth fibres are cleaned by running water and distilled water. Then, the fibres are dried in the open sunlight area for 3 days until their colour turned from green to dark brown. This drying process is commonly used to remove the moisture content of the fibres. Epoxy resin is used as a matrix material with a combination of hardeners on a particular standard like LY556 and HY951 with a mixing ratio of 10 : 1 [11]. Table 1 explains the essential properties of hyacinth fibre and epoxy matrix materials. In a natural fibre composite, epoxy resin, which has high thermal stability, is mostly used as a matrix material to withstand the high temperature and enhance the mechanical properties of the reinforcement. These matrix materials were purchased from Covai Seenu & Company, Coimbatore, Tamil Nadu, India. Figure 1 clearly describes the extraction process of water hyacinth plant fibres.

2.1. Fabrication of Composites. After the fibre extraction process is completed, different weight percentages of the composite sample are prepared (15, 20, 25, 30, and 35%). Different weight percentages of fibre reinforcement are mixed with epoxy matrix material by using the compression moulding machine. In the hot press compression moulding machine, the upper plate temperature is set to 110°C and the lower plate temperature is 120°C. Individual plate temperature is used to reducing the curing time of the composite sample. After the particular temperature is fixed on both plates, 1500PSI hydraulic pressure is applied to both the top and bottom plates. The time for curing and compression loading, for a proposed $300 \times 125 \times 3$ mm composite plate, is fixed as 30 minutes. Figure 2 clearly explains the fabrication process of hyacinth reinforced fibre composites.

2.2. Wear Test Apparatus. The pin on disc (POD) testing machine is used to examine the water hyacinth fibre composite's dry sliding behaviour [12]. Easy availability, low cost, and quick handling methods are the reasons to use this apparatus commonly in the polymer matrix composites for wear applications. Initial verifications and surface preparation on disc material are carried out in advance to the experimentation [13]. Very thin and sharp brushes are used to clean the composite samples before and after the tests. Figure 3 shows the pin on disc apparatus.

Table 1: Mechanical properties of epoxy resin and water hyacinth plant fibre.

Properties	Epoxy resin	Water hyacinth fibre
Density (g/cm^3)	1.12	1.02
Tensile strength (MPa)	34	3.15
Tensile modulus (GPa)	3.4	1.8
Elongation (%)	2.24	3.7

Figure 1: Extraction process of water hyacinth plant fibres.

Figure 2: Fabrication process of water hyacinth plant fibre composite.

Once the wear test is finished, the average roughness of the sample is calculated with a different region. Volume loss of the natural fibre composite wear specimen is the measure before and after testing by utilizing an electronic weight balance machine [14, 15]. The initial weight is assigned as W1, the final weight is assigned as W2, then the volume loss is measured,, and five readings are taken in each samples for confirmation. Volume loss is calculated by using the following equation:

$$\mathrm{VL} = \frac{\nabla w}{\rho}. \tag{1}$$

2.3. Erosion Apparatus and Experimental Procedure. Water hyacinth natural fibre composite sample is tested with the DUCOM TR470 model erosion wear tester with a nozzle diameter of 1.5 mm. 20–35 μm alumina powder is used as the erodent material. The composite test samples are cut as per ASTM standards (G76 (2013)) with the dimension of $25 \times 25 \times 3$ mm [16]. Figure 4 shows the air jet erosion test apparatus.

Before conducting the experiment, the sample is fully cleaned by pressurised air and dry cloth. The output response is measured in g/min. The erodent rate is governed by following equation:

$$\mathrm{Er} = \frac{W_b - W_a}{t}. \tag{2}$$

Impinged surface hardness is measured by utilizing the micro Vickers hardness test. From the different impact regions, the five observations are taken for the calculations [17]. Density of the natural fibre composite is tested with the help of the Archimedes principle. The composite samples' theoretical density and experimental density are also measured [18].

2.4. Experimental Design. The combination of the output result process of dry sliding wear and erosive wear is determined by utilizing the design of the experiment method [19]. Normally, the full factorial technique is used to find the effect of different factors with n levels. This experiment method was used as sequence operation to find out the minimum amount of wear and erosion of the sample. In a full factorial method, the

Figure 3: Pin on disc machine under the specimen test.

Figure 4: Air jet erosion test apparatus.

output response is involved in all combinations of the factor levels [20]. In dry sliding wear, the three factors applied load (A), sliding time (B), and sliding speed (C) are in control. Similarly, impact angle (A), particle velocity (B), and erodent discharge rate (C) are the factors used to design the erosion experiments. Tables 2 indicates the control factors and level for dry sliding wear used in water hyacinth composite material. Table 3 indicates the control factors and level for erosive wear used in water hyacinth composite material.

2.5. Morphological Analysis. The morphological studies in worn surface of the composite is revealed with scanning electron microscope. Ziess SEM is used to capture high-resolution images following standard working conditions.

3. Result and Discussion

3.1. Volume Loss. When using natural fibre as a reinforcement of the polymer matrix composites, the tribology properties are increased. This work briefly discussed the most influencing process parameters to get the minimum amount of wear like weight loss and volume loss. Increase in load at a maximum has highly influenced the material to reach maximum wear rate, and the same has been proved with existing literatures. The Taguchi orthogonal array experiments are based on the full factorial technique. By using the factorial technique, sliding speed, load, and influencing time parameters are determined. In this dry sliding experiment, the above three parameters are the most effective parameters. A dry sliding technique is used to determine the main effect, interaction effects, and their plots. Wear resistance of the water hyacinth-based composite is improved in some conditioning parameters. Epoxy matrix material resin easily penetrates the hyacinth fibre reinforcement, and it leads to strong interlocking. This dry sliding experiment decreased the interlocking property of the reinforcement and matrix material of the composite sample. Tables 4 and 5 describe the experimental design and its observation made through analysis of variance [21].

The expoxy material plays a vital role in increasing the mechanical strength and bonding of natural (bio) fibre. But a higher amount of fibre content decreases the mechanical property and internal bonding of the two states. Based on the experimentation, the wear rate varies with respect to increase in fibre weight percentage. Therefore, it has been confirmed that 30% (wt.) has good wear resistance compared to other combination. Conventionally, when a higher load acts for a long time, it leads to wear because a particular amount of heat is generated at the surface of the matrix and fibre reinforced sample. Figure 5 shows the main effect plots of the dry sliding output means and SN ratios of the hyacinth fibre sample.

However, the material removal rate is higher, and it leads to the weight loss and volume loss of the composite sample. From the literature surveys, compared to the other natural fibres, water hyacinth fibre with epoxy-based composite gives a positive effect on the test samples. Figure 6 clearly shows the residual plots for the dry siding output with respect to the frequency and standard residual.

3.2. Wear Mechanism. In general, the wear process takes place on the counter-face of the disc and the mating surface of the pin. Several types of plateaus have been formed. Generally speaking, plateaus are divided into two phases: dusty plateaus and rough plateaus. In the tribology system, the friction film affects the tribology performance. In the initial sliding process of the epoxy polymer composites reinforced with hyacinth natural fibres, debris in the form of fibre-matrix bulk found removed from the composite due to sliding friction following the pullout mechanism. There is evidence of fibre trapping near the sliding surface of the disc and in the friction layer. A dry sliding wear system's frictional layer is the layer that is most affected by the tribology performance of the pin on the disc. The frictional layer detaches from the machine surface when the load parameters are high. There is a high rate of material removal from the final debris and fragments, which attach to the disc with a friction layer. Due to the high friction, the film transferred smoothly during the test. It is apparent from this smooth transfer that the material has the least friction. A high volume loss at the test site is also one of the reasons for the loss.

Table 2: Control factors and levels for dry sliding wear test.

Factors	Levels		
	I	II	III
Load (N)	10	20	30
Time (s)	20	10	7
Speed (rpm)	160	320	479

Table 3: Control factors and levels for air jet erosion test.

Machining parameters	Symbol	Levels			Time
Impact angle (degree)	IA	30	45	60	10
Discharge (g/min)	EV	1	2.5	3.3	10
Erodent velocity (m/s)	DR	28	41	72	10

Table 4: Experimental observation for dry sliding wear test.

S. No.	Load (N)	Time (t)	Speed (rpm)	Output
1	10	20	160	0.00160
2	10	20	320	0.00220
3	10	20	479	0.00280
4	10	10	160	0.00150
5	10	10	320	0.00290
6	10	10	479	0.00340
7	10	7	160	0.00170
8	10	7	320	0.00260
9	10	7	479	0.00370
10	20	20	160	0.00150
11	20	20	320	0.00240
12	20	20	479	0.00450
13	20	10	160	0.00250
14	20	10	320	0.00340
15	20	10	479	0.00520
16	20	7	160	0.00360
17	20	7	320	0.00420
18	20	7	479	0.00640
19	30	20	160	0.00624
20	30	20	320	0.00790
21	30	20	479	0.00856
22	30	10	160	0.00290
23	30	10	320	0.00370
24	30	10	479	0.00460
25	30	7	160	0.00290
26	30	7	320	0.00260
27	30	7	479	0.00340

3.3. Erosive Wear. From the air jet erosion, the responses on the individual process parameters are discussed in detail. To recognize the effect of individual parameters, the graph is prepared by one parameter that is constant over another. Increasing the discharge rate (DR) leads to a higher erosion of the test samples [22]. At a 90-degree angle, the erodent strikes the surface of the material with respect to impact velocity. After impingement, the behaviour particle varies with respect to counter material. On the soft matrix, the material clings, and hard surface erodes fracture. This reacts with the responses on the surface. In addition, the erodent velocity will influence the response of wear rate. Tables 6 and 7 explain the experimental and analysis of variance observation of WH sample erosion test. Figure 7 indicates the mean effect plots of output and SN ratios on WH composite erosion test.

At 45 degrees, the particle slides at a maximum velocity, and shear rate increases. It has maximum material removal compared to other impact angle [23]. Figure 8 clearly indicates the normal probability plots and histogram plots of the hyacinth fibre composite erosion test with respect to the frequency and standard residual.

Table 5: Analysis of variance observation.

Source	DF	Seq SS	Adj SS	Ads MS	*F*	*P*	Contribution (%)
Load	2	0.000045	0.000045	0.0000015	12.37	0.002	26.33
Time	2	0.000023	0.000023	0.000023	1.79	0.194	3.83
Speed	2	0.000003	0.000003	0.000003	9.73	0.005	20.76
Error	20	0.000043	0.000043	0.000002			
Total	26	0.000088					

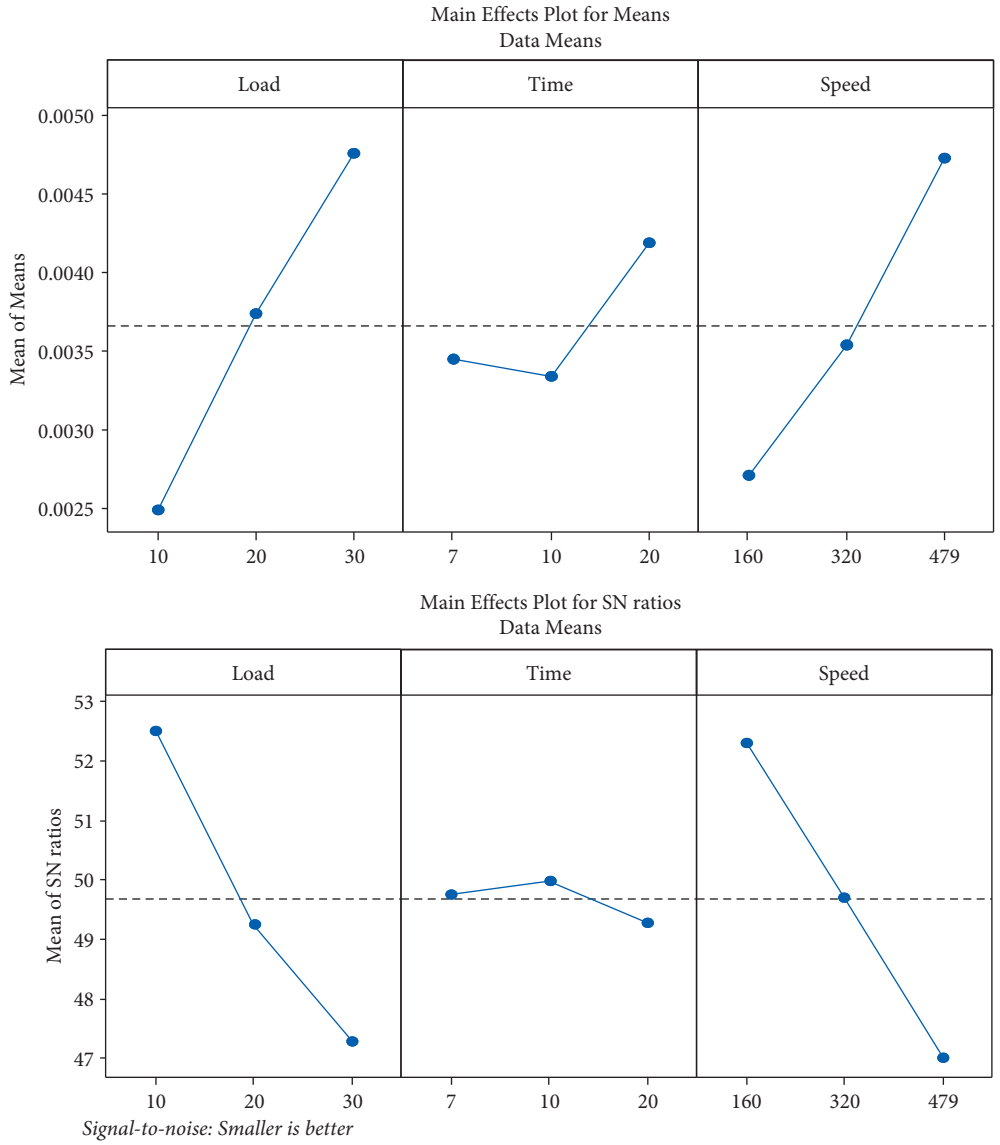

Figure 5: Main effect plots for means and SN ratios.

3.4. Erosive Wear Mechanism. Water hyacinth composite samples are evaluated through erosive wear with an air jet erosion machine. There is a high rate of wax discharge, which leads to erosive wear. It is the double erosion rate that takes up half of the erodent velocity increment. Our work focuses on determining the erosion rate of the hyacinth composite sample based on erosion rate parameters such as erodent velocity, impact angle, and discharge rate. In addition to a range of impact angles (30°, 45°, and 60°), erodent velocity varies (28, 41, and 72) and the discharge rate lies in the range of (1, 2.5, and 3.3).

3.5. Surface Morphological Studies. The wear morphology of the worn surface is studied with scanning electron microscope for different process parameters. It is clear to confirm that the common wear mechanism such as pullouts, fibre buckling, fracture in matrix material, phase debonding, and

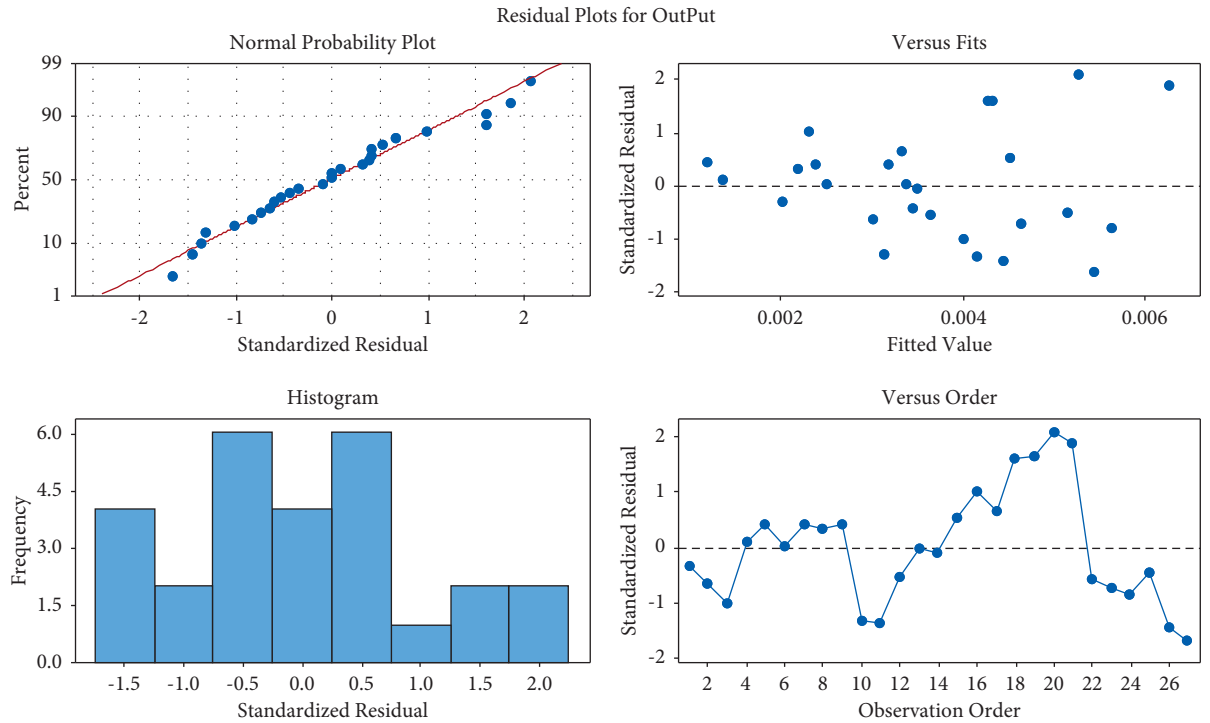

Figure 6: Residual plot output on dry sliding wear test.

Table 6: Experimental observation for air jet erosion test.

S. No.	IA (degree)	EV (m/s)	DR (g/min)	E_r 10^{-3} (g/min)
1	30	28	1	8.214
2	30	28	2.5	6.324
3	30	28	3.3	3.625
4	30	41	1	11.452
5	30	41	2.5	9.625
6	30	41	3.3	8.540
7	30	72	1	16.420
8	30	72	2.5	13.480
9	30	72	3.3	10.980
10	45	28	1	6.470
11	45	28	2.5	5.780
12	45	28	3.3	4.162
13	45	41	1	9.320
14	45	41	2.5	7.520
15	45	41	3.3	5.300
16	45	72	1	13.490
17	45	72	2.5	11.460
18	45	72	3.3	9.640
19	60	28	1	7.870
20	60	28	2.5	3.640
21	60	28	3.3	3.410
22	60	41	1	8.590
23	60	41	2.5	7.625
24	60	41	3.3	6.320
25	60	72	1	9.650
26	60	72	2.5	9.640
27	60	72	3.3	8.140

Table 7: Analysis of variance observation.

Source	DF	Seq SS	Adj SS	Ads MS	F	Contribution (%)
IA	2	31.535	0.108	0.1077	0.11	11.79
EV	2	153.258	26.330	26.3297	27.89	57.32
DR	2	53.292	7.191	7.1911	7.62	19.93
IA × EV	4	8.796	8.716	8.7165	9.23	3.26
IA × DR	4	1.691	1.691	1.6911	1.79	0.63
EV × DR	4	0.007	0.007	0.0065	0.01	0.00
Error	8	18.878	18.878			
Total	26	267.377				

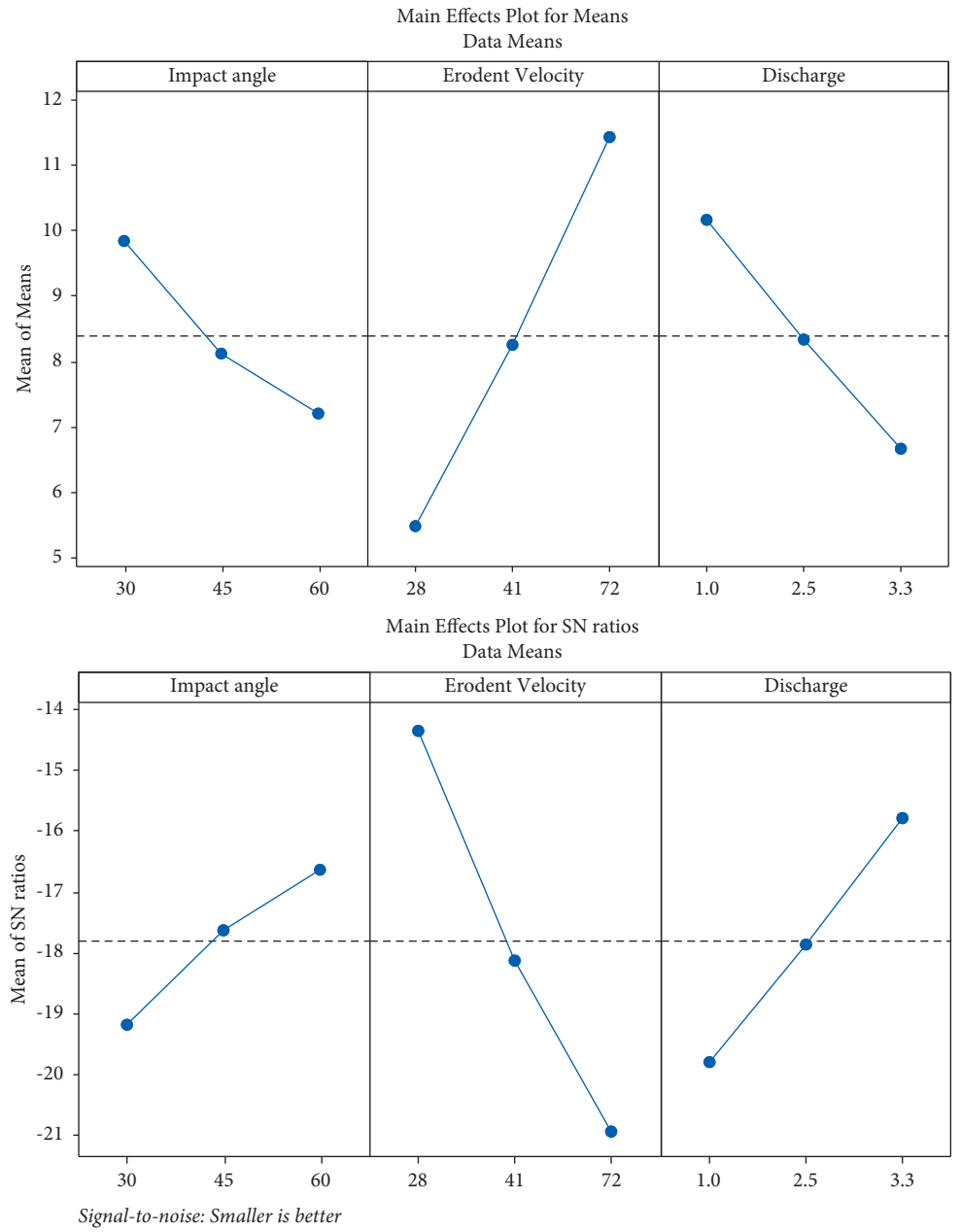

Figure 7: Main effect plots for means and SN ratios.

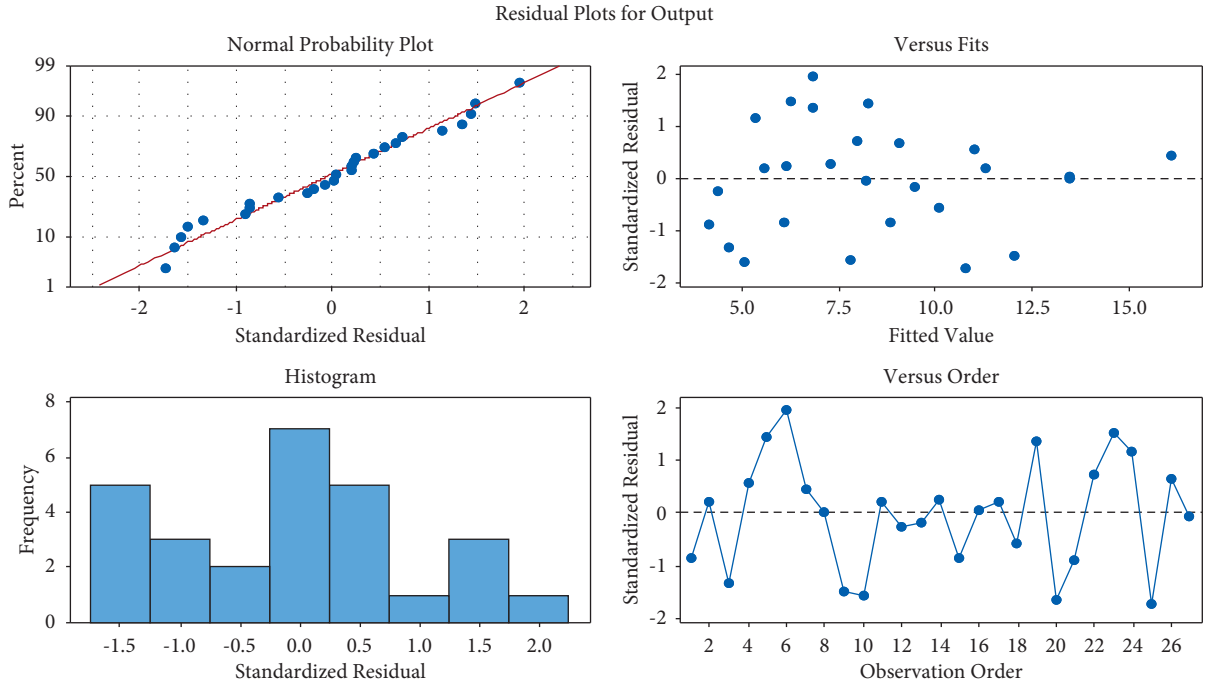

Figure 8: Residual plot output on dry sliding wear test.

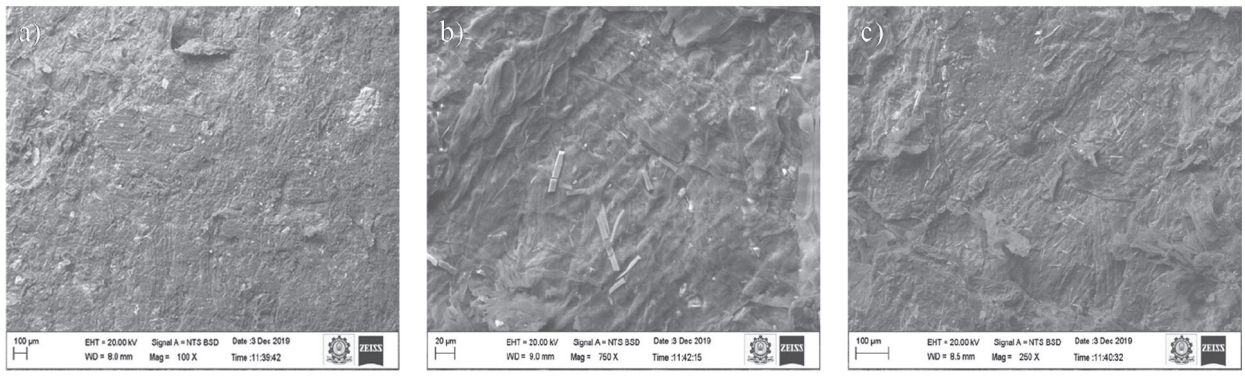

L=10 N, T=20 m, N=479 rpm (a)

L=20 N, T=20 m, N=479 rpm (b)

L=30 N, T=20 m, N=479 rpm (c)

Figure 9: Electron image of water hyacinth composite material worn surface observed on the samples tested at different process conditions. (a) $L = 10$ N, $T = 20$ m, and $N = 479$ rpm. (b) $L = 20$ N, $T = 20$ m, and $N = 479$ rpm. (c) $L = 30$ N, $T = 20$ m, and $N = 479$ rpm.

transformation due to sliding particles are noticed [24]. From the observation of the wear experiment, the good interfacial locking between the fibre and matrix phase has led to the good wear performance of the natural composites. Wear surface of the test samples is shown in Figure 9.

Figure 9(a) displays a very close view of the scanning electron microscope images and the fibres pulled out during the matrix phase by showing so many holes. In Figure 9(b), the epoxy resin matrix phase bonding is clearly visible. There is strong interfacial bonding between fibre and epoxy resin matrix because of this. Composite performance was greatly affected by this bonding property. Figures 9(a)–9(c) illustrate that a load of 30 N applied over a period of 20 minutes has higher friction than a load of 10 N applied over the same period. As the speeds decrease, the friction on the surfaces increases. Due to applied load, the materials are prone to high shear and led to a maximum surface damage [25–28]. Figures 10(a)–10(d) show the different impact angles (30°, 45°, and 60°) as well as the erodent velocity and discharge rate along with each crack, cleavage pattern, angle impingement, and weave pattern on a crater surface with appropriate angles of impact.

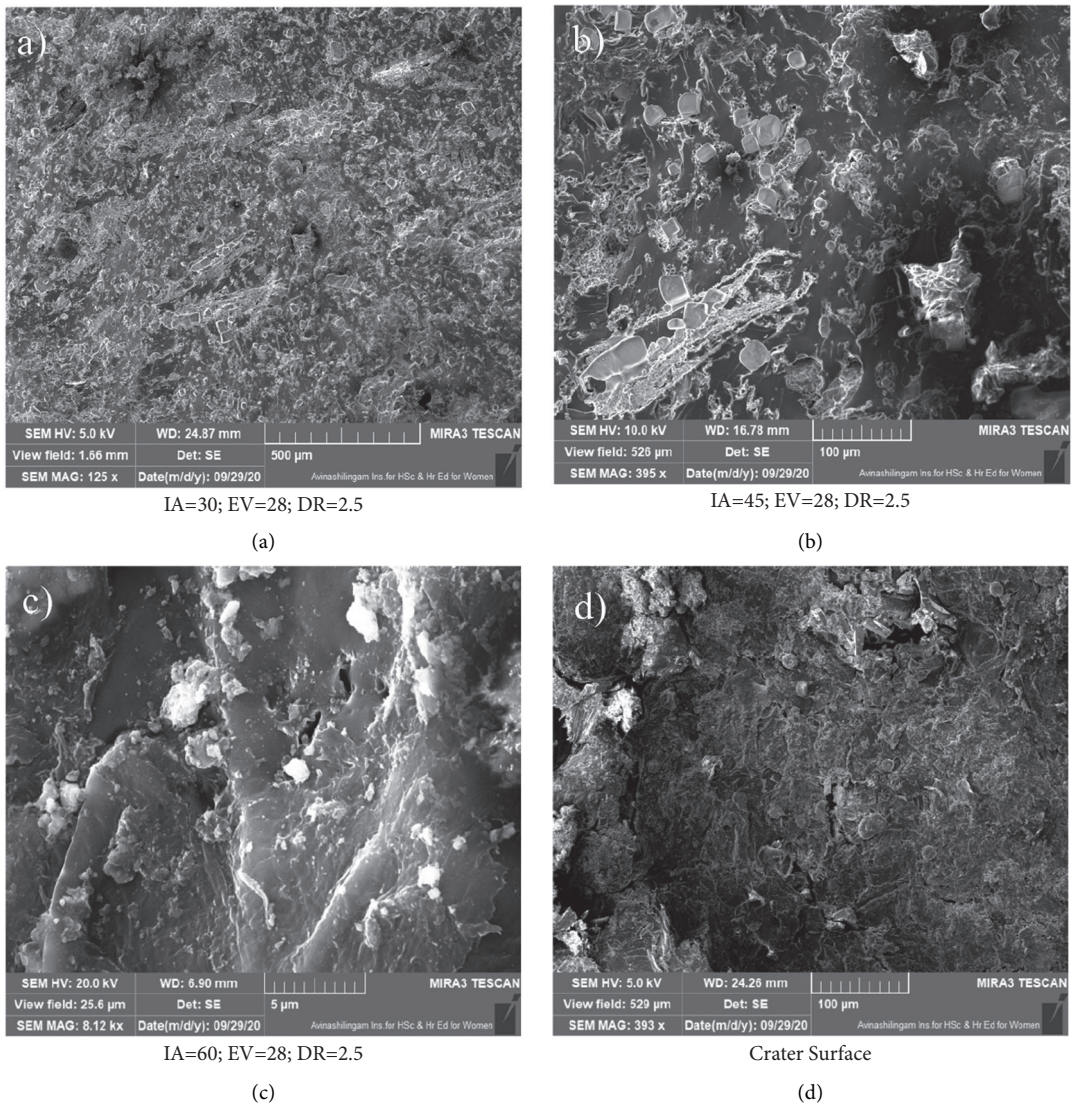

IA=30; EV=28; DR=2.5

(a)

IA=45; EV=28; DR=2.5

(b)

IA=60; EV=28; DR=2.5

(c)

Crater Surface

(d)

Figure 10: Surface images of the erosion sample at various working conditions. (a) IA = 30; EV = 28; DR = 2.5. (b) IA = 45; EV = 28; DR = 2.5. (c) IA = 60; EV = 28; DR = 2.5. (d) Crater surface.

4. Conclusion

Compression moulding is used to prepare both dry sliding and erosion test specimens. The following conclusions are drawn from the wear test and erosion test of water hyacinth plant fibre composites:

(i) Water hyacinth natural fibre enhances the fibre-matrix interfacial bonding with the respective percentage: 30 > 35 > 25 > 20 > 15.

(ii) The volume loss of the hyacinth composite is reduced by 26%.

(iii) When the nozzle angle is decreased simultaneously, the wear rate is increased.

(iv) From the analysis of variance, the influence of individual parameters is identified. Air jet erosion particle velocity has a maximum contribution of 58% towards surface wear followed by erodent discharge (20%) and impact angle (11%). Similarly, in sliding wear, the applied load has a maximum contribution followed by sliding velocity and sliding duration.

(v) The surface defect of the erosion test is to find out 45°, and the wear sample is highly affected at 30 N with 479 rpm speed.

(vi) Fibre pullouts and surface fracture are the common failure observed through the scanning electron microscope.

Data Availability

No data were used to support this study.

Conflicts of Interest

The authors declare that they have no conflicts of interest.

References

[1] V. Arumuga prabu, M. Uthayakumar, V. Manikandan, N. Rajini, and P. Jeyaraj, "Influence of redmud on the mechanical, damping and chemical resistance properties of banana/polyester hybrid composites," *Materials & Design*, vol. 64, pp. 270–279, 2014.

[2] N. Rajini, J. W. Jappes, S. Rajakarunakaran, and P. Jeyaraj, "Dynamic mechanical analysis and free vibration behavior in chemical modifications of coconut sheath/nano-clay reinforced hybrid polyester composite," *Journal of Composite Materials*, vol. 47, no. 24, pp. 3105–3121, 2013.

[3] K. Balamurugan, M. Uthayakumar, M. Ramakrishna, and U. T. S. Pillai, "Air jet erosion studies on Mg/SiC composite," *Siliconindia*, vol. 12, no. 2, pp. 413–423, 2020.

[4] E. SurojoE, Jamasri, V. Malau, and M. N. Ilman, "Effects of phenolic resin and fly ash on coefficient of friction of brake shoe composite," *ARPN J Eng Appl Sci*, vol. 9, pp. 2234–2240, 2014.

[5] A. Viswanath, H. Dieringa, K. K. Ajith Kumar, U. T. S. Pillai, and B. C. Pai, "Investigation on mechanical properties and creep behavior of stir cast AZ91-SiCp composites," *Journal of Magnesium and Alloys*, vol. 3, no. 1, pp. 16–22, 2015.

[6] M. Patel, D. Patel, S. Sekar, P. B. Tailor, and P. V. Ramana, "Study of solid particle erosion behaviour of SS 304 at room temperature," *Procedia Technology*, vol. 23, pp. 288–295, 2016.

[7] A. Karantzalis, "al- (Al9 Co2 , Al13Co4) powder metallurgy processed composite materials: analysis of microstructure, sliding wear and aqueous corrosion," *Mater Sci Eng with Adv Res*, pp. 52–59, 2017.

[8] Z. Leman, S. M. Sapuan, M. Azwan, M. M. H. M. Ahmad, and M. A. aleque, "The effect of environmental treatments on fiber surface properties and tensile strength of sugar palm fiber-reinforced epoxy composites," *Polymer - Plastics Technology and Engineering*, vol. 47, pp. 606–612, 2018.

[9] B. Rashid, Z. Leman, M. Jawaid, M. J. Ghazali, M. R. Ishak, and M. A. Abdelgnei, "Dry sliding wear behavior of untreated and treated sugar palm fiber filled phenolic composites using factorial technique," *Wear*, vol. 380-381, pp. 26–35, 2017.

[10] P. C. Verma, R. Ciudin, A. Bonfanti, P. Aswath, G. Straffelini, and S. Gialanella, "Role of the friction layer in the high-temperature pin-on-disc study of a brake material," *Wear*, vol. 346-347, pp. 56–65, 2016.

[11] M. S. Senthil Kumar, N. Mohana Sundara Raju, P. S. Sampath, and U. Vivek, "Tribological analysis of nano clay/epoxy/glass fiber by using Taguchi's technique," *Materials & Design*, vol. 70, pp. 1–9, 2015.

[12] B. Shivamurthy, K. Murthy, P. C. Joseph, K. Rishi, K. U. Bhat, and S. Anandhan, "Mechanical properties and sliding wear behavior of jatropha seed cake waste/epoxy composites," *Journal of Material Cycles and Waste Management*, vol. 17, no. 1, pp. 144–156, 2015.

[13] T. G. Mamatha, A. Patnaik, S. Biswas, and P. Kumar, "Finite element modelling and development of SiC-filled ZA-27 alloy composites in erosive wear environment: a comparative analysis," *Proceedings of the Institution of Mechanical Engineers - Part J: Journal of Engineering Tribology*, vol. 225, no. 11, pp. 1106–1120, 2011.

[14] M. M. Khan and G. Dixit, "Abrasive wear characteristics of silicon carbide particle reinforced zinc based composite," *Siliconindia*, vol. 10, no. 4, pp. 1315–1327, 2018.

[15] M. A. Chowdhury, U. K. Debnath, D. M. Nuruzzaman, and M. M. Islam, "Experimental evaluation of erosion of gunmetal under asymmetrical shaped sand particle," *Adv Tribo*, vol. 2015, pp. 1–31, 2015.

[16] M. M. Khan and G. Dixit, "Evaluation of microstructure, mechanical, thermal and erosive wear behavior of aluminum-based composites," *Siliconindia*, vol. 12, no. 1, pp. 59–70, 2020.

[17] N. Sumrith and R. Dangtungee, "Mechanical properties of water hyacinth fiber reinforced bio-based epoxy composite," *Key Engineering Materials*, vol. 818, pp. 7–11, 2019.

[18] N. Flores Ramirez, Y. Sanchez Hernandez, J. Cruz de Leon, S. R. Vasquez Garcia, L. Domratcheva Lvova, and L. Garcia Gonzalez, "Composites from water hyacinth (Eichhornea crassipe) and polyester resin," *Fibers and Polymers*, vol. 16, no. 1, pp. 196–200, 2015.

[19] V. Karthikeyan, A. N. Balaji, and V. Vignesh, "Effect of rope mat and random orientation on mechanical and thermal properties of banana ribbon-reinforced polyester composites and its application," *International Journal of Polymer Analysis and Characterization*, vol. 21, no. 4, pp. 296–304, 2016.

[20] M. N. Norizan, K. Abdan, K. Abdan, M. S. Salit, and R. Mohamed, "Physical, mechanical and thermal properties of sugar palm yarn fibre loading on reinforced unsaturated polyester composite," *Journal of Physical Science*, vol. 28, no. 3, pp. 115–136, 2017.

[21] P. Gopal, S. Bordoloi, R. Ratnam et al., "Investigation of infiltration rate for soil - biochar composites of water," *Acta Geophysica*, vol. 67, no. 1, pp. 231–246, 2019.

[22] S. A. Ghani and B. Y. Lim, "Effect of treated and untreated filler loading on the mechanical , morphological , and water absorption properties of water hyacinth fibers- low density polyethylene composites," *Applied Mechanics and Materials*, vol. 679, pp. 184–188, 2009.

[23] A. Buasri, N. Chaiyut, T. Petsungwan, Y. Boonyuen, and S. Moonmanee, "Effect of surface treatment on interfacial and properties of water hyacinth fiber reinforced poly(lactic acid) composites," *Advanced Materials Research*, vol. 463-464, pp. 449–452, 2012.

[24] S. Chonsakorn and S. Srivorradatpaisan, "Effects of different extraction methods on some properties of water hyacinth fiber," *Journal of Natural Fibers*, vol. 16, no. 7, pp. 1015–1025, 2018.

[25] D. O. Okia, C. K. Ndiema, and M. S. Ahmed, "Physical and chemical properties of water hyacinth," *Based Composite Briquettes*, vol. IV, pp. 28–36, 2016.

[26] M. Karina, H. Onggo, and A. Syampurwadi, "Physical and mechanical properties of natural fibers filled polypropylene composites and its recycle," *Journal of Biological Sciences*, vol. 7, no. 2, pp. 393–396, 2007.

[27] M. Saha, H. Rahman, and A. Ali, "Effect of fibre loadings on mechanical properties of water hyacinth fibre reinforced poplypropylene composites," in *Proceedings of the Int Conf Mech Eng Dhaka*, pp. 18–20, Bangladesh, 2011.

[28] R. Melentiev and F. Fang, "Investigation of erosion temperature in micro-blasting," *Wear*, vol. 420-421, pp. 123–132, 2019.

Hindawi
Advances in Materials Science and Engineering
Volume 2021, Article ID 8337568, 11 pages
https://doi.org/10.1155/2021/8337568

Research Article

Investigation into Mechanical Properties and Sliding Wear Behavior of Friction Stir Processed Surface Composite Material

Anbuchezhian Nattappan,[1] G. Suganya Priyadharshini,[2] T. Satish Kumar,[3] T. Velmurugan,[4] M. Makeshkumar,[5] and Haiter Lenin Allasi[6]

[1]*R.M.D Engineering College, Kavaraipettai, Tiruvallur, Tamil Nadu, India*
[2]*Department of Mechanical Engineering, Coimbatore Institute of Technology, Coimbatore, Tamil Nadu, India*
[3]*Department of Mechanical Engineering, Amrita School of Engineering, Amrita Vishwa Vidyapeetham, Coimbatore, Tamil Nadu, India*
[4]*Department of Mechanical Engineering, Sri Ramakrishna Engineering College, Coimbatore, Tamil Nadu, India*
[5]*Department of Mechanical Engineering, KPR Institute of Engineering and Technology, Coimbatore, Tamil Nadu, India*
[6]*Department of Mechanical Engineering, Wollo University Kombolcha Institute of Technology, P.O. Box 208, Kombolcha, Ethiopia*

Correspondence should be addressed to Haiter Lenin Allasi; drahlenin@kiot.edu.et

Received 18 August 2021; Accepted 30 October 2021; Published 19 November 2021

Academic Editor: JT Winowlin Jappes

Copyright © 2021 Anbuchezhian Nattappan et al. This is an open access article distributed under the Creative Commons Attribution License, which permits unrestricted use, distribution, and reproduction in any medium, provided the original work is properly cited.

One of the different and pioneering solid-state techniques, friction stir processing (FSP), is employed for the production of surface composites. In this research, the matrix selected was copper-nickel (CuNi) with hard boron carbide particle as reinforcement. The objective of the current research work is to produce reinforced 90/10 copper-nickel surface composites reinforced with B_4C fabricated via FSP. The influence of tool rotational speed on macrostructure, microstructure, grain size analysis, microhardness, and wear studies of friction stir processed (FSPed) CuNi/B_4C surface composites was assessed. For high rotational speed (1400 rpm) of stir tool, the modified surface area found is a maximum of 44.4 mm^2 with uniform dispersion of hard particle reinforcement. The presence of hard particle in the surface area is revealed through the electron imaging and the spectroscopic results. Spectra mapping shows the uniform distribution of hard particle over the FSPed area, and the evidence is obtained with XRD analysis. From the experimentation, it is interesting to report that the reinforcements have decreased the surface hardness for an increased rotational speed of stir tool. The hardness recorded for minimum rotational speed is 223 HV which has gradually decreased to 178 HV for 1300 rpm. It has directly influenced the wear rate of modified FSPed, as hardness is directly proportional to wear behavior. The worn surface and fractured morphology of the CuNi/B_4C surface composites were also studied using Field Emission Scanning Electron Microscope (FESEM).

1. Introduction

The evolution of modern material science and techniques of material synthesis has developed the production of composite materials with enhanced performance for use in aerospace and other demanding industrial applications. Composite materials are one of the essential and versatile engineering materials. The development in the field of material science and technology has made the production of advanced composite materials possible. Composite materials possess a unique combination of properties such as high strength, high toughness, lightweight, low cost, good damping capacity, wear resistance, corrosion resistance, hardness, conductivity, creep strength, fatigue strength, negative thermal expansion coefficient, and unusual combinations of electrical and magnetic properties depending on their alloying elements and processing techniques.

Cupronickel (CuNi) alloy is extensively used for high temperature and corrosion resistance applications. The

typical applications are in marine and petrochemical sectors including components for ship and boat hulls, desalination plants, and heat exchangers, as well as multicore cabled tubes for hydraulic and pneumatic lines. It has been selected for the superior properties of the materials [1]. However, this alloy is extremely susceptible to mechanical failure before its predicted lifetime [2], due to harsh and demanding tribological conditions. To meet such demanding mechanical and surface property requirements, this alloy can be subjected to surface processing techniques.

Friction stir processing (FSP) has emerged as a distinctive and pioneering solid-state technique to produce surface composites. FSP was developed based on the principles of Friction Stir Welding (FSW) [3–5]. FSP is a green and energy efficient technology because, during FS process, heat is produced from friction and plastic deformation without any noise or gaseous emission, as in conventional welding processes. FS processing results in a defect-free recrystallized zone with fine-grained microstructure. FS processing produces significant changes in regions close to the processed zone, without affecting the base metal [6]. Due to the frictional force and heat produced, the substrate metal is extruded and forged behind the tool forming a surface coating over the surface of the substrate metal. The type of tool material selected, its size, and tool profile play a key role in determining the quality of the weld. Mahmoud et al. [7] employed FSP to disperse SiC particles uniformly onto the surface of A1050-H24 aluminium alloy. Microstructural characterization of the developed surface composites indicated that SiC particles were dispersed uniformly onto the aluminium surface with the aid of square profile tools when compared to other profiles. Outstanding hardness, high melting point, high resistance to chemical agents, and high neutron absorption pave the way to the boron carbide (B_4C) being acceptable in the fields of nuclear applications, lightweight armors, and fast breeders [8]. Nuclear industries use boron carbide extensively due to its high neutron absorption [9].

From the comprehensive literature survey, it was found that difficulties involved in liquid phase technique have led to the evolution of solid-state processing approach. Most of the researchers' studies on FSP are related to aluminium alloy, copper, stainless steel, and magnesium alloy compacted with and without carbide, nitrides, and oxide particles. It was found that there is no work related to fabrication and characterization of cupronickel (90% Cu and 10% Ni) (CuNi) alloy based surface composite processed through FSP. The proposed research explores the microstructural properties, mechanical properties, and dry sliding wear behavior of CuNi surface composite reinforced with B_4C processed using green and energy efficient FSP technique.

2. Experimental Procedure

Commercially available CuNi sheet of size 100 mm × 50 mm × 6 mm was selected as matrix material in the current study. From the results of optical emission spectroscopy analysis, nickel (11.43 wt%) is the major alloying element together with 0.03 wt% Zn, 0.79 wt% Mn, and 1.20 wt% Fe, and the rest is copper. As received, CuNi matrix and the reinforcement (B_4C) are shown in Figure 1. The square groove of 100 mm length, 2.5 mm depth, and 0.7 mm width was made at the center of each plate employing wire EDM for adding the B_4C ceramic particles. Two-stage friction stir processing of the plates was carried over employing primitive made FSW. Initially, tungsten carbide pinless tool helps to close the groove so as to avoid B_4C ceramic particles spilling out during FSP. In the subsequent stage, a FSP tool made of the same WC material, with shoulder diameter of 25 mm and taper pin profile with pin tip diameter of 3 mm and pin root diameter of 5 mm to a span of 3 mm, was used. The FSP procedure to produce surface composite is schematically shown in Figure 2.

The FSPed specimen of size 10 mm × 50 mm × 6 mm was prepared from FSP plates by sectioning. The FSPed samples were polished and etched with several emery papers. The two types of etchants used in the friction stir zone are (i) Kalling's reagent (an optimized composition of CuCl, HCl, and ethanol, with the soaking time being 30 seconds) and (ii) a combination of $FeCl_3$, ethanol, and HCl which was exposed for 40 seconds. Macrostructure analysis was exposed using digital image scanner, and an image analyzer was used to measure the surface area of the composite. The microstructures of the FSPed samples were studied using optical microscope and FESEM. The microhardness of the developed surface composites was studied at different areas like thermomechanically affected region, heat affected region, and stir region. The parameters used for microhardness tests are load of 300 g and dwell time of 20 seconds. Dry sliding wear test was performed with ASTM G99-04 standard to study the friction, and wear of the developed surface composites under the condition of 30 N was applied. The other parameters considered for the dry sliding wear tests are sliding velocity and sliding distance of 1.5 m/s and 2500 m.

3. Results and Discussion

The rotating tool consists of a pin of required diameter and length, and a concentric outsized diameter shoulder. Both the pin and shoulder control the penetration depth along the plate. When the pin tool contacts the matrix metal, the shoulder of the tool decides the depth of the pin. The contact between the shoulder and the matrix metal causes a forging force that leads to generation of localized fractional heat to soften the parent material and mixes the hard particles with the help of pin protrusion. During FSP, the tool is rotated at the required speed, and the plate to be processed moves (traverse speed) against the rotating tool to complete a pass in the selected area. While transporting the parent metal from the advancing side to the retreating side, hot working action takes place due to the tool rotation.

To study the influence of stir tool rotational speed on CuNi/B_4C surface composite, probable trials were done with several varying speeds. The optimized rotational speed is from 1000 rpm to 1400 rpm (with an increment of 200 rpm), while fixing the other parameters (traverse speed = 30 mm/min, groove width = 0.7 mm, axial load = 6 kN, carbide

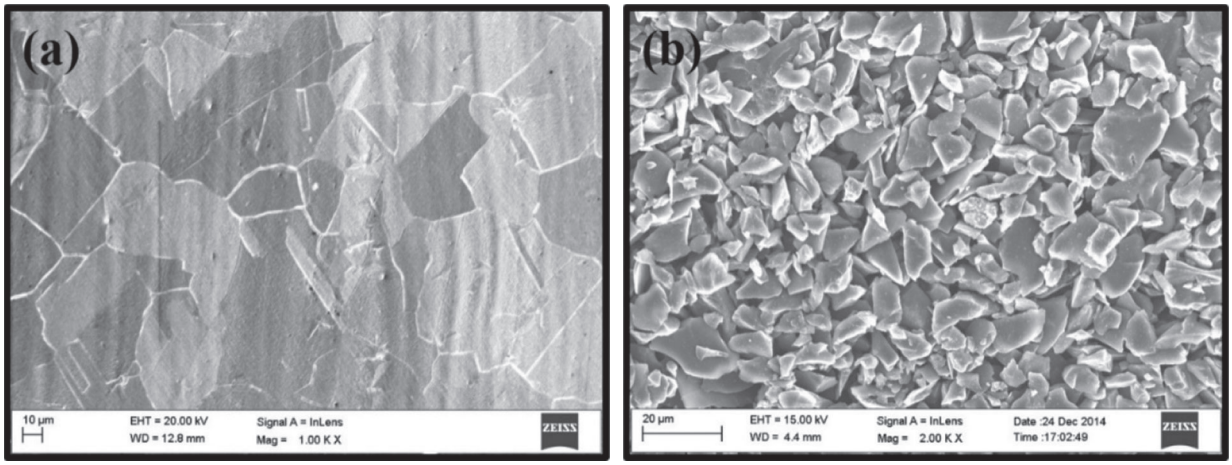

Figure 1: FESEM image of (a) CuNi and (b) boron carbide particle.

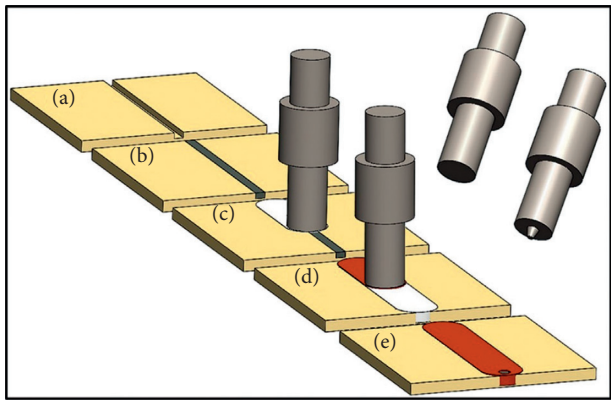

Figure 2: Friction stir processing and different stages: (a) preparation of groove; (b) charging the groove with ceramic particles; (c) processing via tool without pin; (d) processing via tool with pin; (e) processed plate.

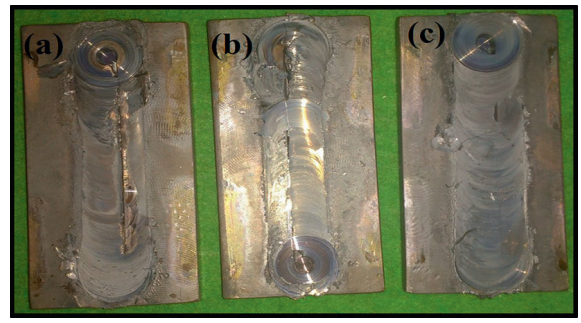

Figure 3: Defects that occurred during FSP trial: (a) tunnel defect; (b) tool dragging; (c) crack formation.

particle content B_4C). Some of the defects like tool dragging insufficient plastic flow and cracks were also found during trials as shown in Figure 3. The attainment in the FSP is the formation of smooth crown appearance, which is achieved through the above set of parameters.

Based on the stir tool geometry and selected process parameters, the level of quality can be measured. During processing, the bulk material was subjected to severe plastic deformation and hardened due to repeated cycle. Figure 4 shows the level of distribution of heat generated during the process (using FLIR T1K infrared (IR) camera). It indicates that the maximum heat generated at stir zone while processing is approximately 734°C and down to a minimum of 166°C. The phase transformation of CuNi alloy starts from 1100°C, and thus the change in surface of the material is a mechanical fusion. It leads to surface hardening and strain hardening through plastic deformation with reference to stir tool plunge area.

3.1. Macrostructure of CuNi/B_4C Surface Composites. The variation of the stirred area with reference to various tool rotational speed is shown in Figures 5(a)–5(e). The

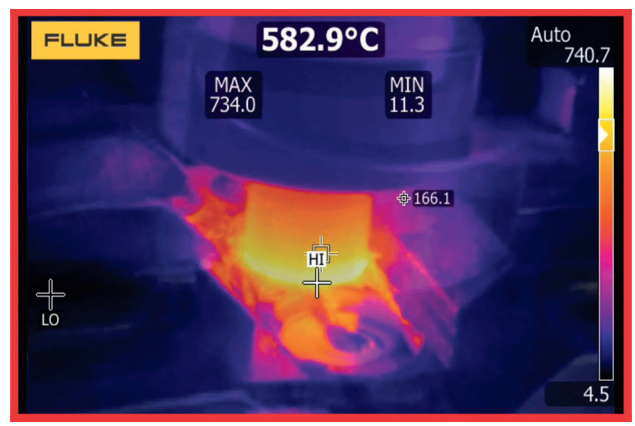

Figure 4: Thermal image of the stir zone during surface processing of CuNi with a reinforcement of B_4C particle at 1200 rpm.

parameters like tool plunge shoulder, groove width, and traverse speed of the process were kept constant. The movement of tool shoulder on the CuNi substrate results in the formation of frictional heat. The total frictional heat produced during the FSP depends upon the tool rotational speed. When the tool rotational speed was low, the formation of surface on advancing side and retreating side was found to be the same as shown in Figure 5(a). When the spindle speed

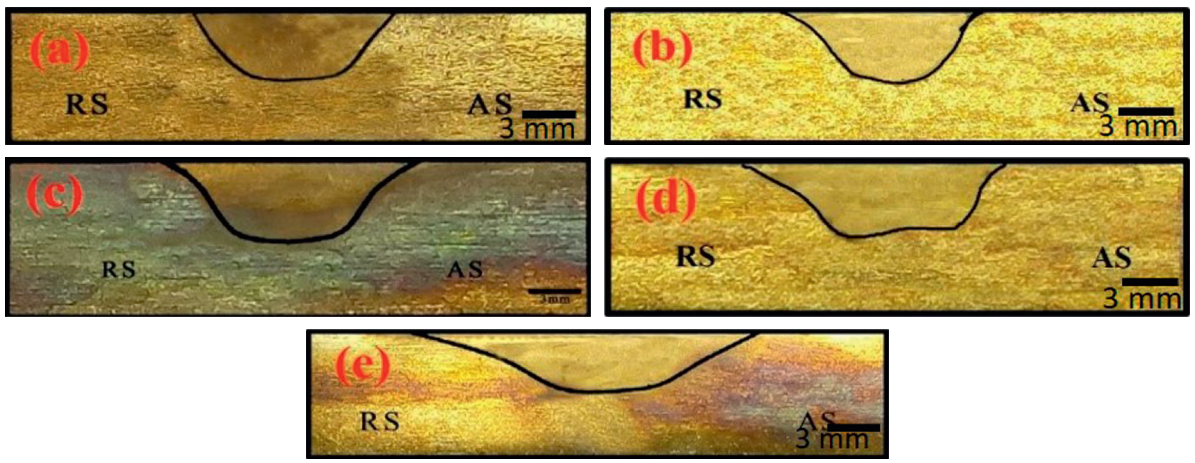

Figure 5: Macro images of CuNi/B_4C surface composite at tool rotational speed of (a) 1000 rpm, (b) 1100 rpm, (c) 1200 rpm, (d) 1300 rpm, and (e) 1400 rpm.

was increased, there was a maximum drag force on the advancing side which stretched along the retreating side. When the tool rotational speed was raised, the stir surface area started to diverge as shown in Figures 5(b)–5(e). The effect of the whirling speed was pronounced at the top side of the groove, and it was neutral at the bottom of the groove. This can be confirmed by the macro images in Figures 5(b)–5(e). The amount of plasticized material and the flow of the material directed towards the stir area depend upon the movement of the FSP tool and the heat generated during the process. The FSP tool progress and frictional heat generated rely upon the process parameters such as FSP spindle (tool rotational) speed, traverse speed, and groove width. The above-selected process parameters produced defect-free CuNi reinforced B_4C surface composite.

The frictional stir area produced with respect to various tool rotational speeds at constant traverse speed, groove width ($S = 30$ mm/min, $W = 0.7$ mm), and B_4C particles is shown in Figure 6. It can also be concluded that the frictional area was increased when the tool rotation speed was increased. There was an increase in plasticized CuNi at the FSP area as shown in Figures 5(a)–5(e) which is due to the high frictional heat generation resulting from the increase in the tool rotation speed. From the above observations, it can be concluded that there was an increase in FSP area when the tool rotation speed was increased, which matches the results suggested by [10].

3.2. Microstructure Analysis. The optical microscopic studies of different tool rotation speeds were carried out for studying the presence and distribution of carbide particulates in CuNi matrix as shown in Figures 7(a)–7(e). Onion ring-like structure formation is a prominent feature of FSP which is because of the generation of frictional heat produced during the spindle rotation, and the forward motion of tool forces the matrix material around the retreating side of tool. Woo et al. and Chaitanya et al. [11, 12] concluded that the onion ring structure formation is mainly due to proper selection of process parameters during the FSP. During the FSP of CuNi/

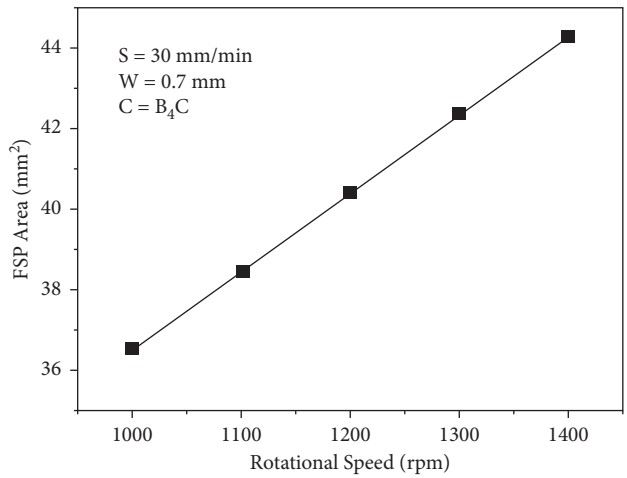

Figure 6: Variations in stir area of CuNi/B_4C surface composites as a function of tool rotational speed.

B_4C surface composite, the presence of onion ring-like structure can be clearly seen when the tool rotational speed is 1200 rpm at 30 mm/min traverse speed for a groove width of 0.7 mm. During the stir process, carbide particles are uniformly distributed within the base metal in various zones including dynamically plasticized stir zone. The FSPed samples were further investigated by spectroscopic analysis (multipoint and mapping), and the results are shown in Figures 8 and 9. The XRD spectra are shown in Figure 10, which confirms the absence of oxides on the FSPed area. The lack of formation of third phase at the stir zone indicates that FSP is a useful technique for the fabrication of CuNi/B_4C surface composite.

3.3. Grain Size Analysis. The grain refinement zone in the FSPed zone was studied using OM and FESEM micrographs, and it is shown in Figures 11 and 12. The presence of particle distribution and the bonding of the bulk material can be visibly seen. The composite layer was bonded well with CuNi alloy substrate, and no defects like diffusion crack or lack-of-

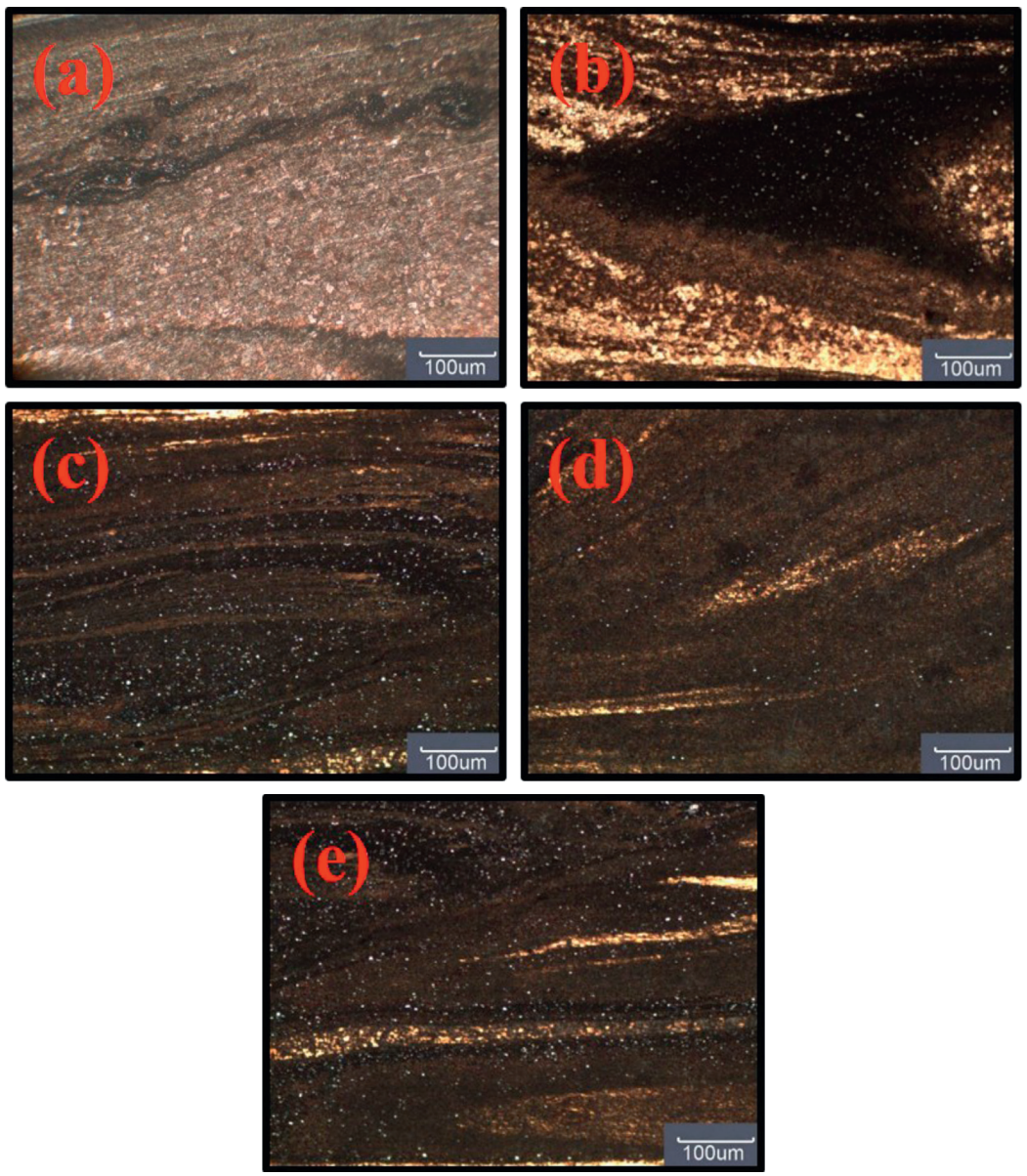

Figure 7: Optical microscopic images of stir zone at various tool rotational speeds of (a) 1000 rpm, (b) 1100 rpm, (c) 1200 rpm, (d) 1300 rpm, and (e) 1400 rpm.

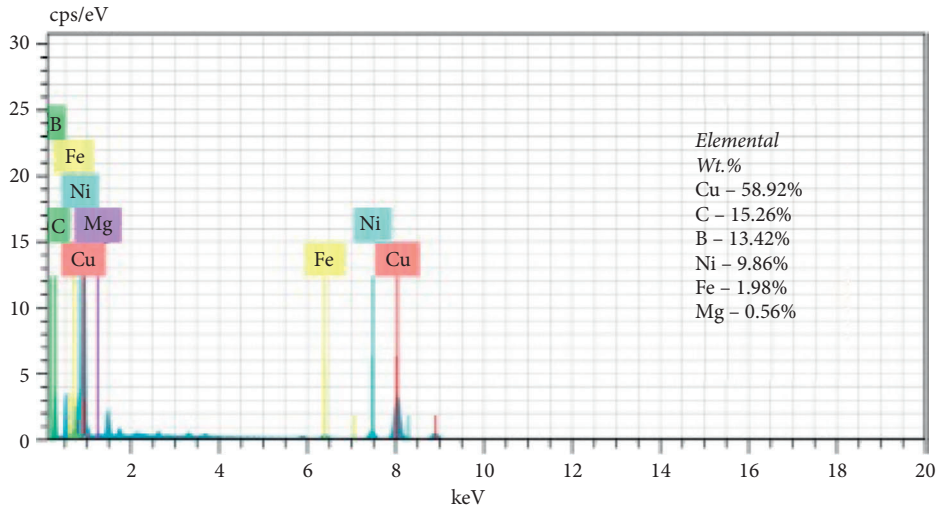

Figure 8: EDS (multipoint) analysis of FSP sample indicating reinforcement of B_4C particle in CuNi alloy.

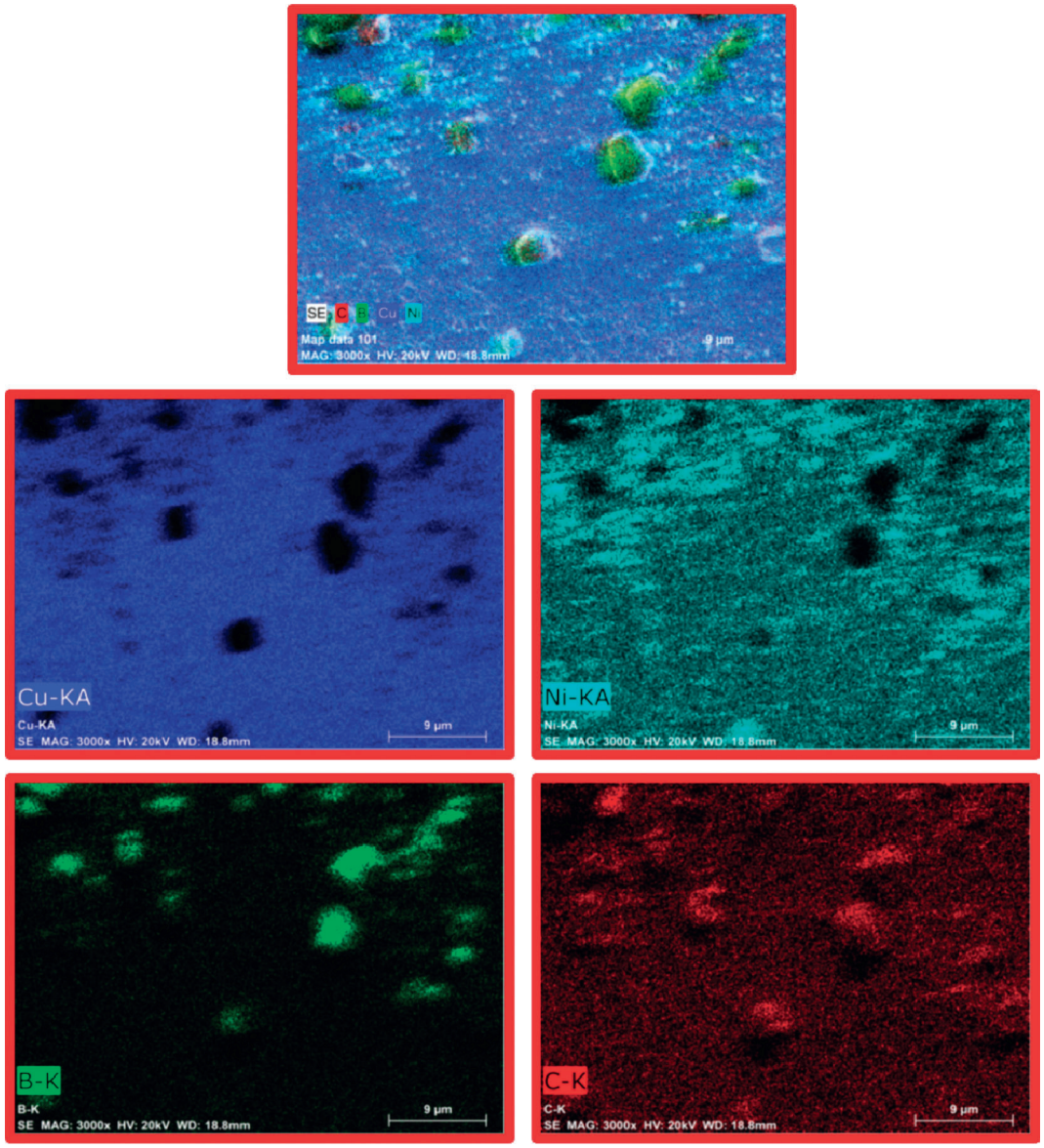

Figure 9: Electron image mapping of FSP sample indicating reinforcement of B_4C particle in CuNi alloy.

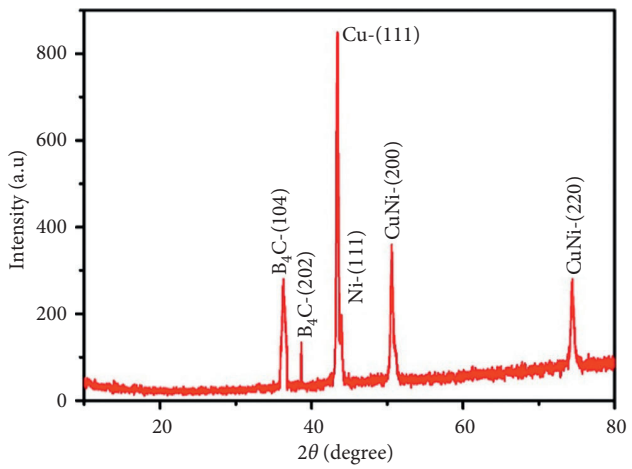

Figure 10: XRD analysis of FSP sample indicating the dominating peaks of reinforced carbide particle and base material.

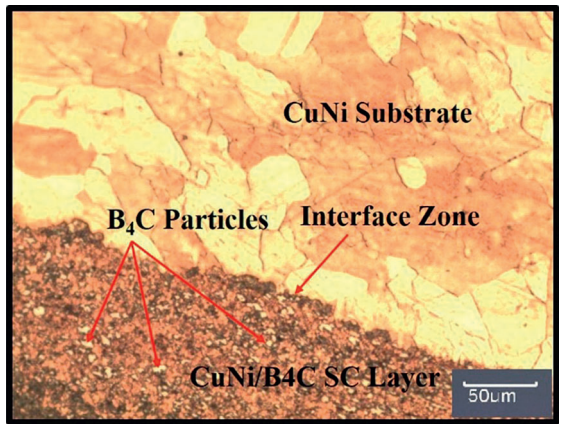

Figure 11: Optical micrograph showing interface zone between CuNi alloy substrate and CuNi/B_4C surface composite layer.

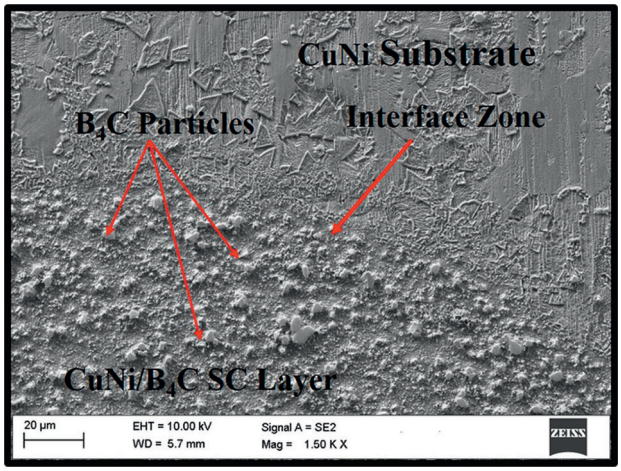

Figure 12: FESEM micrograph showing interface zone between CuNi alloy substrate and CuNi/B_4C surface composite layer.

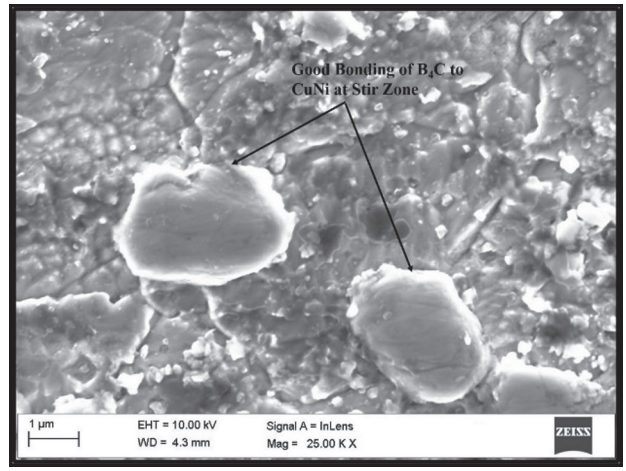

Figure 13: FESEM micrograph showing good interfacial bonding between parent metal and carbide particulates in the stir region.

penetration are visible. Figure 13 shows that B_4C particles appeared at the grain boundary junction (triple point), which confirms the pinning effect along the grain boundaries. The parent material shows a fine grain structure with grain size of ~60 μm, and it gets significantly reduced to ~5 μm at stir zone, which results in good bonding between the particulate and the parent material. When the tool rotates at the stir area, there is a change in metallurgical properties. Figures 14 and 15 show the optical micrographs of the interface between the SZ and TMAZ. Due to the generation of the frictional heat during the FSP, the strain induced plastic deformation of the material which is caused by the tool movement in the soft region, which results in the formation of elongated grain structure in TMAZ zone. The above phenomenon is due to the temperature gradient at different regimes during the FSP [13, 14]. Plastic deformation of the grains resulted in the formation of high-density subgrain boundaries. Due to the generation of the frictional heat between the matrix, reinforcement, and stir tool, the adjacent region undergoes extensive changes in grain structure, which is described as TMAZ and HAZ as depicted in Figures 14 and 15. The thickness of each zone varies according to the tool rotational speed.

3.4. Microhardness Survey of FSPed Composites. The microhardness of the FSPed composites is shown in Figure 16. The result of hardness clearly indicates that the fine dispersion of carbide particles resulted in increase of hardness value. When the amount of carbide particles was reinforced at low level, the microhardness of the composite decreased. Thus, an optimum friction stir process at tool rotational speed of 1200 rpm resulted in better microhardness properties. When the tool rotation speed was at maximum level (1400 rpm), a minor increment of hardness was observed which is due to the increased fragmentation of particulates.

3.5. Wear Rate Evaluation. Sliding wear behavior of FSPed samples was investigated using pin-on-disc machine. The

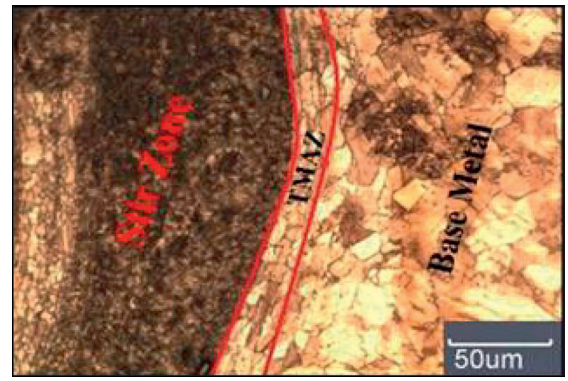

Figure 14: Optical micrograph representing stir zone/TMAZ interface.

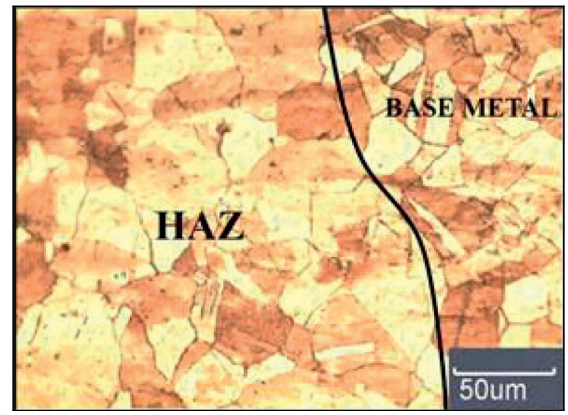

Figure 15: Optical micrograph representing HAZ/base metal interface.

pin material selected was FSPed material, and High Chromium High Carbon (HCHC) steel was used as disc. Wear rate of the FSP composite was based on the height change of the specimen prior to and after the test. It was found that the

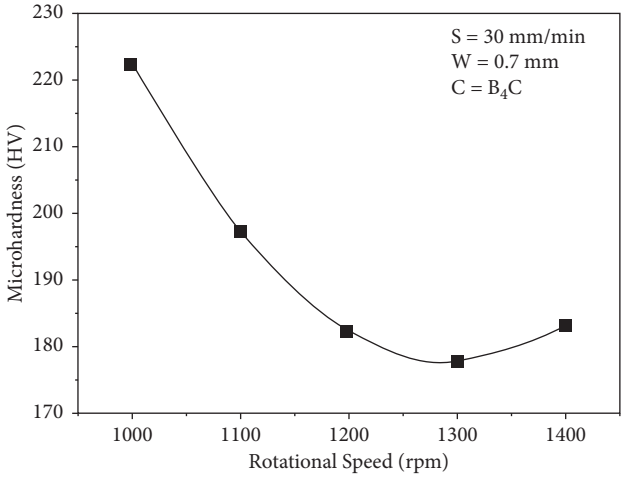

Figure 16: Variations in microhardness as a function of tool rotational speed.

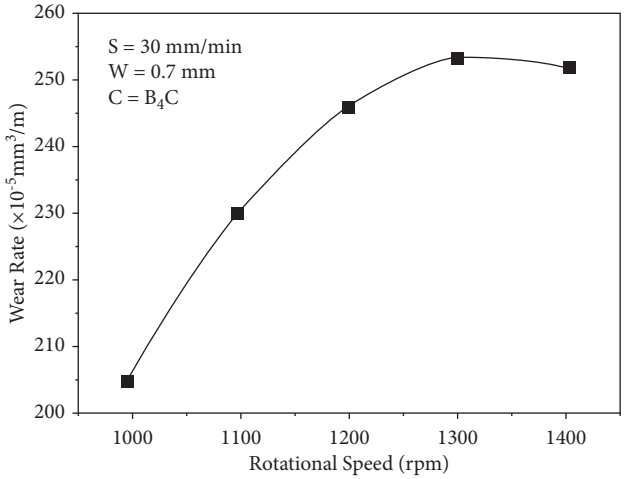

Figure 17: Variations in the wear rate of CuNi/B_4C surface composite as a function of tool rotational speed.

distribution of hard particle in CuNi matrix material had influenced the trend to increase the wear rate with respect to stir speed. The concentration of hard particle at surface modified region will increase the hardness of the composite, and simultaneously wear rate will be decreased as depicted in Figure 17. However, at higher speed, the particles are partially clustered and induce the matrix material to worn out in the form of abrasion. The pin material gets ploughed during the wear process, and the debris formed were found adhering to the disc. Due to this, three-body wear mechanism started operating, and friction increased over the proposed experimental design. To study the wear mechanism, worn surface morphology was carried out, and the FESEM images are shown in Figures 18(a)–18(c). After wear studies, FSP pin debris were collected during the wear, and the same was observed under FESEM to identify the wear mechanism.

At 1000 rpm, the distribution of particle reinforcement was nonuniform when compared to 1200 and 1400 rpm. It is clear that the matrix material can hold limited amount of particle at confined zone (over onion ring) and another region is left free. Figure 18(a) shows the matrix after wear studies indication of less wear scars. Figure 18(b) shows slight wear scars along with abrasive grooves while Figure 18(c) shows severe wear over the track of the pin drive. Figure 19 shows that the real morphology of the worn pin was mapped with the support of spectroscopic analysis. The matrix material with particle reinforcement was clearly seen with naked eyes. The dark blue colour shows the distribution of B4C, and mixed red/green shows the presence of matrix material at a tool speed of 1400 rpm.

Microscopic images of the wear debris collected for (a) 1000 rpm, (b) 1200 rpm, and (c) 1400 rpm are shown in Figures 20(a)–20(c). When tool rotational speed increases, interparticle distance also increases, which can be attributed to severe plastic deformation of the base metal. The matrix material removed from the pin is found adhering over the disc surface, and on continued processing, the adhesive

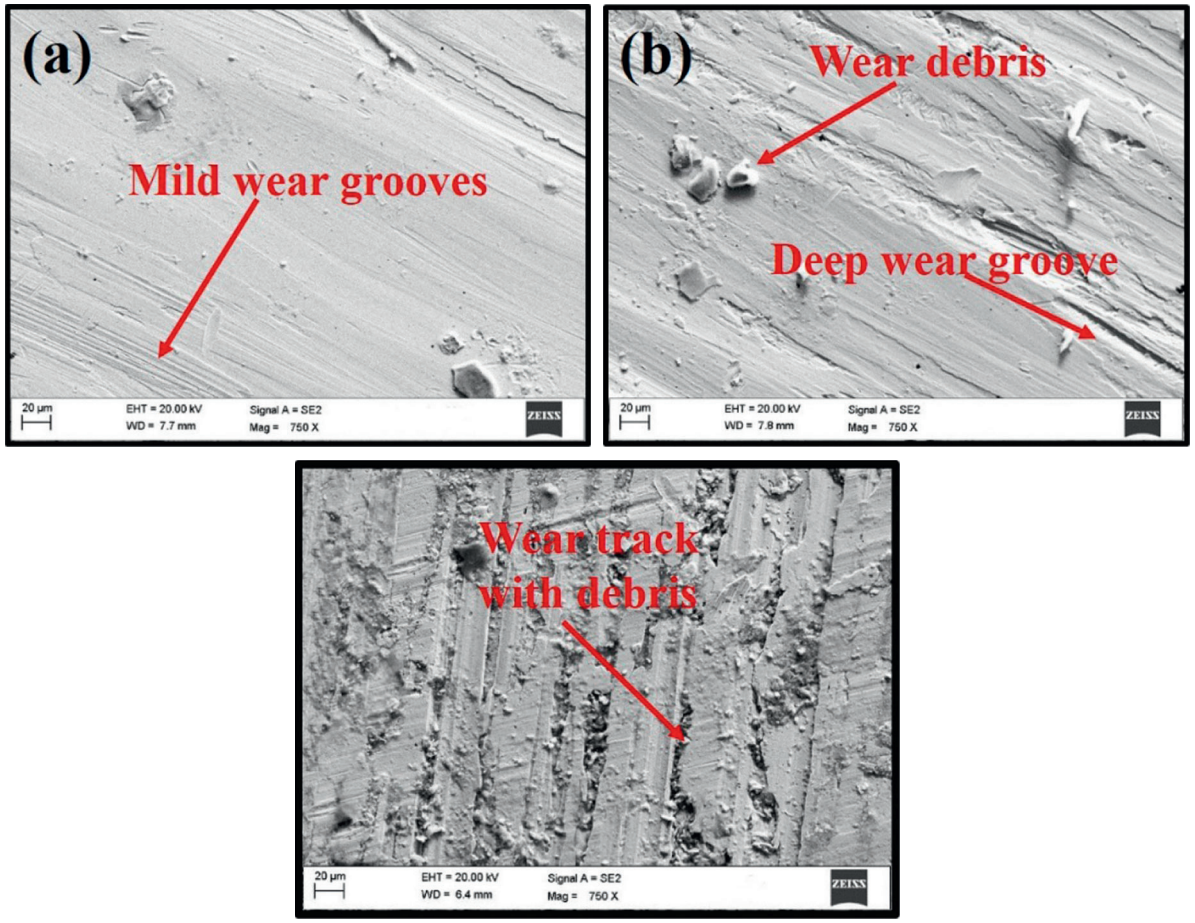

Figure 18: FESEM micrograph of worn surface of CuNi/B_4C surface composite at tool rotational speed of (a) 1000 rpm, (b) 1200 rpm, and (c) 1400 rpm.

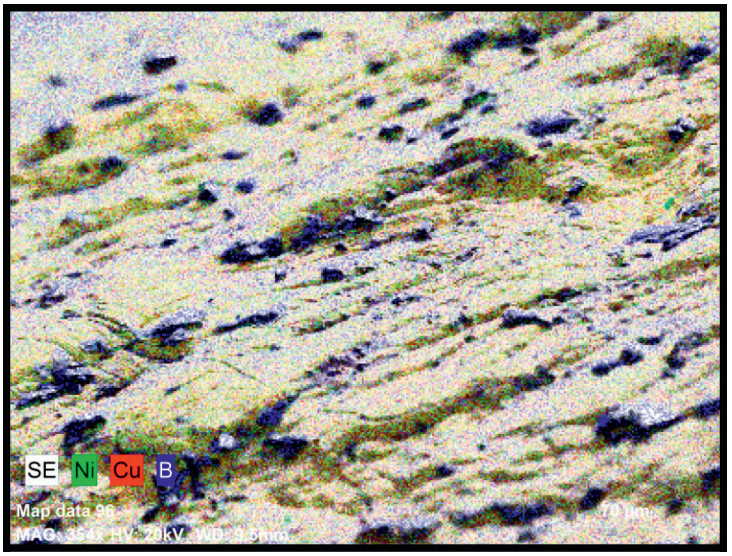

Figure 19: Spectroscopic image (mapping) showing the worn out surface of CuNi/B_4C surface composite at rotational speed of 1400 rpm.

debris were sliced out in the form of flakes. These flakes were CuNi matrix material in the form of thin film-like structure which has been detached from the surface due to heat generation as a result of friction developed. Adhering debris over the disc has highly influenced the wear-friction relation. Thus, the mechanism involved during the pin on disc sliding wear is of abrasive nature resulting in ploughing of matrix material.

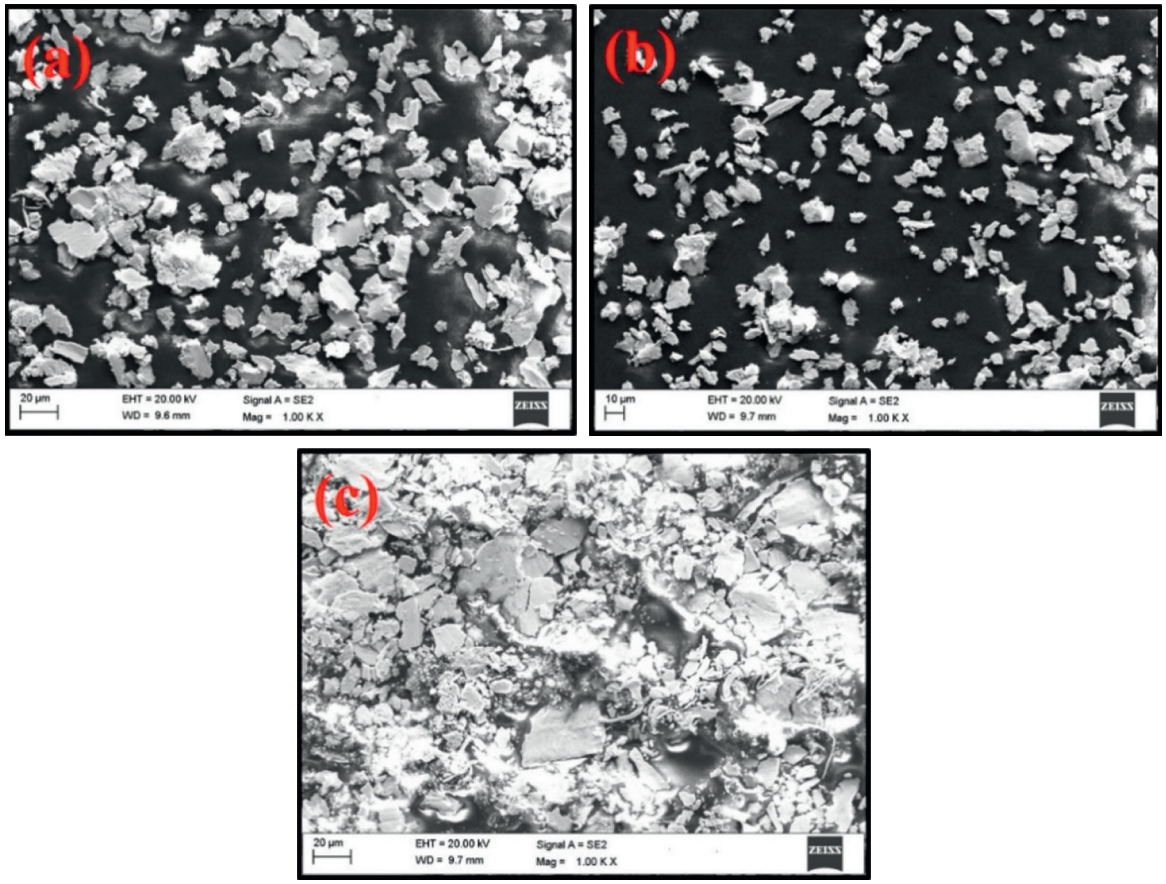

Figure 20: FESEM images of the wear debris collected for (a) 1000 rpm, (b) 1200 rpm, and (c) 1400 rpm.

4. Conclusions

In the current study, CuNi/B_4C surface modified composites were fabricated via FSP, and the influence of tool rotational speed on macrostructure, microstructure, grain size analysis, microhardness, UTS, and wear studies was investigated. The following conclusions can be drawn:

(i) The maximum heat generated at stir zone was found to be 734°C, and the change in surface of parent metal is a mechanical fusion. Optical and FESEM micrographs, EDS, and XRD pattern clearly reveal the presence and the distribution of B_4C hard particles over CuNi parent metal.

(ii) With respect to rotational speed, the variation in the FSPed area has been noticed. For a maximum rotation speed of FSP tool (1400 rpm), the mechanical action of the material found is severe, and the stir/modified area is found to increase (43 mm^2). Subsequently, for minimum rotational speed (1000 rpm), the surface area is found to reduce to 36.6 43 mm^2. This is due to the whirling effect and the mechanical strain on the FSP area.

(iii) The microhardness of CuNi/B_4C surface composites is decreased when the tool rotational speed increases, which is due to the interparticle distance. As the FSP rotational speed increases, the concentration of hard particle reinforcement is found dispersed over the larges, and the hardness is found to drop from 223 HV to 178 HV gradually.

(iv) The wear rate of CuNi/B_4C surface composites decreased with the increase in tool rotational speed. The worn surface morphology shows the presence of tiny size of wear debris at higher tool rotational speed up to optimized value of 1200 rpm. There was an increase in size of the wear debris when the tool rotational speed increased to 1400 rpm.

Data Availability

There are no relevant data to be made available.

Conflicts of Interest

The authors declare that they have no conflicts of interest.

References

[1] D. C. Agarwal and A. M. Bapat, "Effect of ammonia and sulphide environment on 90/10 and 70/30 Cupronickel Alloy," *Journal of Failure Analysis and Prevention*, vol. 9, no. 5, pp. 444–460, 2009.

[2] D. C. Agarwal, "Effect of ammoniacal seawater on material properties of copper nickel alloys," *Br.Corros. J*, vol. 37, no. 2, 2002.

[3] R. V. Vignesh, R. Padmanaban, M. Govindaraju, and G. S. Priyadharshini, "Investigations on the corrosion behaviour and biocompatibility of magnesium alloy surface composites AZ91D-ZrO2 fabricated by friction stir processing," *Transactions of the IMF*, vol. 97, no. 5, pp. 261–270, Article ID 085401, 2019.

[4] S. Sahraeinejad, H. Izadi, M. Haghshenas, and A. P. Gerlich, "Fabrication of metal matrix composites by friction stir processing with different Particles and processing parameters," *Materials Science and Engineering A*, vol. 626, pp. 505–513, 2015.

[5] T. Satish Kumar, S. Shalini, and K. Krishna Kumar, "Effect of friction stir processing and hybrid reinforcement on wear behaviour of AA6082 alloy composite," *Materials Research Express*, vol. 7, no. 2, pp. 195–204, Article ID 026507, 2020.

[6] G. S. Priyadharshini, R. Subramanian, N. Murugan, and R. Sathiskumar, "Surface modification and characterization of zirconium carbide particulate reinforced C70600 CuNi composite fabricated via friction stir processing," *Journal of Mechanical Science and Technology*, vol. 31, no. 8, pp. 3755–3760, 2017.

[7] E. R. I. Mahmoud, M. Takahashi, T. Shibayanagi, and K. Ikeuchi, "Effect of friction stir processing tool probe on fabrication of SiC particle reinforced composite on aluminium surface," *Science and Technology of Welding & Joining*, vol. 14, no. 5, pp. 413–425, 2009.

[8] R. Palanivel, I. Dinaharan, R. F. Laubscher, and J. P. Davim, "Influence of boron nitride nanoparticles on microstructure and wear behavior of AA6082/TiB 2 hybrid aluminum composites synthesized by friction stir processing," *Materials & Design*, vol. 106, pp. 195–204, 2016.

[9] H. S. Chen, Y. Zhang, H. H. Nie, J. F. Wang, and W. X. Wang, "The microstructure and mechanical properties of the B4C/Cu matrix composite fabricated by SPS-HR," *Mater.Sci & Tech*, vol. 34, pp. 1460–1467, 2018.

[10] R. Sathiskumar, N. Murugan, I. Dinaharan, and S. J. Vijay, "Prediction of mechanical and wear properties of copper surface composites fabricated using friction stir processing," *Materials & Design*, vol. 55, pp. 224–234, 2014.

[11] H. Woo, H. Choo, D. W. Brown, and Z. Feng, "Influence of the tool pin and shoulder on microstructure and natural aging kinetics in a friction-stir-processed 6061- T6 aluminium alloy," *Metallurgical and Materials Transactions A*, vol. 38, pp. A69–A76, 2014.

[12] C. Kalangi, V. Bolleddu, and H. L. Allasi, "Tribological characteristics of Carbon nanotubes-reinforced plasma-sprayed Al2O3-TiO2 ceramic coatings," *Advances in Materials Science and Engineering*, vol. 2021, Article ID 8094640, 12 pages, 2021.

[13] A. Haiter Lenin, S. C. Vettivel, T. Raja, L. Belay, and S. Christopher Ezhil Singh, "A statistical prediction on wear and friction behavior of ZrC nano particles reinforced with Al-Si composites using full factorial design," *Surfaces and Interfaces*, vol. 10, pp. 149–161, 2018.

[14] G. Robert Singh, C. E. Singh, M. Sivapragash, L. Anselm, R. S. Kumar, and A. Haiter Lenin, "Tensile and compression behaviour, microstructural characterization on Mg-3Zn-3Sn-0.7Mn alloy reinforced with SiCp prepared through powder metallurgy method," *Materials Research Express*, vol. 7, no. 10, Article ID 106512, 2020.

Hindawi
Advances in Materials Science and Engineering
Volume 2021, Article ID 8094640, 12 pages
https://doi.org/10.1155/2021/8094640

Research Article

Tribological Characteristics of Carbon Nanotubes-Reinforced Plasma-Sprayed Al_2O_3-TiO_2 Ceramic Coatings

Chaitanya Kalangi,[1] Venkateshwarlu Bolleddu,[1] and Haiter Lenin Allasi[2]

[1]*Department of Manufacturing, School of Mechanical Engineering, Vellore Institute of Technology, Vellore 632014, India*
[2]*Department of Mechanical Engineering, Wollo University, Kombolcha Institute of Technology, Post Box No. 208, Kombolcha, Ethiopia*

Correspondence should be addressed to Haiter Lenin Allasi; drahlenin@kiot.edu.et

Received 10 July 2021; Revised 6 August 2021; Accepted 11 August 2021; Published 7 September 2021

Academic Editor: Adam Khan M

Copyright © 2021 Chaitanya Kalangi et al. This is an open access article distributed under the Creative Commons Attribution License, which permits unrestricted use, distribution, and reproduction in any medium, provided the original work is properly cited.

Thermal-sprayed coatings are widely used in various oil and gas industries for wear and corrosion applications. However, increasing performance and requirements make conventional coatings inadequate for future needs. Furthermore, the heat conductivity of bulk materials cannot be minimized easily. Therefore, the use of low porous coating with nanocomposite doping is an effective way to produce coatings with reduced thermal conductivity. Plasma-sprayed Al_2O_3-TiO_2 coatings are found in a wide range of applications recently in many industries because of their exceptional properties including low expenses and ease of availability. In this work, the wear-resistant and low porous coatings of Al_2O_3 + 3 wt%TiO_2 and respective carbon nanotube (CNT) doped coatings are prepared and characterized. The coatings are deposited on the AISI 1020 steel substrate using air plasma spraying. The impact of CNTs reinforcement on the percentage of pores and wear performance of coatings is investigated. Also, wear tracks morphology is investigated to determine the wear mechanism that is responsible for the wear of coatings. From the analysis, it is observed that the formation of cracks as well as micropores is decreased by the addition of carbon nanotubes. Moreover, uniform CNT distribution and good adhesion of coatings with the substrate are the major factors that improve the wear performance of the coated surface.

1. Introduction

Surface engineering plays a vital role in the reduction of wear as well as corrosion-induced damages in hi-tech industries [1, 2]. Material degradation in the service span of thermal engineering is not only disruptive but also inexpedient to the economy of production. To overcome these issues, researchers have developed a protective shield for covering the material of engineering components with feasible ceramic powder coatings. It will prolong the lifespan of a material when the coating is proved to be mechanical (high toughness and high hardness) and resistant to wear damages [3]. Various studies on ceramic coatings have been conducted to determine the mechanical properties as well as the wear resistance on the material surface. These investigations revealed that the wear resistance is greatly influenced by the factors such as hardness, the grain size of powder, binder phase content, phase distribution, toughness, and the coating microstructure [4]. However, because of its excellent chemical strength, ceramic materials are also extensively used in different structural applications. The main key attribute of ceramic coatings is to provide wear resistance in order to achieve high hardness strength. As a result, ceramics have been increasingly utilized in the form of coatings on metallic surfaces to attain stable material characteristics [5–7]. Ceramic coatings are deposited on the surface of the metal substrates through deposition techniques. Of these, plasma-based thermal spraying (i.e., air plasma spraying, APS) is the most popular method adopted for coating deposition under high temperatures and harsh environments.

Thermal barrier coatings (TBCs) are significantly used nowadays to defend the hot section components of aircraft

engines from wear, erosion, pores, and other severe thermal degradations. An average temperature range of about 80°C and hot-spot temperature of 170°C have been reduced in the turbine blades with 250 μm thickness thermal-sprayed coating [8]. Plasma-sprayed TBCs are typically applied to increase the resistance of heat engines against wear and corrosion at a room/high temperature. The most frequently used plasma-sprayed feedstock powders in thermal barrier application are alumina-titania (Al_2O_3-TiO_2) and yttria-stabilized zirconia (YSZ). In recent decades, alumina-titania feedstock containing 3, 13, and 40 wt% compositions of titania are commonly used rather than plain alumina-titania powders. During spraying, these composites are heated up to 4,000°C and accelerated to several hundred m/s in a chemical dynamic environment of plasma-making gases and the surrounding atmosphere [9]. At this condition, the feedstock experiences a high thermal load, in addition to high mechanical load upon reaching the substrate. These extreme conditions can lead to substantial variations in the chemical and microstructural composition of coatings as compared to the feedstock powders and contribute to changes in coatings microstructure [10]. Additionally, alumina-titania coatings are popular due to their sliding wear resistance owing to their excellent mechanical properties. As wear undergoes aggressive corrosion at higher temperatures, the coating should be prepared in such a manner as to withstand wear and corrosion at the same time. On the other hand, TBC characteristics are mainly affected by the pores formed in the microstructure of coatings during spraying. Hence, several experiments are performed to identify the relationship between processing methods, porosity, and microstructure, resulting in properties including heat conductivity, thermal shock resistance, microhardness, fracture toughness, and so on [11, 12].

Porosity is identified as an important feature for corrosion and wear that influences the life span of hot compartments. The presence of pores in the coating is required not only for thermal conductivity reduction but also for the compensation of stress resulting from expansion because of temperature variations and heat effects [13, 14]. Nevertheless, in some cases, pores cause air penetration and gas combustion, which in turn create metal corrosion inside the parts of turbine engines [15]. Therefore, porous optimization on the top coat is significant to enhance the thermal properties for the entire lifetime of the product. The study in [16] indicated that the residual stress of coatings steadily upsurges from 60 MPa compressive stress to 40 MPa tensile stress along with the rise of porosity from 14% to 17%. Also, the authors of [17] investigated the impact of both thermal conductivity and porosity in coated surfaces. It is found that increasing the porosity could block the heat transfer between coating layers. However, low porosity would eliminate the resistance towards corrosion. The study in [18] pointed out that the reduction in thermal conductivity is possibly due to interlamellar pores occurring in the coated regions. Furthermore, it also occurs because of the limited characterization of porous shape and size, total porosity, and distribution of pores in thermal coatings.

The thickness of thermal-sprayed coatings normally ranges between 300 and 400 μm. Numerous studies revealed that within a certain limit, the thick coatings maintain better wear resistance as well as porosity compared to thin coatings, which extends the product lifetime accordingly [19, 20]. However, thick coatings may create micropores, delamination, cracks, and improper mechanical bonding [21, 22]. Likewise, larger internal stress and other aspects will make the thick coating peel off from the coated surface [23]. Thus, thick coatings are usually difficult to be applied in practice. Wear-out failure is another main damage formed in the layers of the material substrate. Moreover, the microstructure characteristics and the wear resistance layer look uneven due to the granularity of ceramic powders. To overcome these drawbacks, the coating powder is mixed with reinforcement components that withstand wear and corrosion. In this research, $Al_2O_3 + 3\,wt\%TiO_2$ ceramic powder is reinforced with CNT nanocomposite for improving the overall wear resistance and reducing the porosity of coatings [24, 25]. The addition of carbon nanotubes is an effective way of improving the mechanical properties and tribological performance of ceramic coatings. Due to their excellent mechanical, electrical, and chemical properties, CNTs possess high tensile strength and stiffness [26]. So, CNTs applied as an additive to increase the performance of a ceramic coating in high-level industries.

Thermal barrier coatings are frequently used in heavy-duty, high-speed industrial applications for equipment protection. An integral part of TBC in a metallic substrate is to prevent the formation of large pores to reduce heat insulation and thermal stresses. However, accurate prediction of porosity is highly complex because of the challenging porous structure and the ultrathin thickness of the coating. In this paper, a conventional ceramic powder $Al_2O_3 + 3\,wt\%TiO_2$ along with 1%, 3%, and 5% CNT-doped combination of $Al_2O_3 + 3\,wt\%TiO_2$ ceramics was prepared and fabricated on the sample steel substrate via air plasma spraying deposition technique. The mechanical and wear characteristics of the coated substrate using these powders are studied and investigated. The main objective of this research is to analyze the wear response and porosity of coatings prepared with conventional ceramic and carbon nanotube mixed powders. Moreover, it investigates the influence of ceramic as well as CNTs reinforced ceramic coatings deposited on the substrate. The microstructure and tribological properties of thermal-sprayed coatings are also systematically analysed, and the wear mechanism has been determined.

2. Experimental Methodology

2.1. Materials. The coatings are deposited on the AISI 1020 steel substrate of dimension $65 \times 55 \times 5$ mm. This is a medium-carbon steel substrate composed of 0.25–0.50% carbon, 0.60–1.65% manganese, 0.4% (maximal) phosphorous, and 0.5% (maximal) sulphur. Carbon steels are extensively used for large industrial applications. $Al_2O_3 + 3\,wt\%TiO_2$ powder with a particle size distribution of about 18–56 μm is taken for coating deposition. This feedstock powder is obtained from Metallizing Equipment Co. Pvt. Ltd, Jodhpur, India. In a typical thermal barrier coating system, two layers

are applied on the surface of the substrate, namely the bond coat and the top coat. Therefore, $Al_2O_3 + 3\,wt\%TiO_2$ ceramic powder is taken for deposition of the top coat, and Ni-5%Al or Ni-5%Cr ceramic powders are taken as bond coat material. The substrates are coated with both conventional ceramics as well as nanocomposite incorporated ceramics. For nanocomposite incorporated powder preparation, multiwalled carbon nanotubes (MWCNTs) are obtained from United Nanotech Innovations Pvt. Ltd., Bangalore, India. The physical properties of MWCNTs include 25 μm outer diameter, 10 microns length, >98% purity, 220 m^2/g specific surface area, and 0.14 g/cm^3 bulk density. The blend of alumina-titania feedstock is subsequently mixed with 1%, 3%, and 5% MWCNTs of approximate diameter 25 μm and length 10 microns for 8 hours at 100 rpm speed to produce the reinforced ceramic composite powder. Agglomeration of powders during blending is avoided using hardened steel balls in the ball milling chamber. It has been learned that up to 5 wt% SiO_2-MgO-coated MWCNTs were added with polymer for coating purposes [27].

2.2. Substrate Preparation. The AISI 1020 steel substrate is cut from a steel bar of width 55 mm and thickness 5 mm using a power saw. A surface grinder Alex NH 500 is used to remove the oxide from the top and bottom surfaces of the substrate and produce 0.1 μm roughness to the surfaces. The top surface of the substrate is grit blasted inside a suction-type cabinet of the grit-blasting machine with alumina grits of mesh size 24 at 100 psi air pressure, and a stand-off distance of 125 mm. This will provide a surface roughness of 5 μm thick, which is essential for achieving superior mechanical anchorage between the substrate and the bond coat. The oxide layers formed during the time gap between surface grinding and grit blasting processes are removed at the final stage of grit blasting. The grit blasted surface is then subjected to ultrasonic cleaning in the isopropanol bath for 10 minutes in order to remove the unwanted dirt particles from the surface. Before bond coat deposition, the wet substrate is then thermally preheated for 150–200°C using a plasma gun with argon/nitrogen as the plasma gas. This will remove oil, grease, water vapour, and foreign particles and present a clean and nascent substrate surface for the bond coat deposition. The temperature variations throughout preheating are monitored via a noncontact instrument called an optical pyrometer.

2.3. Plasma Spraying. The conventional ceramic powder of $Al_2O_3 + 3\,wt\%TiO_2$ and its corresponding CNT-doped mixtures are deposited as the top coat on the steel substrate using the plasma spraying technique. The schematic diagram of plasma-sprayed coating is depicted in Figure 1. Before the top coat deposition, the substrate is coated with an intermediate adhesion layer called a bond coat. Ni-5%Al or Ni-5%Cr composites are applied as the bond coat onto the substrate material. The coatings are deposited onto the substrate using a Sulzer Metco 3MB plasma gun fixed on a CNC X-Y table. The plasma gun uses argon and hydrogen as the primary and secondary gases, respectively. The process parameters of the coating deposition influence the output voltage and arc power per unit hydrogen gas flow rate. A spray angle of 90° is maintained for coating all types of powder composition. Two auxiliary air jets are placed parallel to the plasma flame to cool the substrate during deposition and remove the weakly bonded and unmelted powder particles. The bond coat and the top coat are deposited with a thickness of about 100–150 μm and 250–350 μm, respectively.

2.4. Microstructural Characterization. Cross-sectional samples of dimension $10 \times 5 \times 5$ mm are cut from the coated sample using a low-speed diamond saw (150 low-speed diamond saw, MTI Corporation) for examining the mechanical properties and microstructural characteristics of coatings. The surface characterization of samples is analysed using two microscopes, namely Zeiss Supra 40 field emission scanning electron microscope (FE-SEM) and Zeiss scanning electron microscope (SEM). Before taking SEM, the cross-sectional sample inserts are subjected to thermoplastic cold mount with Geosyn cold mounting compound powder and liquid procured from Geologists Syndicate Private Limited, Kolkata, India. The cold mounted sample inserts are then allowed for surface polishing with three different substances such as SiC abrasive paper (220, 400, 600, 800, and 1,000 grades), diamond paste polishing (grade range 8, 6, 3, and 1 micron), and velvet cloth fixed auto polisher (Struers, LaboPol-21).

2.5. Porosity Measurement. Thermal-sprayed coatings are vulnerable to porosity formation because of the improper fusion between spray substances or gaseous expansion generated on spraying. Therefore, porosity determination is essential in order to observe the effects of variable spray parameters and the appropriateness of coating for its intended purpose. Based on the type of application, low volume or none of the porosity might be endurable. The porosity measurement in this work is carried out as per [29] procedure.

2.6. Wear Characterization. Wear tests have been performed on as-sprayed coatings using Ducom tribometer (wear and friction monitor: TR-20-M24) under different loading conditions (0.5–1.5 kgf) with sliding velocities (0.17–0.5 m/s) for a constant sliding distance of 300 m. Tungsten carbide balls of 6 mm diameter are used as the counter bodies for all tests. The weight loss in the coatings after the wear test is assessed by comparing the weight of samples before and after the wear test with an electronic balance (Mettler Toledo Classic Plus, AB265-s/Fact). The debris formed on the samples during the wear test is manually removed by blowing air while measuring the sample weight after the wear test. The wear test is conducted three times for each load and speed condition to confirm the consistency of results. Furthermore, average weight loss and standard deviation are calculated. It is to be noted that the wear tests are performed in compliance with ASTM G99-05 standards.

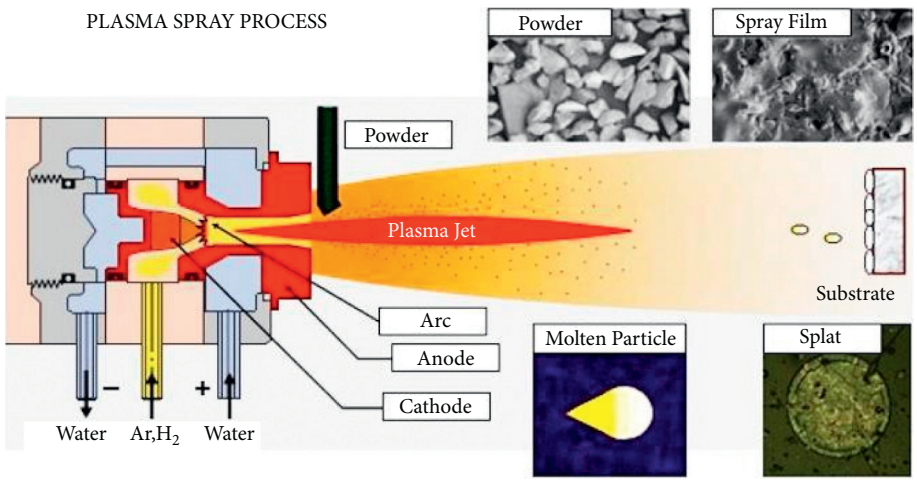

Figure 1: Schematic diagram of plasma spraying technique [28].

3. Results and Discussion

3.1. Coating Thickness. The cross-sectional micrographs of CNTs reinforced $Al_2O_3 + 3\,wt\%TiO_2$ coatings showing coatings thickness are shown in Figure 2. It can be seen from Figure 2 that the coating thickness of the top coat and bond coat are quite different. The average thickness of the top coat is varying in the range of 474–505 μm (Figures 2(a)–2(c)), and the bond coat is obtained with a thickness ranging from 42 to 49 μm. It can also be observed that the adhesion between the coatings and the substrate is very good, and no cracks were noticed. The EDX analysis of $Al_2O_3 + 3\,wt\%$ $TiO_2 + 5\%$ CNTs reinforced coating is shown in Figure 3, and the presence of Ti, C, Al, and so on can be seen in the coating microstructure. Also, the white flakes in the microstructure represent alpha-alumina whereas the sharp edge portions represent titania (Figure 3).

3.2. Phase Analysis. The X-ray diffraction (XRD) patterns for $Al_2O_3 + 3\,wt\%TiO_2$ composite coatings obtained with and without CNTs reinforcement are shown in Figure 4, and the presence of Al_2O_3 and TiO_2 phases and CNTs can be seen clearly. Through EDX and XRD analysis, the presence of these phases in the coating microstructure has been confirmed. It is to be noted that the alpha-alumina present in the coating resists high-temperature intrusion, and the titania is present in the form of rutile titania. It can be observed that the intensity of peaks in the XRD pattern representing TiO_2 and CNTs is very small as their percentage composition is very less. It can also be seen that the presence of CNTs cannot be seen in the 1% CNTs reinforced coatings due to the smaller volume proportion. It can be observed from the intensity of the phases that the phase distribution is similar in all four types of coatings with slight variation in their quantity.

3.3. Porosity Measurement. Figure 5(a) shows the microstructure of $Al_2O_3 + 3\,wt\%TiO_2$ coating without adding CNTs, and Figures 5(b)–5(d) show the microstructure of coatings obtained after the addition of CNTs in 1 wt%, 3 wt %, and 5 wt%, respectively. It is observed from Figures 5(a)–5(d) that micropores are present in the coating microstructure with different sizes. The size of the pores and the number of pores per square millimeter were analysed using MetImage LX software and shown in Figures 5 and 6. It was found that the addition of CNTs reduced the porosity level in the coatings, and this is due to the fact that CNTs are occupying the micropores and resulting in the reduction of the overall porosity percentage.

The variation in porosity in all the coatings is shown in Figure 6. The presence of micropores in size ranges (0–10 μm) occurred more on all coated samples, and gradually, pore volume decreased with an increase in pores size. It can be observed that the 1% CNTs reinforced coating exhibited fewer pores formation than the other coatings, whereas the 3% CNTs reinforced coatings have more pores per square millimeter (see Figure 6). Furthermore, in 5% CNTs reinforced coatings, the number of pores per square millimeter have been decreased. The coating microstructures and MetImage analyzer results indicate that 1% CNTs reinforcement is sufficient for a homogeneous distribution in $Al_2O_3 + 3\,wt\%TiO_2$ coating, and this can reduce the formation of pores in the coating microstructure effectively. The nonuniform melting and distribution of CNTs in the coating increase the percentage porosity in the coatings. The agglomerates of CNTs in the coating may cause nonuniform CNTs melting and thus resulting in a higher percentage of porosity. It has been observed in previous works also that just the nominal addition of CNTs has supported the alumina to retain the liquid state for a long time and develop the good distribution of alumina in CNTs reinforced alumina-titania composite coatings [30]. It can also be observed that the higher coating thickness has resulted in a higher number of pores formed in the coating microstructure.

3.4. Wear Characteristics. The wear tests are conducted at three different load and speed conditions with a constant sliding distance of 300 m using a steel ball at room temperature. The wear characteristics of the coatings are shown

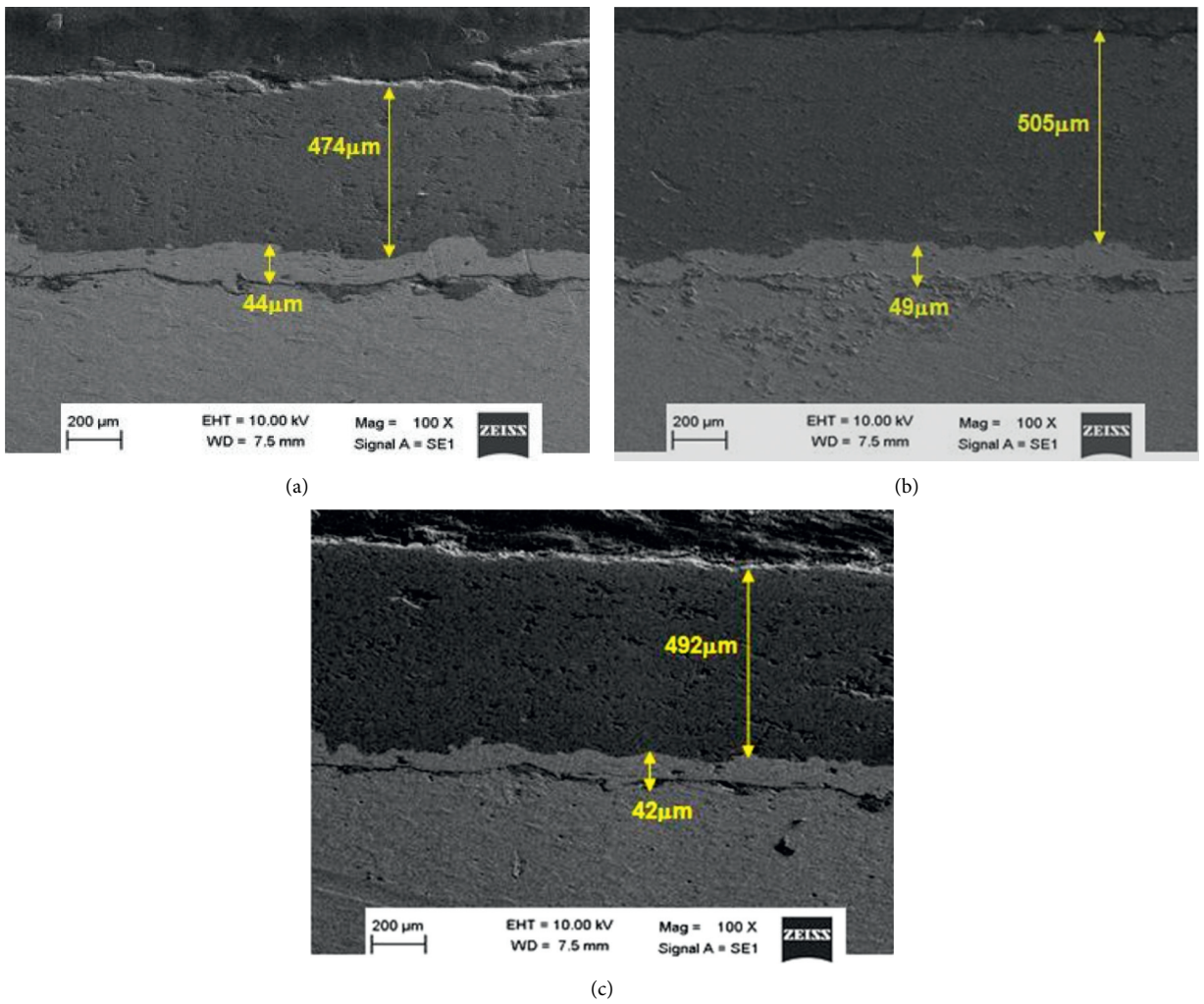

(a) (b)

(c)

Figure 2: SEM micrograph of cross section showing coating thickness of (a) $Al_2O_3 + 3\,wt\%TiO_2 + 1\%CNTs$ reinforced coating, (b) $Al_2O_3 + 3\,wt\%TiO_2 + 3\%CNTs$ reinforced coating, and (c) $Al_2O_3 + 3\,wt\%TiO_2 + 5\%CNTs$ reinforced coating.

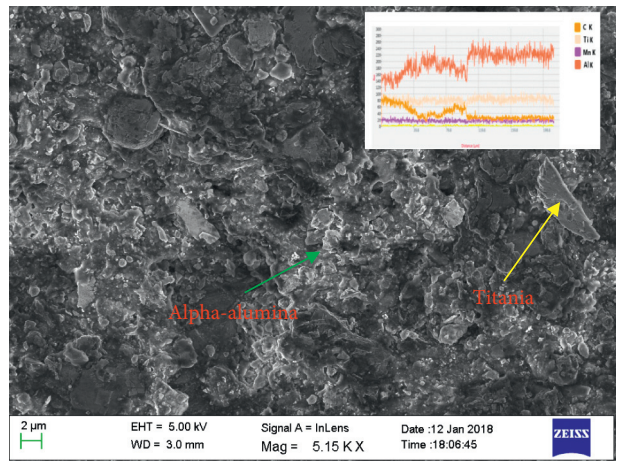

Figure 3: SEM micrograph of $Al_2O_3 + 3\,wt\%TiO_2 + 5\%$ CNTs reinforced composite coating surface with EDX.

in Figure 7. At 0.17 m/s sliding speed, it can be observed that the weight loss of alumina-titania composite coating without CNTs reinforcement is ranging in between 3.1 and 3.6 mg (Figure 7(a)), whereas for CNTs reinforced coatings, the weight loss is changing from 2.5 to 3.4 mg. It can also be seen that in all the coatings, the weight loss is gradually

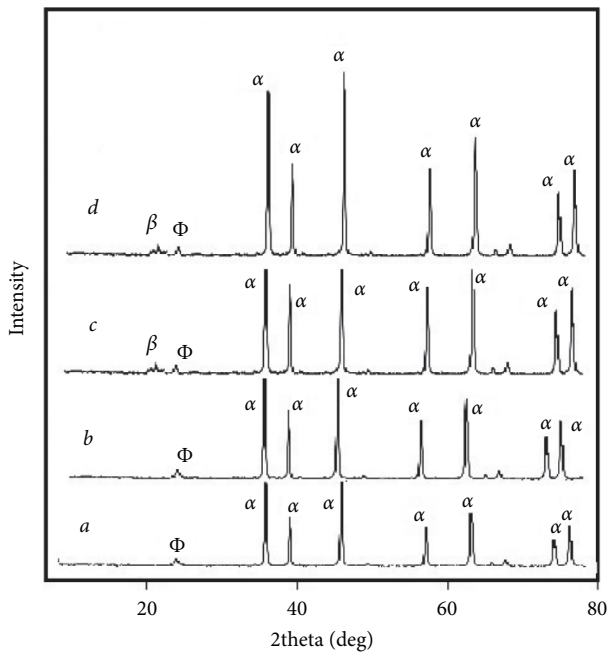

Figure 4: XRD pattern of (a) $Al_2O_3 + 3\,wt\%TiO_2$ coating without CNTs reinforcement, (b) $Al_2O_3 + 3\,wt\%TiO_2 + 1\%$ CNTs reinforced coating, (c) $Al_2O_3 + 3\,wt\%TiO_2 + 3\%$ CNTs reinforced coating, and (d) $Al_2O_3 + 3\,wt\%TiO_2 + 5\%$ CNTs reinforced coating.

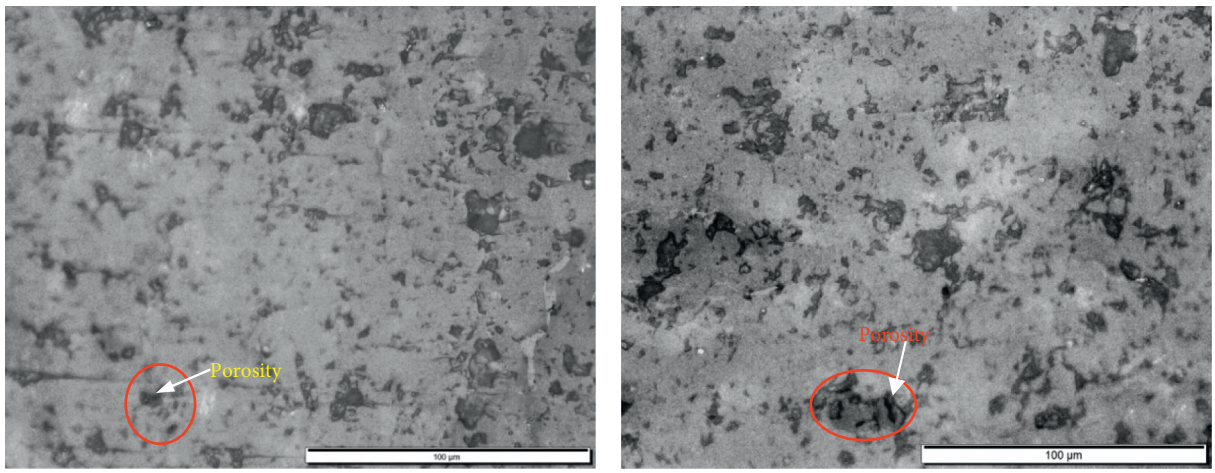

(a) (b)

Figure 5: Continued.

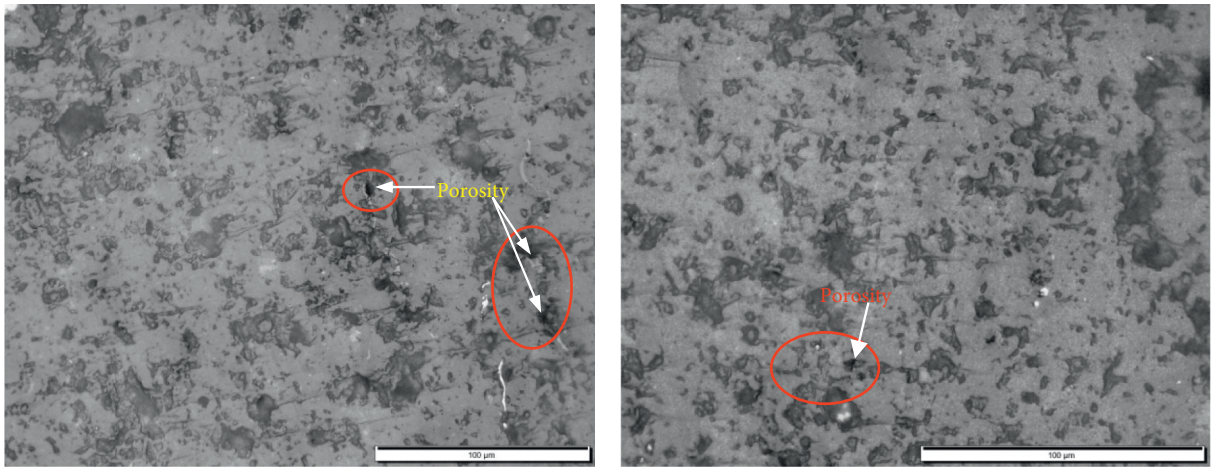

(c) (d)

Figure 5: Optical micrographs of (a) $Al_2O_3 + 3$ wt%TiO_2 composite coating without CNTs reinforcement, (b) $Al_2O_3 + 3$ wt%$TiO_2 + 1$% CNTs reinforced coating, (c) $Al_2O_3 + 3$ wt%$TiO_2 + 3$% CNTs reinforced coating, and (d) $Al_2O_3 + 3$ wt%$TiO_2 + 5$% CNTs reinforced coating.

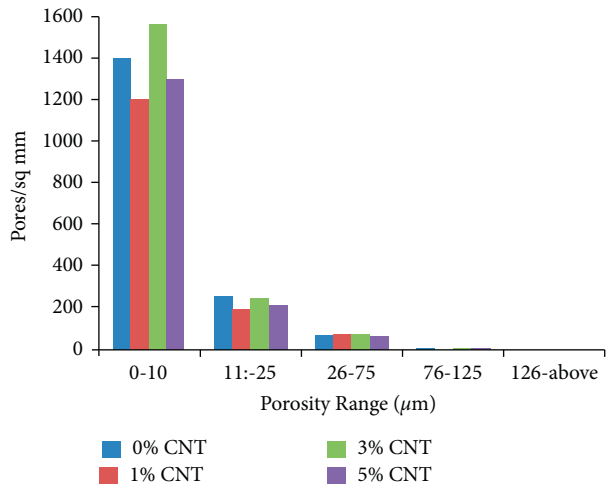

Figure 6: Porosity variation in alumina-titania coatings obtained with and without CNTs reinforcement.

increased with the increase of load except a small decrease at 1 kgf load in the case of coatings obtained without CNTs reinforcement.

The wear characteristics obtained at 0.33 m/s sliding speed are shown in Figure 7(b). At this sliding speed also the trend of the variation in weight loss with respect to the load is almost similar. For coatings obtained without CNTs reinforcement, the weight loss is changing from 3.5 to 4.2 mg, whereas for the coatings with CNTs reinforcement, the weight loss is in the range of 2.6–4.3 mg. It can also be observed that there is a short decrease in weight loss at 1 kgf load in the case of 3% CNTs reinforced coatings (Figure 7(b)). Figure 7(c) shows the wear characteristics of coatings at 0.5 m/s sliding speed. At this highest speed, weight loss is in the range of 3.8–4.2 mg for the coatings obtained without CNTs reinforcement, and it shows that wear rate is very much higher at the highest sliding speed. For CNTs reinforced coatings also, the weight loss is more, and it is in the range of 2.8–3.9 mg. Furthermore, there is a short drop in the weight loss at 1 kg load in the case of 3% CNTs reinforced coatings (Figure 8).

However, it can be clearly seen that the weight loss is increased with the increase in load and sliding velocity. Also, it can be observed that 1 wt% CNTs reinforced coatings exhibited good adhesion of coating with the substrate and resulted in lesser weight loss and thereby higher wear resistance. The factors such as hardness, porosity, and fracture strength might play a significant role in the wear resistance of coatings. It can also be seen that the weight loss in the case of 3 wt% CNTs reinforced coatings and coatings without CNTs reinforcement is almost nearer at all load and speed conditions. Lastly, it can be observed that the weight loss is more in the coatings without CNTs reinforcement, and the weight loss is minimum in the case of 1% CNTs reinforced coatings at all the conditions.

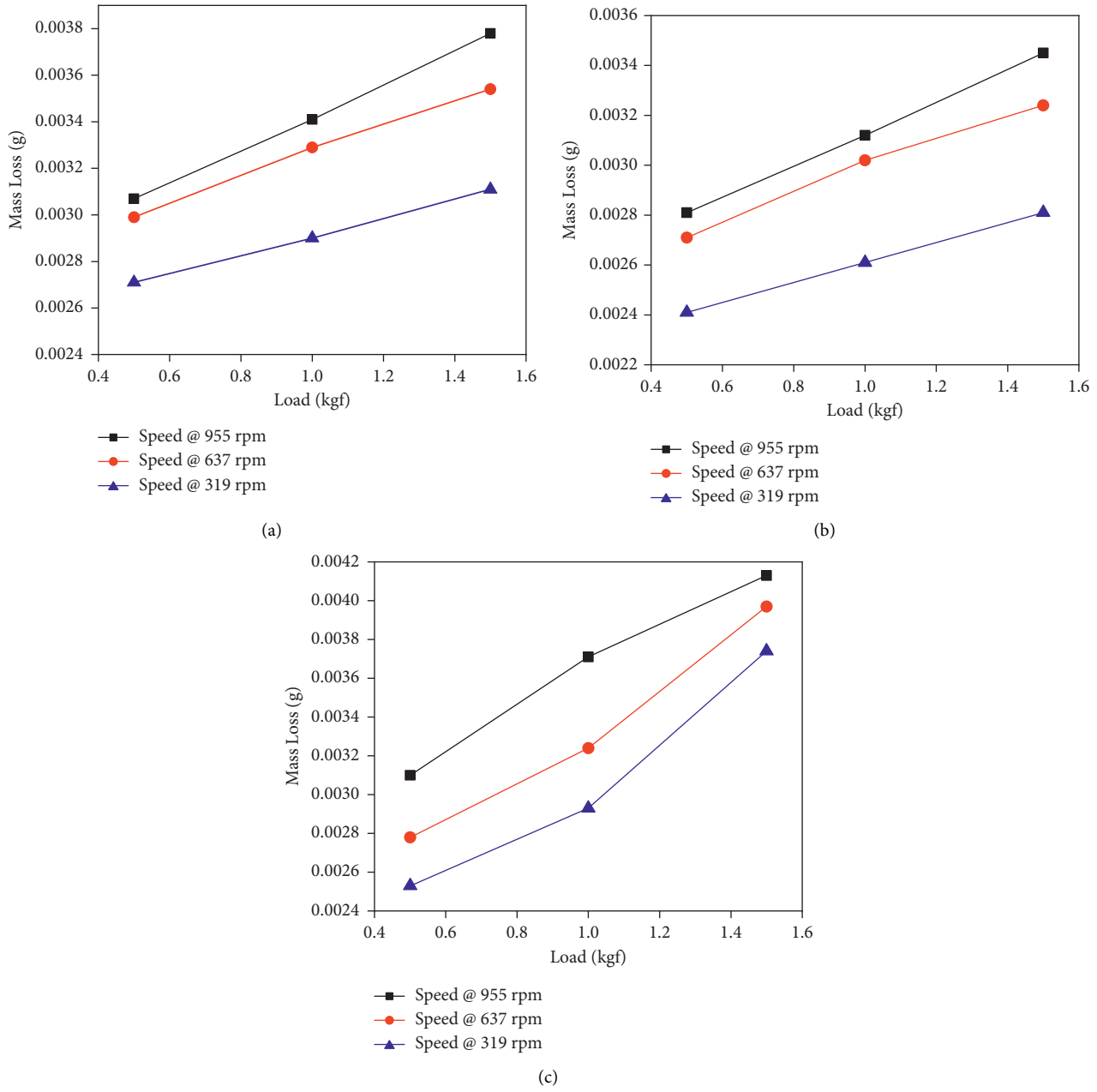

FIGURE 7: Mass loss measured during the experimentation with $Al_2O_3 + TiO_2$ coating for different rotational speeds: (a) $Al_2O_3 + TiO_2 + 1\%$ CNT, (b) $Al_2O_3 + TiO_2 + 3\%$ CNT, and (c) $Al_2O_3 + TiO_2 + 5\%$ CNT.

The wear resistance is directly proportional to the hardness of the sliding surface. For a rotating ball, the hardness is 85 HRC, and for the $Al_2O_3 + TiO_2$, it is 65 HRC. Both the materials are rich in hardness compared to the substrate material. During sliding experimentation, in addition to the influence of surface hardness, the frictional energy generated will highly influence to cause wear. In this research, the reinforcement of CNT in the the $Al_2O_3 + TiO_2$ has simultaneously increased, but in 5%, CNT reinforcement is maintaining the medium value of surface hardness because of more ceramic in the specimen. The behavior of CNT in $Al_2O_3 + TiO_2$ reveals the performance of diamond during sliding analysis. The maximum wear resistance of 5,800 Nm/mm^3 is recorded for 3% of CNT in $Al_2O_3 + TiO_2$. Wear resistance is also influenced by the process condition such as applied load and sliding velocity or speed.

3.5. Wear Mechanism. Figure 9 shows the SEM micrographs of wear track obtained on the worn-out surface of $Al_2O_3 + 3\,wt\%TiO_2$ coatings reinforced with different percentage proportions of CNTs. Microcracks and fragments of coating are observed on the wear track surface (Figures 9(a) and 9(c)), and more fragments of coating material that came out and fallen on the nearby coating can be seen in Figure 9(b). Also, the deep scratch can be noticed, and no

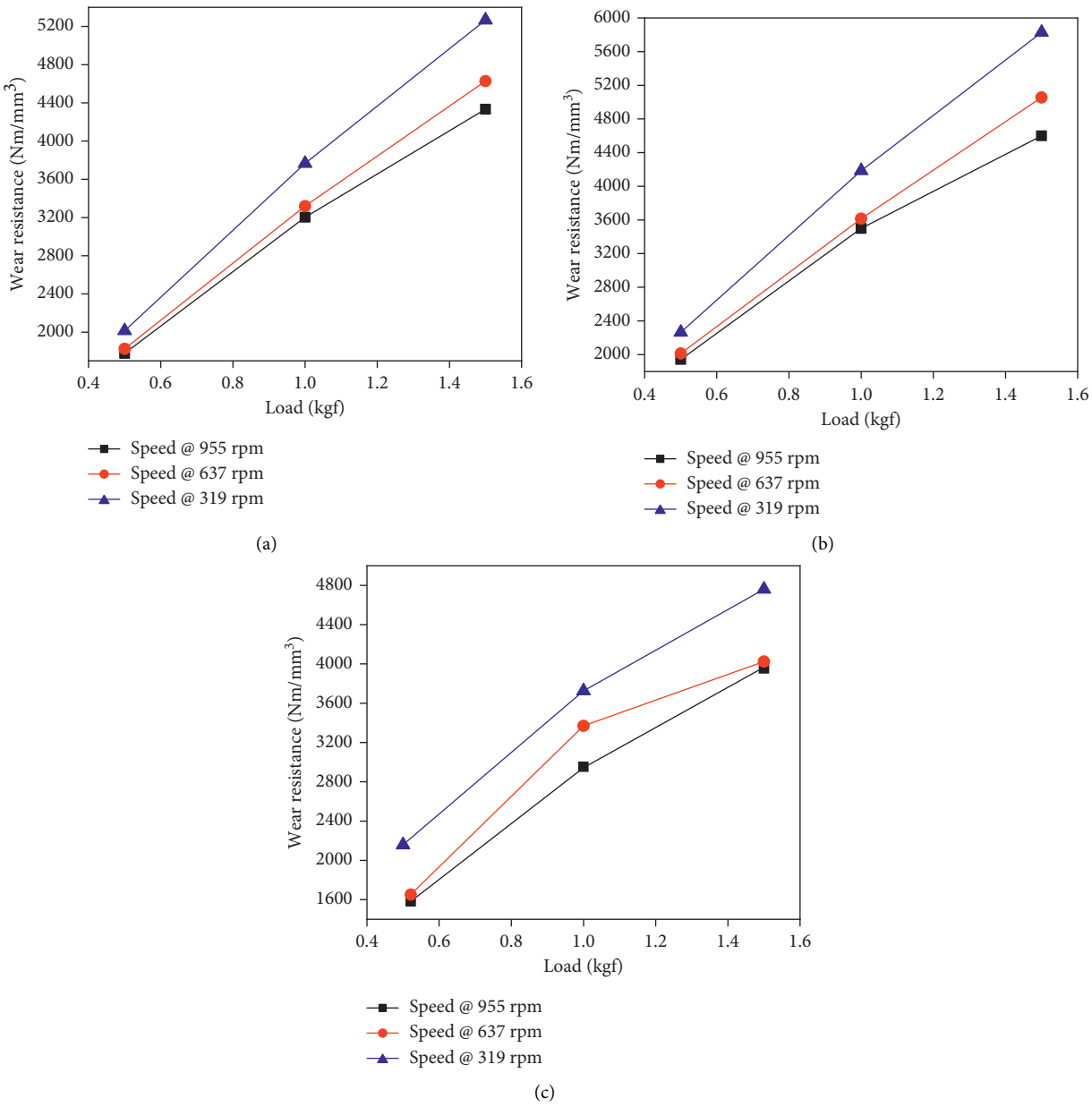

FIGURE 8: Calculated wear resistance for the test experiments on $Al_2O_3 + TiO_2$ coatings for different rotational speeds: (a) $Al_2O_3 + TiO_2 + 1\%$ CNT, (b) $Al_2O_3 + TiO_2 + 3\%$ CNT, and (c) $Al_2O_3 + TiO_2 + 5\%$ CNT.

cracks are observed (Figure 9(b)). The higher fragmentation of coating and crack formation can be attributed to the poor adhesion strength and low ductility of the coating. However, the higher coating thickness and lower percentage porosity reduced the wear loss of these coatings. However, the 3 wt% CNT addition has reduced the formation of microcracks and also the fragmentation of coating, and this can be attributed to the formation of CNTs bridges in the coating microstructure. Similar types of coating fragments were also noticed on the worn surface by [31].

The SEM micrograph of wear track morphology on the worn-out coating surface is shown in Figure 10. It can be observed that there are many microcracks on the worn surface due to cyclic stresses during the wear tests. The debris formed in the coating also can be seen (Figure 10(b)). The uniform mixing of CNT particles melted partially in the coating could improve the wear resistance of coatings. The wetting of the CNTs might be one reason for the good dispersion observed. Therefore, the nanotubes that are dispersed in the slurry appear relatively uniformly distributed over the $Al_2O_3 + 3\ wt\%TiO_2$ particle surface. The 1 wt% CNTs reinforced $Al_2O_3 + 3\ wt\%TiO_2$ coatings are showing the lower porosity minimizing the defects in the worn surface as shown in Figure 10(a). It can also be observed that the wear track width has been increased at a higher load. The wear debris is seen clearly in the 3% reinforced coatings (Figure 10(b)), and the cavities formed in the worn surface are due to the pull-out of coating material. In 5 wt% CNTs

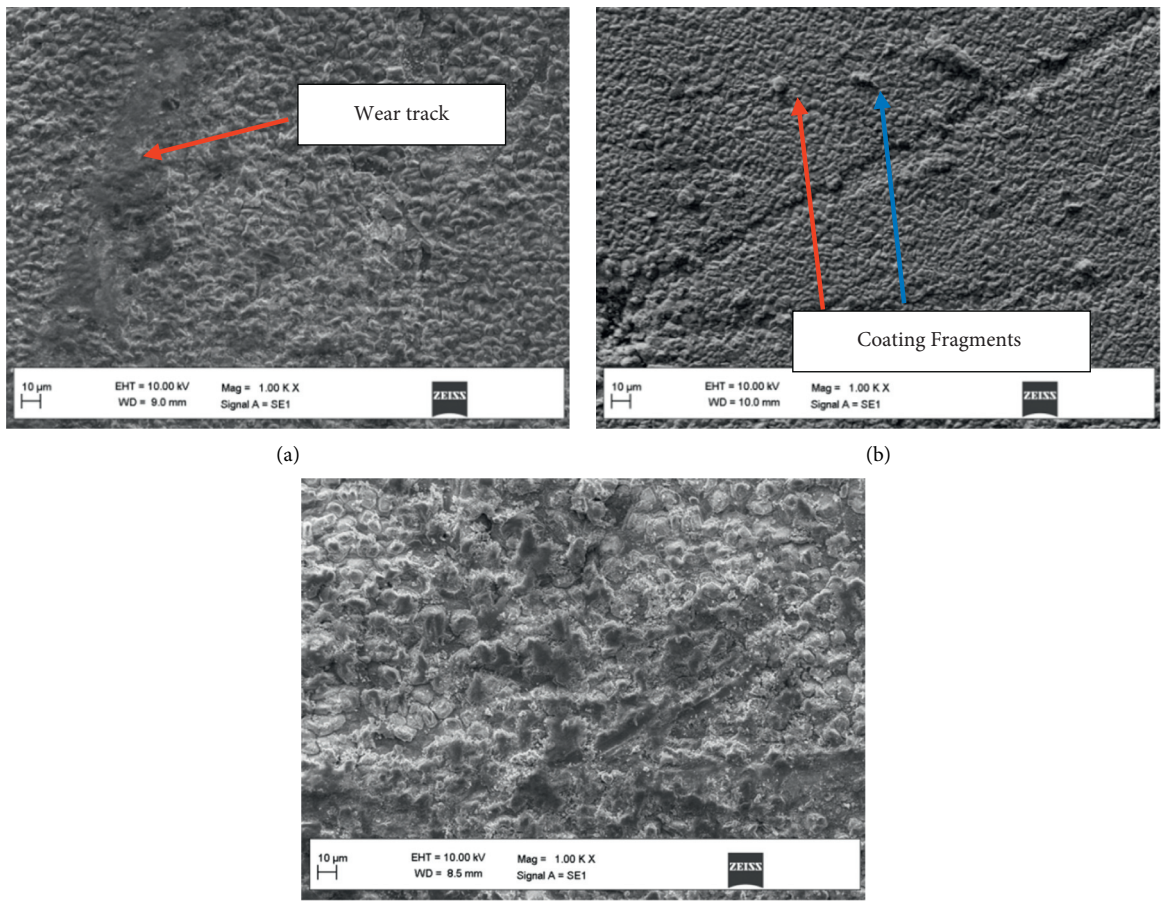

(a) (b)

(c)

Figure 9: SEM micrograph of wear track morphology on the worn-out surface obtained at 0.5 m/s sliding speed and 1 kgf normal load for (a) $Al_2O_3 + 3$ wt%$TiO_2 + 1$ wt% CNTs reinforced coating, (b) $Al_2O_3 + 3$ wt%$TiO_2 + 3$ wt% CNTs reinforced coating, and (c) $Al_2O_3 + 3$ wt% $TiO_2 + 5$ wt% CNTs reinforced coating.

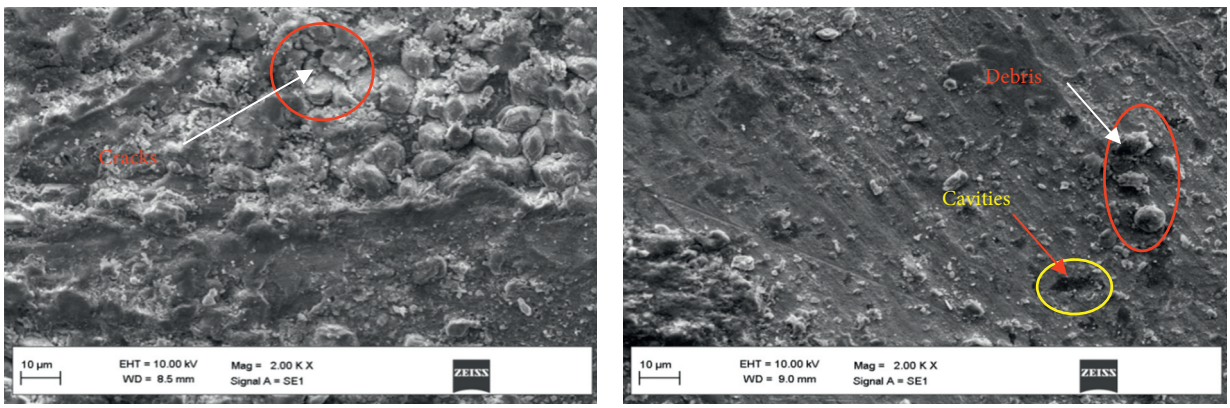

(a) (b)

Figure 10: Continued.

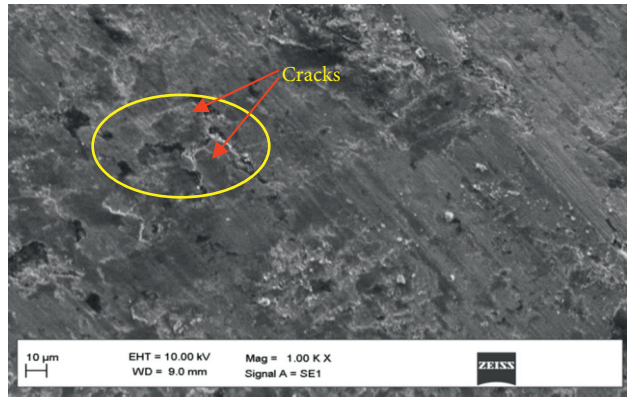

(c)

Figure 10: SEM micrograph of wear track morphology on the worn-out surface obtained at 0.17 m/s sliding speed and 1.5 kgf normal load for (a) $Al_2O_3 + 3$ wt%$TiO_2 + 1$ wt% CNT reinforced coating, (b) $Al_2O_3 + 3$ wt%$TiO_2 + 3$ wt% CNT reinforced coating, and (c) $Al_2O_3 + 3$ wt% $TiO_2 + 5$wt% CNT reinforced coating.

reinforced coatings, the cracks can be observed on the worn-out surface because of higher load and lesser sliding speed, which resulted in more cyclic stresses in the coating material (Figure 10(c)).

4. Concluding Remarks

In this work, the characteristics of the plasma-sprayed coatings obtained with and without CNTs reinforcement are evaluated and compared. Particularly, the percentage porosity and tribological characteristics of the coatings have been investigated thoroughly. The following conclusions can be drawn from this investigation:

(1) In all the coatings investigated, the micropores are present in their microstructure, and the percentage porosity is decreased with the increase of the percentage of CNTs. This is due to the metallurgical fusion and surface reaction of CNT with $Al_2O_3 + TiO_2$. As a result, the metallurgical reaction between the elements has simultaneously increased the surface hardness.

(2) The presence of micropores in 1% and 5% CNTs reinforced $Al_2O_3 + 3$ wt%TiO_2 coatings is minimum, and it has been noticed that the homogeneous distribution of CNTs and formation of CNTs bridges in these coatings have reduced the percentage porosity.

(3) It is also found that the weight loss in the coatings is more at higher loads and higher sliding speeds due to more cyclic stresses induced in the coating during the wear tests.

(4) It is observed that the weight loss is gradually reduced with the increase of CNTs reinforcement between 1 and 5 wt%.

(5) The good adhesion of coating that resulted in lesser weight loss has been observed in the case of 1% CNTs reinforced alumina-titania coatings, whereas in other coatings, very poor adhesion resulting in the formation of cracks has been observed.

(6) However, it can be clearly seen that the addition of CNTs to the alumina-titania coatings will improve their wear resistance and make them suitable for critical tribological applications.

Data Availability

No data were used to support this study.

Conflicts of Interest

The authors declare that they have no conflicts of interest.

References

[1] J. Lei, C. Shi, S. Zhou, Z. Gu, and L.-C. Zhang, "Enhanced corrosion and wear resistance properties of carbon fiber reinforced Ni-based composite coating by laser cladding," *Surface and Coatings Technology*, vol. 334, pp. 274–285, 2018.

[2] F. Wang, F. Zhang, L. Zheng, and H. Zhang, "Structure and corrosion properties of Cr coating deposited on aerospace bearing steel," *Applied Surface Science*, vol. 423, pp. 695–703, 2017b.

[3] A. Lekatou, D. Sioulas, A. E. Karantzalis, and D. Grimanelis, "A comparative study on the microstructure and surface property evaluation of coatings produced from nano-structured and conventional WC-Co powders HVOF-sprayed on Al7075," *Surface and Coatings Technology*, vol. 276, pp. 539–556, 2015.

[4] D. Wang, B. Zhang, C. Jia et al., "Influence of carbide grain size and crystal characteristics on the microstructure and mechanical properties of HVOF-sprayed WC-CoCr coatings," *International Journal of Refractory Metals and Hard Materials*, vol. 69, pp. 138–152, 2017a.

[5] F. Kern, P. Palmero, F. G. Marro, and A. Mestra, "Processing of alumina-zirconia composites by surface modification route with enhanced hardness and wear resistance," *Ceramics International*, vol. 41, no. 1, pp. 889–898, 2015.

[6] J. Mehta, V. K. Mittal, and P. Gupta, "Role of thermal spray coatings on wear, erosion and corrosion behavior: a review," *Journal of Applied Science and Engineering*, vol. 20, no. 4, pp. 445–452, 2017.

[7] M. A. Zavareh, A. A. D. M. Sarhan, B. B. A. Razak, and W. J. Basirun, "Plasma thermal spray of ceramic oxide coating on carbon steel with enhanced wear and corrosion resistance for oil and gas applications," *Ceramics International*, vol. 40, no. 9, pp. 14267–14277, 2014.

[8] M. Peters, C. Leyens, U. Schulz, and W. A. Kaysser, "EB-PVD thermal barrier coatings for aeroengines and gas turbines," *Advanced Engineering Materials*, vol. 3, no. 4, pp. 193–204, 2001.

[9] G. Mauer, R. Vaßen, and D. Stöver, "Detection of melting temperatures and sources of errors using two-color pyrometry during in-flight measurements of atmospheric plasma-sprayed particles," *International Journal of Thermophysics*, vol. 29, no. 2, pp. 764–786, 2008.

[10] A. Richter, L. M. Berger, Y. J. Sohn, S. Conze, K. Sempf, and R. Vaßen, "Impact of Al2O3-40 wt.% TiO2 feedstock powder characteristics on the sprayability, microstructure and mechanical properties of plasma sprayed coatings," *Journal of the European Ceramic Society*, vol. 39, no. 16, pp. 5391–5402, 2019.

[11] P. Carpio, Q. Blochet, B. Pateyron et al., "Correlation of thermal conductivity of suspension plasma sprayed yttria stabilized zirconia coatings with some microstructural effects," *Materials Letters*, vol. 107, pp. 370–373, 2013.

[12] S. Tailor, M. Singh, R. M. Mohanty, and A. V. Doub, "Microstructural and thermal properties of plasma sprayed YSZ nano-clusters thermal barrier coatings," *Journal of Cluster Science*, vol. 27, no. 5, pp. 1501–1518, 2016.

[13] N. Curry, N. Markocsan, X. H. Li, A. Tricoire, and M. Dorfman, "Next generation thermal barrier coatings for the gas turbine industry," *Journal of Thermal Spray Technology*, vol. 20, no. 1-2, pp. 108–115, 2011.

[14] N. Curry, N. Markocsan, L. Östergren, X.-H. Li, and M. Dorfman, "Evaluation of the lifetime and thermal conductivity of dysprosia-stabilized thermal barrier coating systems," *Journal of Thermal Spray Technology*, vol. 22, no. 6, pp. 864–872, 2013.

[15] F. Cernuschi, "Can TBC porosity be estimated by non-destructive infrared techniques? a theoretical and experimental analysis," *Surface and Coatings Technology*, vol. 272, pp. 387–394, 2015.

[16] A. Portinha, V. Teixeira, J. Carneiro et al., "Residual stresses and elastic modulus of thermal barrier coatings graded in porosity," *Surface and Coatings Technology*, vol. 188-189, pp. 120–128, 2004.

[17] A. Kulkarni, A. Goland, H. Herman et al., "Advanced neutron and X-ray techniques for insights into the microstructure of EB-PVD thermal barrier coatings," *Materials Science and Engineering*, vol. 426, no. 1-2, pp. 43–52, 2006.

[18] W. Chi, S. Sampath, and H. Wang, "Microstructure-thermal conductivity relationships for plasma-sprayed yttria-stabilized zirconia coatings," *Journal of the American Ceramic Society*, vol. 91, no. 8, pp. 2636–2645, 2008.

[19] Z. Piao, B. Xu, H. Wang, and C. Pu, "Effects of thickness and elastic modulus on stress condition of fatigue-resistant coating under rolling contact," *Journal of Central South University of Technology*, vol. 17, no. 5, pp. 899–905, 2010.

[20] Z. H. Wen, Y. Bai, J. F. Yang, and J. Huang, "Effect of vacuum re-melting on the solid particles erosion behavior of Ni60-NiCrMoY composite coatings prepared by plasma spraying," *Vacuum*, vol. 134, pp. 73–82, 2016.

[21] N. Serres, F. Hlawka, S. Costil, C. Langlade, and F. Machi, "Microstructures and environmental assessment of metallic NiCrBSi coatings manufactured via hybrid plasma spray process," *Surface and Coatings Technology*, vol. 205, no. 4, pp. 1039–1046, 2010.

[22] N. Serres, F. Hlawka, S. Costil, C. Langlade, and F. Machi, "An investigation of the mechanical properties and wear resistance of NiCrBSi coatings carried out by in situ laser remelting," *Wear*, vol. 270, no. 9-10, pp. 640–649, 2011.

[23] S. Sivaprakasam, M. O. Sikder, L. Ramalingam, G. Kaur, J. M. Dufour, and N. Moustaid-Moussa, "SLC6A14 deficiency is linked to obesity, fatty liver, and metabolic syndrome but only under conditions of a high-fat diet," *Biochimica et Biophysica Acta (BBA)-Molecular Basis of Disease*, vol. 1867, no. 5, Article ID 166087, 2021.

[24] G. M. T. Basha, A. Srikanth, and B. Venkateshwarlu, "Effect of reinforcement of carbon nanotubes on air plasma sprayed conventional Al2O3-3% TiO2 ceramic coatings," *Materials Today: Proceedings*, vol. 20, pp. 191–194, 2020.

[25] F. Huang, H. Xu, W. Liu, and S. Zheng, "Microscopic characteristics and properties of titaniferous compound reinforced nickel-based wear-resisting layer via in situ precipitation of plasma spray welding," *Ceramics International*, vol. 44, no. 6, pp. 7088–7097, 2018.

[26] M. A. Samad and S. K. Sinha, "Mechanical, thermal and tribological characterization of a UHMWPE film reinforced with carbon nanotubes coated on steel," *Tribology International*, vol. 44, no. 12, pp. 1932–1941, 2011.

[27] K. Nemeth, N. Varro, B. Reti et al., "Synthesis and investigation of SiO2-MgO coated MWCNTs and their potential application," *Scientific Reports*, vol. 9, no. 1, pp. 15113–15211, 2019.

[28] Y. Zhang, T. T. Zuo, Z. Tang et al., "Microstructures and properties of high-entropy alloys," *Progress in Materials Science*, vol. 61, pp. 1–93, 2014.

[29] E2109-01, *Standard Test Methods for Determining Area Percentage Porosity in Thermal Sprayed Coatings*, ASTM International, West Conshohocken, PA, USA, 2014.

[30] J. G. Thakare, R. S. Mulik, and M. M. Mahapatra, "Effect of carbon nanotubes and aluminum oxide on the properties of a plasma sprayed thermal barrier coating," *Ceramics International*, vol. 44, no. 1, pp. 438–451, 2018.

[31] K. Yang, J. Li, Q. Wang, Z. Li, Y. Jiang, and Y. Bao, "Effect of laser remelting on microstructure and wear resistance of plasma sprayed Al2O3-40% TiO2 coating," *Wear*, vol. 426, pp. 314–318, 2019.